ICUS REPORT 2008 - 02

INTERNATIONAL CENTER FOR
URBAN SAFETY ENGINEERING

INSTITUTE OF INDUSTRIAL SCIENCE
THE UNIVERSITY OF TOKYO

JOINT STUDENT SEMINAR ON CIVIL INFRASTRUCTURES
July 3-4, 2008

Edited by

Kyung-Ho Park, Shinji Tanaka and Seok-Won Lee
ICUS, IIS, The University of Tokyo, Japan

ISBN 4-903661-21-0

Serial Number 30

Joint Student Seminar on Civil Infrastructures

3-4 July 2008
Bangkok, Thailand

Co-Organized by

School of Engineering and Technology,
Asian Institute of Technology (AIT), Thailand

International Center for Urban Safety Engineering (ICUS)
Institute of Industrial Science
The University of Tokyo, Japan

BK-21 Global Leaders in Construction Engineering,
Korea University, Korea

Research Team for Maintenance Technology of Infrastructure,
Konkuk University, Korea

and
King Monkut's University
of Technology North Bangkok, Thailand

Edited by

Dr. Kyung-Ho Park, Dr. Shinji Tanaka and Dr. Seok-Won Lee

Organization Teams

Dr. Kyung-Ho Park (AIT, Thailand)
Dr. Pison Udomworrat (KMUT-NB, Thailand)

Dr. Shinji Tanaka (UT, Japan)
Dr. Wataru Takeuchi (UT, Japan)
Dr. Kawin Worakanchana (UT, Japan)
Dr. Shinya Hanaoka (TIT, Japan)

Dr. Jung-Sik Kong (KU, Korea)
Dr. Seok-Won Lee (KKU, Korea)
Dr. Young-Uk Kim (MU, Korea)

JOINT STUDENT SEMINAR ON CIVIL INFRASTRUCTURES

ICUS Report No. 30, July 2008

PREFACE

As our activities expand beyond the border, international collaboration becomes more and more important. And, to build up a good relationship with other communities during young school days will be of advantage in the future. Considering this background, we planned and organized “the joint student seminar on civil infrastructure”, so as to foster international friendship and communication among universities from 3 countries; Thailand, Japan and Korea.

The objectives of this seminar are,
1) to experience the organization of international seminar,
2) to improve the presentation skill,
3) to share the research information and friendships.

The number of participants was 55, consist of 8 faculties and 47 students from Konkuk University, Myongji University, Korea Advance Institute of Science and Technology, KMUT-NB, The University of Tokyo and Asian Institute of Technology universities. On the first day, we had a presentation session, having 5 faculties’ lectures and 17 students’ presentations. The topics were varied from all areas of civil engineering and every student did their best in his/her presentation as well as in the discussion. On the second day, we had a field visit to the Suvarnabhumi airport rail link and city air terminal project. Looking at a huge scale project, the students could learn technologies, project management, cultural differences, and so on.

Although it was a first trial of this kind of joint seminar, it was really successful and fruitful judging from the students’ response. We believe this seminar gave not only knowledge and information but also a lot of other stimuli to the students. And we hope to continue to hold this kind of interchange activities in the future, too.

Finally, we would like to express our sincere gratitude for those who kindly supported and contributed to the success of this seminar.

KYUNG-HO PARK, SHINJI TANAKA, SEOK-WON LEE

Table of Contents

Welcome board

Registration

Booth at seminar

Opening ceremony (Dr. Park)

Dr. Pennung Warnitchai

Prof. Kimiro Meguro

Dr. Gye-Chun Cho

Dr. Shinji Tanaka

Dr. Pison Udomworarat

Mr. Tomoya Kawasak

Mr. Sung-Woo Choi

Mr. Adisorn Owatsiriwong

Mr. Yusuke Matsumura

Ms. Seon-Ah Jo

Mr. Phuong Tung Hoang

Mr. Michael Henry

Mr. Tran Viet Dung

Mr. Ekkachai Yooprasertchai

Mr. Hiroaki Ebizuka

Mr. Weeraporn Phongtinnaboot

Mr. Tae-Min Oh

Mr. Yong-Hun Eom

Mr. Hiroaki Nishiuchi

Mr. Naoki Sorimachi

Mr. Kittipong Suweero

Presentation Airport Rail Link

Field Trip: Airport Rail Link and City Air Terminal

Group Photo

Invited Lectures

SEISMIC EVALUATION OF EXISTING REINFORCED CONCRETE BUILDINGS

PENNUNG WARNITCHAI and MATRIN SUTHASIT
School of Engineering and Technology
Asian Institute of Technology, Thailand
pennung@ait.ac.th

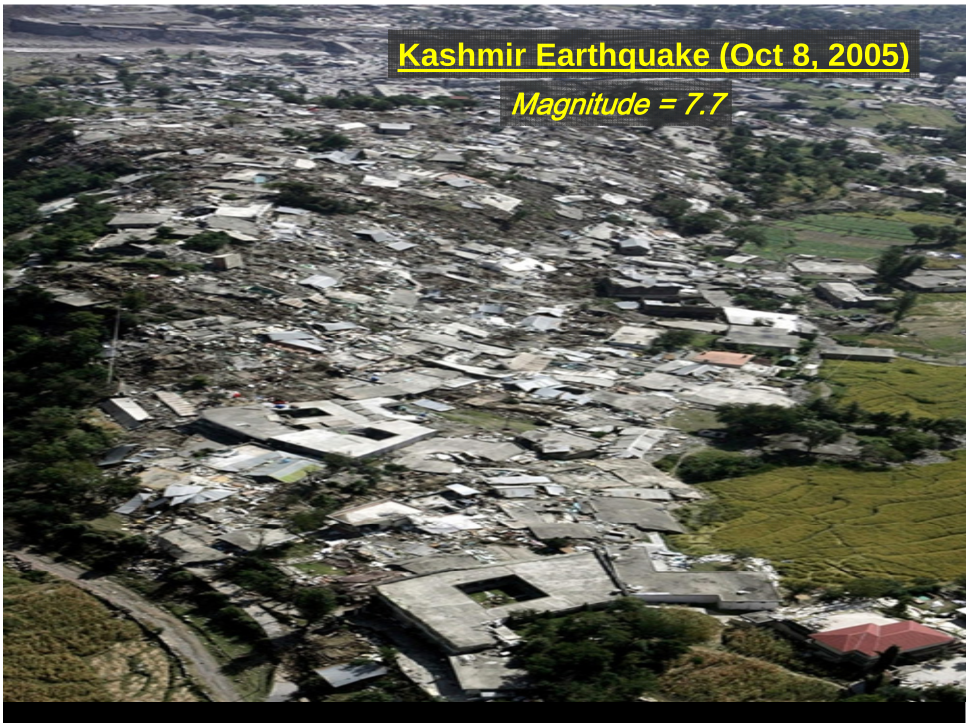


Balakot, Kashmir Earthquake (2005)
Magnitude = 7.7


BPKP Building (Sewon, Yogyakarta, 2006)
Yogyakarta Earthquake (2006)
Magnitude = 6.2


ISI Building (Sewon)
Yogyakarta Earthquake (2006)
Magnitude = 6.2


Brittle Failure in Column

Nonductile Reinforcement Details

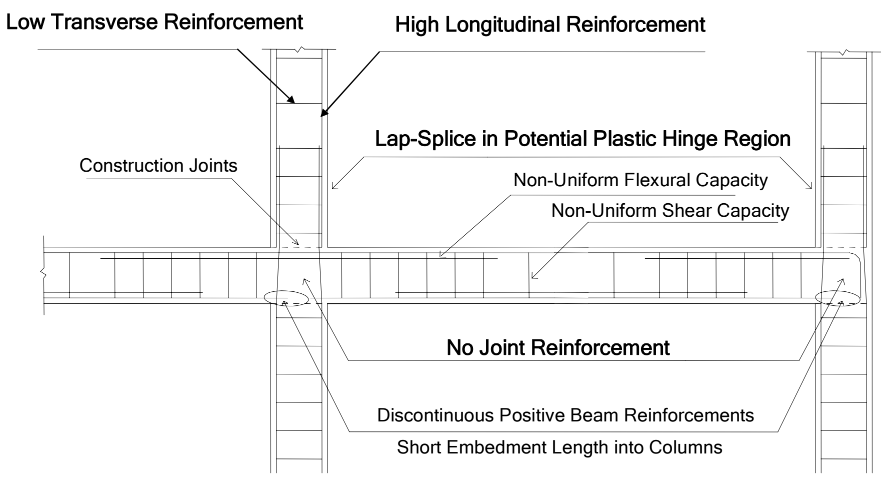

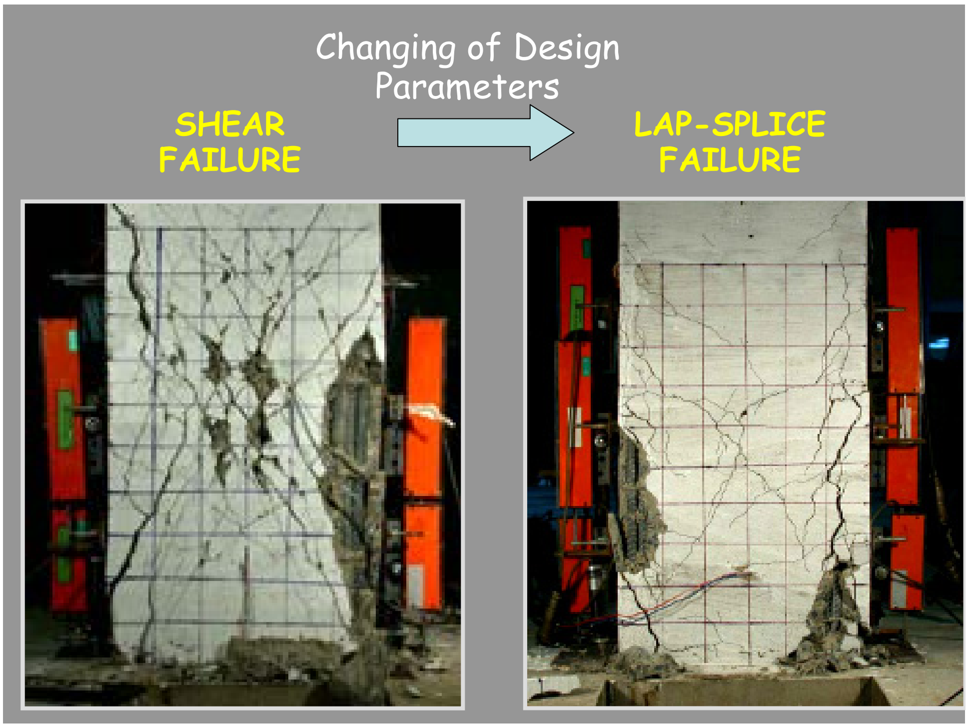
Changing of Design Parameters
SHEAR FAILURE
LAP-SPLICE FAILURE

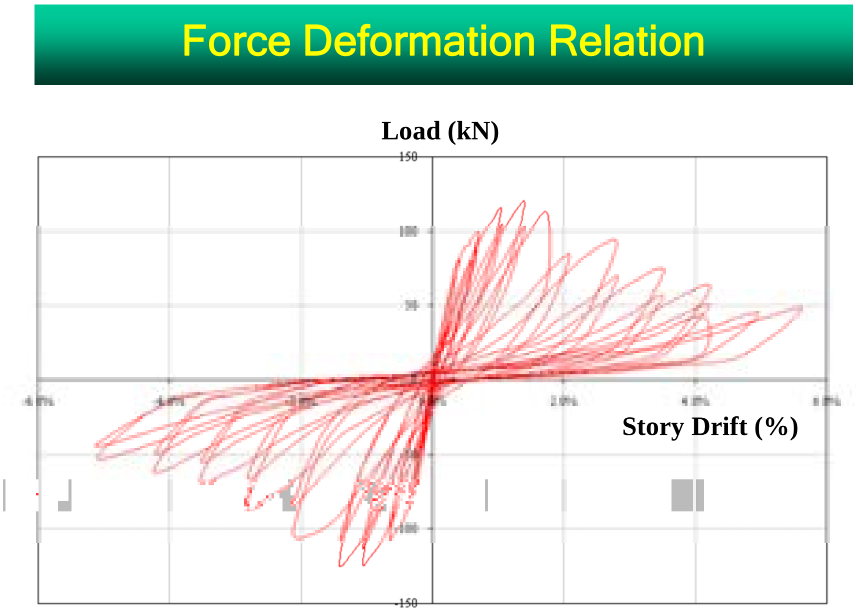
Force Deformation Relation
Load (kN)
150
100
50
-100
-150
2.0%
4.0%
Story Drift (%)

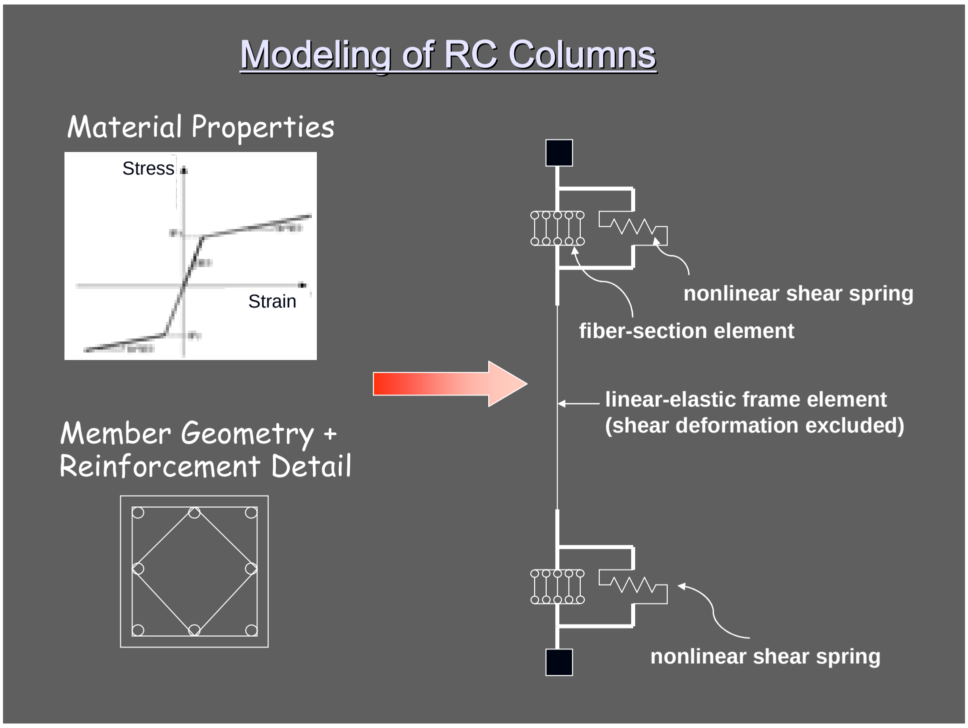
Modeling of RC Columns
Material Properties
Stress
Strain
Member Geometry +
Reinforcement Detail
nonlinear shear spring
fiber-section element
linear-elastic frame element
(shear deformation excluded)
nonlinear shear spring

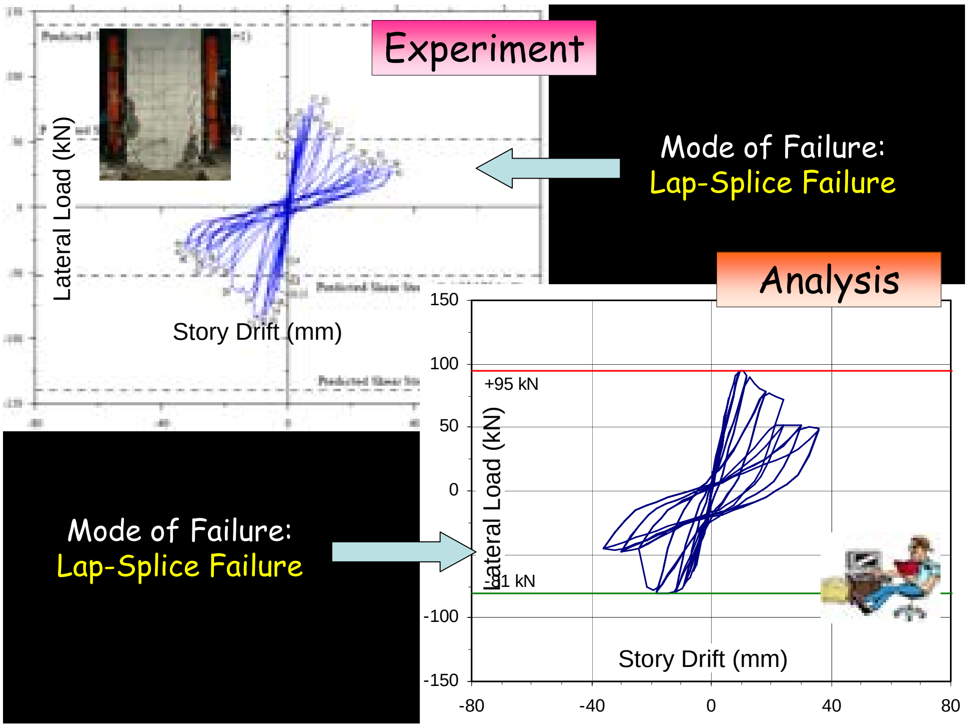
Experiment
Lateral Load (kN)
Story Drift (mm)
Mode of Failure:
Lap-Splice Failure
Analysis
Mode of Failure:
Lap-Splice Failure
150
100
50
0
-100
-150
+95 kN
Lateral Load (kN)
Story Drift (mm)
-80
-40
0
40
80

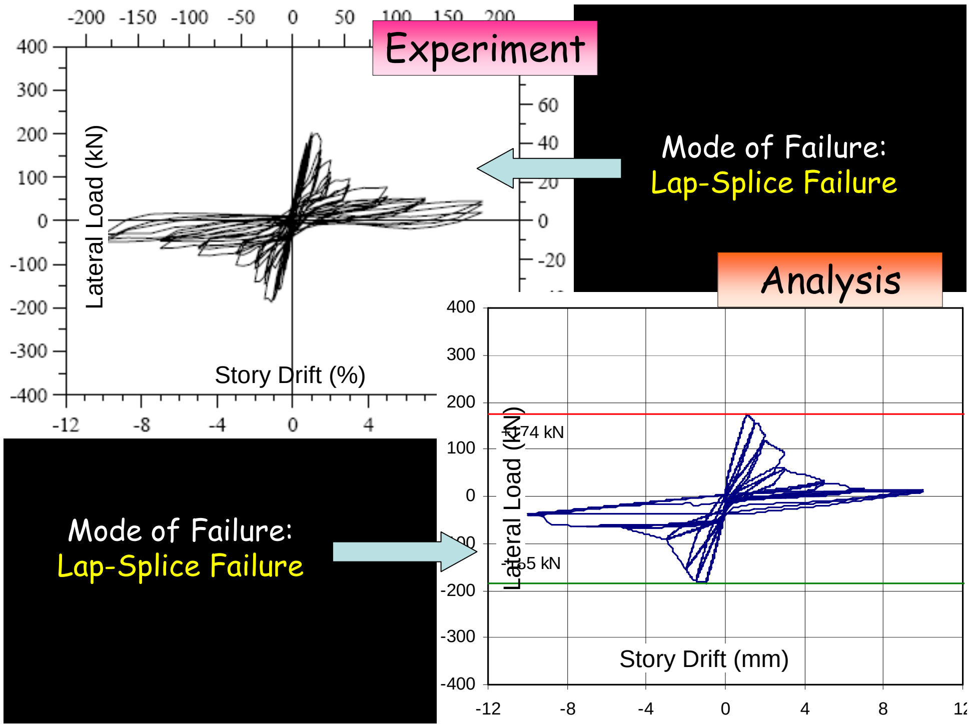
Experiment
Mode of Failure:
Lap-Splice Failure
Lateral Load (kN)
Story Drift (%)
Analysis
Mode of Failure:
Lap-Splice Failure
174 kN
Story Drift (mm)

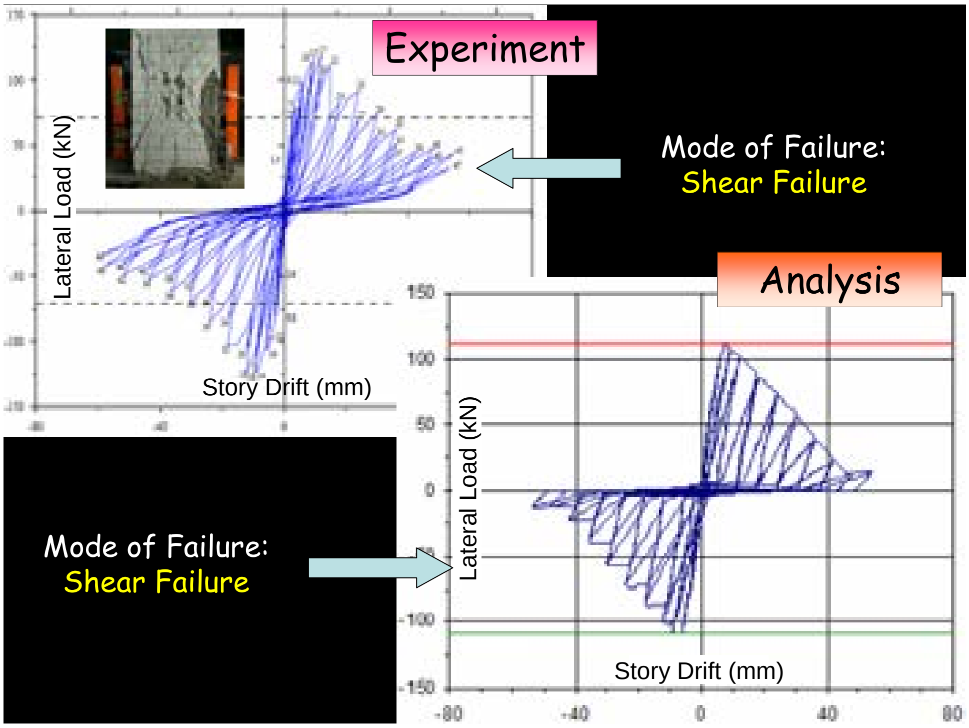
Experiment
Mode of Failure:
Shear Failure
Lateral Load (kN)
Story Drift (mm)
Analysis
Mode of Failure:
Shear Failure
Lateral Load (kN)
Story Drift (mm)

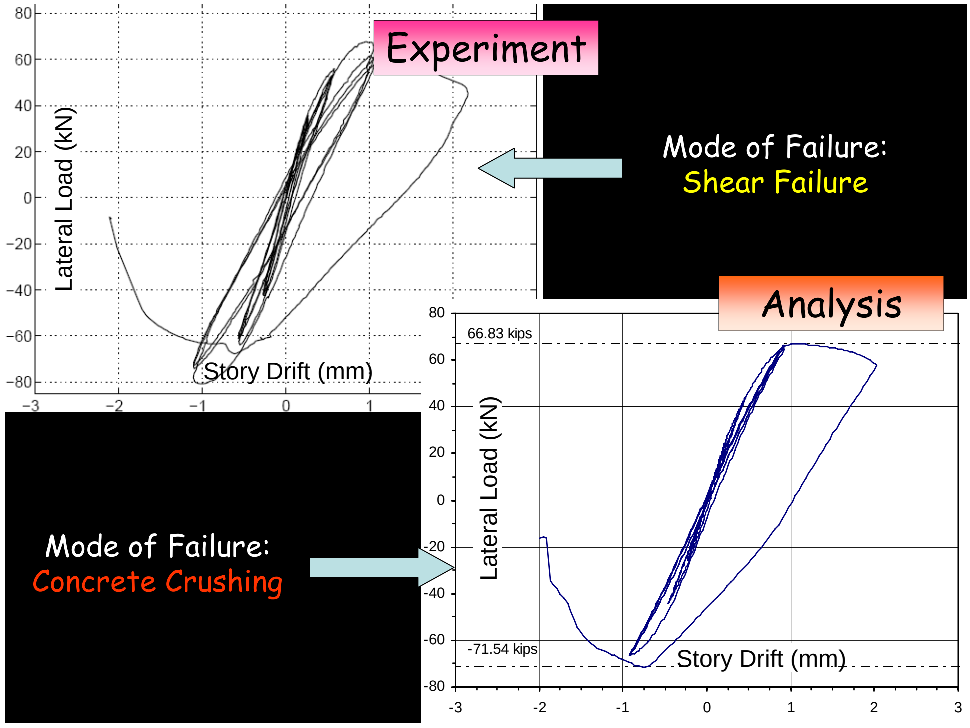
Experiment
Analysis
Mode of Failure:
Shear Failure
Mode of Failure:
Concrete Crushing
Lateral Load (kN)
Story Drift (mm)
66.83 kips
-71.54 kips
80
60
40
20
0
-20
-40
-60
-80
-3
-2
-1
0
1
2
3


Beam-Column Joint Failure

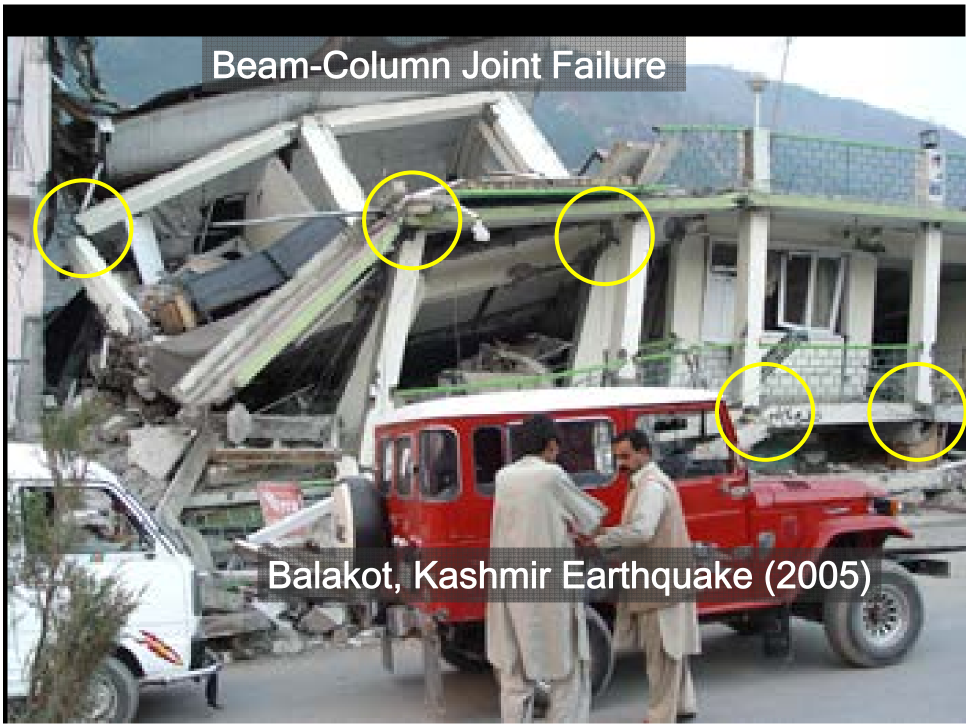
Beam-Column Joint Failure
Balakot, Kashmir Earthquake (2005)

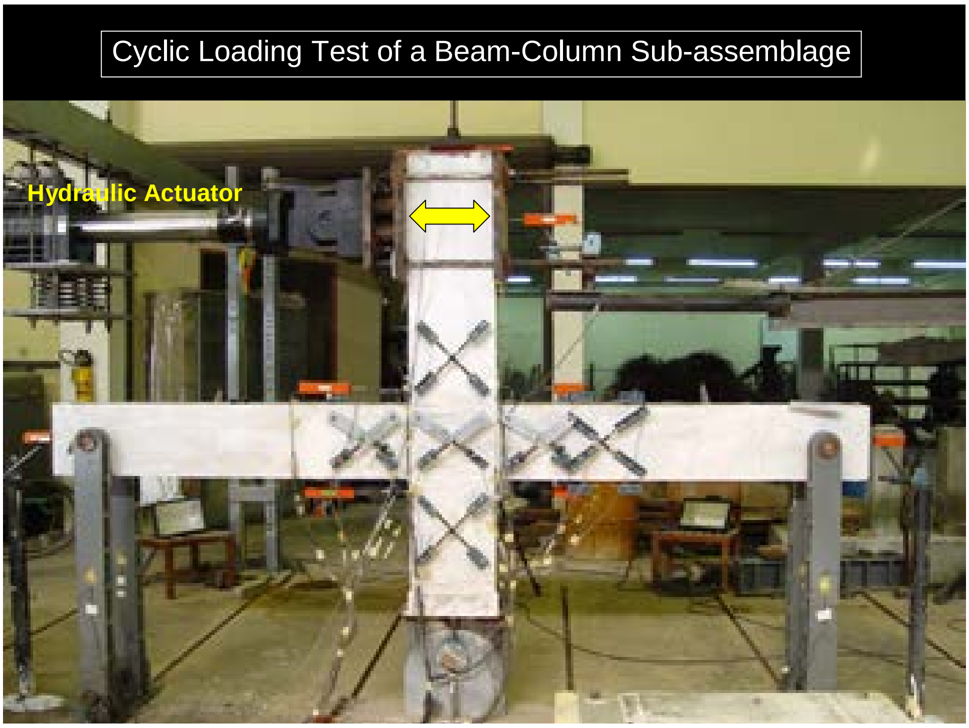
Cyclic Loading Test of a Beam-Column Sub-assemblage
Hydraulic Actuator

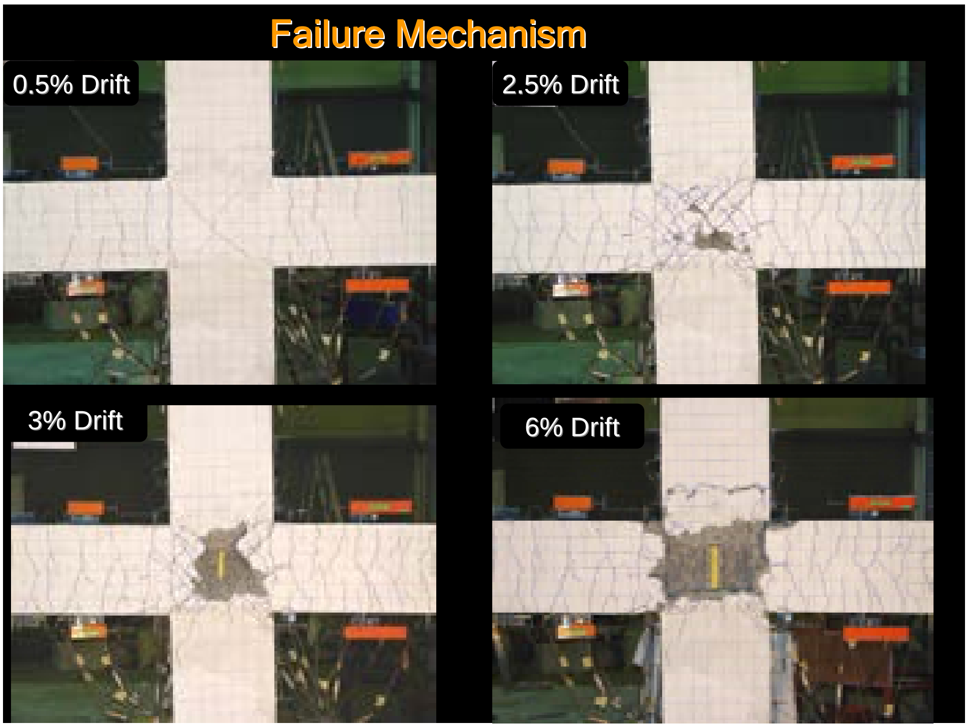
Failure Mechanism
0.5% Drift
2.5% Drift
3% Drift
6% Drift

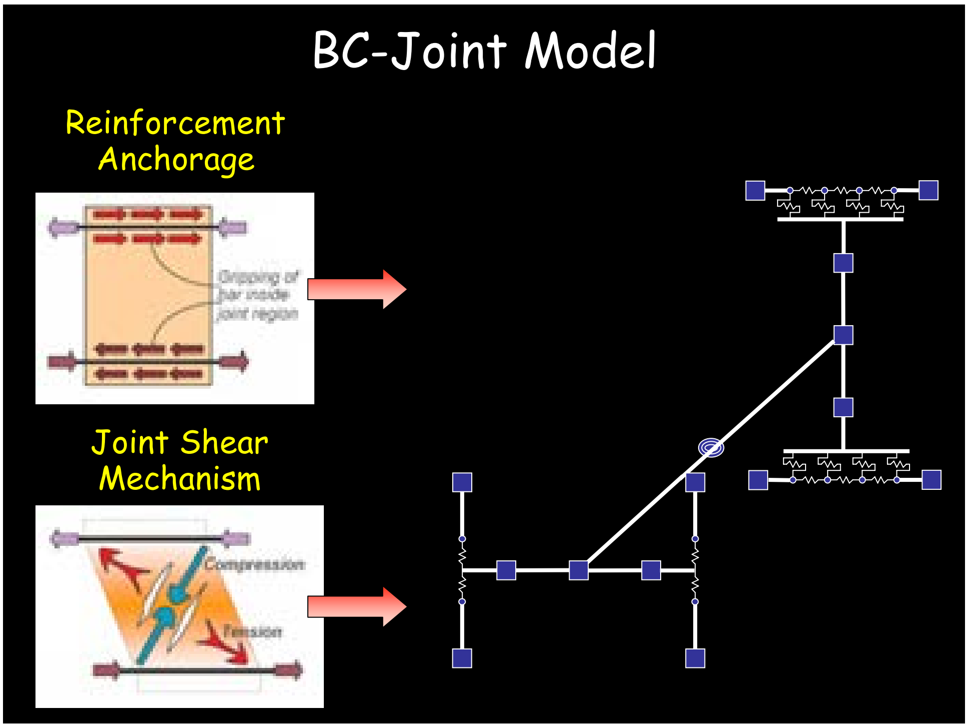
BC-Joint Model
Reinforcement Anchorage
Gripping of bar inside joint region
Joint Shear Mechanism
Compression
Tension

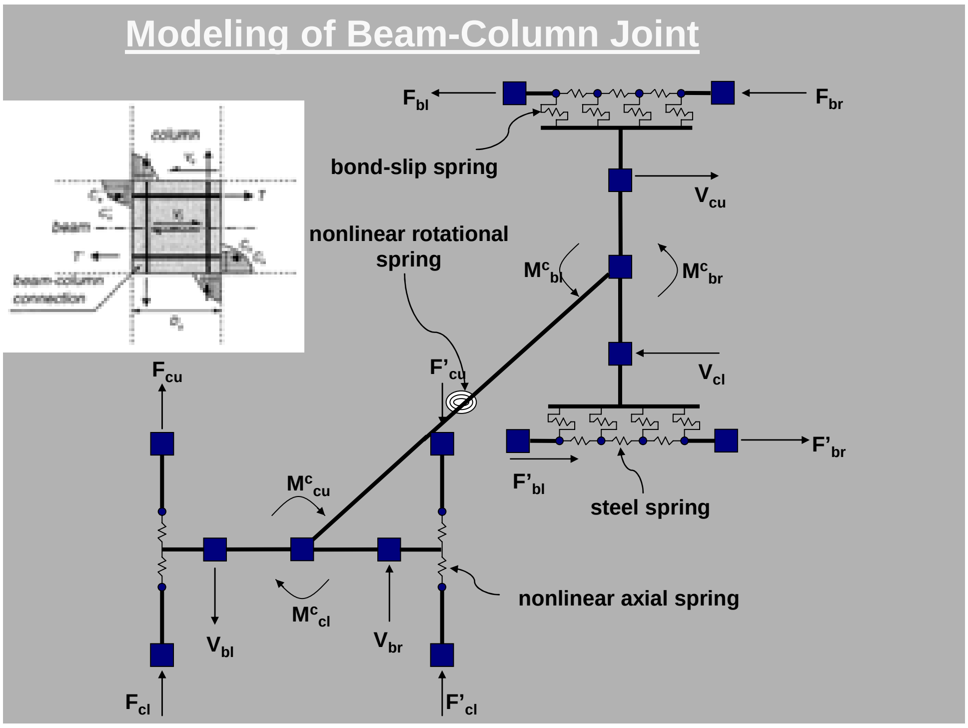
Modeling of Beam-Column Joint
bond-slip spring
nonlinear rotational spring
steel spring
nonlinear axial spring
column
beam
beam-column connection

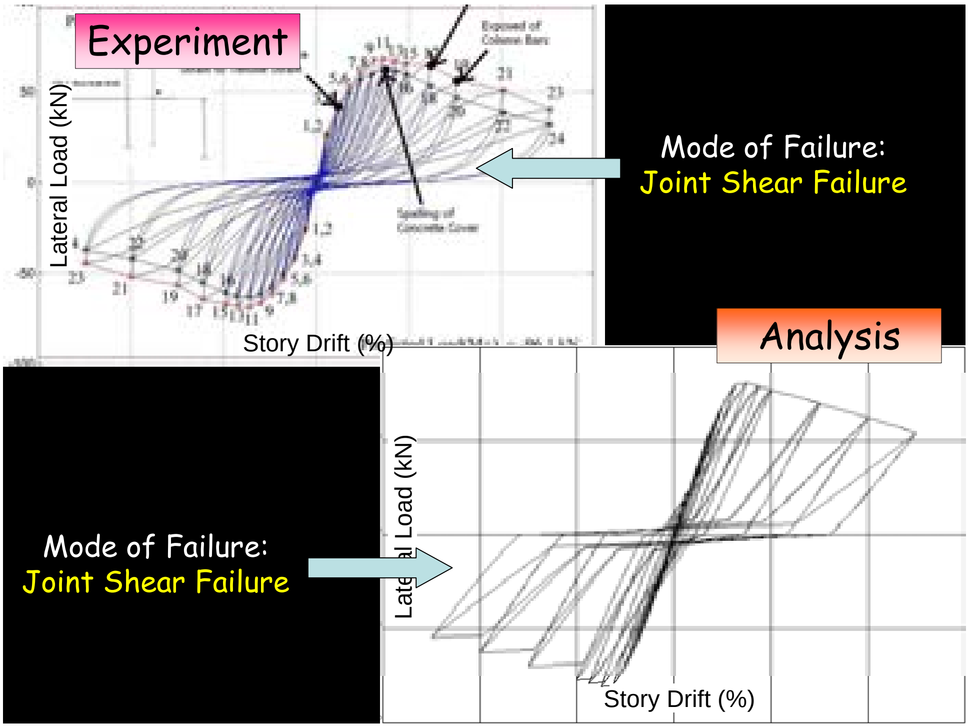
Experiment
Lateral Load (kN)
Story Drift (%)
Mode of Failure:
Joint Shear Failure
Analysis
Mode of Failure:
Joint Shear Failure
Lateral Load (kN)
Story Drift (%)

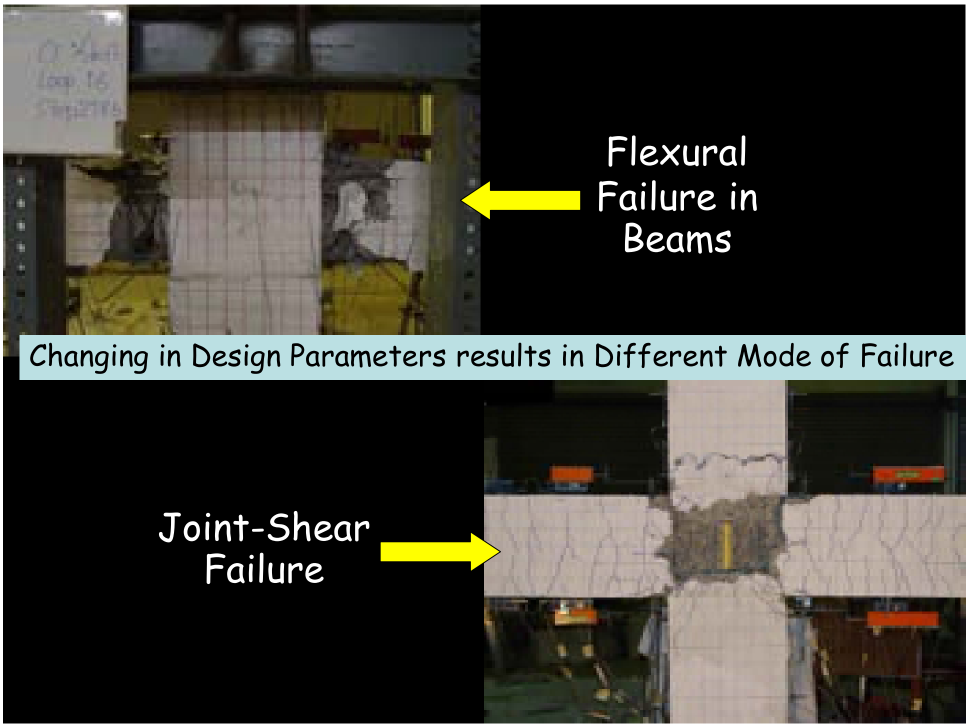
Flexural Failure in Beams
Changing in Design Parameters results in Different Mode of Failure
Joint-Shear Failure

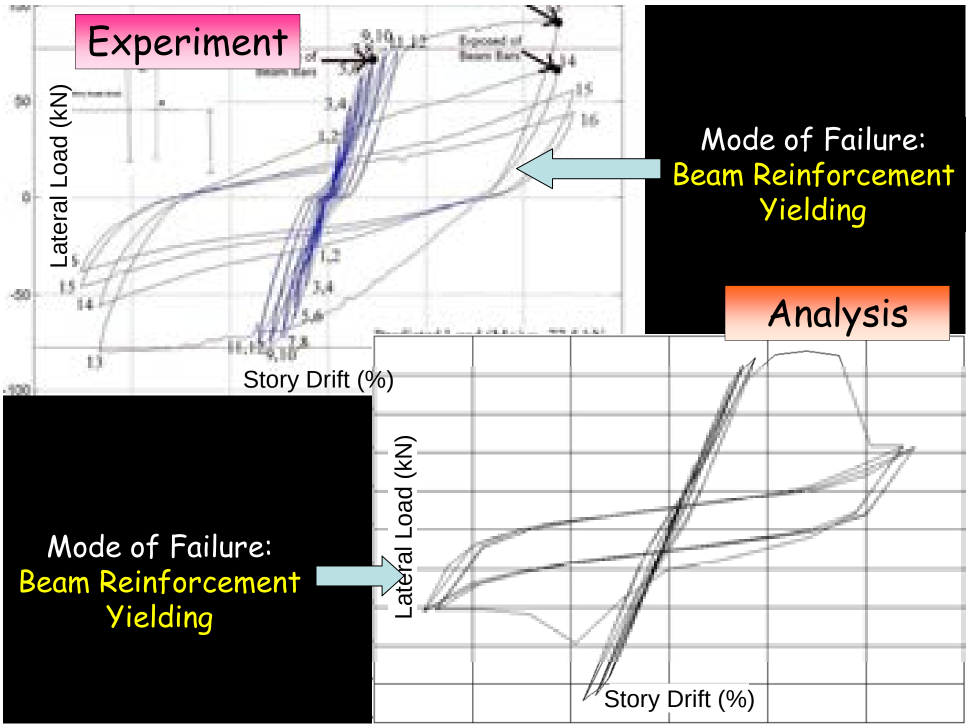
Experiment
Lateral Load (kN)
Story Drift (%)
Mode of Failure: Beam Reinforcement Yielding
Analysis
Mode of Failure: Beam Reinforcement Yielding
Lateral Load (kN)
Story Drift (%)

Masonry Infill Wall Failure

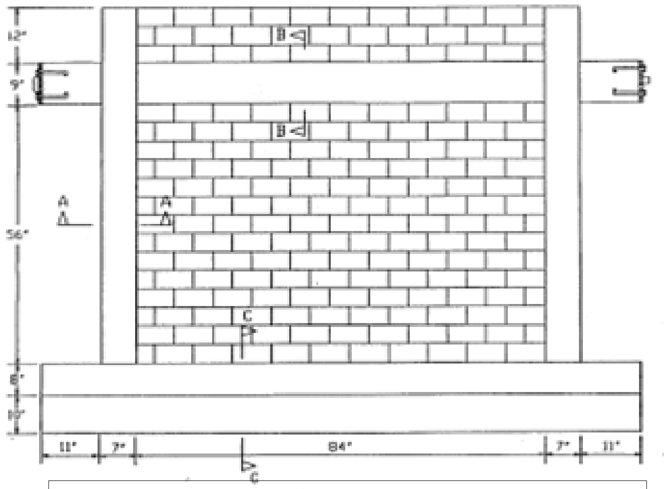

Quasi-Static Experiment of GLD RC frame with infill wall conducted by Mehrabi et al. (1994) at University of Colorado, Boulder

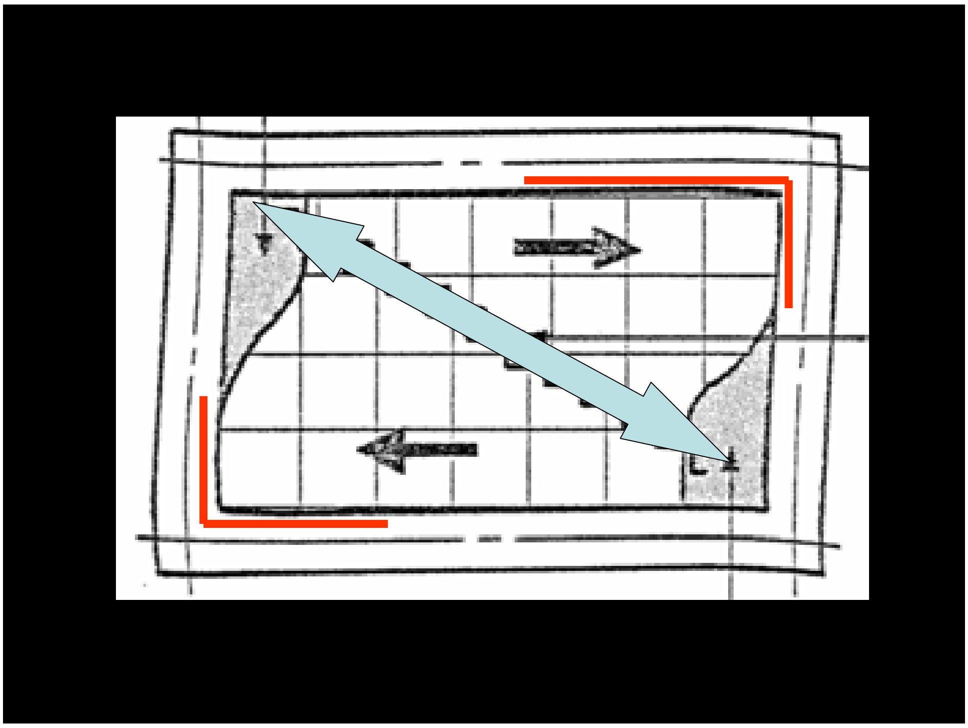

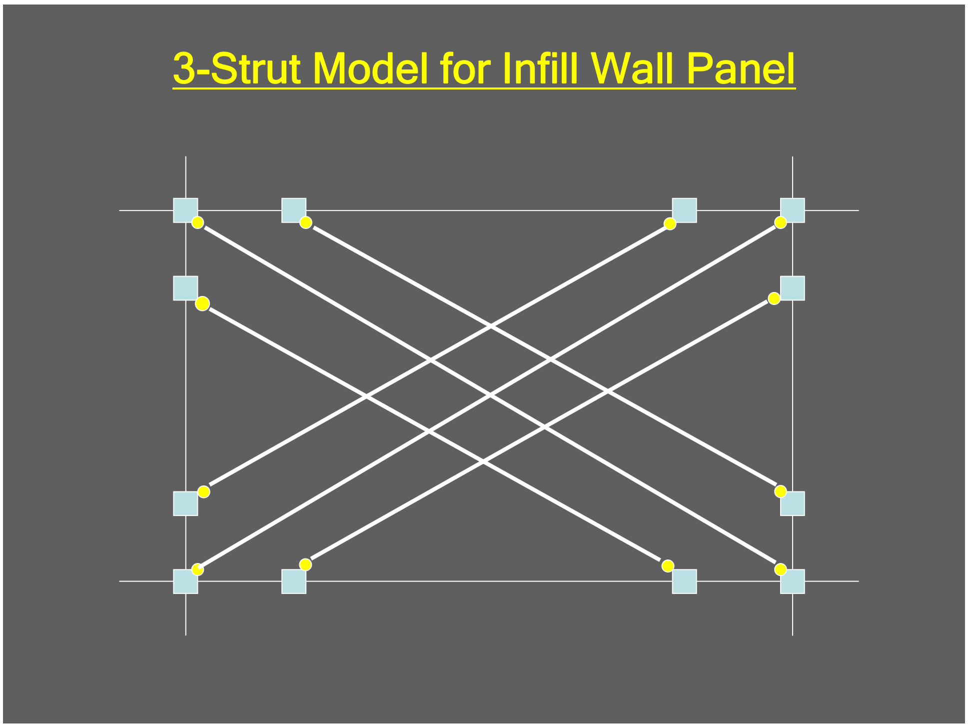

Comparison—RC Frame with Masonry Infill Wall

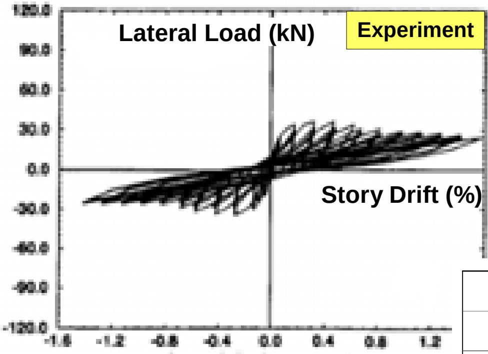

Mode of Failure: Infill Wall Failure

Mode of Failure: Infill Wall Failure

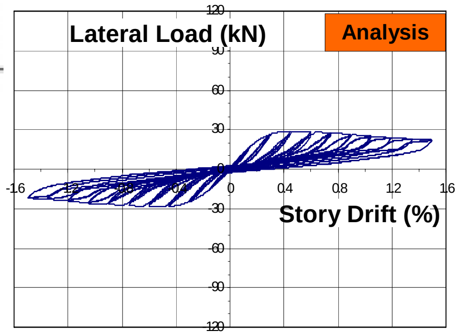

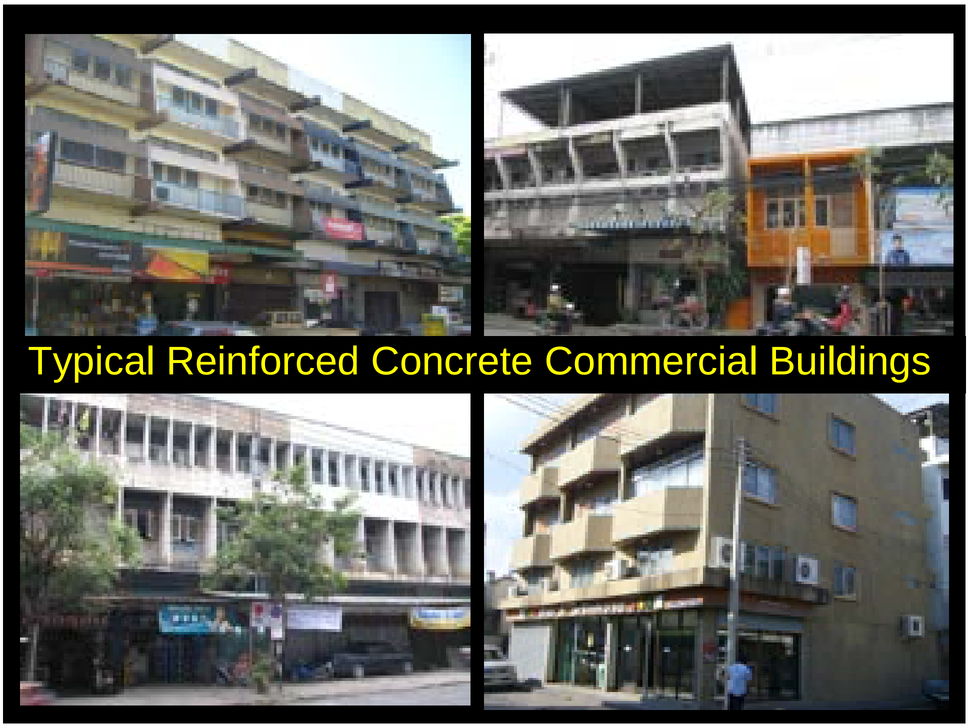
Typical Reinforced Concrete Commercial Buildings

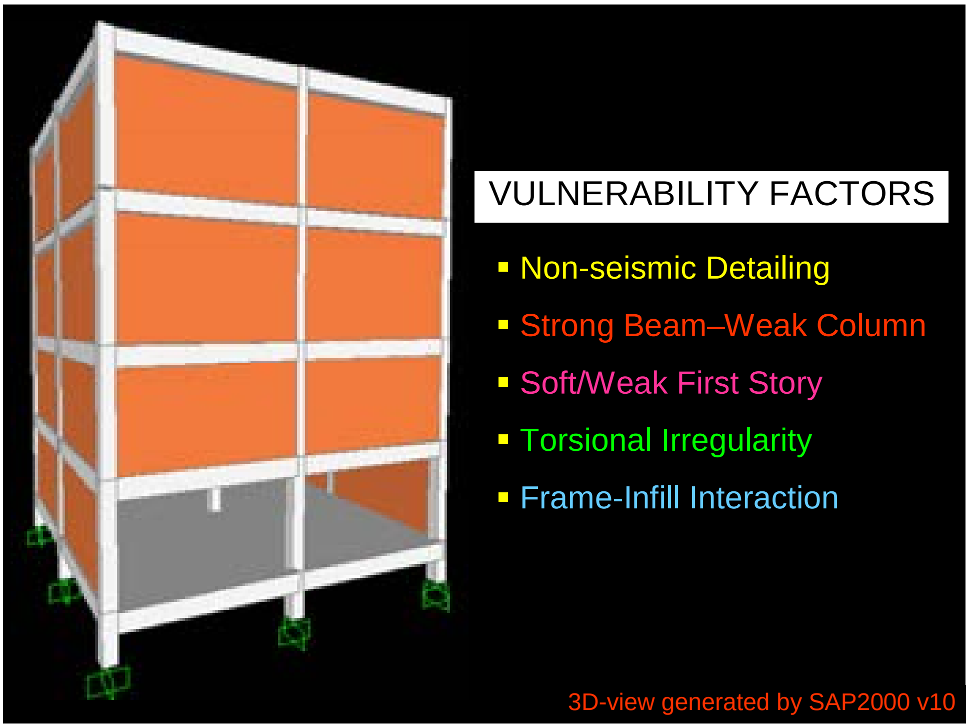
VULNERABILITY FACTORS
Non-seismic Detailing
Strong Beam–Weak Column
Soft/Weak First Story
Torsional Irregularity
Frame-Infill Interaction
3D-view generated by SAP2000 v10

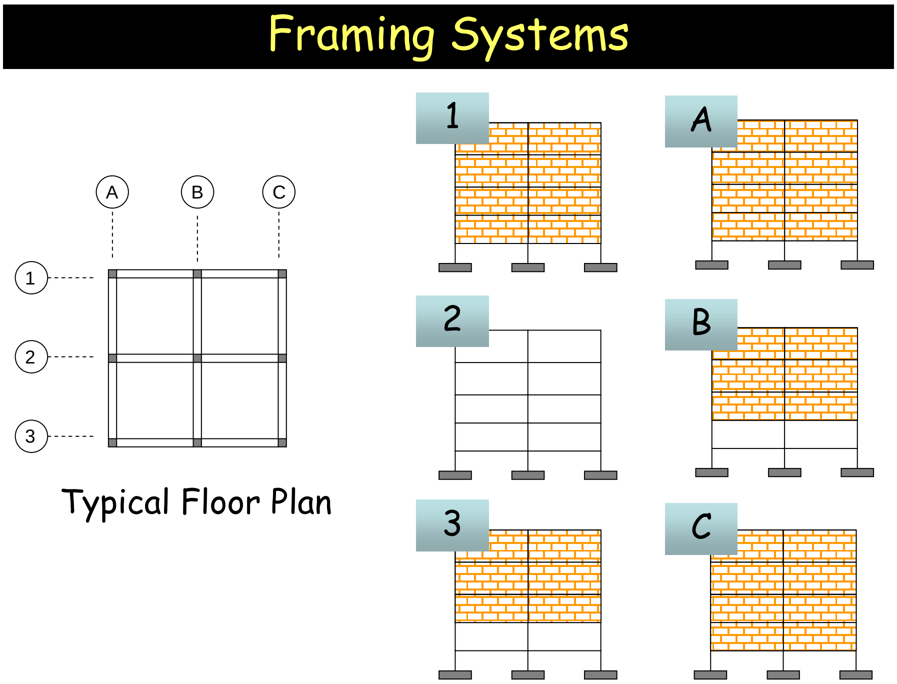
Framing Systems
A
B
C
1
2
3
Typical Floor Plan
1
A
2
B
3
C

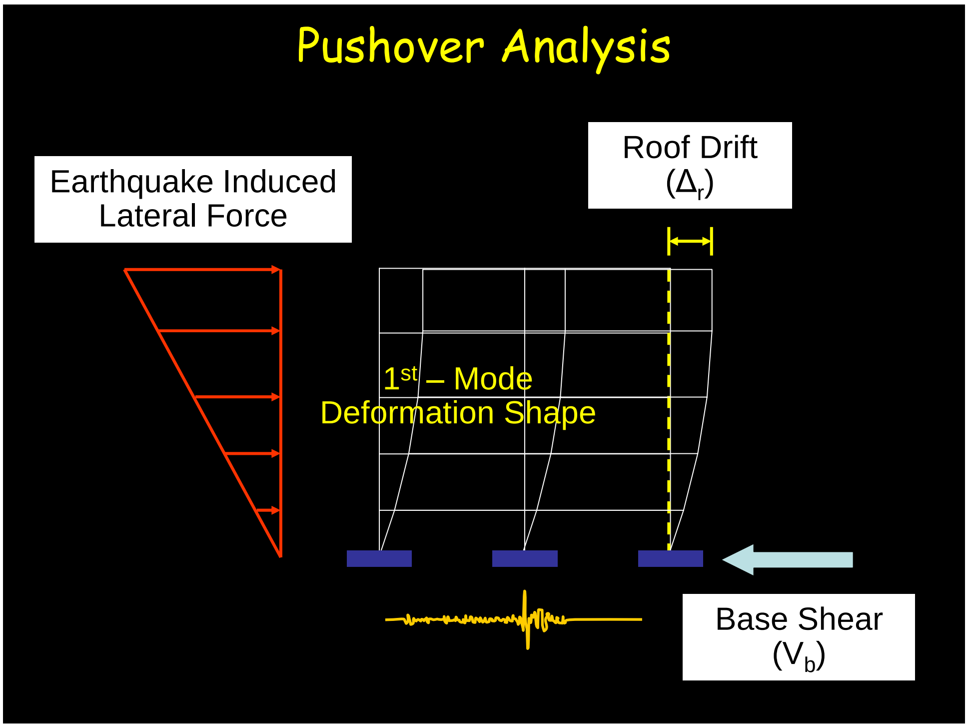
Pushover Analysis
Earthquake Induced Lateral Force
Roof Drift (Δ_r)
1^{st} – Mode Deformation Shape
Base Shear (V_b)

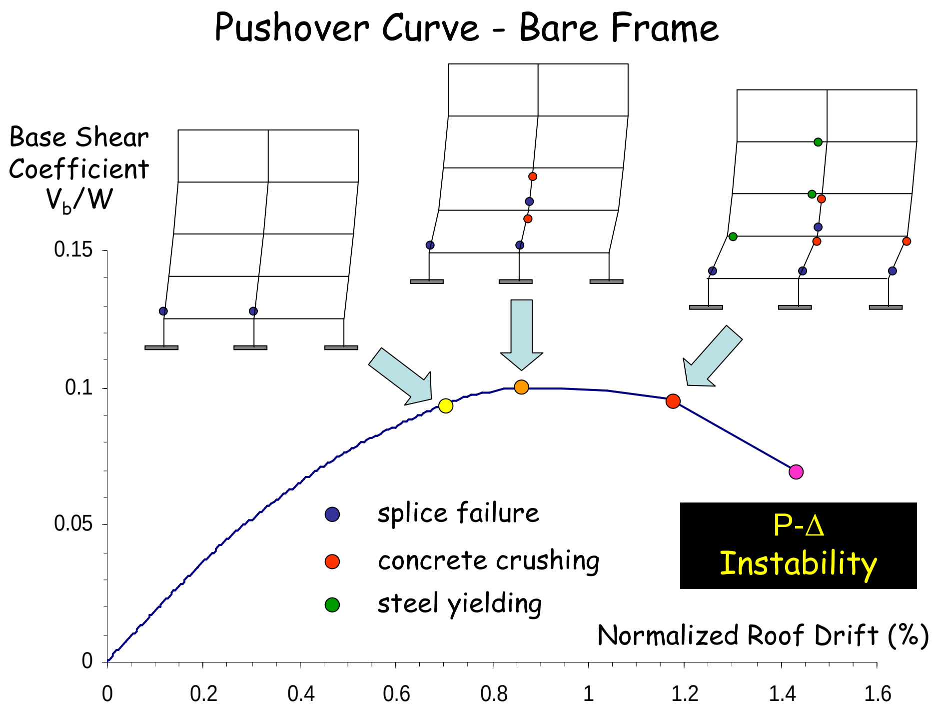
Pushover Curve - Bare Frame
Base Shear Coefficient V_b/W
0.15
0.1
0.05
0
splice failure
concrete crushing
steel yielding
P-Δ Instability
Normalized Roof Drift (%)
0
0.2
0.4
0.6
0.8
1
1.2
1.4
1.6

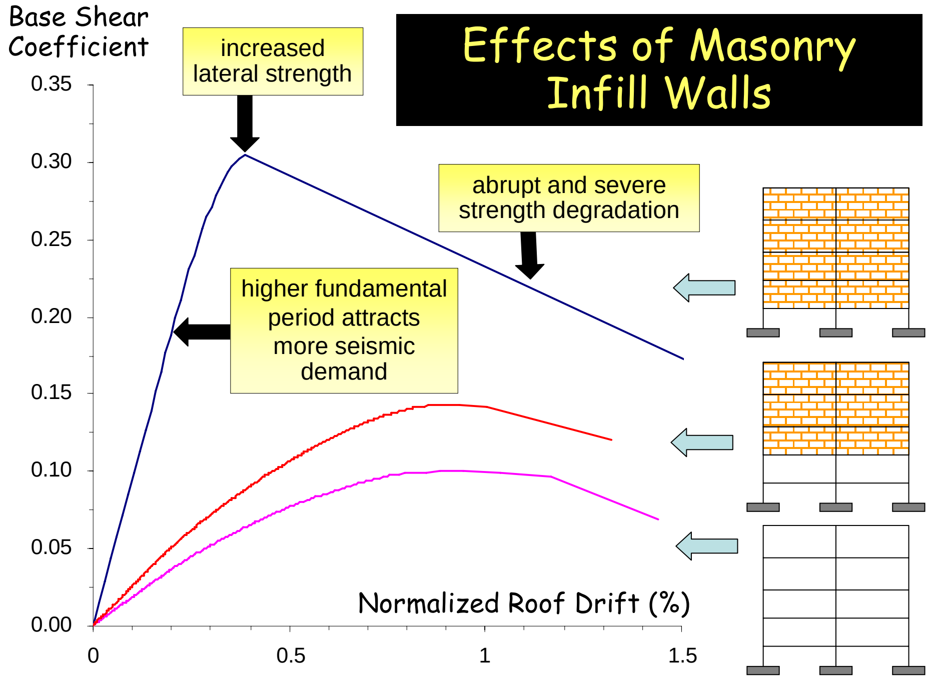
Base Shear Coefficient
increased lateral strength
Effects of Masonry Infill Walls
abrupt and severe strength degradation
higher fundamental period attracts more seismic demand
0.35
0.30
0.25
0.20
0.15
0.10
0.05
0.00
Normalized Roof Drift (%)
0
0.5
1
1.5

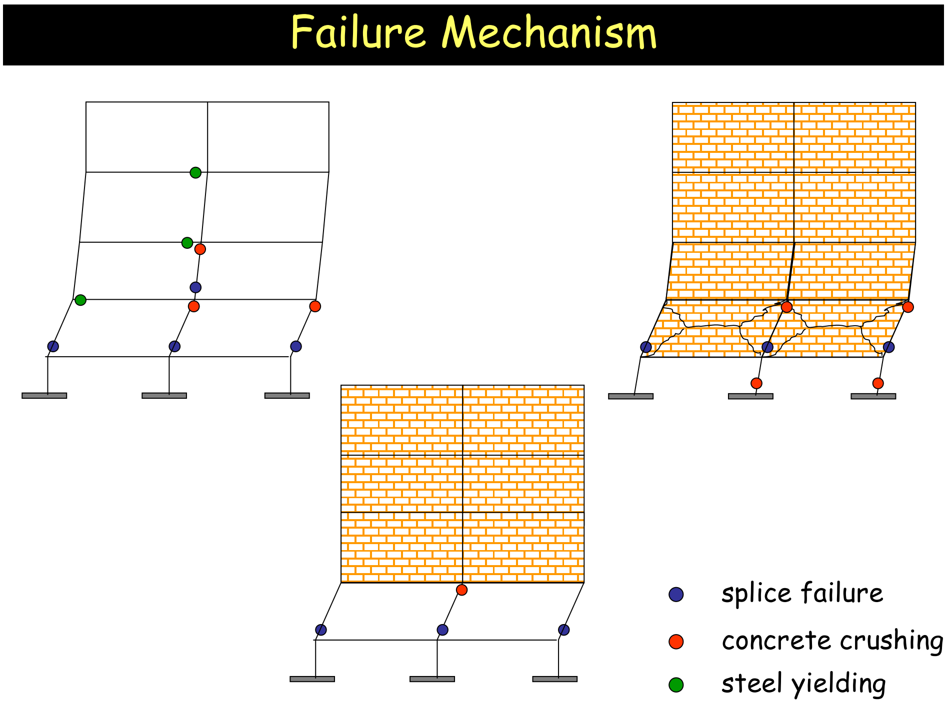
Failure Mechanism
splice failure
concrete crushing
steel yielding

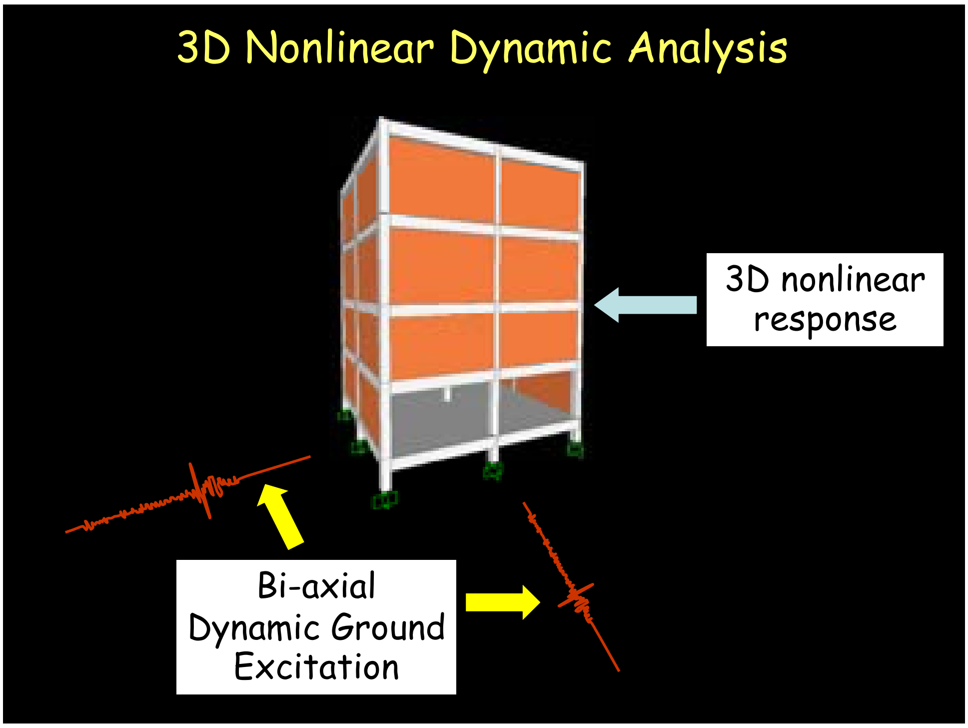
3D Nonlinear Dynamic Analysis
3D nonlinear response
Bi-axial Dynamic Ground Excitation

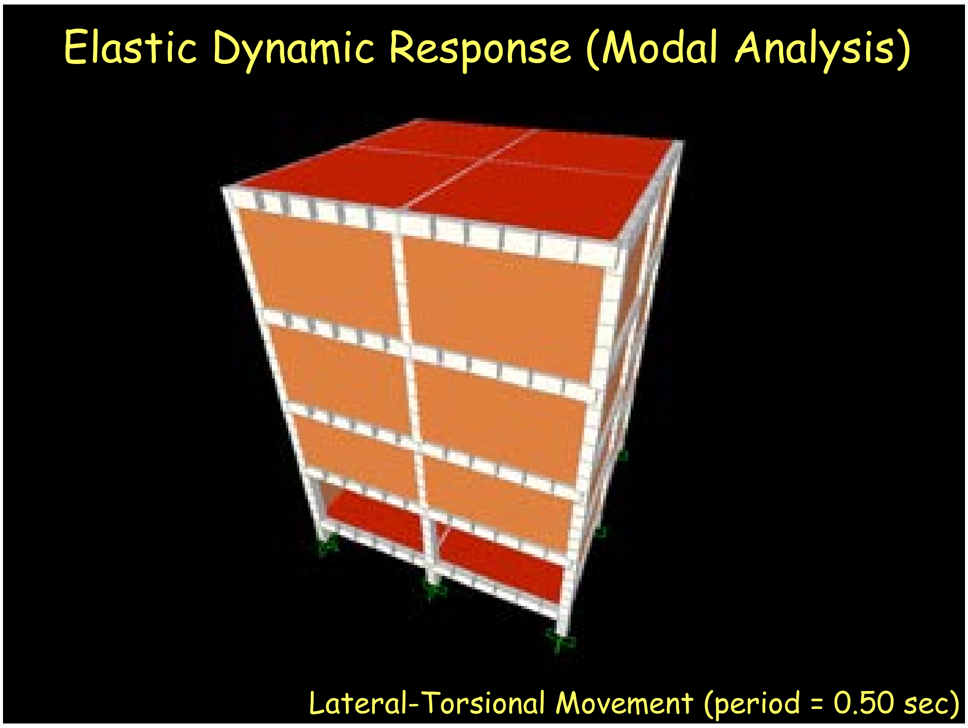
Elastic Dynamic Response (Modal Analysis)
Lateral-Torsional Movement (period = 0.50 sec)


Soft-story Collapse of RC Buildings in the 1999 Chi-Chi Earthquake (Taiwan)

Applied Earthquake Ground Motions

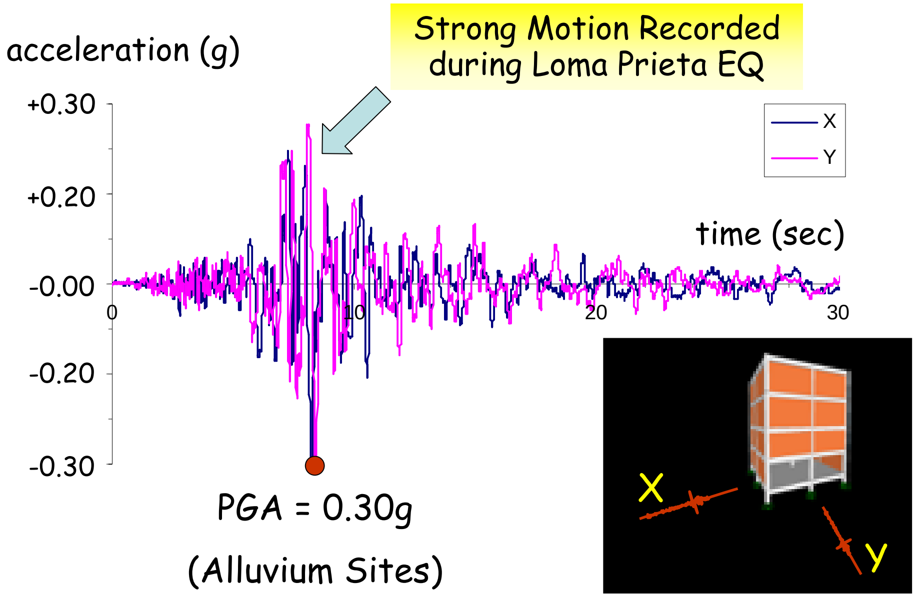

Building Response in X-direction

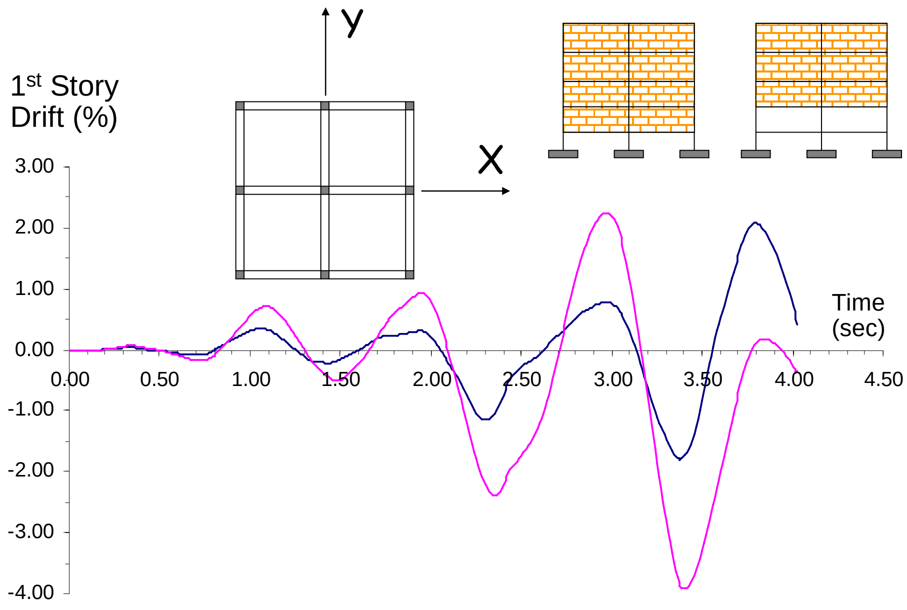

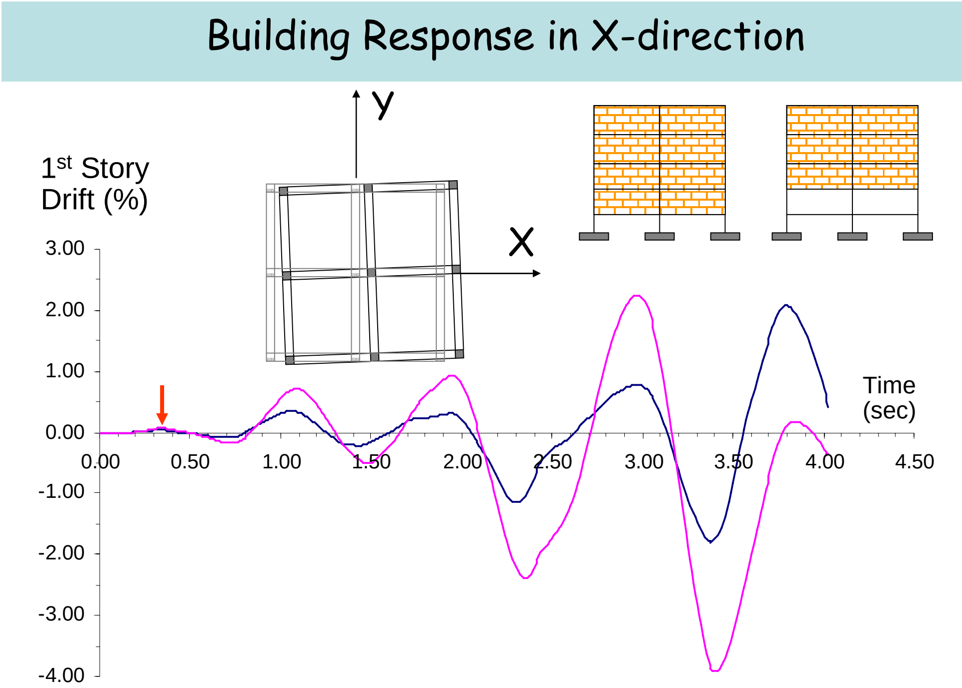
Building Response in X-direction
Y
X
1st Story
Drift (%)
3.00
2.00
1.00
0.00
-1.00
-2.00
-3.00
-4.00
0.00
0.50
1.00
1.50
2.00
2.50
3.00
3.50
4.00
4.50
Time
(sec)

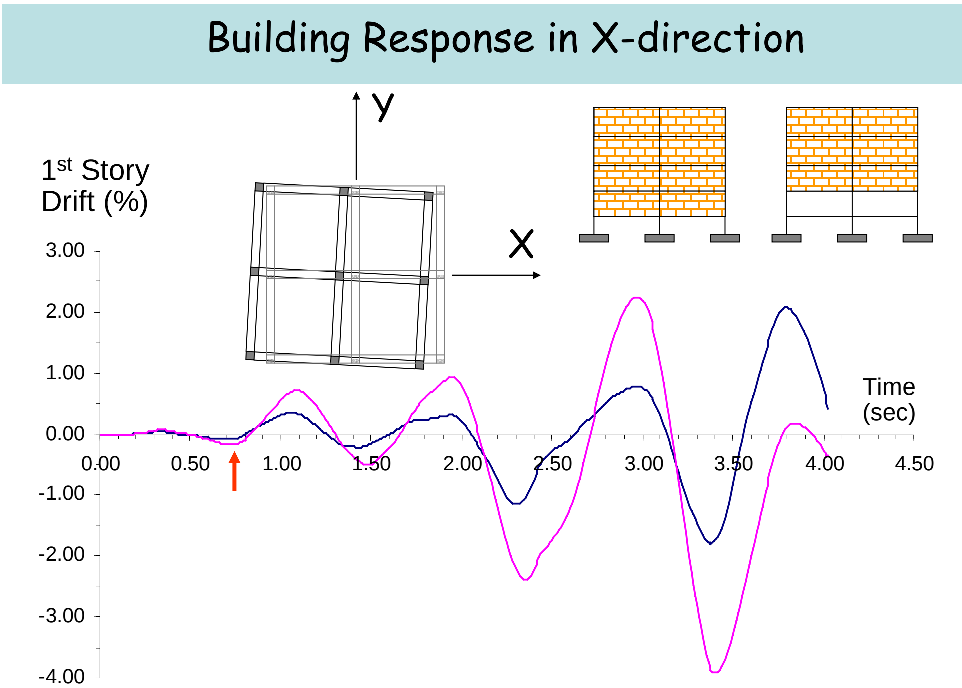
Building Response in X-direction
Y
X
1st Story
Drift (%)
3.00
2.00
1.00
0.00
-1.00
-2.00
-3.00
-4.00
0.00
0.50
1.00
1.50
2.00
2.50
3.00
3.50
4.00
4.50
Time
(sec)

Building Response in X-direction

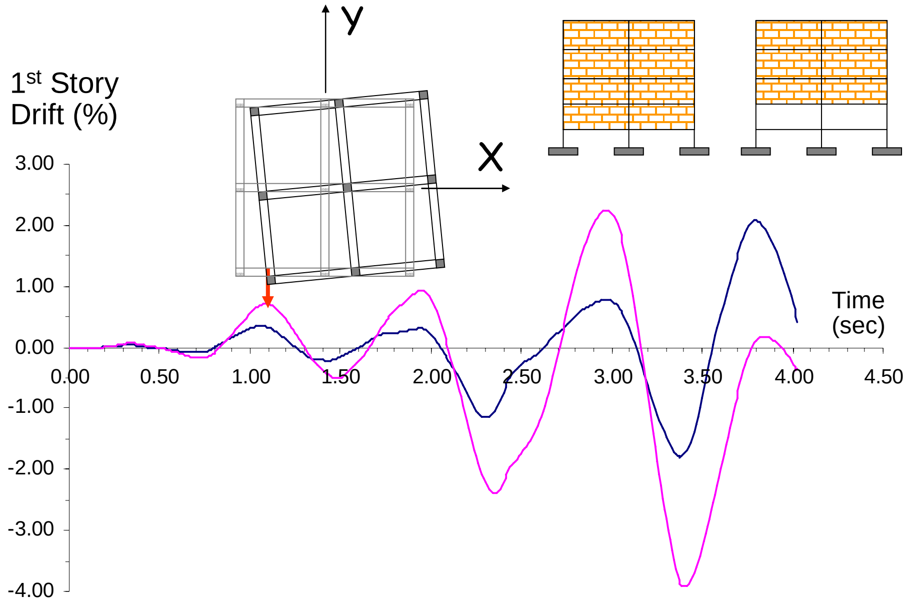

Building Response in X-direction

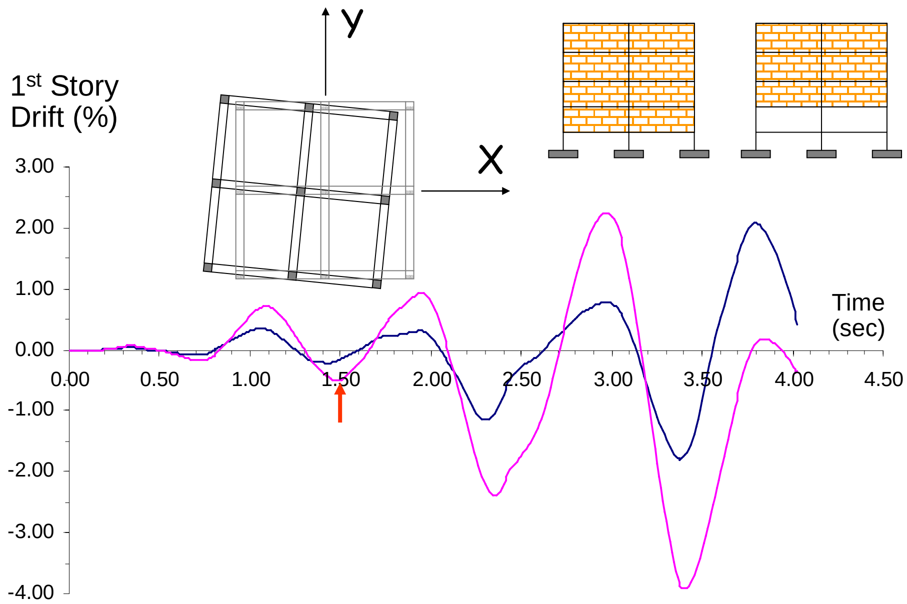

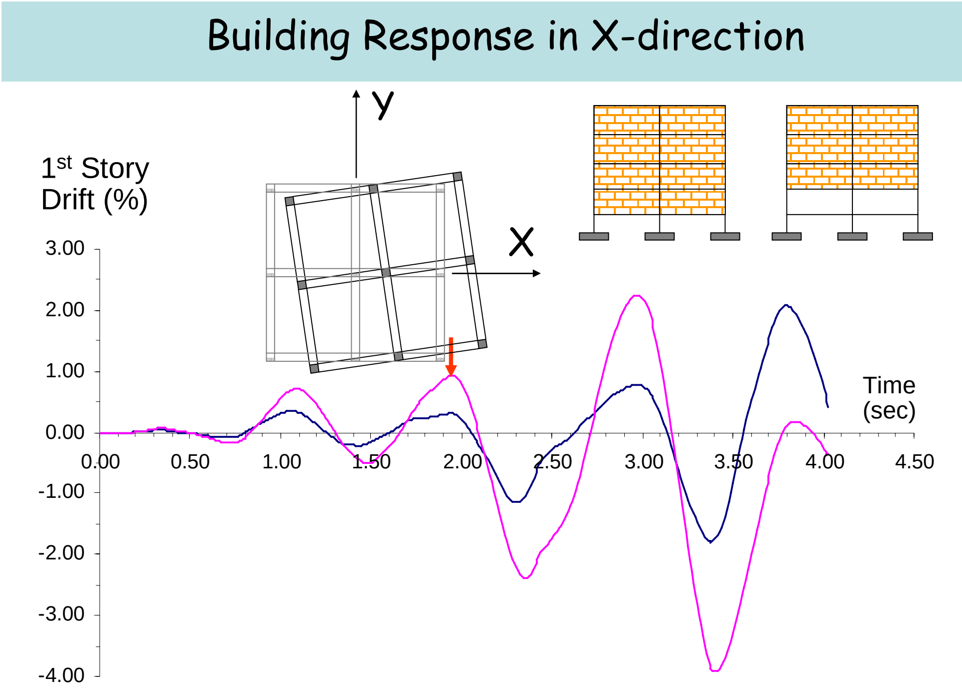
Building Response in X-direction
Y
X
1st Story
Drift (%)
3.00
2.00
1.00
0.00
-1.00
-2.00
-3.00
-4.00
0.00
0.50
1.00
1.50
2.00
2.50
3.00
3.50
4.00
4.50
Time
(sec)

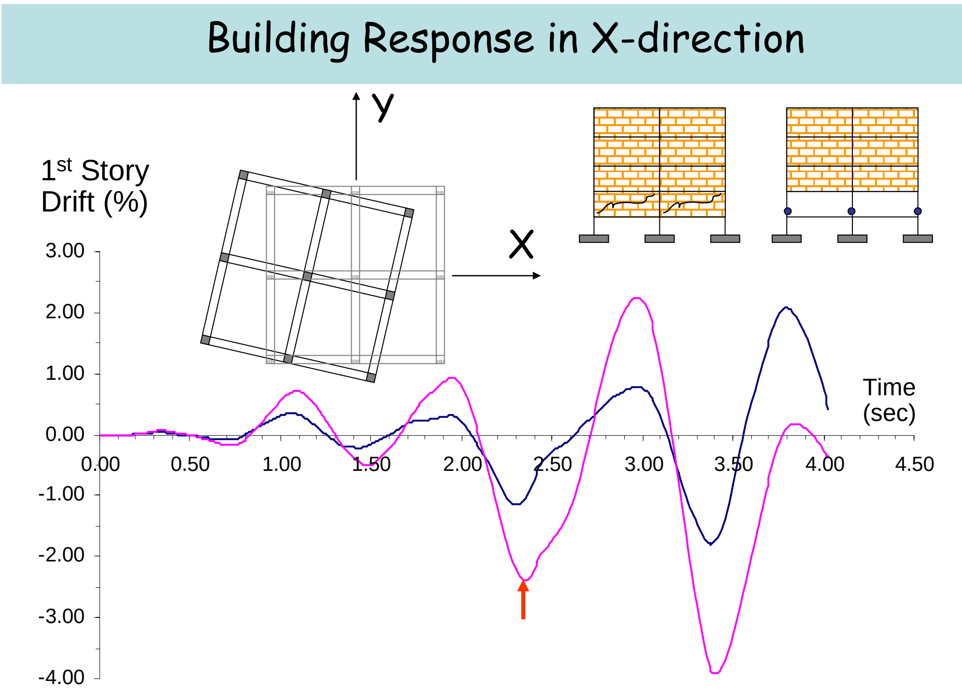
Building Response in X-direction
Y
X
1st Story
Drift (%)
3.00
2.00
1.00
0.00
-1.00
-2.00
-3.00
-4.00
0.00
0.50
1.00
1.50
2.00
2.50
3.00
3.50
4.00
4.50
Time
(sec)

Building Response in X-direction

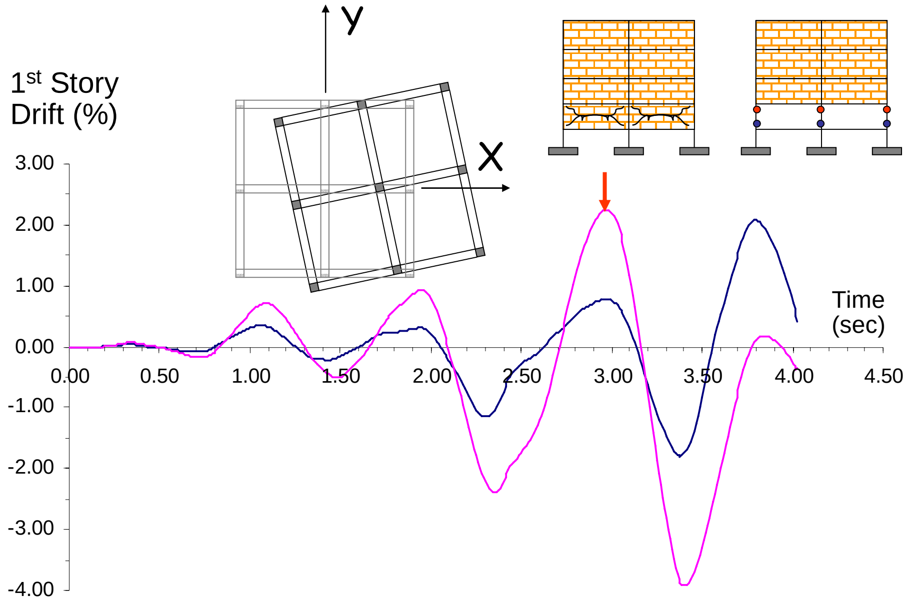

Building Response in X-direction

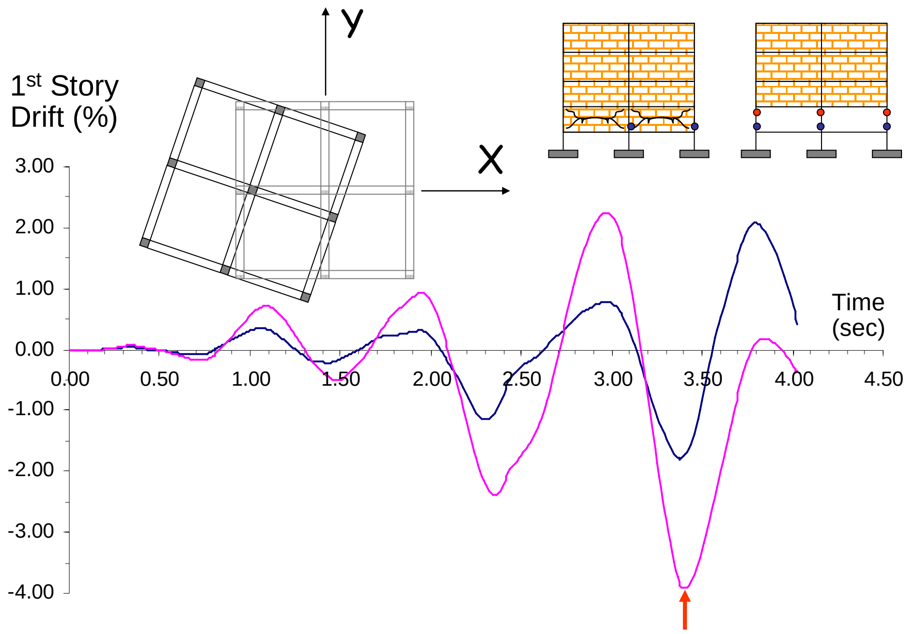

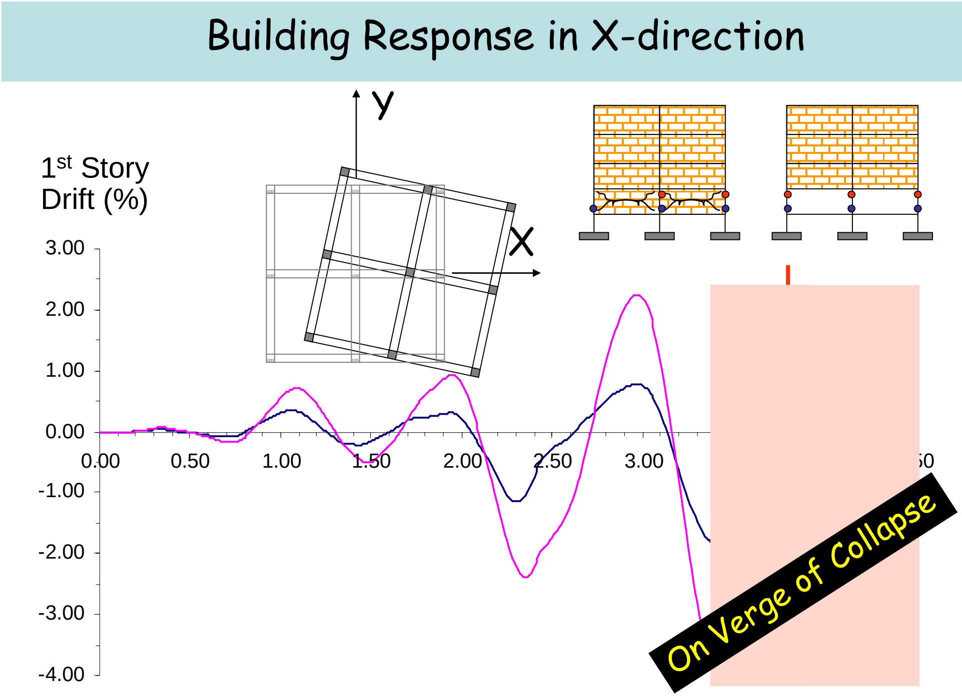

Building Response in X-direction
1st Story Drift (%)
Y
X
3.00
2.00
1.00
0.00
-1.00
-2.00
-3.00
-4.00
0.00
0.50
1.00
1.50
2.00
2.50
3.00
On Verge of Collapse

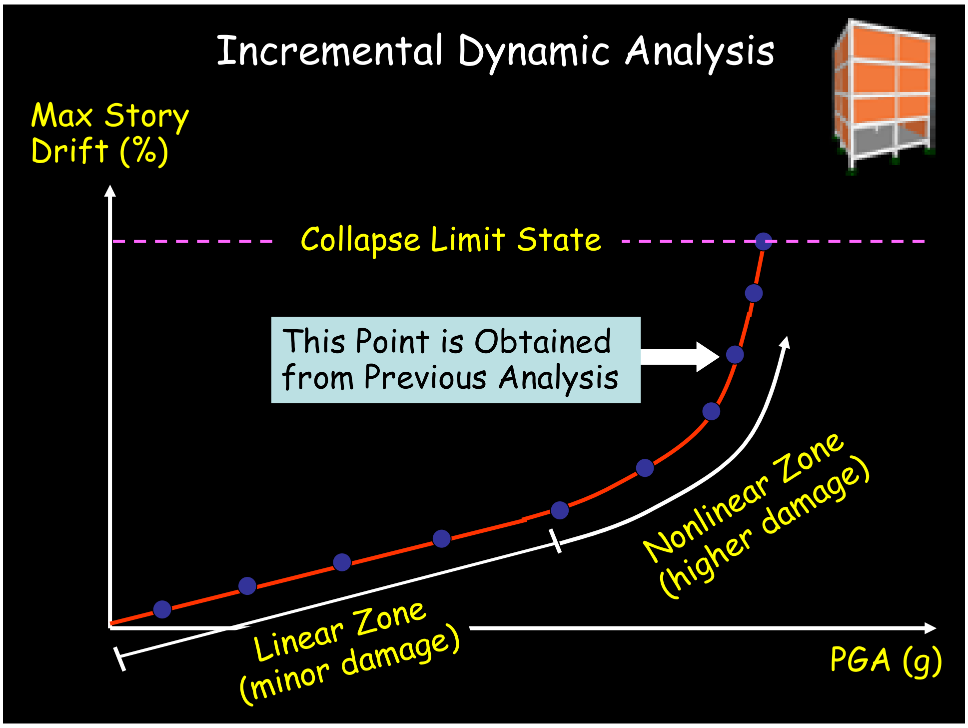

Incremental Dynamic Analysis
Max Story Drift (%)
Collapse Limit State
This Point is Obtained from Previous Analysis
Nonlinear Zone (higher damage)
Linear Zone (minor damage)
PGA (g)

Seismic Retrofitting of Torsional irregularity

Solid walls should be of nonstructural cladding

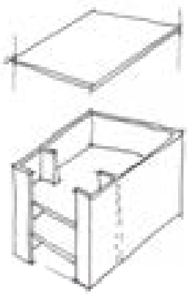

Shear walls are added at or near the open face

Strength and stiff moment-resisting or braced frame is designed for soft front wall

Torsion is accepted, and building is designed to resist the forces and minimize the distortion they cause

EARLY EARTHQUAKE WARNING SYSTEM IN JAPAN

KIMIRO MEGURO
International Center for Urban Safety Engineering
Institute of Industrial Science, The University of Tokyo, Japan
Department of Civil Engineering, The University of Tokyo, Japan
meguro@iis.u-tokyo.ac.jp

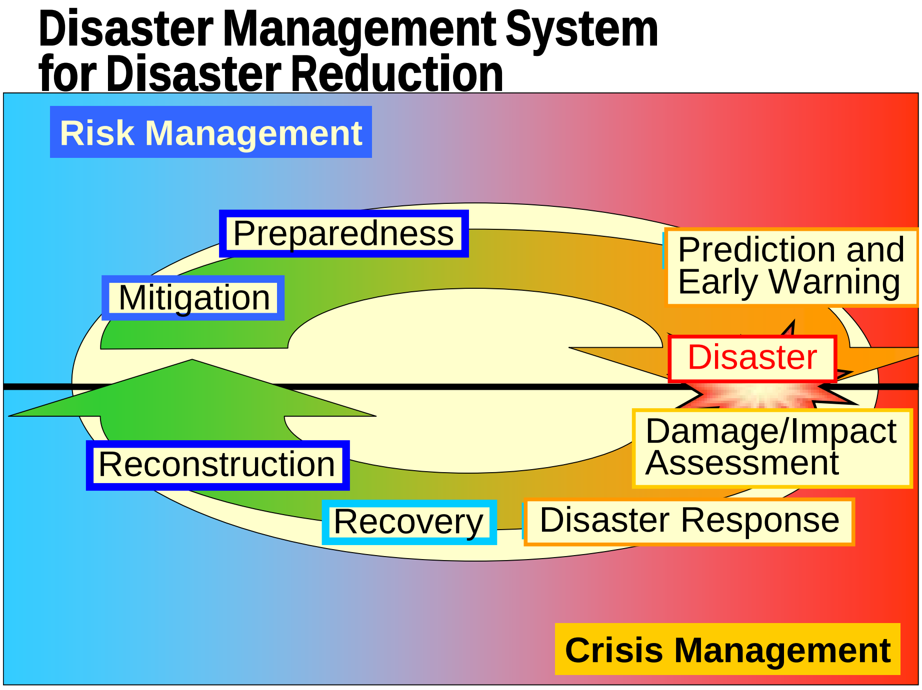

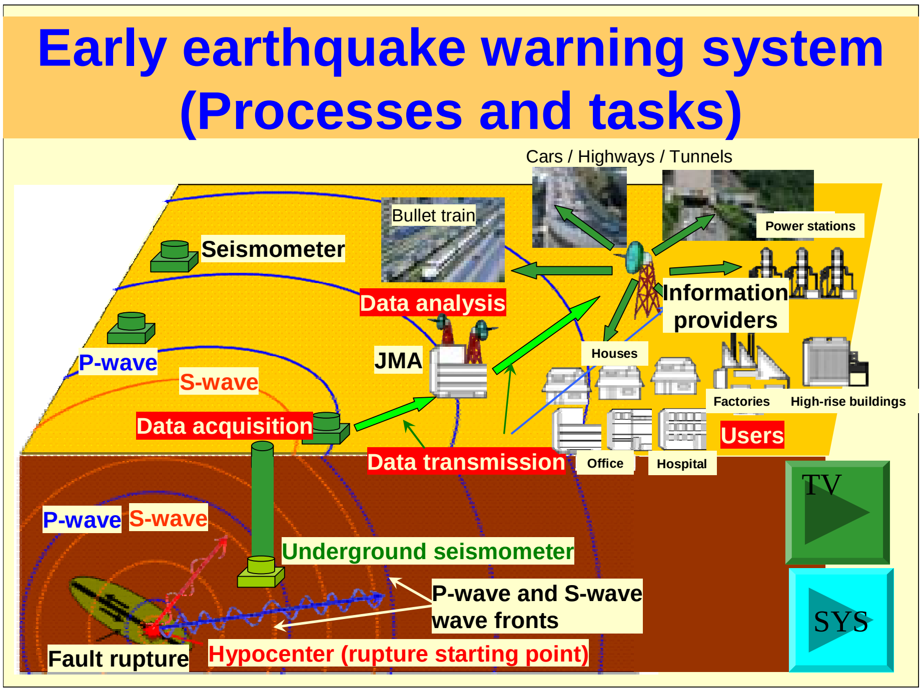

Accuracy of Current Early Earthquake Warning System

Difference on calculated seismic intensity and really observed one (seismic intensity: 4 or more, 350 events)

calculated seismic intensity

really observed seismic intensity

		緊急地震速報での予測震度							
		2以下	3	4	5弱	5強	6弱	6強	7
観測された震度	1以下			10					
	2			14					
	3			72	1	1			
	4	30	81	61	12	3			
	5弱	1	15	19	8	2			
	5強		2	6	3	2			
	6弱			1		1	1		
	6強			1		1	1		
	7				1				

JMA has started operation of early earthquake warning system since October 1st 2007.

Agree: 21 %
Within +/- 1 : 75 %

緊急地震速報の予測震度が4以上または観測震度が4以上	
合計	350
一致	21%
±1階級以内	75%

Accuracy of Current Early Earthquake Warning System

Difference on arrival time (seismic intensity: 4 or more, 350 events)
(calculated arrival time - really observed one)

Number of events

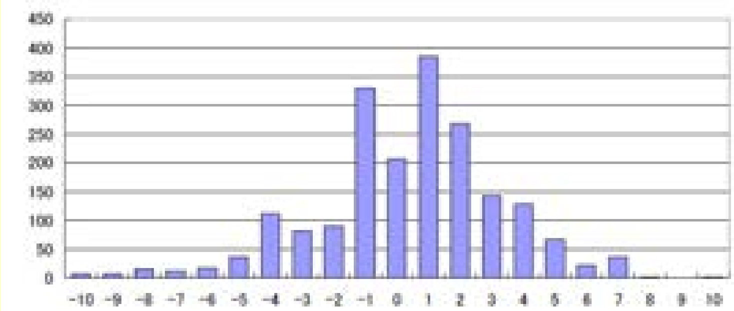

Time Difference (sec)
(calculated arrival time - really observed one)

取り上げた3つのシナリオ地震
Three scenario earthquakes

①想定東海地震：expected Tokai Eq.
分野別被害予測がなされている地域の想定地震

②想定宮城県沖地震：expected Miyagi-ken-Oki Eq.
近々に大きな地震が発生すると認識され、緊急地震速報がその効果を発揮すると考えられる猶予時間が大きな海洋性地震

③1995年兵庫県南部地震：1995 Kobe Eq.
震源が内陸に近く猶予時間が少ないため、緊急地震速報の効果があまり望めない地震

猶予時間別被害軽減率の仮定
Assumption for discussion on effects of EEW system

人的被害
Human Casualty

L Time (s) 猶予時間	Reduce ratio 軽減後被害	軽減前被害 WO info. 死傷	重傷	中等傷
2秒	死傷 Dead	75		
	重傷 Heavily Inj.	15	75	
	中等傷 Moderately	5	15	75
	無傷 No damage	5	10	25
5秒	死傷 Dead	20		
	重傷 Heavily Inj.	60	20	
	中等傷 Moderately	10	50	20
	無傷 No damage	10	30	80
10秒	死傷 Dead	10		
	重傷 Heavily Inj.	30	10	
	中等傷 Moderately	50	30	10
	無傷 No damage	10	60	90
20秒	死傷 Dead	5		
	重傷 Heavily Inj.	15	5	
	中等傷 Moderately	30	15	5
	無傷 No damage	50	80	95

（数字は被害移行率：%）

Based on past experimental results during day time

今回の例では、小学校や工場などでの実証実験の結果に基づいていることから、発災時間としては「日中、活動中」を想定している。

想定東海地震による静岡県の主な都市と猶予時間
Leading time at major cities in Shizuoka Pref.

In Case of the Expected Tokai Eq.

Area 地域	City 主な都市	Location 緯度	経度	L.Time (s) 猶予時間(秒)	Time (s) 分類(秒)
伊豆	下田市	34.676	138.948	16.6	10
熱海	伊東市	34.962	139.105	23.8	20
東部	沼津市	35.092	138.867	22.4	20
富士	富士市	35.158	138.679	21.3	20
中部	静岡市	34.972	138.386	13.7	10
志太・棒原	藤枝市	34.864	138.261	9.8	5
中遠	磐田市	34.714	137.854	4.6	2
北遠	天竜市	34.869	137.819	8.8	5
西部	浜松市	34.708	137.730	5.0	5

震源情報：N34.203, E137.939, D30, M8.0

地震発生から震源決定まで12秒であると仮定

Assuming that it takes 12 seconds to identify the location and magnitude of the event.

猶予時間別人的被害想定と推定被害軽減効果
Disaster reduction effects by EEW system

（対象：東海地震(M8.0),昼12時,予知無）
（in case of Tokai Eq. with M8.0,12:00,without Eq. prediction）

緊急地震速報なし Without EEWS			Heavily Inj.	Moderately	No damage
猶予時間		死者数Dead	重傷者数	中等傷者数	無傷
2秒		392	1889	8760	
L. Time (s) 5秒		1047	5305	23884	
10秒		1152	4358	19724	
20秒		1094	5027	22196	
total 合計		3685	16579	74564	
With EEWS					
緊急地震速報あり合計		673	4362	20455	69338
軽減率（%）Reduction Ratio		82	74	73	

推定人的被害軽減量／Estimated No. of human casualty reduction
死者/Dead：約3000人(-82%)、重傷者/Heavily Inj.：約12,000人(-74%)、中等傷者/Moderately：約54,000人(-73%)、無傷者/No damage：＋約69,000人

緊急地震速報を取り巻く基本的な理解(1)
Basic understanding on early earthquake warning system (1)

◆「緊急地震速報」は有効活用することで大幅な被害軽減が達成される可能性が高い

Early Earthquake Warning System is very useful for disaster reduction when it is used properly.

- 死者の軽減効果（理想的条件下）は
  想定東海地震（82%減）、Expected Tokai Eq.
  宮城県沖地震（94%減）、Expected Miyagi-ken-Oki Eq.
  1995年兵庫県南部地震（1%減）、1995 Kobe Eq.
- エレベータ閉じ込め事故の軽減効果は、
  千葉県北西部地震（M.6.0, 2005/7/23,16:34）で97%減、
  宮城県沖地震（M7.2, 2005/8/16, 11:46）で100%減。

緊急地震速報を取り巻く基本的な理解 (2)
Basic understanding on early earthquake warning system (2)

◆「緊急地震速報」を有効活用するための事前準備の重要性

- 技術的課題と環境整備(制度を含む)にかかわる課題

◆ Importance of preparation on both technology and social issues before the event

- Without this, the system cannot be used for disaster mitigation.

◆「緊急地震速報」を有効に活用できないケースの存在

- 「緊急地震情報」の適切な活用と、これに過度に期待しない仕組みとの両輪体制の整備
- インフラや建物の耐震補強への積極的に取り組み

◆ Cases when the system is not effective

- Development of two systems: 1) a system that makes proper use of the 'Early earthquake warning'; and 2) a system that does not depend too much on the 'Early earthquake warning'
- Active promotion of infrastructure and house retrofitting

Basic Knowledge
for Effective Use of
Real-Time Earthquake Information,
Earthquake Early Warning System

Basic terminologies

L: Focal distance, $L = \Delta t \cdot Vp \cdot Vs/(Vp\text{-}Vs)$

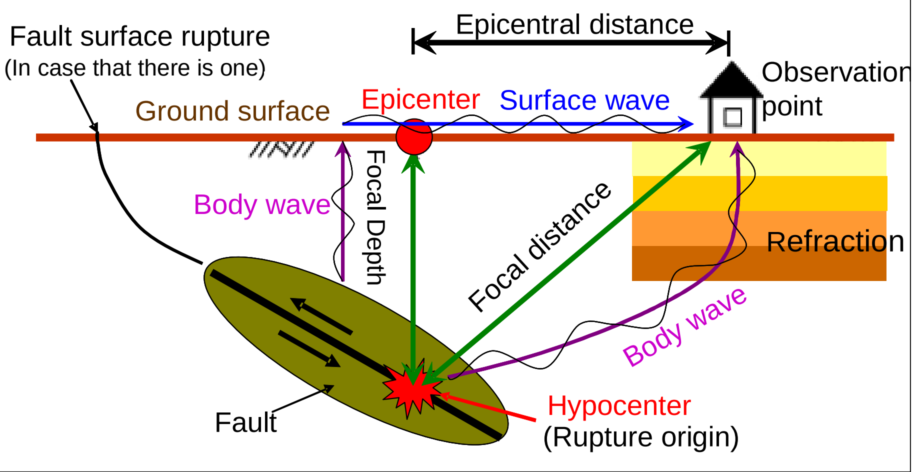

Types and characteristics of seismic waves

(In order of wave propagation velocity, P-wave＞S-wave＞Surface-wave)

Seismic waves

- **Body waves** (Travel directly from the hypocenter to the observation point.)
  - **P-wave** (Primary wave) (Longitudinal, compression wave. Its component is along the propagation direction. Usually felt as an up-down movement. It has a high propagation velocity)
  - **S-wave** (Secondary wave) (Shear, transverse wave. Its component is perpendicular to the propagation direction. Usually felt as side movement. Propagation velocity is slower than that of P-waves.
- **Surface waves** (Travel to the surface and then to the observation point. Propagation velocity is slower than that of body waves. Affects large tanks and bridge, and high rise buildings. Two types: Rayleigh and Love waves.)

P-wave

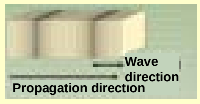

S-wave

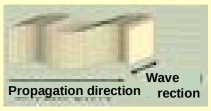

L: Focal distance

$L = \Delta t \cdot Vp \cdot Vs/(Vp\text{-}Vs)$

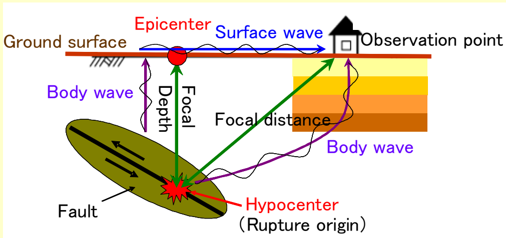

Three important characteristics of ground motion causing damage

(1995 Kobe ground motion observed at Kobe Marine Meteorological Observatory)

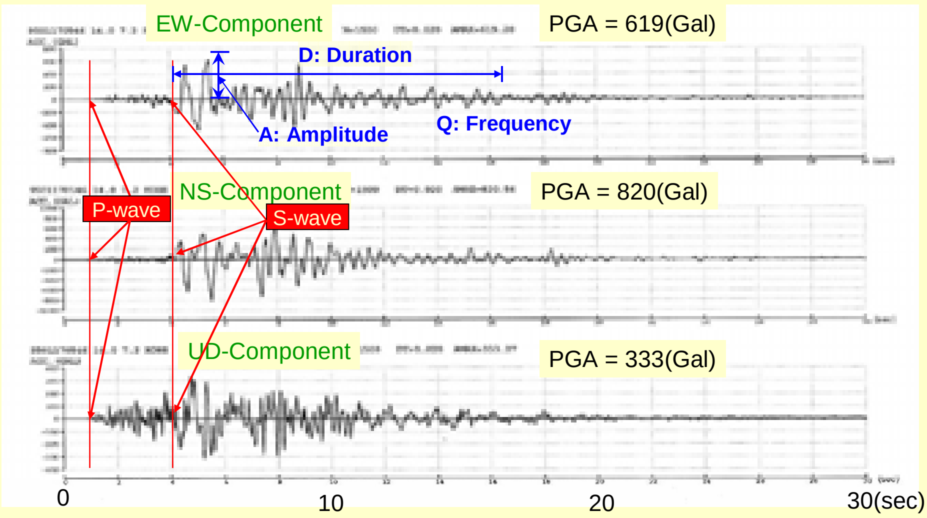

Issues for Effective Use of Early Earthquake Warning System

- Issues in General
- Issues for information providers to provide quickly and correctly
- Issues for information receivers to respond quickly and correctly

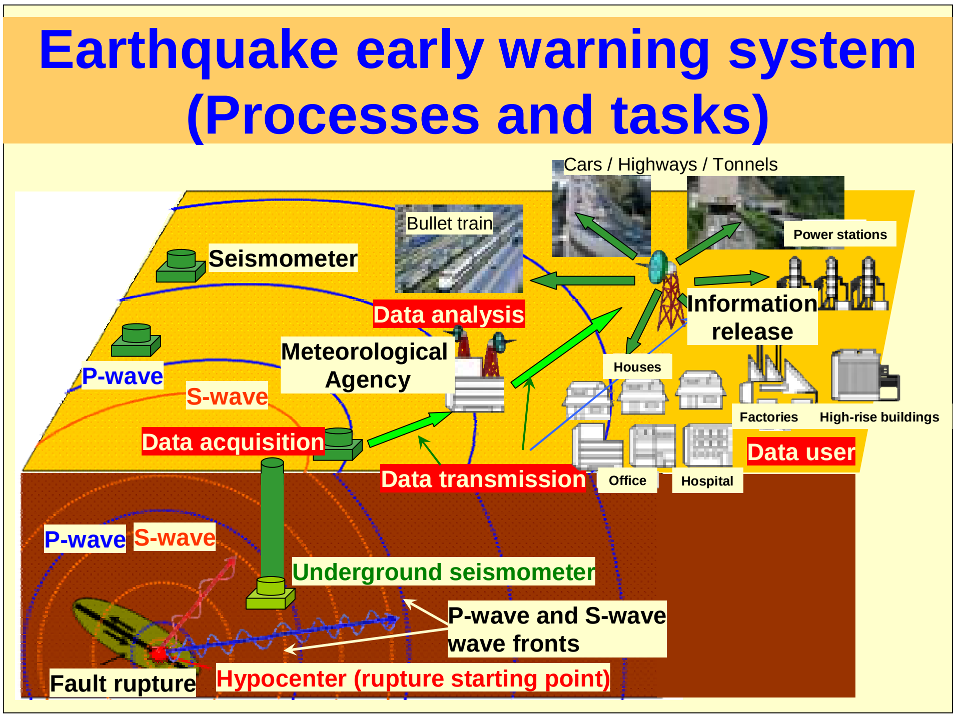

Outline of the tasks involved in the earthquake early warning

1) The nearest seismometer detects P-waves.
2) This information is promptly sent to JMA.
3) JMA evaluates the event location, occurrence time, magnitude, etc.
4) JMA sends these information to broadcasting and disaster related organizations.
5) These organizations send the information accurately and promptly with due consideration of the users.
6) Users make the most of this information based on their situation and the available time for action.

Earthquake early warning system (Processes and tasks)

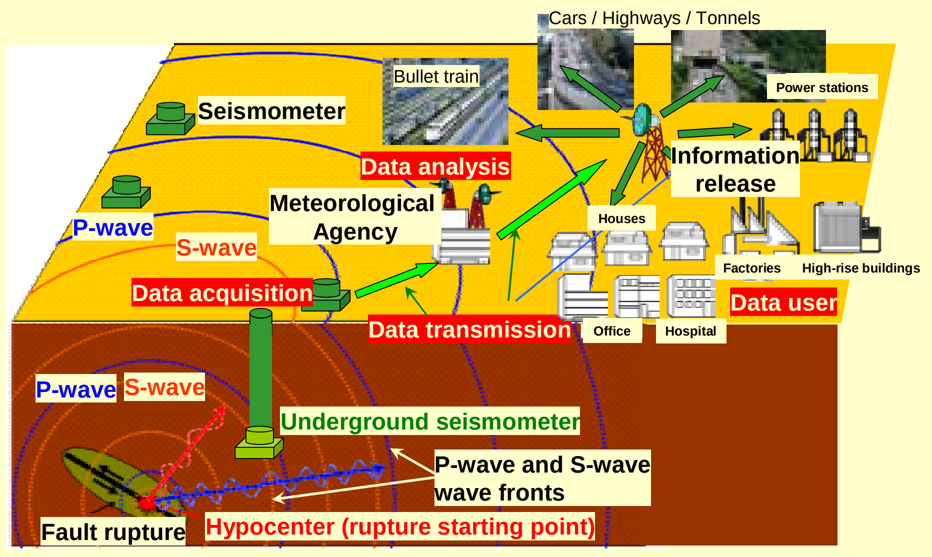

How do ground motion characteristics affect damage?

	Source characteristics		Propagation path and distance		Local site effect	
Representa-tive parameters	Magnitude（M）(Source effect)		Focal distance (Between observation point and fault)		Ground conditions Topography	
	Larger	Smaller	Longer (Further)	Shorter (Closer)	Hard soil	Soft soil
A: Maximum amplitude	Becomes larger	Becomes smaller	Becomes smaller (Attenuated)	No change	No change	Amplification (However, if soil liquefies, the shaking becomes less intense)
D: Strong motion duration	Becomes longer	Becomes shorter	Becomes longer (However, amplitude becomes smaller, then damage decreases)	No change	No change	Becomes longer
Q: Frequency content	Low frequency component increases	High frequency component increases	Low frequency content increases (Because high frequency component attenuates faster)	No change	No change	Low frequency content increases (Predominant period becomes longer, low frequency waves amplify)

Relation between ground motion parameters and earthquake early warning

	Source characteristics	Propagation distance and path	Observation point topography, soil conditions, others
Relation to earth-quake early warning	There is a trade off between accuracy and time. Earthquake is an spatial and temporal event and its magnitude becomes bigger as the fault plane area becomes larger. In case of a large earthquake, it takes time for the rupture to take place. As a result, it takes time to identify it and issue the warning, leaving shorter time for action. If the warning is issued sooner – with less certainty – more time for action is available but also a larger chance of an inaccurate evaluation.	The time between the warning and the shaking is shorter if the focal distance is shorter. The warning system is not so effective for locations close to the epicenter of large earthquakes. This areas are expected to have the largest damage. The system is most effective for locations not so close to the epicenter of a large earthquake.	Even for the same magnitude and focal distance, the shaking amplitude, frequency content and duration can be very different depending on the observation location. Even in the same building, the shake at the basement or at higher up floors is very different. In a car, on a viaduct or a bridge, the shake is affected by the dynamic response of the viaduct/ bridge. At a building construction site, the response changes with the changing characteristics of the structure being built.

Lessons Learnt from Recent Disasters

- **Importance of Structural Strength**
- **Lack of Imagination Capability**
  - **Politicians, Governments,**
  - **Researchers, Scientists**

  and
  - **Mass Media, General Public**

Meguro Lab.
IIS, The University of Tokyo

What will happen around you when you feel strong ground motion?

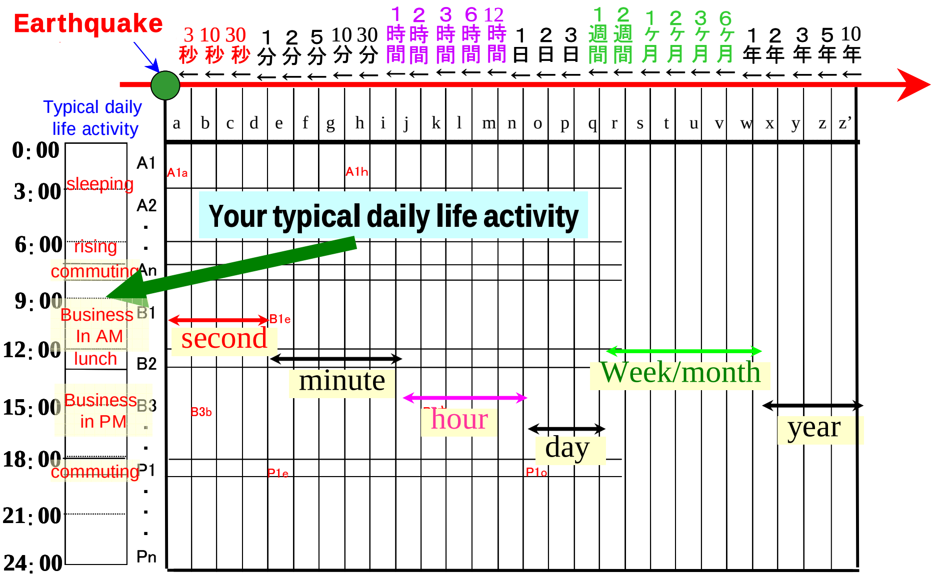

Important points in Meguro Method

1. 徹底した当事者意識

   Fully understanding that earthquake is your own problem

2. 健常者＝潜在的災害弱者の認識

   Abled person = temporary undisabled person

3. 個人としての多面性の認識

   Understanding multiple tasks that individual person has

4. 自分の死後の物語を考える

   Consider the story after you died in disaster

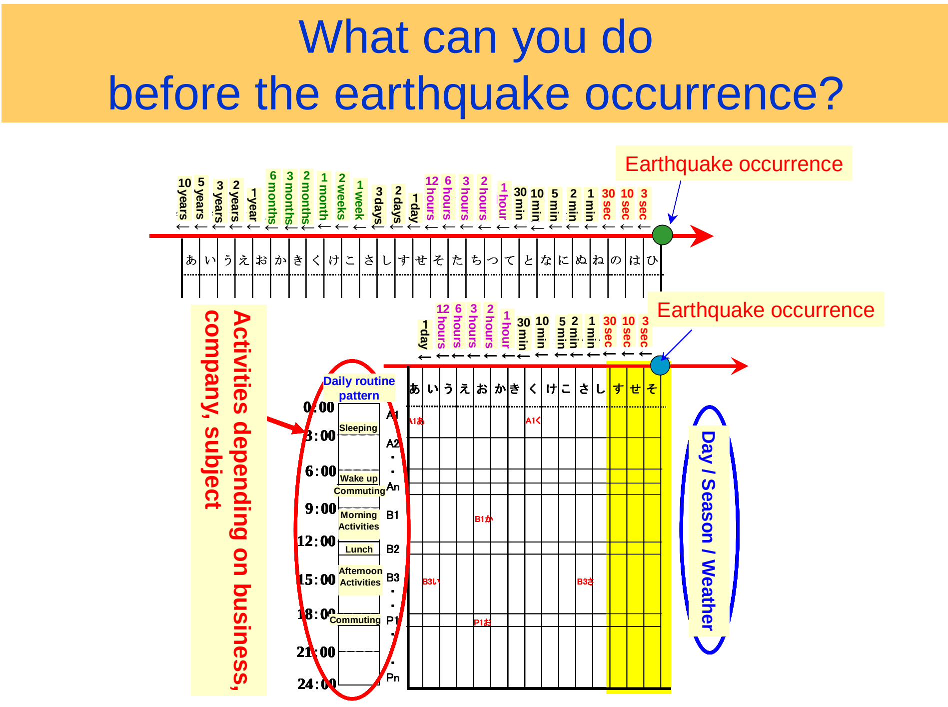
What can you do
before the earthquake occurrence?
Earthquake occurrence
Earthquake occurrence
Activities depending on business, company, subject
Daily routine pattern
Sleeping
Wake up
Commuting
Morning Activities
Lunch
Afternoon Activities
Commuting
Day / Season / Weather

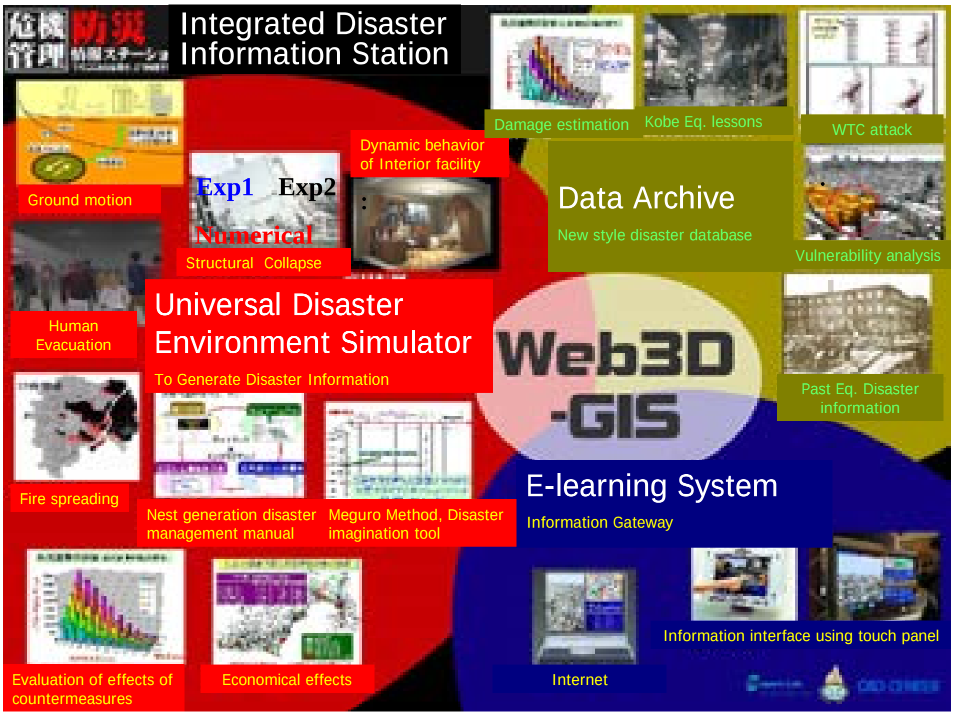
Integrated Disaster Information Station
Ground motion
Dynamic behavior of Interior facility
Exp1 Exp2
Numerical
Structural Collapse
Human Evacuation
Universal Disaster Environment Simulator
To Generate Disaster Information
Fire spreading
Nest generation disaster management manual
Meguro Method, Disaster imagination tool
Evaluation of effects of countermeasures
Economical effects
Damage estimation
Kobe Eq. lessons
WTC attack
Data Archive
New style disaster database
Vulnerability analysis
Web3D -GIS
Past Eq. Disaster information
E-learning System
Information Gateway
Internet
Information interface using touch panel

Direct and Indirect Effects of earthquake early warning

Effects of early earthquake warning

（Direct effects are usually discussed. However, indirect effects are also very important, often overlooked, and should be discussed.）

	Direct effect	Indirect effect
Positive impact	Early earthquake warning can reduce damage	Opportunity to promote disaster countermeasures before the event
Negative impact	Improper use of the disclosed information may lead to more damage.	-Unreal sense of safety hampering disaster countermeasure implementation -Influence on stock market etc.

Levels of effects of early earthquake warning

	Direct effect	Indirect effect
Positive impact	○	◎
Negative impact	×	××

Issues for efficient use of early earthquake warning

- **Discussion/consideration on how to use this system under different conditions**
  Different uses, available time, occurrence time, information accuracy, user spatial/temporal location ←**Discussion (Meguro method)**
- **In case of a system problem (failure to disclose, unsent warning, etc)**
  Failed safe system, redundancy, back-check system
- **System/structure to avoid misusing correct information**
  Education system set in advance

Reliable system management

From your side, what is the most important issue?

Key points for efficient use (1)

From the warning issuing agency view point…

◆Improvement of disaster imagination capacity

- Information disclosure with its proper way of use (before and during the event)

◆Multiple steps information disclosure considering the capacity of the user

- From simple to advance use of the information

◆Continuous efforts towards higher accuracy and reliability

- Methodology and system

◆Education of users for better understanding of 'Early earthquake warning' including the situations in which it cannot be effectively used for any reasons

- Development of two systems:
  1) a system that makes proper use of the 'Early earthquake warning'; and
  2) a system that does not depend too much on the 'Early earthquake warning
- Active promotion of infrastructure and house retrofitting

Key points for efficient use (2)

From the viewpoint of the users…

◆Improvement of disaster imagination capacity

- Personal base (company, commuting way, town, family, room, etc)

◆Improvement of the understanding on ….

- Meaning (Usefulness and limitation) and the use of 'Early earthquake warning'
- Importance of preparation and training before the event
  - Without this, the system cannot be used for disaster mitigation.
- Cases when the system is not effective
  - Development of two systems:
    1) a system that makes proper use of the 'Early earthquake warning'; and
    2) a system that does not depend too much on the 'Early earthquake warning'
  - Active promotion of infrastructure and house retrofitting

Conclusions

What do I expect from the early earthquake warning?

Encouragement for understanding and implementing concrete countermeasures before the event especially disaster imagination capacity

◆Early warning system can become catalyst for promoting seismic retrofitting and reconstruction of weak structures

◆Increase disaster imagination capacity

→ Hard and soft countermeasures to create disaster resilient "environment" and "people"

Promote「Indirect plus」
Reduce「Indirect minus」

Promote「Direct plus」
Reduce「Direct minus」


ICUS, IIS
University
of Tokyo
Thank you
Kimiro MEGURO

GEOPHYSICAL CHARACTERIZATION OF GEO-MATERIALS

GYE-CHUN CHO and TAE-HYUK KWON
Department of Civil and Environmental Engineering
KAIST, Korea
gyechun@kaist.edu
kikig@kaist.ac.kr

ABSTRACT

Elastic and electromagnetic waves can be used to gather important information about geo-materials. To facilitate geophysical characterization of geo-materials, their fundamental properties are discussed and experimental procedures are presented for both elastic and electromagnetic waves. The shear wave measurements centered on monitoring changes in effective stress during consolidation, multi-phase phenomena related to capillarity, microscale characteristics of particles, and small-strain stiffness of jointed rock masses related to joint conditions. The electromagnetic wave measurements focused on stratigraphy detection in layered soils, the estimation of the void ratio and its spatial distribution, conduction in unsaturated soils, nucleation of gas hydrate in pore spaces and weak zone prediction in water-saturated rock masses. Compressional wave measurements were used to capture hydrate formation in pore spaces and to identify the shotcrete bonding state to a hard rock surface. Experimental results suggest that mechanical waves allow studying contact phenomena, the evolution of interparticle forces, bulk stiffness of pore fluids and discontinuity characteristics, while electromagnetic waves give insight into the characteristics of the pore fluid phase and its spatial distribution.

1. INTRODUCTION

Small perturbation elastic and electromagnetic waves allow characterization of geo-materials (i.e., soils and rock masses) without causing any permanent effect (Santamarina et al. 2001, 2004). The physical interpretation of these measurements (i.e., elastic and electromagnetic wave parameters) permits inferring important information on the geo-materials and its physical processes. Soils are particulate and multi-phase materials (i.e., air, fluid and solid mineral). Rock masses are discrete media involving intact rocks, joints, joint-filling materials, and water. Their properties and the interaction among distinct phases can be captured using elastic and electromagnetic wave parameters. This interpretation can be local or global, depending on the scale of interest.

In order to apply geophysical characterization method to particulate materials and discrete media, their fundamental properties are first discussed, and then diverse applications including laboratory experimental procedures and analytical models are presented for both elastic and electromagnetic waves.

2. CHARACTERISTICS OF GEO-MATERIALS

2.1 Soils as particulate materials

The properties of particulate materials are governed by their physical characteristics (e.g., geometry and strength of grain), effective stress, presence of water (e.g., saturated or unsaturated condition), global void ratio (or porosity), temporal scales (e.g., drained or undrained condition), and spatial scales (e.g., fabric, packing) among others. These factors are discussed to gain insight into the fundamental behavior of particulate materials.

2.1.1 Microscale characteristics

The geometry of a soil grain reflects its chemical composition and formation history and affects soil behavior. Both size and shape are required to properly describe the particle geometry. Particle size is the most relevant parameter in assessing the relative balance between skeletal, electrical and capillary forces between neighboring particles. Particle shape is characterized by three dimensionless ratios: sphericity, roundness and roughness (Wadell 1932, Powers 1953, Krumbein and Sloss 1963, Barrett 1980). Sphericity indicates whether one, two, or three of the particle dimensions are of the same order of magnitude, and it is defined as the diameter of the largest inscribed sphere relative to the diameter of the smallest circumscribed sphere. Roundness is quantified as the average radius of curvature of surface features relative to the radius of the maximum sphere that can be inscribed in the particle. Roughness describes the surface texture relative to the radius of the particle. Convex particle surface profiles can be approximated with a Fourier series or through optical microscopy. Image analyzers can be used to automate particle sizing and shape determination (e.g., Yudhbir and Abedinzadeh 1991, Kuo et al. 1996). The relevance of particle shape on soil strength is intuitively accepted and supported by some experimental evidence. For example, the interparticle friction angle increases with angularity and surface roughness (Frossard 1979, Santamarina and Cascante 1998, Santamarina and Cho 2004, Cho et al. 2006).

2.1.2 Effective stress

When a soil is saturated, the granular skeleton and the pore fluid share the total boundary stress σ applied to a soil mass. The portion carried by the skeleton is the effective stress σ'. If the pore fluid pressure is u, the effective stress σ' is equal to the total stress σ minus the pore fluid pressure u (i.e., $\sigma' = \sigma - u$; Terzaghi's effective stress concept). Following Coulomb's failure criterion (i.e., $\tau = \sigma' \tan \phi$, where ϕ is the friction angle of the soil), the shear strength τ is a function of the effective stress σ' (Heyman 1997). In addition, stiffness (at small or large strain) and dilatancy (i.e., the volume change upon shear may be either positive or negative; Schofield 1998) are related to the effective stress.

2.1.3 Presence of water

Contrary to saturated soils, the presence of two non-miscible fluids adds interfacial tension (i.e., surface tension) and capillary forces between particles. This is typically the case between air and water, or water and organic fluids. In unsaturated soils, the negative pore-water pressure in menisci that exists due to capillarity at particle contacts increases the interparticle forces, changes the small-strain stiffness, and alters the soil strength (Fredlund and Rahardjo 1993, Cho 2001). All forms of conduction and diffusion processes depend on the size and connectivity of the menisci as well. Furthermore, the equivalent effective stress due to capillary forces increases with decreasing degree of saturation, decreasing particle size (or increasing specific surface), and increasing coordination of the particles (Cho and Santamarina 2001).

2.1.4 Void ratio

The void ratio (or porosity) is affected by the grain size distribution of the soil and the particle shape. In general, well-graded soils produce higher maximum densities while platy particles (i.e., clay) have a wider range of densities. According to the critical state soil mechanics approach, the undrained response of a soil is uniquely related to the initial void ratio (Roscoe et al. 1958, Schofield and Wroth 1968). For example, a lower void ratio for a given soil renders a higher undrained shear strength. Thus, the undrained shear strength can be estimated from critical state parameters and the initial void ratio.

2.1.5 Spatial variation

The spatial variability of soil parameters affects the macroscale soil response. The effects of spatial variability on soil behavior have been studied in the context of geoprocesses such as soil liquefaction (Popescu and Prevost 1996, Popescu et al. 1997), slope instability (Yong et al. 1977, Tonon et al. 2000), seepage (Griffiths and Fenton 1993, Fenton and Griffiths 1996), and settlement (Paice et al. 1996). The inherent variability of soil properties in natural soil deposits can be very large. Spatial variability has an important effect even in relatively small laboratory specimens as well. The presence of multiple internal spatial scales is associated with the development of multiple temporal scales for processes taking place within the medium such as consolidation, permeability, fluctuation of the capillary fringe, chemical diffusion, aging, creep and cementation (Santamarina et al. 2001). For example, the excess pore water pressure that builds up during shear is determined by the rate of pore water pressure generation versus the rate of pore water pressure dissipation. In turn, both mechanisms are related to the spatial variation of void ratio (Dobry and Petrakis 1990). The internal structure of a soil can be characterized using statistical parameters that summarize the average property (e.g., mean) and the variability (e.g., standard deviation). These parameters are used in the common case of particle size distribution but in the less frequently assessed case of void ratio distribution. However, the spatial distribution of the local values can play a critical role in global behavior, even in soil deposits that have the same global statistics (Cho 2001).

2.2 Rock masses as discrete media

Rock as an engineering material is heterogeneous and often discontinuous. These discontinuities are ubiquitous in a rock mass in the form of bedding planes, joints, shear zones, and faults; and can be sized from a small crack (e.g., fissures) to a planar crack (e.g., joints, bedding planes) which are up to 10 m. The properties of a rock mass are governed by the characteristics of intact rock, joint conditions (e.g., roughness, aperture and filling materials), orientation of joints, stress state, and presence of water among others. Particularly, the presence of joints and their characteristics determine the behavior of the rock mass, including its strength, stiffness, and all forms of conduction and diffusion–hydraulic, electrical, chemical and thermal. Thus, these factors are influential to the properties of mechanical and electromagnetic wave propagation in rock masses.

3. MECHANICAL AND ELECTROMAGNETIC WAVES

3.1 Mechanical wave

3.1.1 Wave propagation in particulate materials

Small-strain deformations in particulate materials take place at constant fabric (small-strain conditions apply when the strain level is lower than the elastic threshold strain). Under this condition, the soil deformation observed at the macroscale is the integration of contact level deformations. The stiffness of a soil is dependent on the nature of individual particle contacts, the interparticle contact area, and the interparticle forces (e.g., skeletal, electrical, and capillary forces). The Hertz-Mindlin model of contact behavior shows that the stiffness of two spheres in contact is non-linear and stress-dependent. The simplest expression is of the form (Stokoe *et al*. 1991, Santamarina *et al*. 2001)

$$V_s = \sqrt{\frac{G}{\rho}} = \alpha \left(\frac{\sigma'_{mean}}{1kPa} \right)^{\beta} \qquad (1)$$

where V_s is the shear wave velocity [m/s], G is the shear stiffness [kPa] in the small-strain regime, ρ is density [kg/m^3], the α-factor is the shear wave velocity at 1 kPa, σ'_{mean} is the mean state of effective stress in the propagation plane (e.g., $\sigma'_{mean} = (1+K_o)\ \sigma'_v/2$ for the $\sigma'_h = K_o\sigma'_v$ condition where σ'_h is the horizontal effective stress, σ'_v is the vertical effective stress and K_o is the lateral earth pressure coefficient), and the β-exponent reflects the sensitivity of V_s to changes in the mean state of effective stress in the propagation plane. The shear wave velocity in particulate materials only depends on the effective interparticle contact forces and the ensuing contact stiffness, but it is not affected by the bulk stiffness of the pore fluid. For this reason, transverse S-waves (i.e., shear waves) are preferred for the characterization of particulate materials as compared to longitudinal P-waves (i.e., compression waves). In the following section, shear waves are applied to characterize particulate materials, concentrating on changes in effective stress during consolidation, multi-phase phenomena related to capillarity, and microscale characteristics of the particles.

3.1.2 Wave propagation in jointed rock masses

The mechanical characteristics and orientation of joints determine the small and large strain behavior of rock masses and all forms of conduction and diffusion properties (Priest 1993, Guéguen and Palciauskas 1994, Huang et al. 1995). In particular, while the state of stress has little effect on the stiffness of intact rock, it exerts a predominant effect on the wave velocity and attenuation in jointed rock masses (Goodman 1989, Fratta and Santamarina 2002, Zhao et al. 2006).

The wavelength λ is the length scale of the propagating wave. The spacing between joints is a salient length scale in the rock mass, which is $L_{mass}=L_r+L_j$. L_r is the thickness of the intact rock block and L_j is the aperture of the joint. Wave propagation in jointed rocks can be organized into two extreme cases.

Short wavelength ($\lambda \ll L_{mass}$). The short-wavelength or high-frequency case applies when the wavelength is much shorter than the separation between joints $\lambda \ll L_{mass}$. A short-wavelength plane wave transmitting normally to the layering crosses through each component as if in an infinite medium, experiencing the material attenuation of the medium and a partial transmission and reflection at interfaces. Both reflected and transmitted components generated at an interface experience subsequent reflections and transmissions at other interfaces. The transmitted wave experiences dispersion and attenuation (Fratta and Santamarina 2002)..
The transmission coefficient depends on the relative mechanical impedance between the rock blocks and the filling, and on the ratio between the thickness of the joint, L_j, and the wavelength of the traveling wave within the filling, $\lambda=V/f$. If the joint thickness is very small compared with the wavelength ($\lambda \gg L_J$) and with the length of the rock block ($L_r \gg L_j$; that is, the joint ratio approaches $\eta=0$), the transmission coefficient theoretically becomes T=1.0, and the wave does not detect the presence of the joint. However, experimental data show that energy loss and time delay take place at joints even in closed joints (Pyrak-Nolte et al. 1990a, 1990b).

Long wavelength ($\lambda \gg L_{mass}$). Long-wavelength case applies when the wavelength λ is much longer than the spacing between joints *S*. This is the most common situation in seismology and field seismic investigation [*White, 1983*] and can be considered as an equivalent continuum for the problem of wave propagation (Fratta and Santamarina 2002). The group velocity in periodic, discrete media is a function of the ratio between the wavelength λ and the internal spatial scale of the medium, which in this case is the joint spacing S. If the velocity for an infinite wavelength is V^{∞}, then the group velocity V^{λ} for wavelength λ can be estimated as (Brillouin 1946, Santamarina et al. 2001):

$$V_g^{\lambda} = V^{\infty} \cos\left(\frac{\pi S}{\lambda}\right) \tag{2}$$

Thus, a jointed rock mass is as a low-pass filter and the group velocity tends to zero when $\lambda \to 2S$. The long wavelength approximation requires $\lambda/S >> 2$. Long-wave length propagation does not experience reflections at interfaces because the wave travels through the medium as in a continuum without noticing the presence of interfaces. However, losses in the two media contribute to the total loss in the medium.

3.2 Electromagnetic wave

3.2.1 Electromagnetic properties in particulate materials

Small-perturbation electromagnetic waves propagate through the soil mass without causing any permanent effect. The physical interpretation of these measurements permits inferring important properties about soil mass including porosity, volumetric water content, pore fluid characteristics (e.g., permittivity and ionic concentration), fabric anisotropy, and the interaction among distinct phases in soils (for a detailed review see Santamarina et al. 2001).

There are three electromagnetic properties. The electrical conductivity σ (or resistivity $\rho = 1/\sigma$) is a measure of charge mobility in response to an electric field. Conductivity in wet particulate media reflects the contributions of the particle conductivity (generally small), the bulk fluid conductivity, and surface conduction due to the increased counter-ion concentration in the double layer surrounding the particles. Thus, the connectivity of phases is related to the conductivity of soil-water mixtures, which allows the possible assessment of stratigraphy detection in layered soils and conduction in unsaturated soils.

The complex dielectric permittivity κ^* is frequency-dependent, and involves both a real part κ' and an imaginary part κ'':

$$\kappa^* = \kappa' + j \cdot \kappa'' \tag{3}$$

The real dielectric permittivity κ' represents the polarizability of the material, while the imaginary permittivity captures polarization losses κ''_{pol}. The measured effective imaginary permittivity κ''_{eff} combines polarization losses and Ohmic conduction σ losses,

$$\kappa''_{eff} = \kappa''_{pol} + \frac{\sigma}{\omega\varepsilon_0} \tag{4}$$

where ε_0 is the permittivity of vacuum ($\varepsilon_0 = 8.85 \cdot 10^{-12}$ F/m). The dielectric permittivity of soil-water mixtures depends on the type of soil, including mineralogy and its specific surface, porosity, pore fluid characteristics, the volumetric fluid content, and the frequency of the applied electric field. Thus, the dielectric permittivity of a soil is closely associated with water content and void ratio.

Finally, the complex magnetic permeability μ^* captures the magnetizability and the magnetization losses of the material. Most soils are non-ferromagnetic, therefore, the complex permeability μ^* is the permeability of vacuum μ_0 ($\mu^* = \mu_0 = 4\pi \cdot 10^{-7}$ H/m). In the following section, electromagnetic waves are applied to characterize particulate materials.

4. APPLICATIONS OF GEOPHYSICAL CHARACTERIZATION

4.1 Effective stress

Particle deformation at contacts (exacerbated by angularity), bending of platy particles, and contact slippage (facilitated in smooth particles) determine the deformability of soils under zero-lateral strain K_o-loading. In order to evaluate the changes in effective stress during consolidation, oedometric tests (K_0 condition) were performed on undisturbed Pusan clay specimens (D_{50} = 7 μm, G_s = 2.71). Piezoelectric bender elements (i.e., bimorphs; series-type) were mounted on the top and bottom platens to send and to receive shear waves. Travel time of bender elements' tip-to-tip distance was measured and shear wave velocity is calculated. The volume change of each specimen (diameter = 7.5 cm) was measured at various vertical effective confinements in the range of approximately 1 to 400 kPa.

Figure 1 shows the variation of void ratio and shear wave velocity versus consolidation time under a certain loading where the hollow circles are experimental test results and the solid line is a trend. It seems that the shear wave velocity enables estimating the change in effective stress (i.e., dissipation of excessive pore water pressure) during consolidation. When a soft soil in situ is subjected to additional loading, its consolidation process can be monitored using in-situ shear wave velocities.

Figure 2 shows the variation of void ratio and shear wave velocity versus applied vertical stress. As the vertical stress increases, the void ratio decreases and the shear wave velocity increases. The empirical relation of shear wave velocity to applied vertical stress is documented in Figure 2(b), where ϕ is the interparticle friction angle (20° for the soil used). Experimental results suggest that the shear wave velocity is uniquely related to the state of stress, so that it can be used to assess the state of stress and its change during the consolidation process.

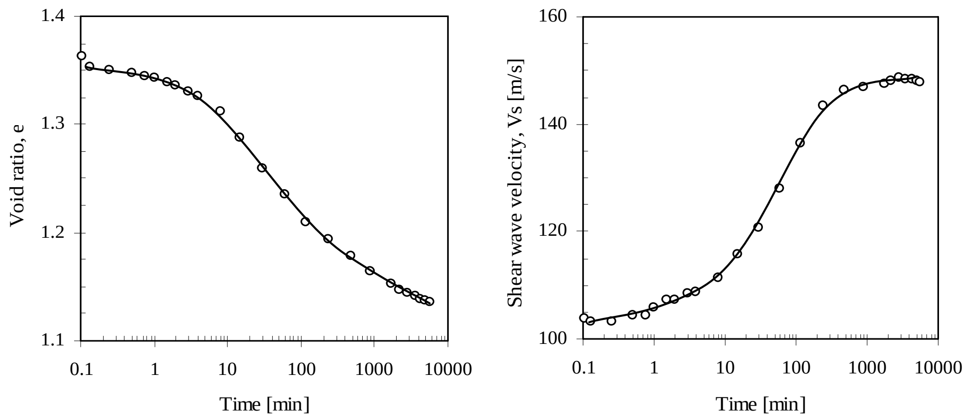

(a) Void ratio (b) Shear wave velocity

Figure 1: The void ratio and shear wave velocity versus consolidation time.

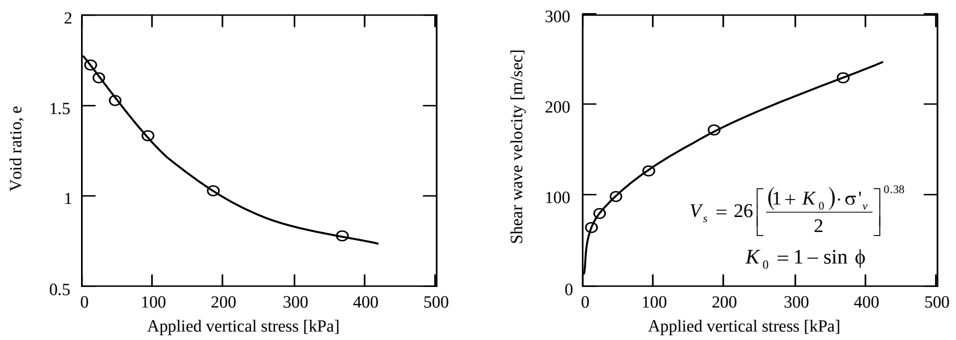

(a) Void ratio (b) Shear wave velocity

Figure 2: The variation of void ratio and shear wave velocity versus applied vertical stress.

4.2 Multi-phase Phenomena – Capillarity

In order to explore the implications of capillarity on stiffness in unsaturated particulate materials, drying tests were performed while monitoring the saturation of the specimen with shear waves and electrical resistivity. A drying cell was made for this purpose (Details can be found in Cho and Santamarina 2001 and Choi et al. 2004). The cell consists of an acrylic glass shell, an aluminum top platen, and an aluminum bottom platen. The metal platens, which were connected to a LCR meter with wires, acted as electrodes. Piezoelectric bender elements were mounted on the top and bottom platens to send and receive shear waves. This configuration allowed continuous monitoring of the shear wave velocity and the electromagnetic properties of specimens made of two soils. The LCR meter was used to gain low frequency electromagnetic properties (e.g., resistance and reactance; the resistivity ρ can be calculated from the relation of $\rho = R{\cdot}L/A$ where R is the resistance, L is the specimen length, and A is the specimen area).

The tested soil was Keum River sand (D_{50} = 0.4 mm, uniform grain size). The void ratio of the natural sand specimen was e = 0.76. The drying cell for the soil specimens was suspended with a flexible wire inside an incubator. The wire acted on an external scale that allowed the weight of the specimen to be monitored, in order to compute the water content or the degree of saturation. The temperature was kept constant at 50°C to avoid changes in surface tension (surface tension decreases with increasing temperature), and changes in confinement due to the expansion and shrinkage of the cell.

The measured shear wave velocity is plotted versus the corresponding degree of saturation in Figure 3a. As the degree of saturation decreases from the saturated condition (S=100%) to the dry condition (S=0%), the shear wave velocity increases continuously and shows no drop even at the perfectly dry condition, S=0% (Figure 3a). The zero degree of saturation is confirmed by measuring the weight of the specimen after further drying at high temperature (i.e., 100°C). The jump in shear wave velocity near S=0% may be explained by stiffening mechanisms, such as fines migration to the contacts of the larger particles, salt precipitation, and bonding due to ion sharing. The similarity between the grain-size distribution plot and the shear wave velocity plot is noticeable, highlighting the importance of the grain-size distribution on capillarity (see also Cho and Santamarina 2001).

In Figure 3a, point A is related to the air-entry value in the water-retention curve, which is the air phase breaks through the pore structure. Large pore size governs the magnitude of the effective stress increase in high degrees of saturation. A uniform coarse-grained soil like the Keum river sand tends to have a uniform-sized pore distribution, rendering the gentle slope between points A and C. Point B indicates the transition zone between the funicular (continuous water) and pendular (discontinuous water) stages. Salt precipitation is expected as drying proceeds from the point C to the peak velocity at S = 0%. Experimental results suggest that the shear wave velocity captures the change in effective stress caused by capillarity in unsaturated soils. This is particularly valuable in the pendular regime where direct measurement of the negative pore-water pressure is not feasible.

The resistivity (ρ) of the specimen is plotted versus the corresponding the degree of saturation. When the degree of saturation decreases, the resistivity increases. The resistivity in the sand specimen increases continuously with the decrease of water content (Figure 3b). The air-entry value in the water-retention curve cannot be detected from resistivity measurements, suggesting that the percolation of the air phase minimally affects the variation in resistivity. The resistivity-degree of saturation trend is represented by a bi-linear line. The transition point D, at the intersection of these two lines, is related to the percolation threshold, which is the critical water fraction when the continuous phase becomes disconnected (i.e., completion of pendular stage). The resistivity of soil-water mixtures is dependent on the degree of saturation, thus, the presence of water and the interaction between the water and soil particles in unsaturated media can be assessed using electromagnetic measurements.

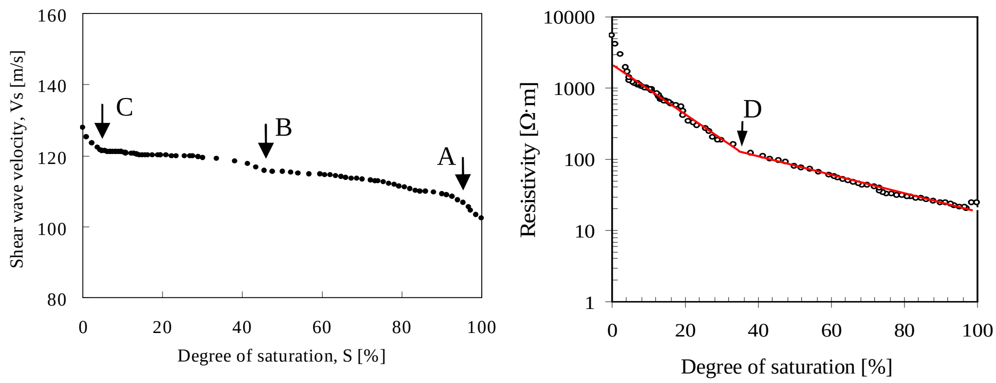

(a) Shear wave velocity (b) Electrical resistivity

Figure 3: Shear-wave velocity and electrical resistivity versus the degree of saturation during drying process of Kuem River sand.

4.3 Microscale characteristics – Particle Shape

Spheres with rough surfaces may have the same average contact area as spheres with smooth surfaces, but rough surfaces are composed of many small asperities which can be modeled as cones. The stiffness of a conical contact is smaller than that of a spherical contact because an equivalent increase in contact area requires more strain in a conical contact. As the force between particles increases, the global spherical shape of the rough particles begins to have a greater influence on the contact behavior than the shape of the asperities, and the stiffness of the rough particle contacts approaches that of a smooth particle. When many different sized asperities are present on particle surfaces, only the largest ones are initially in contact, therefore the actual contact area is lower than in the spherical case and the stiffness is lower (Santamarina and Cascante 1998, Yimsiri and Soga 1999).

Non-spherical, platy or ellipsoidal particles tend to favour the formation of inherently anisotropic fabrics and enhance the development of stress-induced fabric anisotropy. The small-strain longitudinal and shear stiffness reflect fabric anisotropy even under isotropic confinement. The effect of particle orientation on shear wave velocity anisotropy under isotropic effective stress conditions is explored with two sets of specimens; one made of mica flakes and the second prepared with rice grains (Santamarina and Cho 2004). Preferential particle alignment during specimen preparation is readily confirmed in both cases. Experimental results show that the shear wave velocity is higher when the direction of wave propagation is parallel to the main axis of the particles, as compared to the shear wave velocity in specimens where particles are aligned in the direction of particle motion; the ratio $V_{S\text{-}HV}/V_{S\text{-}VH}$=1.3-to-1.5 in mica, and $V_{S\text{-}HV}/V_{S\text{-}VH}$= 1.11 in rice (here the first index represents the direction of wave propagation, the second index represents the direction of particle movement, H is the horizontal direction, and V is the vertical direction) . Pennington et al. (1997) report similar ranges in shear wave velocity anisotropy in natural clays.

In order to explore the effect of global particle shape on the small-strain behaviour, the shear wave velocity was measured on specimens made of 16 sands with varying confining stresses. The oedometeric cell was used for this purpose. Based on experimental results, the α-factor and the β-exponent of Equation. (1) for each sand are determined by best-fitting the data. Figure 4 shows the effect of particle shape on the shear wave velocity (where Ir is the irregularity defined as the average of sphericity and roundness). In general, a robust inverse trend between the α-factor and the β-exponent is observed in all types of soils: the stiffer the particles and the denser the packing, the higher the value of the factor α and the lower the β exponent. Experimental results show that as particle shape becomes non-spherical and angular (Ir<0.5), the exponent β increases with decreasing α factor. Thus, angular and non-spherical particles increase the sensitivity of stiffness to the state of stress (refer to Cho et al. 2006 for more detailed experimental data and descriptions).

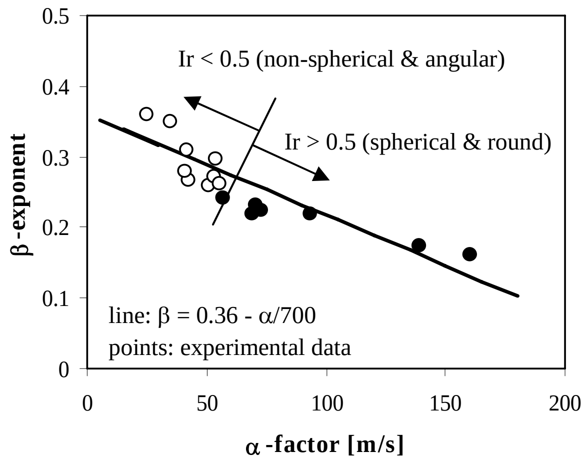

Figure 4: The effect of particle shape on the shear wave velocity. The α-β trend line is from Santamarina et al. (2001).

4.4 Stratigraphy - layer detection

A simple and effective technique is proposed to assess the spatial variability (including layers) of sandy or clayey soil specimens with sub-millimetric resolution. The technique involves a needle-size probe that is pushed into the soil and permits measuring the local electromagnetic properties of the medium along its path. The device and its calibration are described in detail in Cho et al. (2004). The probe is a thin, stainless steel needle, with an insulated wire inserted into the needle, and bonded to it with epoxy resin to form a coaxial probe. The tip of the probe is ground and polished to form a sharp edge (25 degrees – single side). The dimensions of the probe are: probe diameter is d_{probe} = 2.10 mm, the wire diameter is d_{core} = 0.63 mm, and the probe length is 152 mm. The electromagnetic properties were determined by measuring either the resistance R and the reactance X, or the magnitude of the impedance $|Z|$ and the phase angle θ ($Z^* = R + j \cdot X$) using an HP-4192A Hewlett Packard low frequency impedance analyzer.

The ability of the electrical needle probe to resolve interfaces was explored using sandy and clay specimens. Two tests were performed. The first test involves a three-layer sand specimen made of Ottawa 20-30 sand (D_{50} = 0.72mm; round), Ticino sand (D_{50} = 0.58mm; angular), and Ottawa F-110 sand (D_{50} = 0.12mm; round) prepared by water pluviation. The needle probe was gradually pushed into the specimen. The variation in the corrected impedance with depth is shown in Figure 5(a). The three sand layers are distinguished. The layers with larger particles (i.e., Ottawa 20-30 and Ticino sands) exhibit higher variance than the layer composed of smaller particles (i.e., Ottawa F-110).

The second test involved kaolinite (D_{50} = 5μm; LL = 50), Georgia red clay (D_{50} = 7μm; LL = 40), and bentonite (D_{50} = 0.6 μm; LL = 250), each individually mixed with water at the liquid limit. Then, the water-clay mixtures were stacked in a glass container and stored for a month to reduce the possible contrast in electro chemical potential between the layers. The variation in impedance with depth was determined with the needle probe (Figure 5b). The three clay layers are clearly distinguished. Bentonite shows the lowest variability in the impedance. The characteristic internal length scale of soils can be determined by the needle probe, for example, the distance between the thin layers in varved clays.

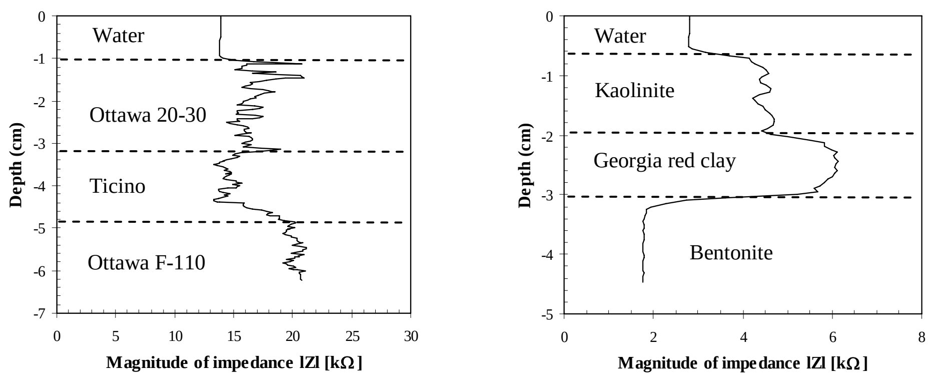

(a) Sand specimen (b) Clay specimen

Figure 5: Stratigraphy detection with the electrical probe at f_r = 1 MHz.

4.5 Void ratio and its spatial distribution

Void ratio (i.e., porosity) is an important soil property within relation to strength, conduction, and diffusion processes. Numerous attempts have been made to evaluate pore size distribution and its spatial variability, using techniques such as mercury porosimetry, gas adsorption, X-ray scattering (Mitchell et al. 1976, Mulilis et al. 1977), small-angle neutron scattering, computed tomography based on X-ray absorption (Desrues et al. 1996), and imaging techniques using cross-sections of impregnated soils (Jang et al. 1999). The mercury porosimetry and gas adsorption techniques are limited to small-size specimens. The X-ray scattering technique, which is an indirect method, requires careful calibration and usually gives qualitative information rather than quantitative information. The computed tomography method requires careful calibration and inversion techniques to smooth the contrast in mass density. Imaging techniques using cross-sections of impregnated soils are practical in sandy soils, however, its implementation is destructive and the same specimen cannot be measured both before and after testing.

A simple and effective technique is proposed herein to assess the spatial variability of sand specimens with sub-millimetric resolution. The technique involves the needle-size probe described in the previous section. The computation of the real relative dielectric permittivity κ' (for simplicity, the term permittivity is used hereafter) from the measured impedance values $|Z^*_{meas}|$ is based on equivalent circuit elements (this approach is valid in the low frequency range, i.e., below 10 MHz). The electrical response of a soil is modeled as a 'lossy dielectric', which involves a resistor and a capacitor in parallel. Therefore, the impedance corresponding to the soil Z^*_{soil} is:

$$Z^*_{soil} = \left[\frac{1}{R_{soil}} + j\omega C_{soil} \right]^{-1} \tag{6}$$

where R_{soil} and C_{soil} are the resistance and the capacitance of the soil respectively, j is the imaginary unit, and ω is the angular frequency.

The void ratio can be estimated from the electromagnetic measurements. In its simplest form, the permittivity κ'_{mea} of saturated soils can be expressed in terms of a volumetric average. Thus, the void ratio e in saturated soils is:

$$e = \frac{\kappa'_{mea} - \kappa'_{s}}{\kappa'_{w} - \kappa'_{mea}} \tag{7}$$

where κ'_w is the permittivity of water and κ'_s is the permittivity of soil particles. The value of $\kappa'_w = 78.5$ is used for water and $\kappa'_s = 6$ for the mineral that makes the particles. Permittivity increases with void ratio in saturated soils.

Ottawa F-110 sand (D_{50} = 0.12 mm, $e_{\max}$ = 0.848, $e_{\min}$ = 0.535) was used to explore specimen preparation effects. Six triaxial specimens with a nominal diameter of 75mm and height of 150mm were prepared. A circular aluminum split mold and a 0.033cm thick latex membrane are used to form and hold the specimen. The specimens were prepared by air pluviation, moist tamping, and water pluviation procedures.

Before triaixial testing, the electric needle probe was gradually inserted into the specimens to estimate spatial variability. The complex impedance Z^* was measured every 0.5 mm, corrected for stray parameters, and permittivity was calculated. Finally, the local void ratios were estimated from the permittivity. The results are shown in Figure 6 (other data can be found in Cho et al. 2004). It is observed that the specimen prepared by the moist tamping method has the highest variation in void ratio, while the specimen prepared by water pluviation shows the lowest variation. Comparing the result from standard undrained triaxial tests, it is noticeable that the spatial distribution of void ratio affects the undrained strength, that is, the higher the variation in local void ratio, the lower strength.

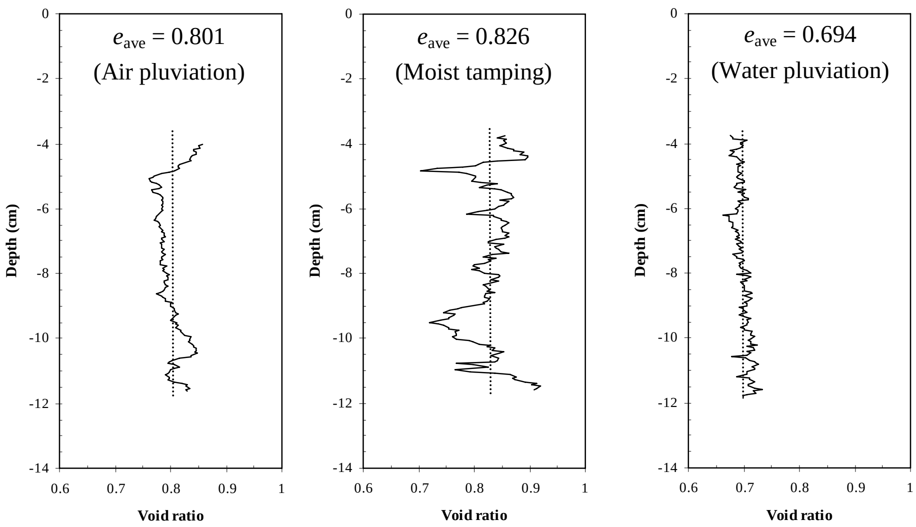

Figure 6: Void ratio variability for different specimens (f_r = 1MHz, voltage= 1V). The value e_{ave} is the global void ratio of the specimen and the parenthesis represents the specimen preparation procedure.

4.6 Pore fluid composition - gas hydrate formation

Mechanical wave and electromagnetic wave capture the characteristics of pore fluids including volumetric composition of pore fluids and phase transformation of pore fluids. (i.e., gas hydrate formation, water freezing, or vaporization during drying). This section proposes the wave-based measurements of gas hydrate-bearing sediments. Nucleation and accumulation of gas hydrate in sediments are monitored during hydrate formation.

Experiments were designed to investigate the formation and destabilization of gas hydrate-bearing sediments. All the experiments were conducted in a cylindrical cell (i.e., volume 3.17 cm^3; internal diameter 6.35 mm; height 100 mm), instrumented to measure temperature, pressure, electrical resistance and P-wave velocity. The cell was submerged in a bath, the temperature of which was controlled between 20°C and -10°C by circulating coolant from a cooler. The fine-grained sands (Ottawa F110 sand; uniform grain size; mean diameter = 120 μm grain size) were compacted in the reaction cell at a porosity $\phi = 0.397$ and no effective stress was applied.

First, the sediment specimen was fully saturated with water and pressurized to 4 MPa. Liquefied CO_2 was injected with approximate 5 MPa of pressure, and pore water in the specimen was saturated with dissolved CO_2 molecules chemically diffused from one end of the specimen. After several days, CO_2 dissolution terminated, as determined by monitoring pressure, and the sediment sample in the reaction cell was thereafter stabilized for 24 hours. Then, under an initial pressure of 4.7 MPa, sediments were cooled to 0.5°C. Temperature, pressure inside the system and electrical resistance were monitored during the formation process. P-wave velocity was periodically measured.

Figure 7 shows the evolution of temperature, pressure inside the sediment specimen, V_P, and resistance during cooling. Phase transformation (hydrate nucleation) began at approximately 2°C, showing a temperature jump due to release of heat by exothermic reaction and a sudden drop of pressure at roughly 230 min after the start of cooling. Resistance in sediments suddenly jumped due to decreased connectivity of water resulting from hydrate nucleation. V_P of the sediments remains almost constant until solid hydrate crystals nucleate. As soon as the hydrates started to form in pores, an apparent increase of V_P (from ~1650 m/s to ~1740 m/s, as shown in Figure 2) was noted, as the bulk modulus of the hydrate crystals is higher than that of the pore water. In addition, as the hydrate crystal growth proceeded by diffusion of dissolved CO_2 and pore spaces were filled with solid hydrate (hydrate accumulation). V_P continued increasing up to almost 2700 m/s.

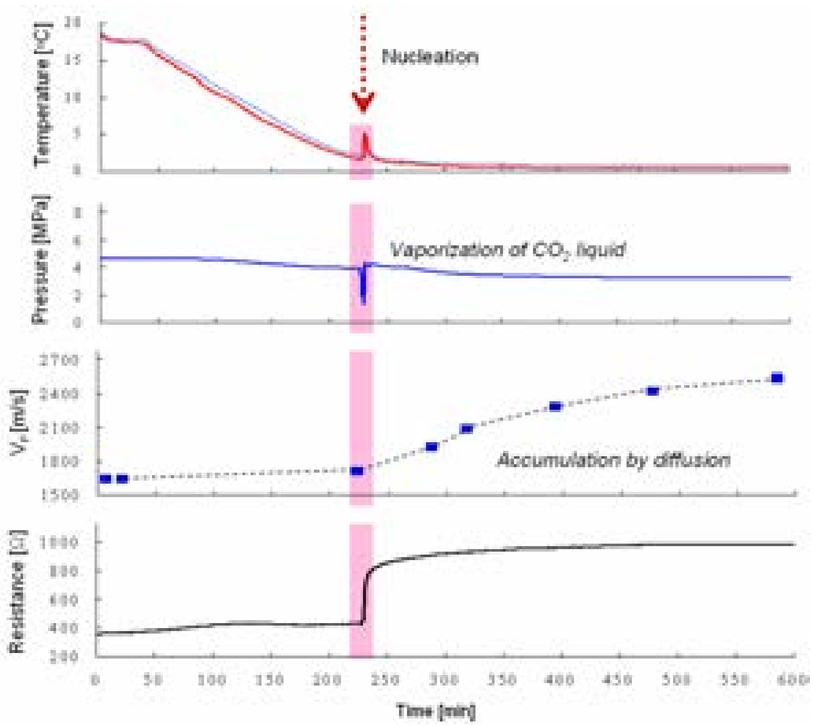

Figure 7: Monitoring of formation of CO_2 hydrate in sediments.

Several field and laboratory test results with synthetic hydrates support the pore filling hypothesis for the hydrate growth habit. In turn, compressional wave is more sensitive to capture the hydrate formation rather than shear wave, since an increase in bulk stiffness of pore fluids occurs prior to the shear stiffness of the skeleton during the formation of a small fraction of hydrate in pores. Electrical resistivity also provides complementary information, particularly on the pore fluid composition and hydrate quantity.

4.7 Shear wave propagation in jointed rock masses - stress state and joint condition

The stress level and joint condition affect shear wave propagation through regularly jointed rock masses. In this section, measurements of velocity and attenuation are conducted using a resonant column device designed for jointed rocks.

Shear waves are not affected by geometry; consequently, the torsional shear wave velocity and attenuation measured in a cylindrical bar apply to the infinite medium (Kolsky 1963). Furthermore, there is no geometric attenuation in bars. Based on these observations, we developed a torsional resonant column device to study long-wavelength shear wave propagation through jointed rocks. The cylindrical column is formed by vertically stacking rock disks on top of a high impedance steel base in order to create a free-fixed system. A light metal cap sits on top of the rock column, and the axial load is hung from the top cap by means of a rod that runs along a central hole drilled in each rock disc. Two accelerometers are mounted on the top cap to detect torsional motion. They are placed at diametrically opposite locations and their axes are aligned normal to the radius of the column. Figure 8 shows the jointed rock column and peripheral electronic devices.

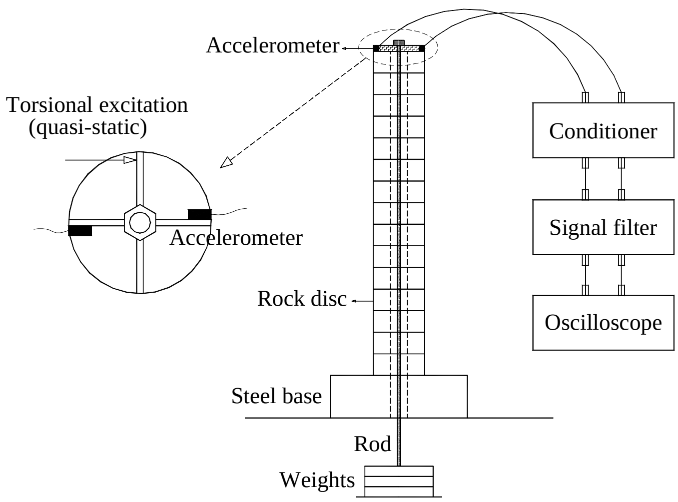

Figure 8: The rock resonant column testing device.

The torsional excitation is created by suddenly releasing the column from a quasi-static deformation enforced at the top of the column, allowing it to vibrate freely. The average strain level was kept below $\gamma = 10^{-5}$ in all tests. Each column is subjected to staged loading to the desired maximum normal stress (400 to 700 kPa). Wave propagation measurements are conducted at each stress stage during loading, and repeated during unloading after reaching the maximum load.

The signals obtained from the two accelerometers are added to cancel the flexural response. The combined signal is then transformed to the frequency domain to obtain the resonance spectrum. The resonant frequency f_n and the damping ratio D are recovered from the resonance spectrum. The wavelength λ is four times the column length L ($\lambda = 4L$) in first mode free-fixed resonance. Therefore, the torsional shear wave velocity is $V_s=4Lf_n$. Damping ratio D, spatial attenuation α_D and quality factor Q are related as $D = \alpha_D\lambda/2\pi = 1/2Q$ for low-loss conditions. Therefore the propagation parameter α_D [1/m] can be readily computed from the measured values of D.

The propagation velocity increases as the normal stress increases. Furthermore, the wave velocity through the rock mass decreases considerably in the presence of filling material in the joints. The response becomes more stress-dependent as the joint thickness increases, and in the presence of clayey rather than non-plastic gouge material.

The long-wavelength approximation $\lambda >> S$ is the most common situation in seismology and field seismic investigation (White 1983). Hertzian-type contact phenomena suggest a power function for the joint stiffness k_j as a function of the normal stress σ_n:

$$k_j = \psi\left(\frac{\sigma_n}{1\text{kPa}}\right)^{\zeta} \tag{8}$$

where the ζ exponent captures the stress sensitivity of the joint stiffness, and ψ [GPa/m] is the joint stiffness at σ_n=1 kPa. Therefore, the shear wave velocity in the rock mass V_{rm} can be computed:

$$V_{rm} = \sqrt{\frac{1}{\rho_{rm}}\left(\frac{1}{V_r^2\rho_r} + \frac{1}{S\cdot\psi\left(\frac{\sigma_n}{1\text{kPa}}\right)^{\zeta}}\right)^{-1}} \tag{9}$$

This equation captures the effect of joints on rock mass softening. The joint parameters ψ and ζ reflect joint surface properties, gouge type and thickness. They can be determined by measuring the shear wave velocity in the rock mass at different stress levels (Note: the mass density of the rock mass ρ_{rm} and the intact rock wave velocity V_r and density ρ_r must be determined separately).

In analogy to wave propagation in soils, we explore the possibility of using a simpler expression to relate the propagation velocity in the rock mass to the applied normal stress,

$$V_{rm} = \alpha \left(\frac{\sigma_n}{1\text{kPa}} \right)^{\beta} \tag{10}$$

In this case, α is the wave velocity in the rock mass subjected to σ_n= 1 kPa, and β describes the stress-sensitivity of wave velocity in the rock mass. The inverted α-β values are plotted in Figure 9; for comparison, the α-β pairs for a wide range of soils are superimposed on Figure 9 as well. The stress-dependent wave propagation velocity through jointed rock masses is well captured by a power-type relation.

Parameters α-β for rock masses tend to cluster above the cluster for soils. Therefore, wave velocity through jointed rock masses is higher than in soils at the same state of stress. Softer and thicker joints lead to lower stiffness at σ_n = 1 kPa (either factor ψ or α) and higher stress sensitivity (either exponents ζ or β). In general, there is an inverse relationship between stiffness at σ_n = 1 kPa and stress-sensitivity, both in the case of joint stiffness parameters ψ-ζ (Equation 3) and rock mass velocity parameters α-β (Equation 5).

Various joint properties are reproduced in the experiments to study their effect on shear wave propagation. Experimental results show that shear wave velocity increases with increasing normal stress, joint spacing and joint bonding, but it decreases with increasing joint opening and plasticity of the joint filling. The opposite trends are observed between attenuation and rock mass parameters. Well-matched grooved surfaces, as in slickensides, are less detrimental to stiffness and attenuation than mismatched rough surfaces. Analytical models that take into consideration the stress-dependent stiffness and frictional loss in joints and the stress-independent properties of rock blocks properly model experimental observations and permit extracting joint properties from rock mass tests data. Results highlight the prevalent role of joints on propagation velocity and attenuation in jointed rock masses.

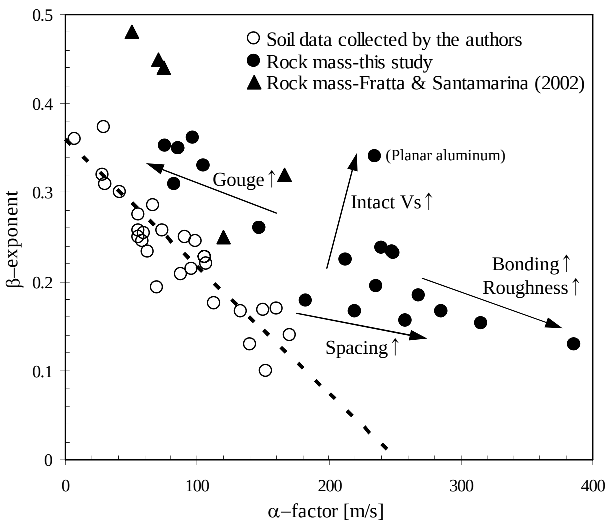

Figure 9: Parameters for the velocity–stress power relation (after Fratta and Santamarina 2002). Data shown as open circles were gathered with a wide range of soils; the regression line $\beta = 0.36 - \alpha/700$ applies to these data.

4.8 Anomaly detection in rock masses - tunnel head prediction

In viewpoint of geotechnical engineering, the prediction of anomaly presence in subsurface and the estimation of its position, size and state play an important role in designing structural foundations and characterizing their overall mechanical behaviors. Particularly, during the construction of tunnels, occurrence of poor rock masses at the tunnel face is a significant threat. However, the prediction of a weak zone remains as a unsolved problem to engineers related to underground space design and construction. Thus, this section presents an enhanced algorithm which effectively detects anomalies in particulate materials using an electrical resistivity survey.

The current of the particulate material with a spherical weak zone as shown in Figure 10 can be expressed using Coulomb's law and Gauss' law:

$$I = \int_0^{l-r} \sigma_{pm} \overline{E_{pm}} \cdot \pi l dl + \int_{l-r}^{l+r} \sigma_w \overline{E_w} \cdot \alpha l dl + \int_{l-r}^{l+r} \sigma_{pm} \overline{E_{pm}} \cdot (\pi - \alpha) l dl + \int_{l+r}^{\infty} \sigma_{pm} \overline{E_{pm}} \cdot \pi l dl \tag{11}$$

where α denotes $\sin^{-1}(r/l)$, r is the radius of the weak zone, σ_w is the conductivity of the weak zone and σ_{pm} is the conductivity of the particulate material.

Given that resistances are measured for each sensor configuration, the coordination of the sensors and the conductivity of the material; unknown parameters such as the size, conductivity and location of the anomaly can be obtained through an inversion algorithm (see Ryu et al. 2008 for more details). A series of experimental tests was performed on anomalies that were different in terms of size, location, and type in order to verify the developed algorithm. A comparison of the predicted and measured values shows that anomalies can be detected effectively using the electrical resistivity–based enhanced algorithm developed in this study.

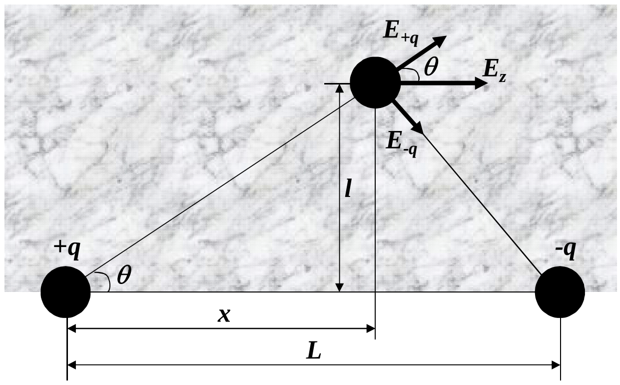

Figure 10: Electric field configuration for detection of spherical weak zone from tunnel face.

4.9 Shotcrete bonding state evaluation using the impact-echo method

Shotcrete is the general term for the cement, sand and fine aggregate concrete that are applied pneumatically and compacted dynamically under high velocity. Shotcrete is an important primary support for tunneling in rock. The bonding state of shotcrete on excavated rock surfaces is a core issue in the safe construction and maintenance of tunnels. Although shotcrete may be applied well initially onto excavated rock surfaces, it is affected by blasting, rock deformation and shrinkage and can debond from the excavated surface, causing problems such as corrosion, buckling, fracturing and the creation of internal voids. The effective non-destructive method is proposed to evaluate the tunnel shotcrete bonding state using the impact-echo (IE) method. Various bonding conditions (i.e., fully bonded, debonded, and void) were simulated using numerical and experimental models. The signals obtained from the numerical and experimental IE tests were analyzed at the time domain, frequency domain, and time-frequency domain (i.e., the Short-Time Fourier transform).

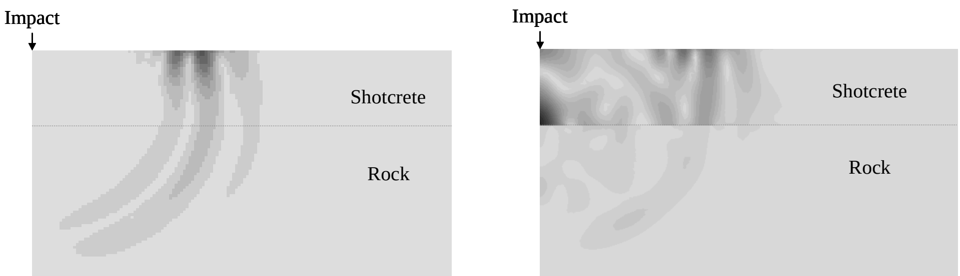

(a) Fully bonded condition (b) Debonded condition

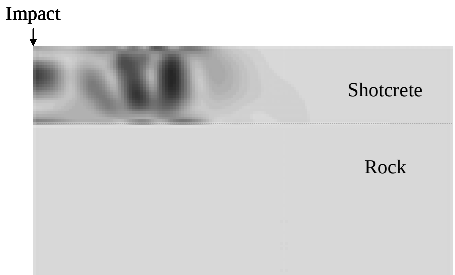

(c) Void condition

Figure 11: Graphical description of wave propagation depending on the shotcrete bonding state.

The typical results of wave propagation (i.e., acceleration) in the finite elements are shown in Figure 11 for different bonding states (0.00018sec after impact). In the case of the fully bonded condition (Figure 11a), the stress wave transmits through the shotcrete and hard rock layers and only slightly reflects from the interface between the shotcrete and hard rock layers. In the case of a debonded condition (Figure 11b), the stress wave transmits part of the way through and partly reflects from the interface, resulting in some part becoming entrapped in the shotcrete layer. Additionally, in the case of a void condition (Figure 11c), the stress wave does not transmit through the interface and completely reflects from the interface, resulting in the entire energy in this case becoming entrapped in the shotcrete layer. This is similar to an ideal free-free boundary condition.

Both numerical and experimental results suggest that the bonding state of shotcrete can be evaluated accurately through distinct changes in the peak amplitude in a time domain analysis, through changes in the resonance frequency and geometric damping ratio in a frequency domain analysis, and through changes in the contour shape and correlation coefficient in a time-frequency analysis.

5. CONCLUDING REMARKS

Soils are particulate and multi-phase materials, thus, their behavior is governed by microscale characteristics, effective stress, the presence of water, global void ratio, and temporal and spatial scales. Rock masses are discontinuous media, and their behavior is determined by the characteristics of intact rock, joint conditions (e.g., roughness, aperture and filling materials), orientation of joints, stress state, and presence of water among others. These properties can be effectively characterized using wave-based techniques. Experiments were performed using both elastic and electromagnetic waves to facilitate the application of wave-based techniques to characterize geo-materials. The shear wave measurements centered on monitoring changes in effective stress during consolidation, multi-phase phenomena related to capillarity, microscale characteristics of particles, and small-strain stiffness of jointed rock masses related to joint conditions. The electromagnetic wave measurements focused on stratigraphy detection in layered soils, the estimation of the void ratio and its spatial distribution, conduction in unsaturated soils, nucleation of gas hydrate in pore spaces and weak zone prediction in water-saturated rock masses. Compressional wave measurements were used to capture hydrate formation in pore spaces and to identify the shotcrete bonding state to a hard rock surface. The main conclusions from this study are as follows:

- When a clay is subjected to a K_o-loading, the shear wave velocity is uniquely related to the state of stress, so that it can be used to assess the state of stress and its changes during the consolidation.

- In unsaturated soils, changes in stiffness are related to changes in interparticle forces such as capillarity, bonding due to ion sharing, buttress effects due to fines migration and cementation due to salt precipitation. Shear waves permit studying the evolution of effective interparticle forces in unsaturated soils. This is particularly valuable in the pendular regime where direct measurements of the negative pore-water pressure are not feasible.

- As the degree of saturation decreases, the shear wave velocity and resistivity in unsaturated soils increase continuously and show no drop at the perfectly dry condition. The relation of shear wave velocity and resistivity to the degree of saturation is unique for each soil, underlining the importance of water content on soil characterization.

- The pore fluid and the mineralogy of grains govern the resistivity of saturated soils, and the amount of water in the soil mass and its connectivity controls resistivity changes in unsaturated soils.

- Angular and non-spherical particles increase the sensitivity of stiffness to the state of stress, rendering high β-exponents.

- The electrical needle-size probe can be used to detect interfaces in layered soils and to effectively assess the spatial distribution of void ratio in saturated soils and other properties in laboratory specimens, with sub-millimetric resolution. The local measurements of complex impedance permit assessing the spatial variability of either porosity, fluid resistivity (i.e., water content), or both.

- P-wave velocity and electrical resistivity capture the nucleation of gas hydrate in sediment pores and provide a means of monitoring the increase of hydrate saturation.

- Shear wave velocity in jointed rock masses increases with increasing normal stress, joint spacing and bonding, and decreases with increasing thickness and plasticity of the joint filling. The rougher the joint, the less sensitive to the stress the wave velocity becomes. On the other hand, shear wave damping in jointed rock masses decreases with increasing normal stress and with rough joints, and exhibits a large increase when joints are filled with gouge materials.

- The joint characteristics are directly related to the criteria for a rock mass classification system. The effect of joint conditions and stress levels on wave velocity can be reflected in rock mass characterization using seismic data so that wave-based rock mass characterization secures more reliability.

- Given that resistances are measured for each sensor configuration, the coordination of the sensors and the conductivity of the material; unknown parameters such as the size, conductivity and location of the anomaly can be obtained through an inversion algorithm.

- The shape of the time-frequency domain contour plot, the value of the correlation coefficient, and the geometric damping ratio gathered from the impact echo method give valuable information to assess the tunnel shotcrete bonding state in situ.

ACKNOWLEDGEMENTS

This research work was funded by the Brain Korea 21 Project in 2008. We wish to express our sincere appreciation to the organizing committees for providing the opportunity to undertake this research work.

REFERENCES

Barrett, P.J., 1980. The shape of rock particles, a critical review, *Sedimentology*, V. 27, pp. 291-303.

Brillouin, L., 1946. *Wave propagation in periodic structures*, McGraw-Hill.

Cho, G.C., 2001. *Unsaturated soil stiffness and post-liquefaction shear strength*, Ph.D. Thesis, Georgia Institute of Technology, p. 288.

Cho, G.C. and Santamarina, J.C., 2001. Unsaturated particulate materials - Particle-level study, *Journal of Geotechnical and Geoenvironmental Engineering*, ASCE, V. 127, No. 1, pp. 84-96.

Cho, G.C., Lee, J.S., and Santamarina, J.C., 2004. Spatial variability in soils: high resolution assessment with electrical needle probe, *Journal of Geotechnical and Geoenvironmental Engineering*, ASCE, V. 130, No. 8, August, pp. 843-850.

Cho, G.C., Dodds, J., and Santamarina, J.C., 2006. Particle shape effects on packing density, stiffness, and strength: natural and crushed sands, *Journal of Geotechnical and Geoenvironmental Engineering*, ASCE, V. 132, No. 5, May, pp. 591-602.

Choi, J.S., Song, K.I., Cho, G.C., and Lee, S.W., 2004. Characterization of unsaturated particulate materials using elastic and electromagnetic waves, *Key Engineering Materials*, V. 270-273, pp. 1653-1658.

Desrues, J., Chambon, R., Mokni, M., and Mazerolle, F., 1996. Void ratio evolution inside shear bands in triaxial sand specimens studied by computed tomography, *Géotechnique*, V. 46, No. 3, pp. 529-546.

Dobry, R. and Petrakis, E., 1990. Micromechanical modeling to predict sand densification by cyclic straining, *Journal of Engineering Mechanics*, ASCE, V. 116, No. 2, pp. 288-308.

Fenton, G.A. and Griffiths, D.V., 1996. Stochastics of free surface flow through stochastic earth dam, *Journal of Geotechnical Engineering*, V. 122, No. 6, pp. 427-436.

Fratta, D., and Santamarina, J.C., 2002. Shear wave propagation in jointed rock: state of stress, *Géotechnique*, V.52, pp. 495–505.

Fredlund, D.G. and Rahardjo, H., 1993. *Soil mechanics for unsaturated soils.* Wiley Inter-Science, New York, p. 517.

Frossard, E., 1979. Effect of sand grain shape on interparticle friction: indirect measurements by Rowe's stress dilatancy theory, *Géotechnique*, V. 29, No. 3, pp. 341-350.

Griffiths, D.V. and Fenton, G.A., 1993. Seepage beneath water retaining structures founded on spatially random soil, *Géotechnique,* V. 43, No. 4, pp. 577-587.

Goodman, R.E., 1989. *Introduction to rock mechanics*, 2nd ed., John Wiley & Sons.

Guéguen, Y., and Palciauskus, V., 1994. *Introduction to the physics of rock*, Princeton University Press.

Heyman, J., 1997. *Coulomb's Memoir on Statics*, An Essay in the History of Civil Engineering, Imperial College Press, p. 212.

Huang, T. H., C. S. Chang, and Z. Y. Yang, 1995. Elastic moduli for fractured rock mass, *Rock Mechanics and Rock Engineering*, V.28, pp. 135–144.

Jang, D.-J., Frost, J.D., and Park, J.Y., 1999. Preparation of epoxy impregnated sand coupons for image analysis, *Geotechnical Testing Journal*, GTJODJ, V. 22, No. 2, pp. 147-158.

Kolsky, H., 1963. *Stress waves in solids*, Dover.

Krumbein, W. C. and Sloss, L. L., 1963. *Stratigraphy and Sedimentation*, Second Edition, W. H. Freeman and Company, San Francisco, p. 660.

Kuo, C.-Y., Frost, J.D., Lai, J.S., and Wang, L.B., 1996. Three-dimensional image analysis of aggregate particle from orthogonal projections, *Transportation Research Record*, No. 1526, pp. 98-103.

Mitchell, J.K., Chatoian, J.M., and Carpenter, G.C., 1976. *The influences of sand fabric on liquefaction behavior*, Report No. TE 76-1, U.S. Army Engineer Waterways Experiment Station, University of California, Berkeley.

Mulilis, J.P., Seed, H.B., Chan, C.K., Mitchell, J.K., and Arulanandan, K., 1977. Effects of sample preparation on sand liquefaction, *Journal of the Geotechnical Engineering*, V. 103, No. GT2, February, pp. 91-108.

Paice, G.M., Griffiths, D.V., and Fenton, G.A., 1996. Finite element modeling of settlements on spatially random soil, *Journal of the Geotechnical Engineering Division*, ASCE, V. 122, No. 9, pp. 777-779.

Pennington, D.S., Nash, D.F.T., and Lings, M.L., 1997. Anisotropy of shear stiffness in Gault clay, *Géotechnique*, V. 47, no. 3, pp. 391-398.

Popescu, R. and Prevost, J.H., 1996. Influence of spatial variability of soil properties on seismically induced soil liquefaction, *Uncertainty in the Geological Environment: from theory to practice*, *Proceedings of*

Uncertainty '96, edited by Schackelford et al., Geotechnical Special Publication No. 58, Vol. 2, pp. 1098-1112.

Popescu, R., Prevost, J.H., and Deodatis, G., 1997. Effects of spatial variability on soil liquefaction: some design recommendations, *Géotechnique*, V. 47, No. 5, pp. 1019-1036.

Powers, M.C., 1953. A new roundness scale for sedimentary particles, *Journal of Sedimentary Petrology*, V. 23, No. 2, pp. 117-119.

Priest, S. D., 1993. *Discontinuity analysis for rock engineering*, Chapman & Hall.

Pyrak-Nolte, L.U., L.R. Myer, and N.G. Cook, 1990a. Transmission of seismic wave across single natural fracture, *J. Geophys. Res.*, V. 95, pp. 8617–8638.

Pyrak-Nolte, L.U., L.R. Myer, and N.G. Cook, 1990b. Anisotropy in seismic velocities and amplitudes from multiple parallel fractures, *J. Geophys. Res.*, V. 95, pp. 11345–11358.

Roscoe, K.H., Schofield, A.N., and Wroth, C.P., 1958. On the yielding of soils, *Géotechnique*, V. 8, pp. 22-53.

Ryu, H.H., Cho, G.C., Sim, Y.J., and Lee, I.M., 2008. Detection of anomalies in particulate materials using electrical resistivity survery - enhanced algorithm, *Modern Physics Letters B*, V. 22, No. 11, pp. 1093-1098.

Santamarina, J.C. and Cho, G.C., 2004. Soil behaviour: the role of particle shape, *The Skempton Memorial Conference*, Thomas Telford, Vol. 1, pp. 604-617.

Santamarina, J.C. and Cascante, G., 1998. Effect of surface roughness on wave propagation parameters, *Géotechnique*, V. 48, No. 1, pp. 129-136.

Santamarina, J.C., Klein, K.A., and Fam, M.A., 2001. *Soils and Waves – Particulate Materials Behavior, Characterization and Process Monitoring*, John Wiley and Sons, LTD, p. 488.

Santamarina, J.C., Rinaldi, V.A., Fratta, D., Klein, K., Wang, Y.H., Cho, G.C., and Cascante, G., 2004. The properties of near-surface soils in relation to elastic and electromagnetic wave parameters, Chapter in *Physical properties of near-surface materials*.

Schofield, A.N., 1998. Don't use the C word, *Ground Engineering*, August, pp. 30-32.

Schofield, A.N. and Wroth, P., 1968. *Critical State Soil Mechanics*, McGraw-Hill Book Company.

Stokoe, K.H., II, Lee, J.N.-K. and Lee, S.H.-H., 1991. Characterization of soil in calibration chambers with seismic waves, *Proceedings of 1st International Symposium on Calibration Chamber Testing*, Elsevier, Potsdam, New York, pp. 363-376.

Tonon, F., Bernardini, A., and Mammino, A., 2000. Reliability analysis of rock mass response by means of random set theory, *Reliability Engineering and System Safety*, V. 70, No. 3, pp. 263-282.

Wadel, H., 1932. Volume, shape, and roundness of rock particles, *Journal of Geology*, Vol. 40, pp. 443-451.

White, J.E., 1983. *Underground sound: Application of seismic waves*, Elsevier.

Yimsiri, S. and Soga, K., 1999. Effect of surface roughness on small-strain modulus: micromechanics view, *Pre-failure Deformation Characteristics of Geomaterials: Proceedings, 2nd International Symposium*, Torino, Italy; edited by M. Jamiolkowski, R. Lancellotta, and D. Lo Presti, 597-602

Yong, R.N., Alonso, E., and Tabba, M.M., 1977. Application of risk analysis to the prediction of slope stability, *Canadian Geotechnical Journal*, V. 14, pp. 540-553.

Yudhbir, and Abedinzadeh, R., 1991. Quantification of particle shape and angularity using the image analyzer, *Geotechnical Testing Journal*, GTJODJ, V. 14, No. 3, pp. 296-308.

Zhao, J., X.B. Zhao, and J.G. Cai, 2006. A further study of P-wave attenuation across parallel fractures with linear deformational behavior, *Int. J. Rock Mech. Min.*, V. 43, pp. 776–788.

TREND OF TRAFFIC ACCIDENTS AND ITS CHARACTERISTICS IN JAPAN

SHINJI TANAKA
International Center for Urban Safety Engineering,
Institute of Industrial Science, The University of Tokyo, Japan
stanaka@iis.u-tokyo.ac.jp

ABSTRACT

Traffic accident is one of the most serious risks in our daily life compared with other natural disasters. This paper reviews the trend of traffic accidents and its characteristics in the case of Japan. Japan becomes a relatively safe country in the world after long efforts to improve traffic safety which keep the number of fatalities decreasing, but the number of accidents is not decreasing, remains high. Specifically, traffic accidents of elderly people, pedestrians and at intersections are major issues currently. These trends are explained with some figures, and some research works to address traffic safety are also introduced.

1. INTRODUCTION

We tend to think that traffic accident is a rare, unlikely and unlucky event. However, even if you yourself have not experienced any traffic accidents in your life before, you may easily find somebody who has experienced it in your family, relatives and friends. Actually, the probability of one person encountering fatal traffic accident in his/her life is 0.5%, the probability becomes 53.4% for injury accidents and much more for non-reported accidents. Thus, traffic accident is not a rare event, but an immediate risk for everybody.

There were two serious traffic accidents in Japan in 2006. One took place in an intercity motorway in the middle of a rainy night. A truck slipped, spun and stopped with its front turned back blocking the carriageway. Thereafter, 20 vehicles collided with it one right after the other. As a result of this accident, 4 fatalities and 10 injuries occurred.

The other tragic accident occurred similarly in the night. A drunk driver collided with a car, at the top of an over-sea bridge, from behind. The car, carrying the five members of a family, dived into the sea due to the impact and the 3 children in the rear seat were killed. This accident, widely covered by the media, resulted in a revision of the Road Traffic Law to toughen the penalty for drunken driving.

Figure 1: Serious traffic accidents in 2006

When we think of disasters, we easily picture natural disasters, such as earthquakes, typhoons, floods, tsunamis and so on. All of them seriously impact our society at once and therefore it is of course quite important to prepare for them. However, if we asses the severity of disasters by the number of deaths, traffic accidents result in much more fatalities than any natural disasters every year in Japan as shown in Figure 2 (although there is a decreasing trend). And, we all remember the Hanshin-Awaji Earthquake Disaster or the Sumatra Tsunami Disaster very clearly, but few of us remember yesterday’s fatal traffic accidents. Traffic accidents should be regarded as man-made disasters affecting urban safety. We should start to tackle it to realize a comprehensive urban safety.

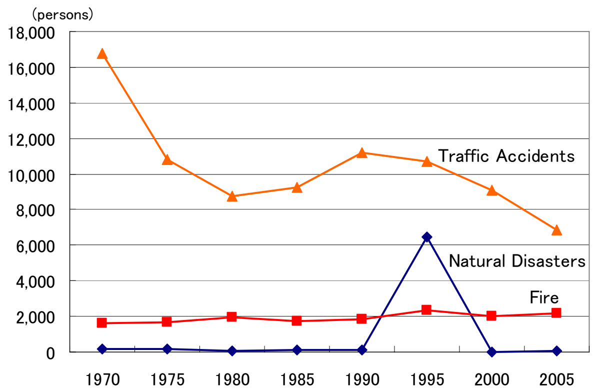

Figure 2: Number of fatalities caused by disasters in Japan

2. TRAFFIC ACCIDENTS IN THE WORLD

First, let us review the situation of traffic accidents in the world. As for the number of fatalities by traffic accidents in different countries, the top three deadliest countries are China, India, and the United States. The former two are the most populated and the last one is the most motorized country. However, if you see the same numbers in relative terms, i.e. number of fatalities per 100 thousand persons as shown in Figure 3, the situation becomes different. China and India are now ranked in the middle, and the most dangerous countries are South Africa, Malaysia and Russia. On the other hand, northern European countries such as Netherland, Sweden, the United Kingdom and Norway, which are regarded as keen on safety measures, are in the safest group. Japan is a relatively safe country next to them. Actually, the Japanese government set a goal in 2003 "to reduce traffic fatalities to less than 5,000 a year and to realize the safest traffic society in the world". If the number achieves this, then "the safest" might become true. Looking at these figures, Japan seems to have fewer problems on the traffic safety issue.

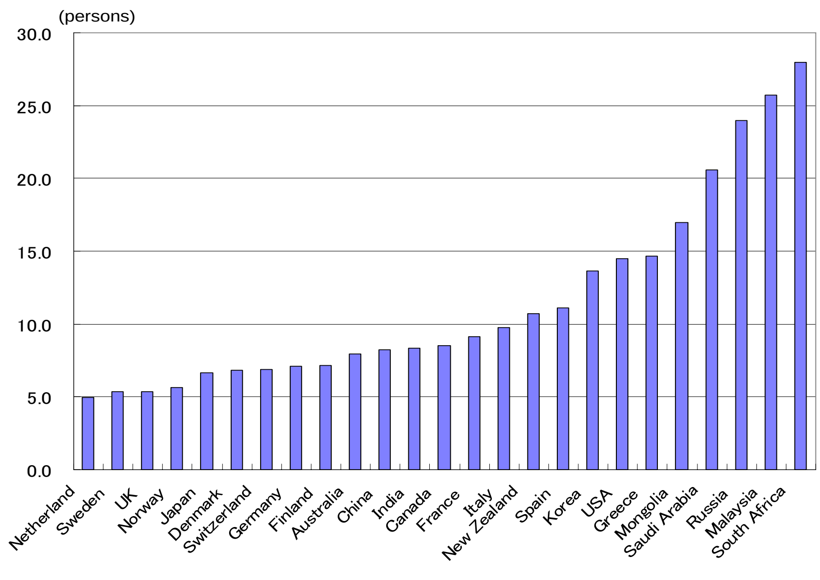

Figure 3: Number of fatalities per 100 thousand persons

3. TRAFFIC ACCICENTS IN JAPAN

3.1 Overall trend

Then, is everything going well in Japan? Figure 4 shows the trend of traffic accidents, fatalities and injuries in Japan. There was a peak in 1970, when the number of fatalities was 16,775. This serious situation was often called "traffic war". After that, the government and the police made a lot of efforts to reduce traffic accidents by, for example, providing sidewalk or cross-over bridges for pedestrians, putting on traffic signals at intersections, obligating seatbelt fastening etc. Vehicle manufacturers also improved their products recently by equipping airbags, impact absorption bodies and so on. Thanks to these countermeasures, the number of fatalities reduced drastically to 5,744 in 2007, which is about one third of the peak value.

However, if you see the number of injuries or accidents, they have been not decreasing or stable in the last 30 years. This is one recent trend of traffic accidents in Japan. Of course, as the volume of vehicles' mileage is also growing rapidly, it is not easy to reduce the number of traffic accidents. Therefore, we need some other countermeasures to realize "the real safest traffic" or "zero-accidents society".

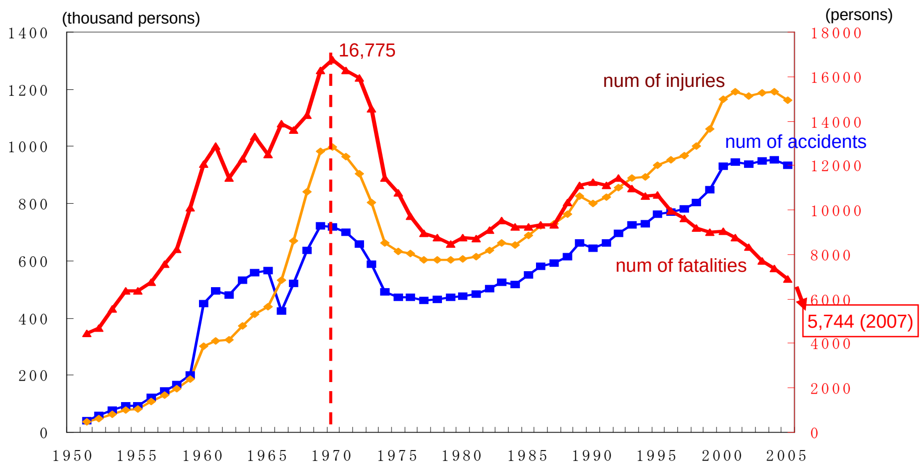

Figure 4: Trend in the number of traffic accidents in Japan

3.2 Accidents by age groups

Next, let us see more specific problems. Figure 5 shows the number of fatalities counted by age groups. The dominant age group is "65 and older", which accounts for 44.2% of fatalities. (Young people group was worse in the 80s but it has improved nowadays.) Actually, the fatality ratio of elderly people in traffic accidents is extremely high compared with other age groups as shown in Figure 6. This means, traffic accidents involving elderly people is likely to become fatal ones. Also, Japanese society itself is aging more and more, therefore, the number of licensed drivers of 65 years old and older is about 8 million today and will double to 17 million in 2030. This transition may cause more serious problems.

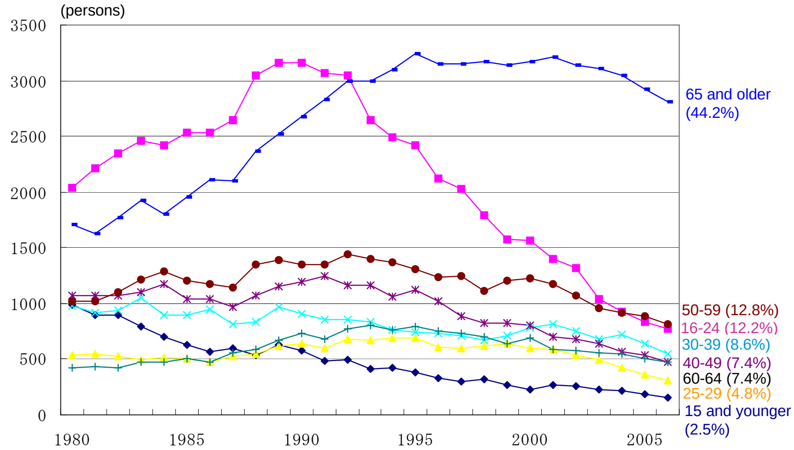

Figure 5: Fatalities by age group

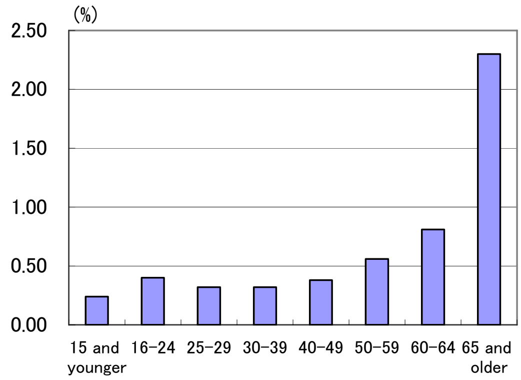

Figure 6: Fatality ratio by age group

3.3 Accidents by transportation modes

Figure 7 shows the fatalities by transportation mode. Here, the largest is in vehicles and the second is pedestrians. Actually, the percentage of pedestrian fatalities out of the total is increasing from 2000. And, the percentage of elderly people (65 and older) is also increasing.

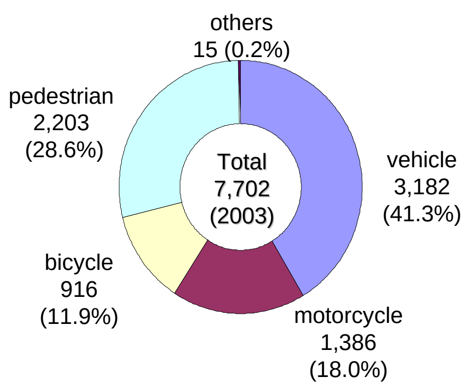

Figure 7: Fatalities by transportation mode

As a result, the graph of fatalities by age groups and transportation modes (Figure 8) suggests that elderly pedestrians are at significantly high risk. The second and the third highest are also elderly people in vehicles or on bicycles. From these results, we can understand that traffic safety countermeasures especially for elderly people, and pedestrians are highly required.

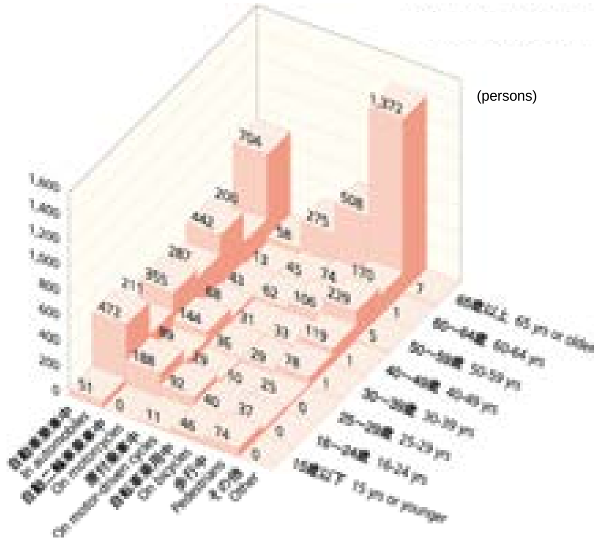

Figure 8: Fatalities by mode and age group

3.4 Types of accidents

Then, what types of accidents are most serious? Figure 9 shows the types of accidents by severity, that is, fatality, severe injury and light injury. From this, we can see that; pedestrian, single and head-on accidents are major fatal accidents. Rear-end accidents is the largest light injury accidents. Intersection head-on is relatively high in all categories. We need different types of countermeasures depending on those accidents types.

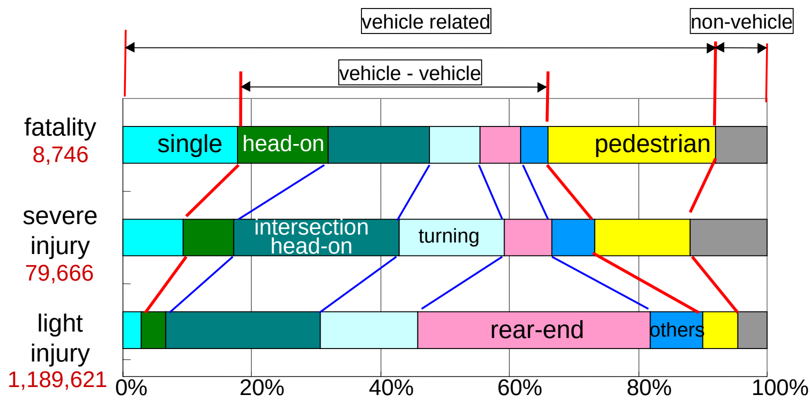

Figure 9: Types of accidents by severity

3.5 Location of accidents

As for accidents locations, Figure 10 shows the ratio of locations where accidents occurred. Accidents at intersections occupy more than half of total accidents, then accidents in straightway is about 40% and the rest is in other locations. As intersection accidents are likely to include not only vehicles but also pedestrians or bicycles, countermeasures at intersections are urgently required.

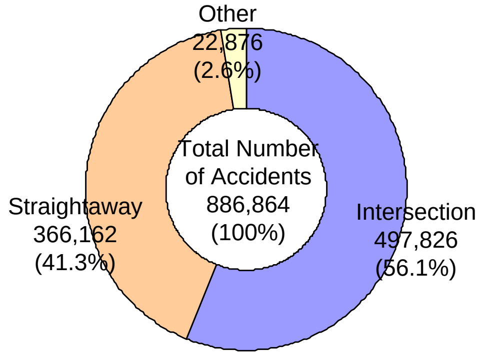

Figure 10: Locations of accidents

3.6 Causes of accidents

Figure 11 shows a survey result investigating causes of accidents. The largest is “delay in recognition”, the second is “errors in judgment” and the third is “errors in operation”. Those three causes can be regarded as “Human errors” and they occupy three quarters of the accidents causes. The rest is “others” like speeding and drinking etc. Of course these traffic violations should be controlled strictly, but we may also need to consider some driver’s assistance system, such as ITS, to reduce accidents caused by human errors.

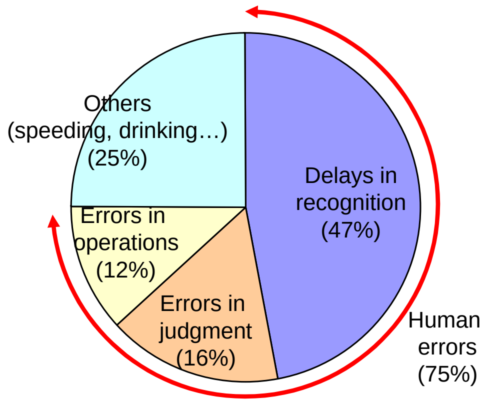

Figure 11: Causes of accidents

3.7 Social loss by traffic accidents

Finally, how much social cost or loss do traffic accidents cause? The Cabinet Office in Japan conducted a research project to estimate the social loss caused by traffic accidents. It classified the loss into five categories, that is, human loss, physical loss, business loss, public loss and non-monetary loss. Here, human loss means medical care cost or salary loss, physical loss means car / structure damages, business loss is caused by worker's absence, public loss is the cost for ambulance, police and cleaning, and non-monetary loss means mental loss like pain, sorrow and trouble.

According to the result, the total loss including non-monetary loss was approximately 60 billion USD in 2007 and the composition is shown in Figure 12. Non-monetary loss occupies quite a large share (35%), which comes mainly from fatal accidents. Even though the number of fatalities becomes less than 6,000, we have to continue efforts to reduce them so that the social loss is reduced, too.

If we see the monetary part by severity, then the loss due to injury accidents especially lighter ones is the hugest because their number is quite large. In any sense, those losses are enormous and continue every year.

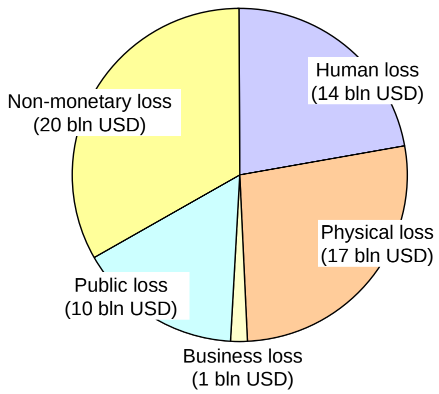

Figure 12: Composition of social loss caused by accidents

4. RESERCHES FOR TRAFFIC SAFETY

To solve the problems mentioned above and to improve the traffic safety, we need researches from the viewpoint of traffic engineering. One of the topics introduced here is about signal control improvement.

Generally in signal control, we need some clearance time (yellow and red signal) to clear the traffic from the intersection when the signal phases change. At this moment, a lot of traffic accidents like head-on, rear-end and pedestrian accidents happen. Therefore, the clearance time is one of the keys to improve traffic safety in urban signalized intersections. We observed actual traffic flows at several intersections using video cameras and examined whether the current signal settings are appropriate to ensure traffic flows in different directions.

The same can be said on pedestrian signals. Currently, pedestrian signal clearance time (flashing signal) is determined by the half the crossing road length and as a result a lot of pedestrians remaining on the road when the signal turns to red. Here we also conducted field observations and analyzed pedestrian walking behaviors, then discussed the feasibility of a new pedestrian signal control method to reduce the number of remaining pedestrians on red.

We sometimes use a driving simulator to analyze driver's behavior when he is faced with a yellow signal and puzzled whether to go or not, which is called "dilemma situation". As the driving simulator can record precise data of vehicle and driver, we can analyze his/her behavior in detailed way, for instance reaction time, vehicle's deceleration etc. After doing this, we would like to propose an advanced signal control which reduces such dilemma situation.

Figure 13: Driving simulator analysis

5. CONCLUDING REMARKS

Traffic accidents are the most important issue to be solved in transportation problems, and will continue to be in the future. Japan's efforts achieved a considerable reduction in the number of traffic fatalities from the peak, but there are still lots of casualties due to traffic accidents. Furthermore, there are still many developing countries which do not have very basic traffic safety facilities like pedestrian sidewalk and traffic signals. We must continue looking for a better solution to achieve a safer traffic, and should contribute to safety improvement in other countries with our experiences.

REFERENCES

Cabinet Office, *White Paper on Traffic Safety in Japan*
National Police Agency, *Road Traffic Accidents Japan*
Fire and Disaster Management Agency, *Statistics on Natural Disasters*
Japan Automobile Manufacturers Association, 2004, *Measures for Safety and Environment*

BOND STRENGTH OF CONCRETE INTERFACE BY USING FRACTURE MECHANICES APPROACH

PISON UDOMWORARAT
Assistant Professor, Department of Civil engineering
King Mongkut's University of Technology, North Bangkok
pisontit@hotmail.com

ABSTRACT

This paper proposes an evaluation of concrete bond strength based on energy approach. A four-point bending test for determining the critical energy release rate or the interfacial fracture toughness is applied to two types of test specimens, i.e., sandwich of steel-concrete-steel specimen and steel-CFRP-concrete specimen. A combination of testing results and path-independent J-integral of finite element model based on Virtual crack extension method can be used to determine interfacial fracture toughness effectively. Moreover, it is found out that the interfacial fracture toughness of steel-concrete-steel specimen depends on surface roughness of steel plates and has average fracture toughness of 26.78 J/m^2 where steel-CFRP-concrete specimen has average fracture toughness of 106.96 J/m^2.

1. INTRODUCTION

To evaluate bond strength at interfaces of two dissimilar materials, experimental methods of evaluations shall be broadly grouped in two categories. The first category attempts to deduce the interface energy through the observed propagation of a pre-existing flaw or crack. The second attempts to measure direct quantities such as normal stress, shear stress from the experiment without considering a pre-existing flaw. Shortcomings found from the first category, is due to its complexity in expression while the second category is a lack of applicability in case of shear stress and normal stress existences simultaneously. The first category seems to meaningfully characterize the bond behavior rather than the second category when combining of both stresses. To deal with two dissimilar materials, interfacial fracture problems are inherently mixed mode, i.e., mode 1 and mode 2 that are very difficult to define by stress intensity factors of the interfacial crack. Therefore, strain energy release rate, G, is usually used as a fracture parameter for interfacial mechanics. Since the strain energy can be seen as finite value and a problem of oscillatory singularity near the crack tip is avoided.

In this study, a four-point bending test has been proposed to evaluate steel-to-concrete and carbon fiber reinforced polymer (CFRP)-to-concrete bond strength. The bond strength are presented in terms of fracture energy (strain energy release rate) by varying the surface roughness of the steel plates for steel-to-concrete specimens. Likewise, the bond strength of CFRP-to-concrete specimens are presented in terms of fracture energy by varying the lengths of pre-existing cracks. Next, finite element analysis based on *J*-integral is also carried out to verify the strain energy release rate of bimaterial interfacial crack. In order to facilitate discussion and a profound understanding, some fundamental concepts of the interfacial fracture mechanics have been reviewed in the next section.

2. INTERFACIAL FRACTURE MECHANICS

As shown in Figure 1, when two isotropic materials with different elastic properties are bonded together and contain any interfacial crack lengths. If they are subjected to any load in x-y plane, such system with the stress concentrations at directly ahead of interfacial crack tip ($\theta = 0$) will always occur in two directions, so-called mixed-mode stress. The mixed-mode stress is inherent of bimaterial and the interfacial crack will extend when such stress reaches to its limit.

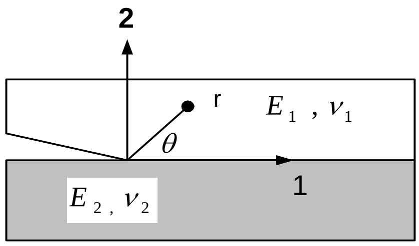

Figure 1: The interfacial crack

The relationship between stress and interfacial stress intensity factor ahead of crack tip ($r, \theta = 0$) was defined by Rice (1988) in terms of a complex form as

$$\sigma_{22} + i\sigma_{12} = \frac{Kr^{i\varepsilon}}{\sqrt{2\pi r}} \tag{1}$$

where σ_{22} = normal stress, σ_{12} = shear stress, $i = \sqrt{-1}$, and complex stress intensity factor as $K = K_1 + iK_2$ (Mode I, Mode II intensity factor)

$$\varepsilon = \frac{1}{2\pi} ln\left(\frac{1-\beta}{1+\beta}\right) \tag{2}$$

The quantity ε is a measure of the elastic mismatch of the bimaterial pair. If the two materials have identical elastic properties, or if they are incompressible$(\nu_1 = \nu_2 = 0.5)$, then $\varepsilon = 0$ and the stress fields reduced to those for homogeneous material. Relative displacements at location behind crack tip can be expressed in terms of the interface stress intensity factor as

$$\delta_2 + i\delta_1 = \frac{4\left(1/\overline{E_1} + 1/\overline{E_2}\right)}{\left(1+2i\varepsilon\right)\ \cosh\left(\pi\varepsilon\right)} \mathrm{K}\sqrt{\frac{r}{2\pi}} r^{i\,\varepsilon} \tag{3}$$

Where $\delta_2 =$ vertical displacement $= u_2\ (r, \theta = \pi) - u_2\ (r, \theta = -\pi)$, $\delta_1 =$ horizontal displacement $= u_1\ (r, \theta = \pi) - u_1\ (r, \theta = -\pi)$, $E_j =$ modulus of elasticity, $\overline{E_j} = E_j$ for plane stress condition, $\overline{E_j} = E_j /(1 - \nu_j^2)$ for plane strain condition, and Dundur's elastic mismatch parameter as

$$\beta = \frac{1}{2} \frac{\mu_1 \left(1 - 2\nu_2\right) - \mu_2 \left(1 - 2\nu_1\right)}{\mu_1 \left(1 - \nu_2\right) + \mu_2 \left(1 - \nu_1\right)} \tag{4}$$

where ν = Poisson's ratio, μ = shear modulus, subscript of 1 and 2 designated to above and bottom materials, respectively.

If $\varepsilon \neq 0$, then, the oscillatory singularity is existed at the crack tip. Consequently, the relevant characterizing to stress distribution around crack tip or crack surface displacement as $r \to 0$ cannot be available. Thus, the use of phase angle, ψ , arctangent of Mode II to Mode I intensity factor, which is in character of mixed mode to interpret the crack tip stress, is suit as expressed below

$$\begin{aligned} \psi &= \tan^{-1} \left(\frac{K_2}{K_1}\right) \\ &= \tan^{-1} \left(\frac{\operatorname{Im} K r^{i\,\varepsilon}}{\operatorname{Re} K r^{i\,\varepsilon}}\right) \end{aligned} \tag{5}$$

Without a physical meaning, the complex form of the phase angle from equation (3), $r^{i\varepsilon}$, could be substituted by a dimensionless complex variable, $\lambda^{i\varepsilon}$ as shown below

$$\psi = \tan^{-1} \left(\frac{\operatorname{Im} K \lambda^{i\,\varepsilon}}{\operatorname{Re} K \lambda^{i\,\varepsilon}}\right) \tag{6}$$

where $\lambda = r / L$, $L =$ characteristic length such as crack length

Generally, factor toughness of dissimilar materials can be defined by either interfacial stress intensity factor, *K* or strain energy release rate, *G*. Strain energy release rate, *G*, is superior and broadly used for interfacial crack toughness than stress intensity factor due to its simplicity. As from the study of Matos et al. (1989), Sun and Qian (1997), it was shown that the results from their analysis based on energy method worked very well. Besides, interfacial stress intensity factor, *K*, is directly related to energy release rate. As suggested by Malyshev and Salganik (1965), strain energy release rate can be expressed in terms of interfacial stress intensity factor as well, and the interfacial crack will be formed as $G = G_C$ (strain energy release rate reaches critical strain energy release rate) or $|K| = |K|_c$ where

$$G = \frac{\left(1/\overline{E}_1 + 1/\overline{E}_2\right)}{2\cosh^2(\pi\varepsilon)}|K|^2 \tag{7}$$

3. EXPERIMENTAL SETUP

3.1 Four point bending specimen

Generally, the study of interfacial crack requires either four-point bend specimen or other test configurations, as shown in Figure 2. Because a steady-state of strain energy release rate (independent of crack length) is existed for crack propagation between inner loading points.

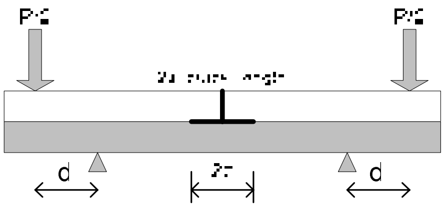

Figure 2: Four point bending specimen

The steady-state strain energy release rate can be calculated by the elementary beam theory by transforming the beam section as

$$G_{ss} = \frac{M^2}{2EB}\left(\frac{1}{I_c} - \frac{1}{I_g}\right) \tag{8}$$

where $M = Pd/2$, $E =$ elastic modulus, $I_c =$ moment of inertia of crack beam , $I_g =$ moment of inertia of uncrack beam , and $B =$ width of section.

3.2 Steel-concrete-steel specimens

Four point bending specimen (2 layers) was originally proposed by Charalambides et al. (1989) and Matos et al. (1989), in order to determine fracture resistance and stress intensities between bimaterial interfaces by means of the *J*-integral together with the virtual crack extension method. In this study, a modified four point bending specimen (3 layers, Steel-Concrete-Steel) is introduced for determining interface fracture energy by adding additional steel plate layer at the top of concrete layer. Figure 3 shows a sketch of the modified four point bending specimen. An idea of introducing modified bending specimen for steel-concrete-steel interfaces is that concrete is brittle in nature and 2 layers simple four point bending specimen may not induce cracking along the interfaces, because vertical cracking may occur in concrete layer prior to interface crack propagation. Beside that bottom substrate needs to elastically bend until cracking at interface occurs.

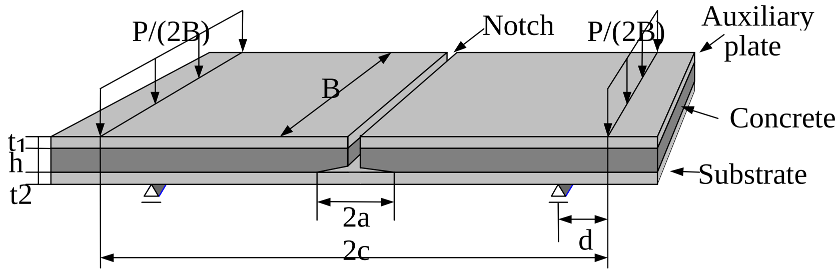

Figure 3: Modified four point bending specimen

The test specimens were prepared by placing cement mortar between two controlled roughness steel plates, i.e., 50 μm , 80 μm and 120 μm . Steel substrate and auxiliary plates were designed to have the same dimension 50×300×5.8 mm. All steel plates are made of SM400 steel class of which the elastic modulus is approximately about 210000 MPa. The mechanical of the concrete mortar are listed in Table 1.

Table 1: Cement mortar mechanical properties

	σ_c (MPa)	**E (GPa)**	**ν**
Mortar	31.6	19.89	0.17

There are totally 15 specimens, i.e., 5 specimens for each surface roughness 50 μm , 80 μm and 120 μm which are designated as R50, R80 and R120, respectively. Figure 4 shows experimental setup of the test specimen. The distance between inner loading points 2c is 200 mm where the distance between upper and lower loading points d is 30 mm. The load was applied by displacement control method with very low speed of 0.1 mm per minute.

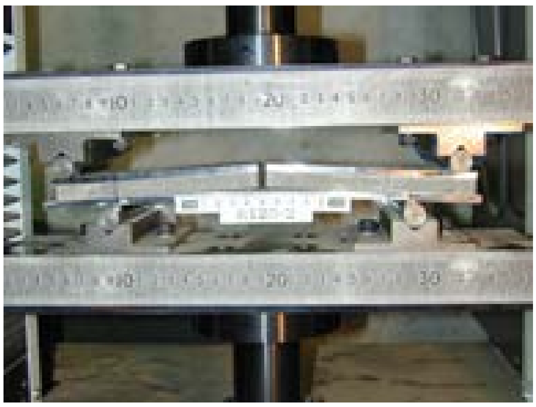

Figure 4: Setup of the steel-concrete-steel test specimen

3.3 Steel-CFRP-Concrete specimens

When concrete beam externally reinforced with the CFRP plate, it cannot be directly tested as in section 3.2 because of its relatively low flexural stiffness of CFRP. A plate can be curved along with the deflection of beam; concrete had ruptured before a plate debonded. To capably control debonding, a new test configuration has been proposed in order to improve flexural stiffness of the CFRP plate. In this study, steel plates with a dimension of 12×50 mm. and 500 mm. in length, were bonded with CFRP plate. Ten of specimens, as shown in Figure 5 and 6, concrete blocks of 50×100×150 mm. were bonded to the other face of CFRP. Before bonding together, a vinyl tape was stuck to both ends of blocks with having 5-to-23-mm. in length to initiate interfacial precracks. Figure 7 shows experimental setup of the test specimen.

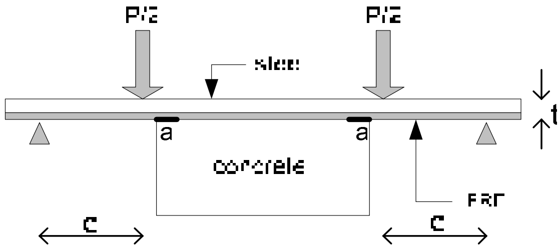

Figure 5: Four point bending test

Figure 6: Specimen preparation

Figure 7: Setup of the steel-CFRP-concrete test specimen

Table 2 contains the properties of the CFRP and epoxy resin, relevant to this study. The products of CFRP and adhesive resin were provided by the Sika (Thailand) Co., Ltd.

Table 2: Properties of CFRP and epoxy resin

CFRP	Type S512
Width (mm)	50
Thickness (mm)	1.2
Elastic Modulus (GPa)	177

Epoxy Sika cabodur – 30	Adhesive
Static E-modulus (GPa)	12.8
Adhesive Strength (MPa)	4 (concrete failure)
Shear Strength (MPa)	15 (concrete failure)

4. FOUR POINT BENDING SPECIMEN TEST RESULTS

A typical load-displacement from the experiments is shown in Figure 8. The experimental results evidently suggest that the graph consists of two slopes. The point where the first slope changes to the second slope can be defined as the initial crack extension point. The stiffness of the composite drops down to be the stiffness of steel substrate. Therefore, critical load (P_{cr}) corresponding to the constant energy release rate can be indicated.

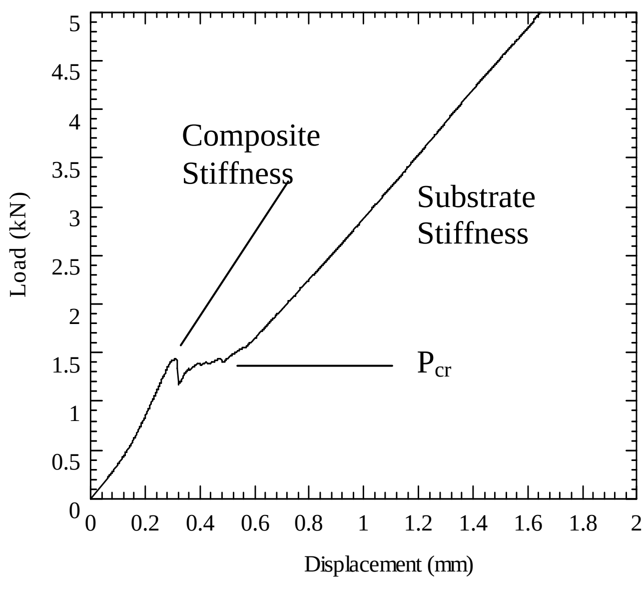

Figure 8: Typical load-displacement response

By substituting the critical load into equation (8), the critical strain energy release rates, G_c, can be determined. Similarly, using equation (7), critical stress intensity factor, $|K|_c$, can be determined. From the test results, average energy release rates of steel-concrete-steel specimens are plotted as a bar chart as shown in Figure 9. The results indicate that the energy release rate depends slightly on the plate surface roughness. The energy release rate increases as the roughness increases. However, the test results show a very small discrepancy for the roughness 50-120 μm . The average energy release rate of steel-concrete-steel is about 26.78 J/m^2.

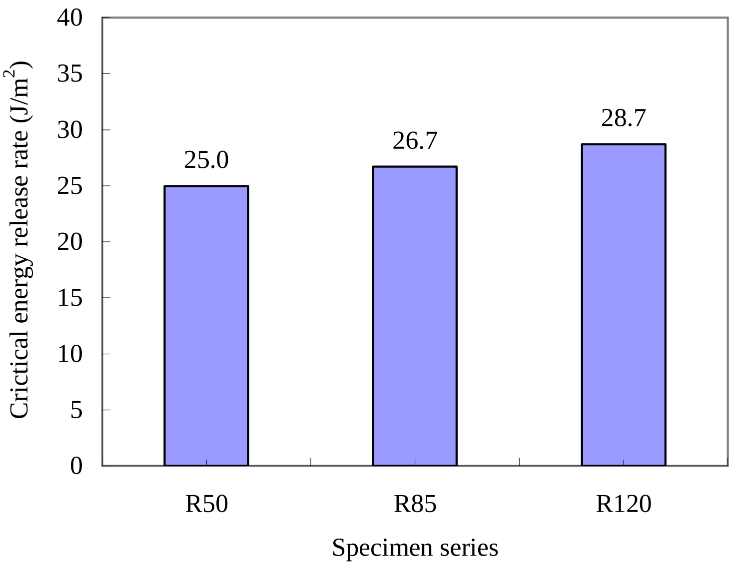

Figure 9: Average energy release rate of steel-concrete-steel specimens with various surface roughness

Table 3 shows critical energy release rate, G_c, of steel-CFRP-concrete specimens of various precrack sizes. The G_c are relatively equal and quite constant along with the crack lengths. This means that steady-state of strain energy release rate (independent of crack length) is existed for crack propagation between inner loading points. The average energy release rate of steel-CFRP-concrete is about 106.96 J/m^2.

Table 3: Critical energy release rate of steel-CFRP-concrete specimens with various precrack sizes

Crack length (mm.)	**5**	**9**	**13**	**17**	**21**	**23**	**Average**
$G_c \left(J/m^2\right)$	103.91	104.79	105.5	107.99	123.77	116.39	106.96

5. FINITE ELEMENT MODEL AND ANALYTICAL RESULTS

Finite element software so-called ABAQUS is used to determine *J*-integral and crack surface displacement. As shown in Figure 10, a steel-concrete-steel model mesh consists of 1250 eight-node plain strain biquadratic elements. At the area in vicinity of the crack tip, finite element meshes are modeled by wedge shape eight-node singular elements. The singular element is formed by the 8-node element by coalescing the three nodes to the one at the tip, whilst a square root singularity in the strain field at the tip is obtained by placing the first node away from that point at one quarter of the distance to the second point. Similarly, as shown in Figure 11, steel-CFRP-concrete model consists 1563 elements: CFRP beam (transformed section of CFRP-steel beam) and concrete block. Material properties are: $E_s = 200\ GPa$, $\nu_s = 0.30$, $E_{FRP} = 177\ GPa$, $\nu_{FRP} = 0.30$, $E_c = 19.89\ GPa$, and $\nu_c = 0.17$.

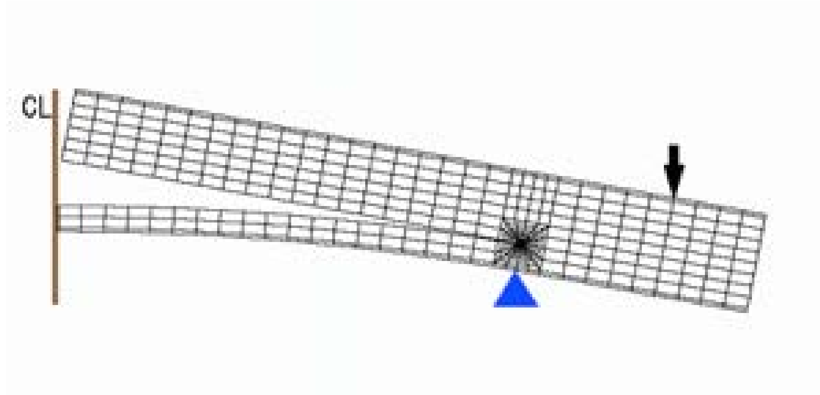

Figure 10: Finite element model for steel-concrete-steel specimen

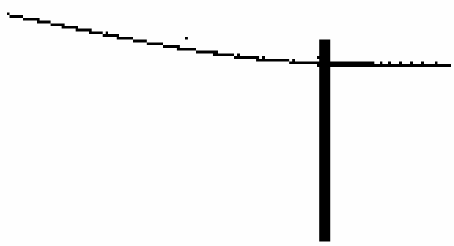

Figure 11: Finite element model for steel-CFRP-concrete specimen

To extract mode mix fracture resistance, the numerical method is applied in combination with crack surface displacement method proposed by Matos et al. (1989). The stress intensity factor can be determined by inversing Equation (3) as

$$K = \left[\frac{(1+2i\varepsilon \ \cosh(\pi\varepsilon)\overline{E}_1\overline{E}_2}{4(\overline{E}_1+\overline{E}_2)} \right] \left(\frac{2\pi}{|x|} \right)^{\frac{1}{2}} |x|^{-i\varepsilon} (\delta_y + i\delta_x) \qquad (9)$$

Where $|x|$ is the distance from crack tip to any node on coordinate ($|-r|, \theta=0$). The variables in complex displacement term, $(\delta_y + i\delta_x)$, are the results of FEM. Considering all rings surrounded the crack tip, G is determined by substituting $|K|$ into equation (7). The G is then compared with J-integral among those rings of the biquadratic element mesh. The one provides G equal to J-integral, parameters of such ring, i.e., $|x|$ and δ, will be chosen to calculate the phase angle as

$$\psi = \phi_u + \phi_c - \varepsilon \ln\left(\frac{|x|}{L}\right) \qquad (10)$$

where $L =$ crack length, $\phi_u = \arctan(\delta_x / \delta_y)$, $\phi_c = \arctan(2\varepsilon)$

Figure 12 illustrates energy release rate versus crack length from steel-concrete-steel finite element model as an example. Constant energy release rate can be obtained while crack propagates in between inner loading supports. Subsequently, the energy release rate from the finite element analysis decreases with increasing in crack length. Figure 12 shows phase angles plotted against crack lengths. It is found that phase angle slightly increases along with crack length. The average phase angle of steel-concrete-steel specimen is approximately about 46°. Similar manner is applied to determine average phase angle of steel-CFRF-concrete specimen which is about 35°.

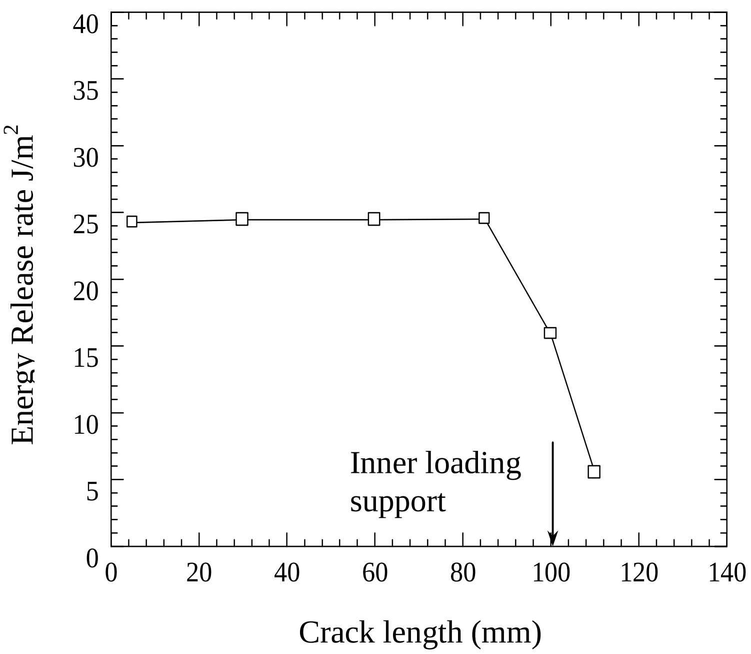

Figure12: Plot of energy release rate versus crack length

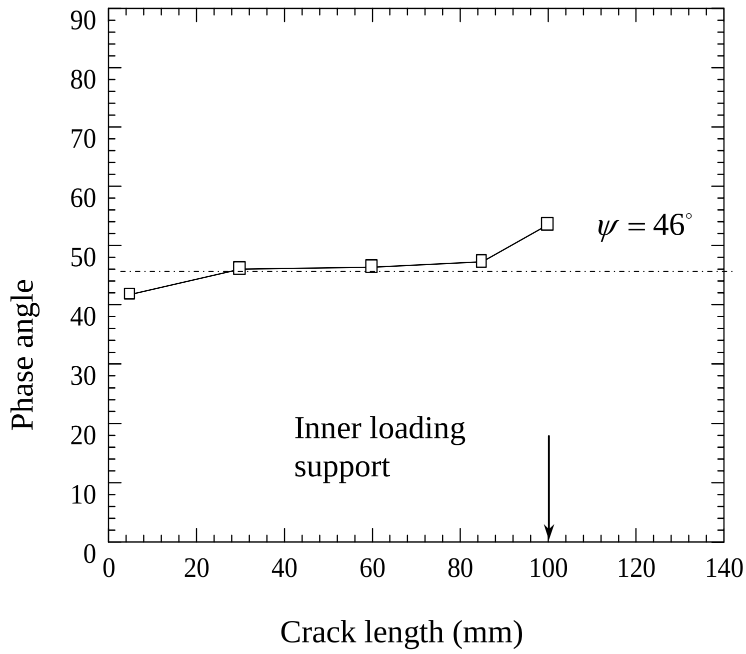

Figure13: Plot of phase angle versus crack length

6. CONCLUDING REMARKS

This research presents a possibility to evaluate bond strength via the use of energy release rate. The results indicate that the steady-state of the energy release rate is existent, therefore, the use of the energy concept to characterize the behavior of debonding is possible. According to the fracture mechanics approach, fracture toughness representing by energy release rate is somewhat smooth, unique, and independent of phase angle. The critical energy release rate can be served as an indicator for bond strength criterion. It is found out that the interfacial fracture toughness of steel-concrete-steel specimen depends on surface roughness of steel plates and has average fracture toughness of 26.78 J/m^2 where steel-CFRP-concrete specimen has average fracture toughness of 106.96 J/m^2.

REFERENCES

Charalambides, P. G., Lund, J., Evans, A. G. and McMeeking, R. M., 1989. A Test specimen for determination the fracture resistance of bimaterial interfaces. *Journal of Applied Mechanics*, Vol. 56, 77-82.

Malyshev, B.M. and Salganik, R.L., 1965. The strength of adhesive joints using the theory of crack. *International Journal of Fracture*, Vol. 5, 114-128.

Matos, P. P. L., McMeeking, R. M., Charalambides, P. G. and Drory, M. D., 1989. A method for calculating stress intensities in bimaterial fracture. *International Journal of Fracture*, Vol. 40, 235-254.

O'Down, N. P., Shih, C. F. and Stout, M.G., 1992. Test geometries for measuring interfacial fracture toughness. *International Journal of Solids Structures*, Vol. 29, 517-589.

Rice, J.R., 1988. Elastic fracture mechanics concepts for interfacial cracks. *Journal of Applied Mechanics*, Vol. 55, 98-103.

Sun, C.T. and Qian, W., 1997. The use of finite extension strain energy release rate in fracture of interfacial cracks. *International Journal of Solids Structures*, Vol. 34, 2595-2609.

Student Presentations

INTERMODAL MODE CHOICE BETWEEN JAPAN AND RUSSIA

TOMOYA KAWASAKI and SHINYA HANAOKA
Tokyo Institute of Technology, Japan
tomoyakawasaki@gmail.com
hanaoka@ide.titech.ac.jp

ABSTRACT

For the first time in Japan-Russian trade history, in 2006, export cargoes from Japan to Russia firstly overtook import of Japan from Russia in monetary terms. This is due to the high economic growth as well as other East European countries. Current dominant freight mode between Japan and Russia is maritime transportation (SEA), which is now saturated due to an excess in west bound (W/B) cargo volume. Under this circumstance, there is a need to be considered whether other freight transport mode such as Trans-Siberian Railway (TSR) and intermodal transport mode of maritime and air (SEA&AIR) can be a viable alternative mode in this route and to develop freight mode choice model with the objective of identifying which factors should be reformed so as to enhance other alternative modes.

Data on SEA&AIR transport characteristics from interview survey are analyzed for the decision making in adopting an alternative mode of SEA. The prime time of SEA&AIR service is from the late 1980s to the early 1990s due to the high fare of air transport (AIR). At the present time, demand on SEA&AIR service significantly declines and is not expected to recover due to several reasons such as Economies of Scale (EOS), risk on transshipment process, size of container, low fare of AIR and growth of Supply Chain Management (SCM). Hence, it is clear that the SEA&AIR no longer is suitable as an alternative mode of SEA. On the other hand, TSR has a potential to be developed into a viable alternative, since there are several advantages of TSR such as leadtime, mass-transit, consistent haulage by the same container and so on.

Mode choice model on international logistics is developed by using the discrete choice model by Stated Preference (SP) method. The SP questionnaire survey was conducted with five potential users (shippers) of TSR in Japan. The results show that security factor receiving the highest weight. From the study, it can be concluded that in order to secure the users of TSR, it should be reformed with a security factor at its top priority.

1. INTRODUCTION

1.1 General

Recently, Trans-Siberian Railway (TSR) re-rises as Russian economy has been better off in these years. According to the report of International Monetary Fund (IMF), GDP growth rate of Russia in the year of 2007 is +7.6%. As a result of the above fact which trend might last for several years, international trade in Russia has been activated especially in the west part of Russia with Far East Asian countries. As for trade between Japan and Russia in the view of Japan, export in 2006 firstly overtakes import by approximately US$200 million in the trading history between Japan and Russia.

Currently, cargoes between Asia and Russia is dominantly transported by maritime transport (SEA) via the Suez Canal, which is overwhelming other transport modes in terms of mode share. In 2001, cargo volume of Asia-Europe route was recorded 6.4 million TEU/year. On the other hand, the use of rail transport including TSR from Asia to Russia in 2001 is accounted only about 40-50 thousand TEU/year, which share is only less than 1%. Wang (2006) reports that as for cargo from/to Japan, it is estimated 10,000TEU/year in approximate value including cargoes via Pusan where port is virtually hub port for TSR. In this way, South Korea positively uses TSR; however, Japanese companies tend to use SEA rather than TSR. The share rate of TSR use by country in 2006 is “South Korea : China : Japan = 63 : 33 : 4”. Tsuji (2007) insists that the reason of low occupancy rate of Japan towards TSR use is not only its performance but also “bad image” towards TSR.

1.2 Purpose of the study

Although SEA is dominantly operated between Japan and Russia, sea ports in Russia are suffered from lack of space and decrepit. Moreover, SEA is now saturated by plenty of cargoes, thus, alternative freight transport mode of SEA is highly required to make haulage between Japan and Russia facilitating. Under this circumstance, we consider that TSR may be acted as an alternative transport mode of SEA. Tsuji (2008). Moreover, SEA&AIR, being one of the intermodal transport modes, might also be one of the competitors of SEA since SEA&AIR has unique characteristics such as short leadtime, enabling to manage uncertainty and so on although it takes relatively high cost. However, there are unfortunately almost no summary articles and reports of SEA&AIR, hence its characteristics, trend, advantage and disadvantage are not identified so far. Therefore, to clarify the characteristics of SEA&AIR itself can be considered as a quite significant work. In addition, shippers’ preference on mode choice which would affect on planning for constructing public facilities and infrastructure should be known for making logistics network smooth, as well as for TSR’s strategy such as price setting. Therefore, mode choice model between Japan and Russia is highly needed to examine for planning of logistics network.

2. FREIGHT TRANSPORT MODE BETWEEN JAPAN AND RUSSIA

2.1 SEA transportation

SEA transportation via Suez Canal (approximately 22,000km), is generally shipped via port of Hamburg, Rotterdam, Finland or Saint Petersburg, and then, shipped again to the final destination, Moscow, which totally takes approximately 35-40 days. Most of land haulage in Russia uses railway instead of truck by the intention of the government of Russia. The port of Saint Petersburg holds several problems as follows;

- Only a call at a port by vessels with icebreaker for freeze-up is possible.
- Since the depth of the water is not deep enough, large-sized containership is not possible to call at a port.
- Since there is only one arrival port in addition to recent increase in cargo volume, congestion is chronically occurred.
- Since a container terminal does not have hinterland, there is no enlarged space there.

Due to the above facts, operation of punctual shipment which is a crucial attribute in the view of Supply Chain Management (SCM) is quite difficult to conduct. In general, delay time on SEA from Japan to Moscow is generally said to be approximately 5-7days.

2.2 Trans-Siberian Railway (TSR)

TSR, originated at Vladivostok bound for Moscow (9,297km), is currently connecting to Finland, and other East European countries. In addition to east side of Russia, TSR also reaches the northeastern part of China, North Korea, Mongolia, Kazakhstan, and Uzbekistan with many branch lines, and gauge size is occasionally different from other countries' as shown in Table 1.

Table 1: Difference of gauge size by country

Gauge Class	Size (mm)	Adopting Country
Wide Gauge	1,520	Russia (TSR), CIS, Baltic States, Afghanistan, Finland, Mongolia
Standard Gauge	1,435	Europe (excluding Finland), China (TCR), North Korea, South Korea, Japan (Shinkansen)
Narrow Gauge	1,067	Japan (Railroad Line), Russia (Sakhalin, partially)

Source: Tsuji (2008)

Most of TSR section has already been completed to be double-tracked, except the bridge of Amur River (2,658m) near Khabarovsk. Besides, electrification was completed all along the TSR at the end of 2002.The maximum haulage capacity per one train might be approximately

200,000TEU/year. According to the report of Tsuji (2008), the most attractive point of TSR is its short distance and leadtime. Comparing TSR with SEA, total distance of TSR (about 10,000km) is only less than a half of total distance of SEA via Suez Canal (about 22.000km). Generally, TSR uses high speed transport train called block train and its total leadtime from Japan to Moscow can be reduced up to approximately 18 days including SEA from Japan to Vostochny (TSR by block train only takes about 2 weeks) whereas total leadtime of SEA takes approximately 40 days. Block train can be loaded 100-150 TEU and total length is about 1,000m. Average speed is 45-55km/h (approximately 1,200km/day).

Table 2: Attributes of TSR from vostochny

Destination	Frequency (times/week)	Leadtime (days)	NVOCC*	Shipper
Taganrog	3	11	Russian Troika	Hyundai Motors
Izhevsk	7-8	9	FE Trans	Kia Motors
Moscow	1	11-12	Russian Troika	n/a

*Note: *Non Vessel Operating Common Carriers*
Source: Tsuji (2008)

3. ANALYSIS OF SEA&AIR

In order to revealing the potential of SEA&AIR which is considered based on past practice, the interview survey on SEA&AIR and SEA&RAIL (TSR) was 3 times carried out with major large-scale logistics company in Japan on 22nd November 2007, 20th December 2007 and 4th February 2008.

3.1 Reasons of declining SEA&AIR demand

From the interview surveys, it is revealed that SEA&AIR is no longer expected as one of the alternative mode of SEA by five following reasons.

Economies of Scale (EOS): Cargoes transported by AIR are generally packed by belly which is normally able to transport 15 ton at most, and are fixed by pallet (sometimes called slid) which is a flat transport structure that supports belly in a stable fashion while being lifted by a forklift, pallet jack, or other jacking device. Scale of pallet is fixed 100*100 in Asia; thereby large quantity of cargo packed by belly cannot be transported by one haulage. In this case, EOS does not work properly since it is not mass-transportation like transported by container. According to interview surveys, 0.5 tons of lot size is impossible to work EOS even though it depends upon commodity. In addition, appearance of jumbo jet plane can be considered as declining SEA&AIR demand. Since jumbo jet is able to carry approximately 100 tons per haulage, EOS can be worked by AIR only.

Risk on Transshipment Process: Second reason is risk on transshipment process in the relay point, and which might be cause of loss in leadtime due to transshipment time and even waiting time. The convenience of facilities in relay point generally became better than before; however, the weak point is transshipment process itself. It would significantly be reduced shipper's utility since there are several risks such as delay (stuck), missing, theft and damage on goods. Solo-haulage such as AIR and SEA cargo has no transshipment process like vanning and devanning, besides, process such as making LCL (Less than Container Load) cargo FCL (Full Container Load) after the custom clearance is much shorter than SEA&AIR. Its process takes 4-5 days for SEA&AIR according to the interview survey. Since SEA&AIR is generally included this process at least one time, which is more complicated process than SEA due to that container cannot consistently use, it is great disadvantage of SEA&AIR in terms of not only leadtime but also other elements like delay, missing, theft and damage on goods.

Size of Container: Different size of container between SEA and AIR will be a cause of above two reasons such as EOS and risk on transshipment process. Due to the size of container is different, the merit of containerization cannot be utilized at most, and according to the interview survey, it is practically impossible to unify the spec of cargo nowadays.

Low Fare of AIR: All of interviewees had answered that reason of suspending SEA&AIR service is due to low fare of AIR from the late 1900s. In past (until early 1900s from the late 1980s), AIR fare was much more expensive than current price, so freight forwarders reluctantly provide SEA&AIR service as an alternative mode of AIR. One of the main reasons of declining the demand on SEA&AIR service is that AIR fare was getting lower and lower after the Gulf War. Before the reduction in AIR fare, operation of SEA&AIR was beneficial enough since the difference of price between AIR and SEA&AIR is big enough to operate at that time; however, current price's gap is not big enough to get benefit from SEA&AIR operation. For instance, according to the freight forwarder who is currently operating SEA&AIR, only 150JPY/kg is different between SEA and SEA&AIR (where relay point is Singapore) in the route between Japan and Middle East whereas total leadtime is different 16 days in terms of port to port. Becoming large-scale jet of AIR can also be considered as a trend of low fare of AIR freight, for example, Jumbo Jet can currently carry normally 100 ton per haulage. So, demand on SEA&AIR is declining and EOS possibly works by AIR rather than SEA&AIR. Only Jumbo Jet among several types of jets sometimes transports 5 tons of semiconductor devices.

Growth of Supply Chain Management (SCM): According to the most of interviewees, haulage in the idea of SCM requires on-time performance (punctuality) at most rather than other important factors such as quick leadtime. Since there is risk of delay, missing and other incidents violating punctuality in the relay point for transshipment (cancel of service of AIR or SEA) which is causing producing operations in manufacture, line parts tended to avoid to be carried by SEA&AIR. As SCM developed, technology improvement on SEA is remarkable developed as well. SEA transport mode such as container ship, RORO ship and Felly are currently enabling rapid transit and it is punctual enough. By its technology improvement on maritime transport, it is possible to structure SCM by SEA transportation. In this situation, according to the interviewee, there is some possibility to decline demand on AIR haulage in Asia.

3.2 Conclusion of SEA&AIR

As we have seen the analysis on SEA&AIR based upon interview survey until previous section, demand of SEA&AIR will not be expected to grow more. Hence, SEA&AIR is not suitable for one of the alternative freight modes on Japan-Russia (Moscow) route as well as competitor of SEA and TSR. However, in the future, it may be expected few demand on SEA&AIR in the case of that AIR fare rapidly rise due to a jump in crude oil prices that significantly effects on fuel surcharge. In these years, cargoes originated at Japan tended to be transported without AIR due to the background of rise in fuel surcharge and rise in fare due to high competition with Asian countries. So airlift tends to be used for goods when are really needed to be transported by AIR.

4. FREIGHT MODE CHOICE MODELING

The primary objective of this study is to estimate an impact on mode choice by emerging alternative mode (TSR) of SEA focusing on the route between Japan and Russia in order to reveal shippers' preferences and important factor affecting mode choice. To perform our analysis, we have chosen Stated Preference (SP) method rather than Revealed Preference (RP) method which is underlying actual observed behavior. It is not feasible to obtain the respondents' RP on the mode choice in this study since there is almost no practice of SEA&AIR and TSR. Thus, this study applies SP method that is based on several hypothetical scenarios but practical values enough. After that, questionnaire will be formatted by the Design of Experiment (DOE). Obtained data are calibrated by NLOGIT software which is used for estimating Binary Logit (BL) model as described equation (1).

$$P_{iq} = \frac{\exp(\beta V_{iq})}{1 + \exp(\beta_{iq})} \tag{1}$$

where

P_{iq}	=	Probability of that individual q chooses i
β	=	Parameter
V	=	Measureable utility

4.1 Levels of each attributes

As a result of interview survey with freight forwarders, the different independent variables are analyzed in associate with statistical and the goodness-of-fit test. The variables used in this computation are categorized into five elements such as leadtime, cost, punctuality, frequency and security which levels are set based on interview survey. All of independent variables are used to calculate the utility function and develop the freight mode choice models. Since inclusion of many variables might cause complexity and unreasonable result to the models, dependent variables are winnowed. The statistical tests are applied to examine utility function and to calibrate the model. The preferable model is better to have magnitude and sign of statistical test values in harmony with reasonable expectation.

Table 3: Levels of each attributes

Attributes	**Level**	
	SEA	**SEA&RAIL (TSR)**
Leadtime	40days	15days, 25days
Cost*	$7,000	$7,500, $8,500
Punctuality	Punctual, Unpunctual	Punctual, Unpunctual
Frequency	1time/day, 1time/week	1time/day, 1time/week
Security	High, Low	High, Low

*Note: *one-way haulage (Japan-Moscow) by 40' container*

These degrees of level on leadtime and cost are determined as a result of interview survey with three freight forwarders but it is based upon deep examination by using several journal articles, papers and discussion with freight forwarders, hence; these values should be practical enough even if they were in actual international logistics market.

4.2 Model calibration and test

Target numbers of respondents are five shippers, and they all are companies related to automobile and electrical manufacture. Validate sample number is 76 sample sets out of 80 sets. The calibration process is based upon Maximum Likelihood (ML) method. In addition, this study assumes that there is no significant difference in other words, statistically independent among different variables.

4.3 Results of model calibration

The calibration results of BL model are presented in Table 4 showing the estimated coefficients of the variables and the statistic results. Although t-value of both punctuality and frequency is not high, -1.023 and -0.599, respectively, of other variable are relatively high; thus, they can be said statistically significant. Considering a fact that ρ^2 is relatively low, this estimated model will be used as a rough reference for the demand forecasting.

Table 4: Calibration result of binary freight mode choice

Explanatory Variables	**Estimated Coefficients**	**Standard Error**	**t-value**
Model Constants SEA TSR (base)	 1.423382 0	 1.120105 -	 1.271 -
Leadtime (day)	-0.048939	0.047842	-1.023
Cost (US $)	-0.7608e-04	0.000127	-0.599
Punctuality	0.679197	0.352819	1.925
Frequency	0.553472	0.353790	1.564
Security	1.352651	0.354754	3.813
Estimated Statistics	**Values**		
L(β)	-93.2585		
L(0)	-105.3584		
Likelihood Ratio Test	24.1998		
Rho-bar-squared	0.11485		

From the result of calibration process, utility function of each freight mode can be listed as follows;

$$U_{SEA} = -0.048939(leadtime) - 0.7608\text{e-}04(cost) + 0.679197(punctuality) + 0.553472(frequency) + 1.352651(security) + 1.423382$$

$$U_{TSR} = -0.048939(leadtime) - 0.7608\text{e-}04(cost) + 0.679197(punctuality) + 0.553472(frequency) + 1.352651(security)$$

5. CONCLUSION AND DISCUSSION

As any company hugely weight on the attributes of security, estimated model also concludes that the security is weighted at the top priority. Unit change on security has the approximately the twice impact of unit change on punctuality that has more impact rather than frequency. One of the reasons why shippers put a priority on security is that due to a fact that TSR is unknown very much among logistics companies even the information of TSR fare is very difficult to know, which is normally determined by a negotiation (Tsuji, 2008). In case most part of haulage process is unrevealed, shippers may be sensitive to security including theft and damage. In addition, since the damaged commodity no longer is used for line parts, it will link to the tremendous loss in terms of time and cost.

Regarding to the attributes of frequency, as no company was sensitive to it, estimated model also show that frequency has the lowest influence on the overall utility, which is less than half impact of security and less than punctuality as well. This result can be considered as that frequency of at least 1time/week may be acceptable enough for shippers. Company C stated that forwarding commodity is not daily, if frequency is at least 1shipment/week, it cannot be a reason of not use. Hence, although higher frequency is preferable, it can be said that TSR can supply enough frequency to shippers since there is weekly shipment via Pusan, Korea

Estimated model revealed that punctuality is slightly higher impact than frequency but only half effect of security on the overall utility. This result is somewhat lower than we expected since punctuality is revealed quite important attributes as a growth of SCM according to the interview survey. This may be due to the assumption of punctuality is not suitable since it is expressed by “unpunctual” and “punctual”.

This study assumes that each attributes are statistically independent from other attributes. However, in the real world, several affections from other attributes are existed no matter it is small or big. In this study, it can be considered that the attributes of security and punctuality might have an impact each other. For example, in case of the low security, respondents might assume that the probability of happening delay may be high. Considering its fact, each attributes cannot always be said statistically independent one another.

Leadtime and cost are also somewhat low; however, this should be reasonable results since most of companies made a decision by comparing leadtime and cost not as a solo attributes, so shippers may consider these two attributes as one attributes. For example, short leadtime and high cost may be roughly same utility as long leadtime and low cost.

As for the parameter of cost, it is estimated relatively low, which does not affect a significant impact on the mode choice. For example, as percent decrease in cost of TSR by 10 %, percent choice of mode increases only 2%. This might be due to the setting of value of cost. For example, the gap of cost between the values of TSR is $1,000 maximum. If values were set as bigger and smaller like $9,000 and $6,500 that is cheaper than SEA although it is excessive value as well as not practical, parameter of cost will be higher than estimated here.

Sign of each coefficient of each variable are estimated as expected, for example, the parameters of leadtime and cost are with negative sign since the utility is decreased as leadtime and cost get increase. On the other hand, the signs of other variables are estimated with positive sign. The contribution to the overall satisfaction by alternatives is given by these coefficients. The positive sign of constant value in the utility function of SEA can be interrupted as representing the net influence of all unobserved (not explicitly included) characteristics of the option. For example, shippers’ image (reliability) towards mode choice could be included; however, it should be quite difficult to observe in this study. Moreover, SEA-based model which includes constant value in TSR with negative sign is also estimated as shown in Table 5.5. From its model, it can be speculated that there might be several resistance factors towards TSR other than estimated factors.

Russian Railway should open the information and plan of fare in order to secure the users of TSR. Moreover, since security is the most important attributes among the estimated attributes for shippers, security should be improved especially damage on commodity.

REFERENCES

Ben-Akiva M. and Lerman S. R., 1985. *Discrete Choice Analysis: Theory and Application to Travel Demand.* The MIT Press.

Bernd H., 2005. ‘Airport Logistics: Innovative Solutions for Baggage-handling’. Log-forum Vol. 1, Issue 2, No. 5.

Devore J. L., 2000. *Probability and Statistics for Engineering and Sciences*. 5th edition, Duxbury Thomson Learning.

Federal Transportation Administration (FTA)., 2000. *A Self Instructing Course in Disaggregate Mode Choice Modeling*, US. FTA.

Institution for Transport Policy Studies, 2002. *The Report on Flight Service for International Air Cargo.* Institution for Transport Policy Studies.

Kou R., 2007. Analysis on sea port for international competitiveness in Japan. *Journal of Management in Ritsumeikan University*, Vol. 41, No. 1, pp167-188.

Louviere J. J. et al., 2000. *Stated Choice Methods: Analysis and Application.* Cambridge University Press.

Ocean Commerce Ltd., 2006. *International Transportation Handbook 2007.* Ocean Commerce Ltd.

Ohmura H., 2002. *Lecture on Design of Experiment (DOE) and Analysis of Variance.* JUSE Press

Ortuzar J. de D. and Willumsen L. G., 2001. *Modeling Transport*. 3rd edition, John Wiley & sons.

The Workshop on Transportation Engineering., 1995. *Disaggregate Travel Demand Analysis made simple.* SANBI Printing.

Tsuji H., 2007. *The Trans-Siberian Railway Land Bridge: The Main Artery of Japanese-Russian Business.* The Seizando Press.

NON-LINEAR BEHAVIOR OF NEW TYPE GIRDER FILLED BY HIGH-STRENGTH CONCRETE

SUNG WOO, CHOI
Department of Architectural, Civil and Environment Engineering
Korea University, Seoul, Korea
1905vocal@hanmail.net

ABSTRACT

Recently, many studies about high-strength concrete and composite structures are being progressed to get the more economic and stable result in the construction of structure all over the world. One of those studies is about CFTA(Concrete Filled and Tied Steel Tubular Arch) girder that applies an arch structure and a pre-stressed structure to CFT(Concrete Filled Steel Tubular) Structure which is filled with a concrete and improve the stiffness and strength of the structure by the confinement effect of fillers to maximize the efficiency of structure and economic. In this study, non-linear behavior of CFTA girders filled with a general concrete and the high-strength concrete respectively were analyzed by using ABAQUS 6.5-1 and results were compared.

1. INTRODUCTION

1.1 Introduction

Recently, many studies about shape of bridge's superstructure, efficiency of materials and complex structure are being progressed for bridges, more safety, economical and well harmonized into nature, in the construction for structure all over the world. SCP Girder, as an example, which has similar cross section shape of PSC girder is filled with a pre-stressed concrete. In this manner, studies about new types of bridge superstructure which can minimize shortcomings of the existing superstructure of bridge by performance improvement from rearranging of structure shapes and materials, using tensile force, and being beneficial for economic as well as aesthetic part are being progressed.

1.2 Research objective

As mentioned above, studies about new types of synthetic structure and girder system of bridges are being progressed these days. However, as it is hard to be used on actual construction field immediately, it is needed to develop new structure types which can be applied without further delay and minimize some weak points of existing structure stuffs. 'Concrete Filled steel tubular Tied Arch composite (CFTA) girder', one of the new types of complex structure girder, is studied for this purpose. In this study non-linear behavior of CFTA girders filled with normal-strength (30Mpa) concrete and high-strength (150Mpa, 200Mpa) concrete respectively were analyzed and results were compared.

2. CFTA girder (Concrete-Filled and Tied Steel Tubular Arch Girder) and modeling

The top side of CFTA girder filled with concrete in steel tube maintains constant height, while the bottom side of CFTA girder is the arch shape. Besides, prestress is put on steel tendons exposed at the lower part of CFTA girder to improve its safety and to reduce its weight.

The solid drawing and the constituent material of CFTA girder are showed Figure 1 and 2. As like Figure 1, the height of CFTA girder at both ends is 620mm and filled with concrete. As going to the center part, the shape of the inner filled concrete is the arch shape with maintaining 180mm thickness. Tendons are inserted until 520mm from both ends, and then they are exposed to outside because of the arch shape of CFTA girder. The steel box on the concrete arch is the empty and transmits the load from upper part of steel box to the concrete arch. The length of the whole span is 12.2m, the width is 500mm and the displacement control load is applied to perform the non-linear analysis. Besides, material properties and the load condition are as following table 1.

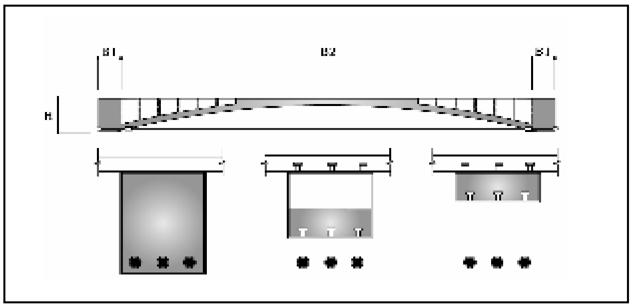

Figure 1: The solid drawing of CFTA girder

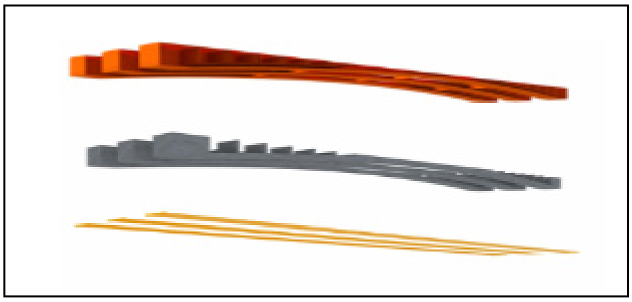

Figure 2: The constituent material of CFTA girder

Table 1: Material Properties and the Load Condition of Members.

	Cocrete			Steel Plate
	30Mpa	**150Mpa**	**200Mpa**	
Modulus of elasticity (Mpa)	26844	43168	47304	200000
Poisson's ratio	0.16	0.16	0.16	0.3
Unit mass(kg/m3)	2500	2500	2500	7700
Acceleration of gravity(m/s2)	9.81			
Pre-tension(MPa)	744.48			

3. The Result of analysis

Even though the high strength concrete has 5 and 6.7 times compression strength as compared with the normal strength concrete respectively, the aspect of the load-displacement curve doesn't have a big difference. Contrary to the expectation that high strength concrete can support 5 and 6.7 times load as compared with normal strength concrete respectively, it means that the non-linear behavior of the high strength concrete is different with the normal strength concrete's. To know differences between the non-linear behavior of the high strength concrete and the non-linear behavior of the normal strength concrete, load-strain curve is drawn for central parts of each strength concrete in Figure 3.1 ~ 3.4.

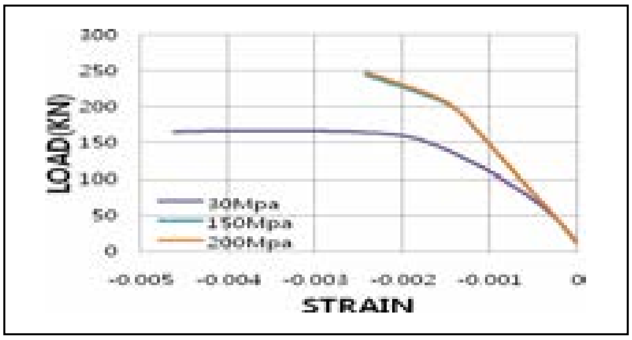

Figure 3.1: Load-strain curve of the top of the slab

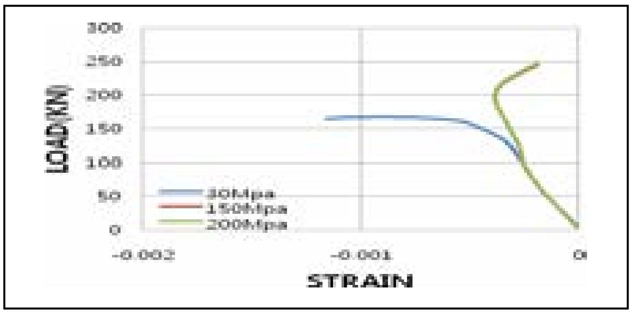

Figure 3.2: Load-strain curve of the bottom of the slab

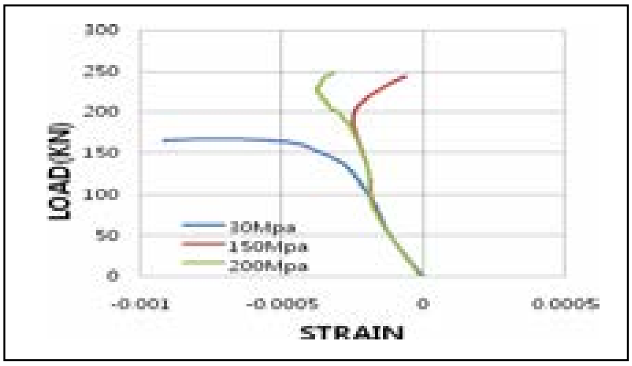

Figure 3.3: Load-strain curve of the top of the conctrte

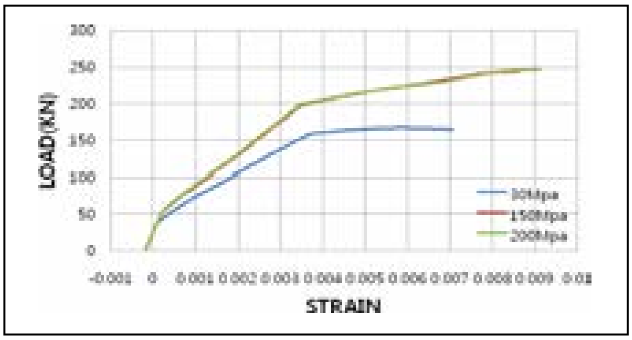

Figure 3.4: Load-strain curve of the bottom of the concrete

As shown in Figure 3.1 ~ 3.4 above, between the high strength concrete and the normal strength concrete, load–strain curves for the top of the slab and the bottom of the filled concrete have just different size but have the same aspect. On the other hand, behavior for the bottom of the slab and the top of the filled concrete is totally different between the high strength concrete and the normal strength concrete. In other words, in case of 30MPa concrete, the bottom of the slab and the top of the filled concrete are continuously under compression from the beginning of loading to the end of the analysis. However, in case of high strength concrete, its condition is turned under compression into under tension from about 200KN. It means that as increasing load, the neutral-axis is going up, therefore the bottom of the slab and the top of the filled concrete are under the neutral-axis and under tension.

In case of non-linear behavior like that, to know the change of the neutral-axis of CFTA girder, it is drawn the change of the neutral-axis at the central section of each concrete for each strength in Figure 4. The reason why the discontinuous part of the graph is appeared is guessed that the point changed the up convexity shape into the down convexity shape is not included in the shown points by analysis program. Therefore, the effective neutral-axis area is started when the load become 25KN because the neutral-axis is appeared in the filled concrete from that time. In case of the normal strength concrete, the neutral-axis is located in the filled concrete at the end of analysis. On the contrary, in case of high strength concrete, the location of the neutral-axis is going up to the slab at the end of analysis. It means that tensional destruction of the filled concrete can be occurred and it is very uneconomic design. Besides, contrary to the definitely different behavior between the high strength concrete and the normal strength concrete, the high strength concrete, 150MPa strength concrete and 200MPa strength concrete, show the similar behavior. As one cause of this phenomenon, both concrete are the high strength concrete so it is possible to be thought that there are some similarities of behavior between them. Also, another cause might be that other conditions such as the strength of steel, the strength of tendon, load condition and so on, except the strength of concrete, are same. Therefore, to get more accurate result, all other conditions have to be fitted to the concrete strength.

As knowing from the result of analysis, there are many differences between the non-linear behavior of the high strength concrete and the non-linear behavior of the normal strength concrete. So if a engineer designs a high strength concrete structure using the specification for the normal strength concrete, it will be very uneconomic, inefficient and also have a low reliability. Consequently, to make the best use of the high strength concrete, it is very important and imperative to make a new specification for the design of the high strength concrete.

REFERENCES

Hak, Lee., Ho, Park., EunHo, Lee., JungHo, Kim., JungSik, Kong., 2007. Behavior of Concrete-Filled and Tied Steel Tubular Arch Girder. *Spring Conference Paper Book 668-693*. Computational Structural Engineering Institute of Korea.

Ho, Park., MyungKyun, Park., KyungHun, Park., JungHo, Kim., 2006. Development of Concrete-Filled and Tied Steel Tubular Arch Girder. *Conference Paper Book 2289-2292.* Korean Society of Civil Engineers.

SungWon, Yoo., KyungWook, Hong., 2000. Bending Analysis and Improvement of Bending Capacity of Pre-stress Concrete Beam Using the Partly Attached Rigid Model. *The collection of learned papers 813-821.* Korean Society of Civil Engineers.

ByungHwan, Oh., SungWon, Yoo., 2000. Bending Behavior Test of PSC Beam Which has the External Steel Wire according to the Shape of Steel Wire and the Number of deflection side. *The collection of learned papers 795-804.* Korean Society of Civil Engineers.

ELASTODYNAMIC ANALYSIS BY BEM USING DOMAIN DECOMPOSITION METHOD AND PARTICULAR INTEGRALS

ADISORN OWATSIRIWONG, BUPAVECH PHANSRI
and KYUNG-HO PARK
School of Engineering and Technology
Asian Institute of Technology, Thailand
adisorn.owatsiriwong@ait.ac.th

ABSTRACT

The paper presents the elastodynamic BEM analysis using the domain decomposition method (DDM) and particular integrals. The domain of the original problem is subdivided into two sub-regions in which each can be treated as sub-problem and independently solved. Particular integral method in association with Houbolt time integration is utilized to formulate the system equation. The iterative coupling approach via alternating Schwarz algorithm is applied to solve each sub-region in turn. To assist convergence rate of the iteration process, an under-relaxation parameter is introduced to the displacement variable. Two numerical example problems are given to demonstrate the accuracy and validity of the present formulation. Comparison of the results is made with those from ABAQUS.

1. INTRODUCTION

Boundary element method (BEM) has long been accepted as an efficient and accurate numerical technique for solving elastodynamic problems. With aid of the domain decomposition method (DDM), nowadays, applications of elastodynamic BEM not only restrict to single-region problems but also extend to the problems involving piecewise inhomogeneities and multi-part assembly.

Early developments of multi-region techniques employing DDM in solid mechanics had focused mainly on the direct coupling approach for the problem involving zone inhomogeneities (Banerjee and Butterfield, 1981; Banerjee 1994; Kane et al., 1990). In such approaches, sub-regions are assembled into a single equation system and solved either by direct or iterative methods. A variant of DDM that does not require direct assembly of the system equations is so-called iterative coupling approach (Smith et al., 1996). Aiming to avoid solving large global equation system and difficult programming issues, many iterative coupling approaches have been introduced mostly in the context of FEM-BEM and BEM-BEM coupling techniques. The early formulations employing iterative coupling method to coupling FE and BE domains can be found in the works of Lin et al. (1996) and Feng and Owen (1996), who presented the Dirichlet-Neumann form of alternating Schwarz algorithm to solve 2D elastostatics. Kamiya et al. (1996) implemented the Neumann-Neumann and Dirichlet-Neumann for FE-BE coupling in parallelization scheme and tested them with 2D potential problems. Elleithy et al. (2001) used a simple 2D elastostatic problem to investigate the effect of various parameters such as relaxation constant, mesh density, and relative area of BE-FE domains. Eleithy and Al-Gahtani (2000) presented various schemes of overlapping DDM based on alternating Schwarz framework to solve simple 2D elastostatic problems by FE-BE coupling. They also mentioned the failure of Dirichlet-Neumann algorithm when Neumann boundary condition is applied to the entire problem domain. In fact, this statement is correct as well when using Dirichlet-Neumann algorithm to analyze multi-region problems in BEM. Recently von Estorff and Hagen (2006) applied double relaxation algorithm to the 2D and 3D elastodynamic problems for FE-BE coupling technique. In most cases, stability and convergence properties of most iterative coupling methods rely on how good the value of relaxation parameter is guessed, but this is not a case for the overlapping DDM.

This paper deals with the elastodynamic BEM analysis using the DDM and particular integrals. The paper is organized as follows: In the next section, the particular integral formulation for approximating acceleration term is presented. In section 3, we describe the DDM based on alternating Schwarz algorithm and how it can be applied to the elastodynamic BEM. Numerical algorithm based on block Gauss-Seidel and block Jacobi forms will also be described. Finally, two numerical example problems are given to demonstrate the validity and accuracy of the present formulation.

2. PARTICULAR INTEGRAL FORMULATION

The governing differential equation for transient elastodynamic analysis of a homogeneous, isotropic body in the absence of body force can be expressed as

$$(\lambda+\mu)\, u_{j,ji} + \mu\, u_{i,jj} = \rho\, \ddot{u}_i \tag{1}$$

where u_i is the displacement, $\ddot{u}_i$ is the acceleration, ρ is the mass density, λ and μ are Lame's constants, commas represent differentiation with respect to spatial coordinates, and *i*, *j* = 1,2(3) for two(three) dimensions. The solution of equation 1 can be represented as a sum of complementary function u_i^c satisfying the homogeneous equation

$$(\lambda+\mu) u^c_{j,ji} + \mu\, u^c_{i,jj} = 0 \tag{2}$$

and particular integral u_i^p satisfying the inhomogeneous equation

$$(\lambda+\mu)\, u^p_{j,ji} + \mu\, u^p_{i,jj} = \rho \ddot{u}_i \tag{3}$$

where superscripts c and p indicate *c*omplementary and *p*articular solutions respectively. Then the total solutions for displacement, traction and stress rates can be expressed as

$$u_i = u_i^c + u_i^p \; ; \quad t_i = t_i^c + t_i^p \tag{4}$$

where t_i^c and t_i^p are the complementary functions and particular integrals for traction, respectively.

2.1. Complementary solutions

The boundary integral equation related to the complementary functions, u_i^c and t_i^c, can be written as (Banerjee, 1994)

$$C_{ij}(\xi)\; u_i^c(\xi) = \int_S \left[G_{ij}(\mathbf{x},\xi)\; t_i^c(\mathbf{x}) - F_{ij}(\mathbf{x},\xi)\; u_i^c(\mathbf{x}) \right] dS(\mathbf{x}) \tag{5}$$

where G_{ij}, F_{ij} are the fundamental solutions for elastostatic equation and $C_{ij}(\xi)$ = 1, 0 and 1/2 depending on the point ξ being in the interior, outside or on a smooth boundary point respectively.

2.2. Particular integrals

In order to eliminate the domain integrals due to the acceleration term, the concept of global shape function can be used. By introducing the global shape function $C_{ik}(\mathbf{x},\xi_n)$, the acceleration $\ddot{u}_i(\mathbf{x})$ can be approximated as

$$\ddot{u}_i(\mathbf{x}) = \sum_{n=1}^{\infty} C_{ik}(\mathbf{x},\xi_n)\, \ddot{\phi}_k(\xi_n) \tag{6}$$

where $\ddot{\phi}_k(\xi_n)$ is the fictitious function. Then the particular integrals for displacement, stress and traction rates can be obtained as

$$u_i^p(\mathbf{x}) = \sum_{n=1}^{\infty} U_{ik}(\mathbf{x},\xi_n)\; \ddot{\phi}_k(\xi_n) \tag{7}$$

$$t_i^p(\mathbf{x}) = \sum_{n=1}^{\infty} T_{ik}(\mathbf{x},\xi_n)\; \ddot{\phi}_k(\xi_n) \tag{8}$$

3. NUMERICAL IMPLEMENTATION

The boundary integral equation (5) can be written in matrix form as

$$[G]\{t^c\}-[F]\{u^c\}=0 \tag{9}$$

Considering the total solutions of equation 4 the complementary functions in equation 9 can be eliminated as

$$[G]\{t\}-[F]\{u\}=[G]\{t^p\}-[F]\{u^p\} \tag{10}$$

If a finite number of ξ_n are chosen, the particular integrals for displacement and traction can be written as

$$\{u^p\}=[U]\{\ddot{\phi}\} \;\; ; \;\; \{t^p\}=[T]\{\ddot{\phi}\} \tag{11}$$

Considering the fictitious nodal values as

$$\{\ddot{\phi}\}=[C]^{-1}\{\ddot{u}\} \tag{12}$$

one can obtain the following equations

$$[G]\{t\}-[F]\{u\}=[M]\{\ddot{u}\} \tag{13}$$

where

$$[M]=\left([G]\left[T\right]-[F]\left[U\right]\right)[C]^{-1} \tag{14}$$

Several time integration schemes have been proposed to deal with equations of the type of equation 13 in FEM. In this study, the Houbolt method is used such that

$$\ddot{u}_{t+\Delta t}=\frac{1}{\Delta t^2}\left(2u_{t+\Delta t}-5u_t+4u_{t-\Delta t}-u_{t-2\Delta t}\right) \tag{15}$$

Considering the equilibrium equation (13) at time $t+\Delta t$ one can obtain

$$\left(\frac{2}{\Delta t^2}[M]+[F]\right)\{u\}_{t+\Delta t}=[G]\{t\}_{t+\Delta t}+\frac{1}{\Delta t^2}[M]\left(5\{u\}_t\right.$$
$$\left.-4\{u\}_{t-\Delta t}+\{u\}_{t-2\Delta t}\right) \tag{16}$$

To solve the system equation (16), boundary variables as well as displacement at interior points are simultaneously treated as the unknown variables. So equation 14 is rewritten as

$$[M]_{b+I}=\left(\begin{bmatrix}[G]_{bb}\\ [G]_{Ib}\end{bmatrix}[T]_b-\begin{bmatrix}[F]_{bb} & [0]\\ [F]_{Ib} & [I]\end{bmatrix}\begin{bmatrix}[U]_b\\ [U]_I\end{bmatrix}\right)[C]_{b+I}^{-1} \tag{17}$$

where $[I]$ is identity matrix, subscript I denotes interior values and subscript b indicates boundary values. By substituting the boundary conditions at time $t+\Delta t$ and taking all the unknowns to the left-hand side, the final system of equation can be rewritten as

$$[A]\ \{x\}_{t+\Delta t} = \{y\}_{t+\Delta t} \tag{18}$$

where x is unknown vector of displacement and traction including displacement at interior points, y is a known vector and A is the coefficient matrix.

4. DOMAIN DECOMPOSITION METHOD

4.1 Introduction

Applying the DDM, the problem domain is subdivided into two regions in which the system equation (18) holds for each (Figure 1). At the interface, the equilibrium and compatibility conditions must be satisfied such that

$$\{u_F^I\}_{t+1} = \{u_F^{II}\}_{t+1} \qquad on \quad \Gamma_F \tag{19a}$$

$$\{t_F^I\}_{t+1} + \{t_F^{II}\}_{t+1} = 0 \qquad on \quad \Gamma_F \tag{19b}$$

It is commonly possible to solve the entire problem either by direct or iterative coupling approach. In the direct coupling approach (Banerjee, 1994), two sub-regions are brought to assemble by utilizing interface boundary conditions in equation 19. The solution can be obtained within a single step if direct solver is also used. On the contrary, the iterative coupling approach allows solving each sub-region independently. Interface boundary conditions will be prescribed iteratively until convergence is reached. Commonly, computational efficiency of the direct method is great, but in some stringent cases either the system matrix could become ill or the results could be numerically unstable. Despite less efficient when implemented on a sequential code, iterative coupling approach offers flexibility and generality to the DDM framework. Since the structure of sub-system matrix is completely retained, implementation of the method is by far simpler than that of direct coupling approach. In this paper, we concentrate only on the indirect coupling approach. The calculation sequence will be described in the next section.

4.2 Iterative coupling DDM

Indirect coupling approach can be performed by so-called alternating Schwarz algorithm. To explain the algorithm, it is useful to rewrite the system equation (18) in partitioned form where traction and displacement unknowns are separated. Consider the system equation

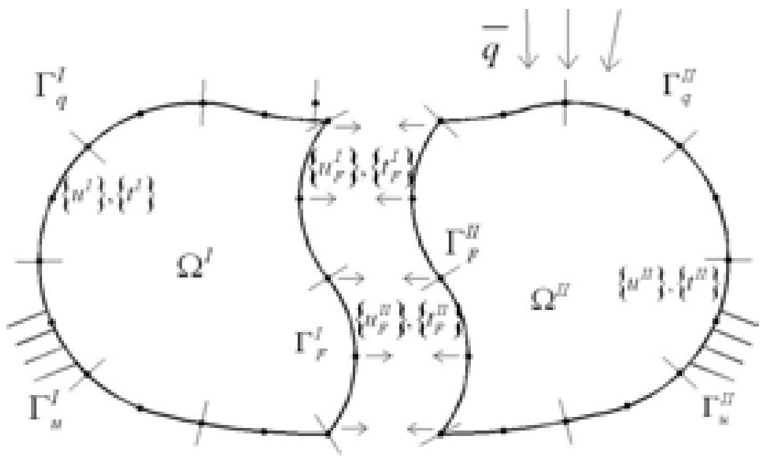

Figure 1: A domain decomposed into two sub-regions

$$\begin{bmatrix} [A]_{11} & [A]_{12} \\ [A]_{21} & [A]_{22} \end{bmatrix} \begin{Bmatrix} \{u\} \\ \{t\} \end{Bmatrix}_{t+\Delta t} = \begin{Bmatrix} \{y\}_1 \\ \{y\}_2 \end{Bmatrix}_{t+\Delta t} \tag{20}$$

where for each region, let $\{u^{I,II}\} = \{\{u^{I,II}\},\{u_F^{I,II}\}\}^T$ and $\{t^{I,II}\} = \{\{t^{I,II}\},\{t_F^{I,II}\}\}^T$. Subscript F denotes the variable that belongs to interface boundary. A sequential form of Dirichlet-Neumann algorithm can be described as follows:

For t =0, Δt *, 2* Δt *,… do*

Assume initial value of $\{u_F^I\}_{t+1}^0 = 0$

For n =1, 2,… do

(1) Solve sub-problem I from

$$\begin{bmatrix} [A]_{11}^I & [A]_{12}^I \\ [A]_{21}^I & [A]_{22}^I \end{bmatrix} \begin{Bmatrix} \{u^I\} \\ \{t^I\} \end{Bmatrix}_{t+\Delta t}^n = \begin{Bmatrix} \{y^I\}_1 \\ \{y^I\}_2 \end{Bmatrix}_{t+\Delta t}^n \tag{21}$$

(2) Apply $\{t_F^{II}\}_{t+\Delta t}^n = -\{t_F^I\}_{t+\Delta t}^n$ *on* Γ_F

(3) Solve sub-problem II from

$$\begin{bmatrix} [A]_{11}^{II} & [A]_{12}^{II} \\ [A]_{21}^{II} & [A]_{22}^{II} \end{bmatrix} \begin{Bmatrix} \{u^{II}\} \\ \{t^{II}\} \end{Bmatrix}_{t+\Delta t}^n = \begin{Bmatrix} \{y^{II,I_F}\}_1 \\ \{y^{II}\}_2 \end{Bmatrix}_{t+\Delta t}^n \tag{22}$$

(4) Apply $\{u_F^I\}_{t+1}^{n+1} = (1-\omega)\{u_F^I\}_{t+1}^n + \omega\{u_F^{II}\}_{t+1}^n$

where ω is an under relaxation parameter to assist convergence. The value is problem dependent. For initial guess, value of ω =0.5 may be used.

(5) Check convergence of the solution from

$$\frac{\left\| \left\{ u_F^I \right\}_{t+\Delta t}^{n+1} - \left\{ u_F^I \right\}_{t+\Delta t}^{n} \right\|}{\left\| \left\{ u_F^I \right\}_{t+\Delta t}^{n+1} \right\|} < \varepsilon \quad (given\ tolerance) \tag{23}$$

(6) Finish current time step if the solution converges, otherwise repeat step (1).

To implement Dirichlet-Neumann algorithm, it is demanded that each subproblem be well-posed. Basically, start-up region can be arbitrary chosen. The present algorithm is considered as a block Gauss-Seidel form. Block Jacobi form of solution can be simply obtained by updating all interface boundary variables together after completion of the iteration step (Smith et al., 1996).

5. NUMERICAL EXAMPLES

5.1 Example 1: A cavity subjected to internal pressure

The first example deals with a cavity subjected to suddenly applied internal pressure. The inner and outer radii of the truncated cavity are taken to be 1 and 10 respectively. The full model under plane strain condition is divided into two sub-regions modeled by 32 quadratic boundary elements and 160 interior points each (Figure 2). Internal pressure is suddenly applied and held constant. The material is linearly elastic with the following properties: E = 94.67, $\nu = 0.23$ and $\rho =$ 1. For the given properties, the theoretical compressional wave speed is computed as $c_1 = 10.47$. The time step Δt is taken to be 0.01.

The radial displacement at point A (2, 0) is plotted against time as shown in Figure 3. It can be shown that the value of compressional wave speed obtained from the analysis model ($\tilde{c}_1 = s / t_q = 1.0 / 0.095 = 10.52$) deviates only 0.47% from the theoretical value, where s and t_q denote the travelling wave distance and tranquil period of particle motion, respectively. Slight fluctuation of ABAQUS result around that of BEM can be noticed. Generally, acceptably good agreement is observed.

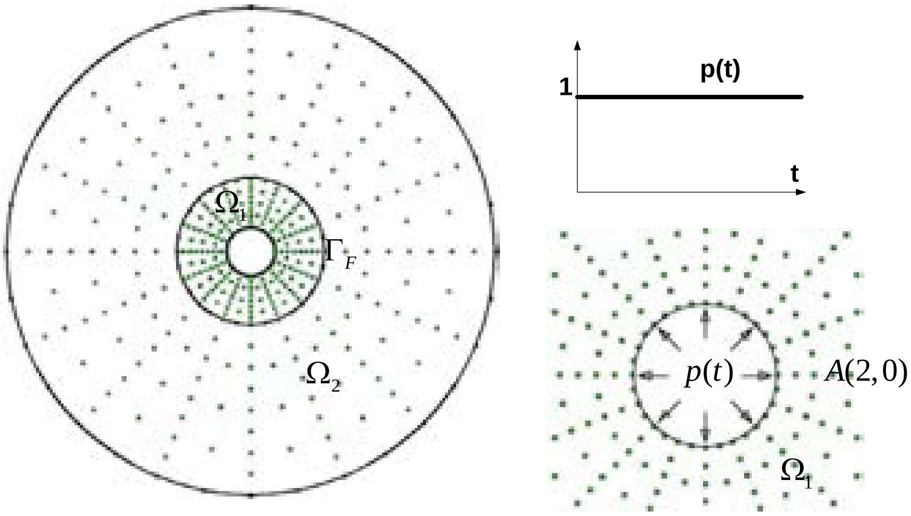

Figure 2: Modeling mesh (Example 1)

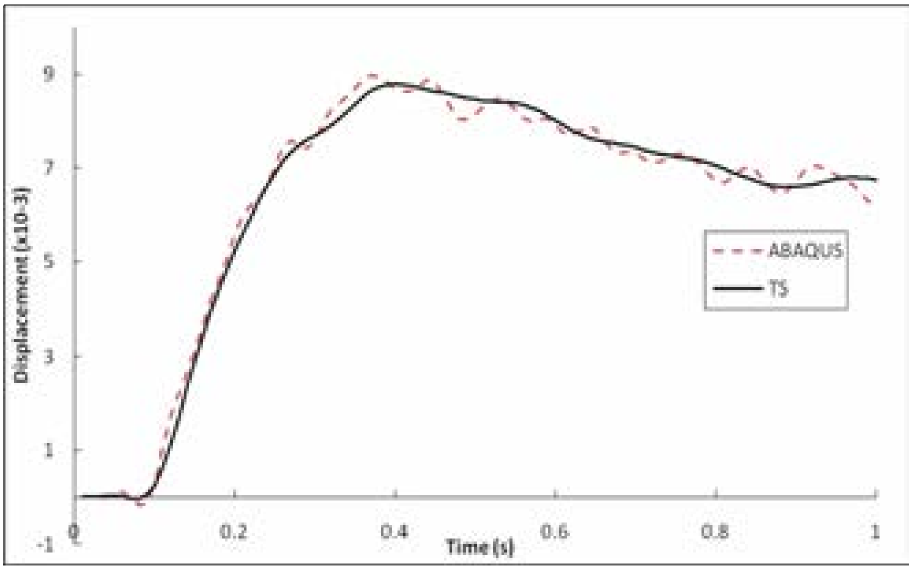

Figure 3: Plot of displacement at point A (2,0) (Example 1)

5.2 Example 2: Seismic analysis of a concrete gravity dam

This example presents seismic analysis of a concrete gravity dam (Owen and Hinton, 1980) with considering foundation-dam interaction. The model under plane strain condition is divided into two sub-regions with different material properties - concrete and rock. Material properties used are E = 3.164x10^6, $\nu = 0.2$ and $\rho =$ 0.269 for concrete dam, and E = 1.8x10^6, $\nu = 0.2$ and $\rho =$ 0.183 for rock foundation. The dam (Ω_1) is modeled by 24 quadratic boundary elements and 73 interior points, while the foundation (Ω_2) is modeled by 26 quadratic boundary elements and 65 interior points (Figure 4). Theoretical sinesweep ground acceleration is prescribed in the horizontal direction. Time history analysis is performed using $\Delta t = 0.01$.

The displacement at dam crest relative to dam base is depicted in Figure 5. Good agreement to ABAQUS's result can be noticed particularly before $t = 2.5$. The non-vanishing result at first time step arises from the prescribed initial conditions i.e. body force and hydrostatic pressure in static steps. The effect of hydrodynamic pressure is omitted from this present example.

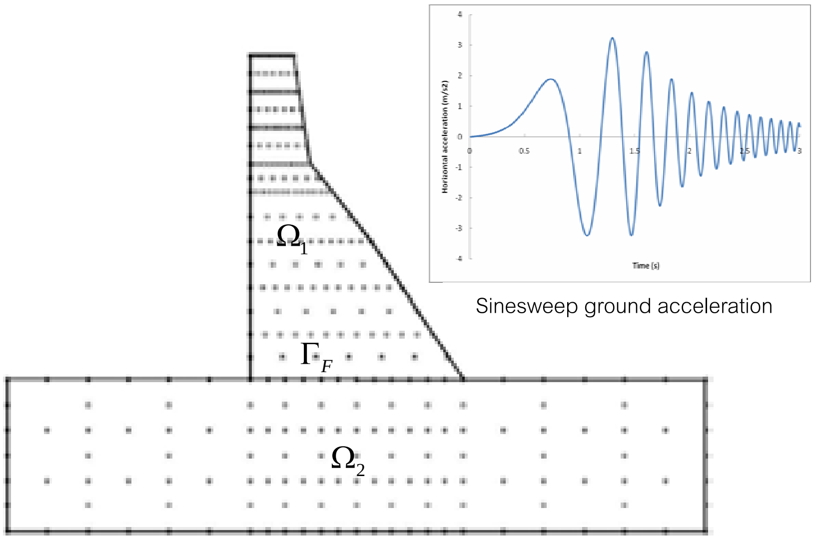

Figure 4: Modeling mesh (Example 2)

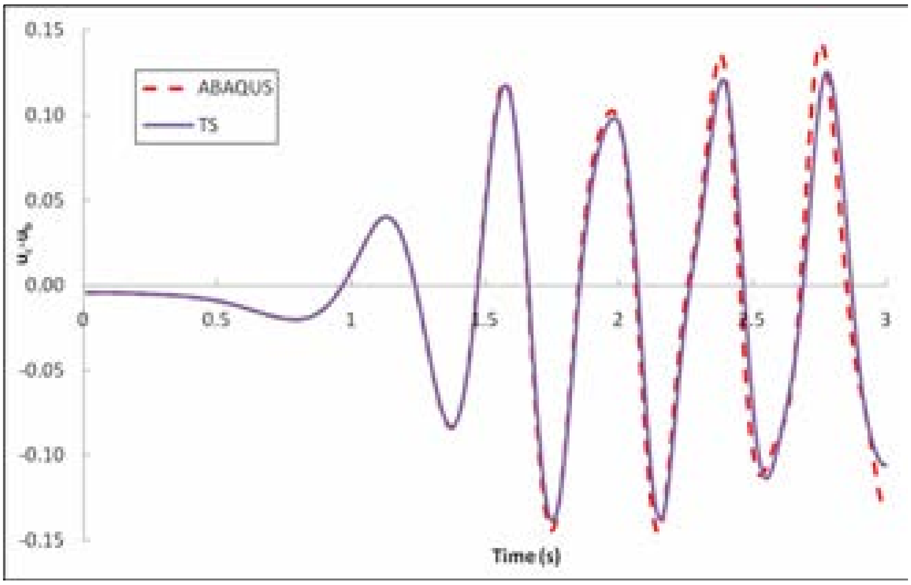

Figure 5: Horizontal crest displacement relative to dam base (Example 2)

6. CONCLUSIONS

A BEM formulation for elastodynamic analysis using DDM and particular integrals has been presented. Based on iterative coupling DDM approach, the analysis domain was subdivided into two regions. Alternating

Schwarz algorithm can then be applied to obtain the solution for each sub-region iteratively until convergence is satisfied. The accuracy and validity of the present formulation is evaluated by comparing the results of two example problems with ABAQUS.

REFERENCES

P.K. Banerjee, R. Butterfield, 1981. *Boundary Element Methods in Engineering Science*, McGraw-Hill: London.

P.K. Banerjee, 1994. *The Boundary Element Methods in Engineering*, McGraw-Hill: London.

W.M. Elleithy, H.J. Al-Gahtani, 2000. An overlapping domain decomposition approach for coupling the finite and boundary element methods. *Eng. Anal. Boun. Elements*. 24, 391-398.

W. M. Elleithy, H.J. Al-Gahtani, M. El-Gebeily, 2001. Iterative coupling of BE and FE methods in elastostatics. *Eng. Anal. Boun. Elements*. 25, 685-695.

Y.T. Feng, D.R.J. Owen, 1996. Iterative solution of coupled FE/BE discretizations for plate-foundation interaction problems. *Int. J. Numer. Meth. Eng*. 39, 1889-1901.

X-W. Gao, T.G. Davies, 2000. 3D Multi-region BEM with corners and edges. *Int. J. Solids Struct.* 37, 1549-1560.

N. Kamiya, I. Hidehito, K. Eisuka, 1996. Parallel computing for the combination method of BEM and FEM. *Eng. Anal. Boundary Elements.* 18, 221-229.

J.H. Kane, B.L.K. Kumar, S. Saigal, 1990. An arbitrary multi-zone condensation technique for boundary element design sensitivity analysis. *AIAA J.* 28, 1277-1284.

C.-C. Lin, E.C. Lawton, J.A. Caliendo, L.R. Anderson, 1996. An iterative finite element-boundary element algorithm. *Comput. Struct*. 39 (5), 899-909.

B. Smith, P. Bjorstad, W. Gropp , 1996. *Domain Decomposition: Parallel Multilevel Methods for Elliptic Partial Differential Equations*, Cambridge University Press.

O. von Estorff, C. Hagen, 2006. Iterative coupling of FEM and BEM in 3D transient elastodynamics. *Eng. Anal. Boun. Elements.* 30, 611-622.

D.R.J. Owen, E. Hinton, 1980. *Finite Elements in Plasticity: Theory and Practice*, Pineridge Press: Swansea.

EVALUATION OF WILDFIRE DURATION TIME OVER ASIA USING MTSAT AND MODIS

YUSUKE MATSUMURA[1], WATARU TAKEUCHI[2],
HARUO SAWADA[3] and YOSHIFUMI YASUOKA[4]
[1-3]Institute of Industrial Science, The University of Tokyo, Japan
[4]National Institute of Environment Studies, Japan
yusukem@iis.u-tokyo.ac.jp

ABSTRACT

In this study, we present an approach to evaluate a wildfire duration time. An-hourly MTSAT imagery is quite powerful to obtain the duration time of rapid fire events such as a grass land fire that cannot be detected with the frequency of MODIS. Research areas are evergreen needleleaf forest in far- east Russia and evergreen broadleaf forest in Sumatra. Our approach is based on a model that the temperature of the pixel becomes higher than the non-fire pixels if there is some wildfire in the pixel. As a result, it is found that fire duration time is detected by comparing the fire pixel which contains hotspots with a non-fire pixel around it. This technique is useful to detect wildfire duration time even land coverage is evergreen needleleaf forests or evergreen broadleaf forests. We can conclude that an-hourly based monitoring provides us with a sufficient time resolution and plays an important role to monitor wild fire duration time despite a lower spatial resolution in 4 kilometer than that of MODIS in 1 kilometer.

1. INTRODUCTION

1.1 Background

Serious wildfire occurs in Asia so frequently. It causes not only threads for inhabitants but also global warming or smog problem for neighbor countries (UNDP, 2001). Most of wild fires occur in hardly accessible places. Therefore, remote sensing is one of very useful tools to find or evaluate the wild fire.

There are many researches to get better information of wildfires. For example, methods of finding wildfire hotspots using high time resolution data such as MODIS are suggested(Kaufman et al., 1997) and detection of burning area using high spatial resolution data such as Landsat TM, SPOT HRV, Terra ASTER(Takeuchi et al., 2005). At the current situation, however, despite the advent of satellite imagery and the growing significance of fires to understand a condition of global forests, no reliable global statistics are available for a wildfire duration time. More information about duration time of wildfires would be needed so far.

MTSAT have thermal infrared sensor in spite of spatial resolution is 4km. By using MTSAT, we can analyze hourly features of wildfires (JMA, 2003). Before MTSAT launched, there is no way to clarify the feature of duration time of wildfires. Clarification of duration time of wildfire contributes to the evaluation of CO_2 emissions by wildfires.

1.2 Objective

The objective of this research is as follows.

1. To evaluate relation between a scale of burning area and spatial resolution by comparing ASTER, MODIS, and MTSAT which spatial resolution is different each other.
2. To clarify the feature of duration time using MTSAT data Myanmar, far east Siberia, and Sumatra.

2. METHODOLOGY

2.1 Wildfire duration time estimation model used in this study

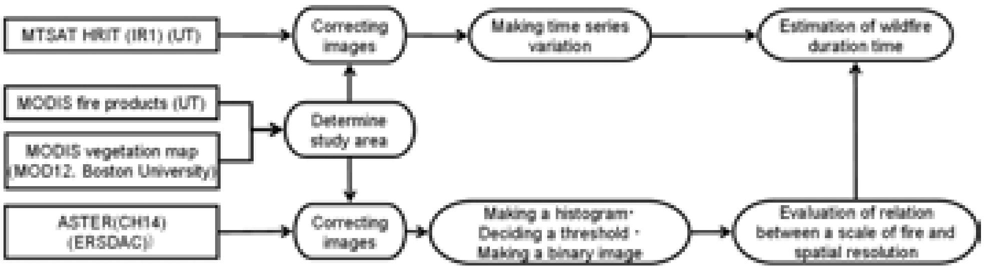

Figure 1: Flowchart of wildfire duration time estimation using MTSAT.

Figure 1 shows the flowchart of wildfire duration time estimation with MTSAT. This research consists of two parts; comparison of burnt area delineation with ASTER, MODIS and MTSAT, the other is the evaluation of wildfire duration time using MTSAT data.

Firstly, three study areas were determined supplemented by hotspot data with MODIS. Secondly, a bunch of satellite dataset was created including ASTER, MODIS and MTSAT with different spatial resolutions 90m, 1km and 4km respectively. They were used to delineate burnt areas and were carried out by using web-based processing systems (http://webmodis.iis.u-tokyo.ac.jp, http://webgms.iis.u-tokyo.ac.jp). Finally, wildfire duration time was estimated with 72-hours time series behaviors of MTSAT thermal infrared imagery by comparing a fire pixel with a non-fire pixel.

2.2 Study areas

Study areas are determined by fire spots data by MODIS, vegetation map by Boston University, and visual judgments from Google earth.

Considering difference of size and vegetation, following three areas are selected; evergreen broadleaf forest in Myanmar (March 23rd in 2007, 96-53’E, 19-13’N), evergreen needleleaf forest in far-east Siberia (July 4th in 2007, 139-26’E, 57-33’N), and evergreen broadleaf forest in Sumatra (Oct. 5th in 2006, 102-43’E, 0-43’S).

3. RESULTS AND DISCUSSIONS

3.1 Comparison of burnt area delineation with ASTER, MODIS and MTSAT

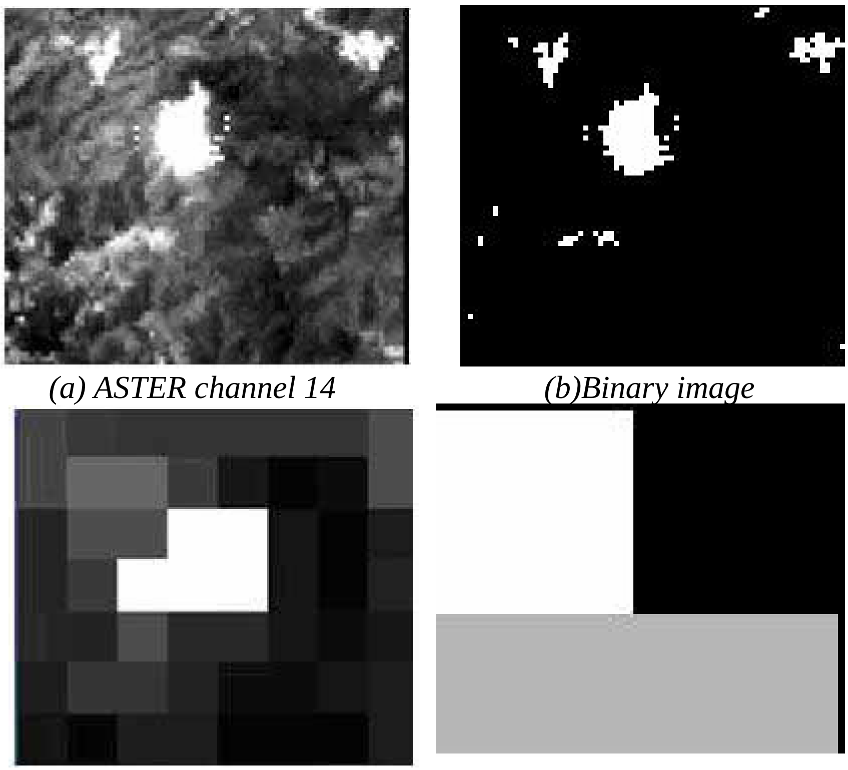

(a) ASTER channel 14 *(b)Binary image*

(c) MODIS channel 31 *(d) MTSAT channel 1*

Figure 2: Thermal infrared imagery of ASTER, MODIS and MTSAT. The area of interest is 8x8 km^2 corresponding to 4 pixels of MTSAT.

Figure 2 shows thermal infrared imagery of ASTER, MODIS and MTSAT. The area of interest is 8x8 km^2 corresponding to 4 pixels of MTSAT. Figure 2-(a) shows ASTER channel 14 imagery. A histogram of ASTER channel 14 shown in Figure 2-(a) was used to determine a threshold between fire pixels and non-fire pixels, and binary image was created as shown in Figure2-(b). The extracted fire-affected area is shown in white colors in the center of the image and area was estimated 1.5 km^2. As a comparison, MODIS channel 31 imagery is shown in Figure 2-(c) over the same area. Spatial distribution of MODIS has consistency with that of ASTER. MTSAT channel 1 imagery shown in Figure 2-(d) shows a fairy good results compared with ASTER and MODIS as well. A fire affected pixel shown in an upper left highlighted in white color has 3K higher than the other three non-fire pixels. It was found that this fire event with the size of 1.5 km^2 is detected by 4km MTSAT thermal infrared imagery.

3.2 Estimation of wildfire duration time using MTSAT

Figure 3-(a) shows the location of intensive wildfire hotspot in Myanmar. Figure 4-(a) shows time series variation of the land surface temperature from MTSAT (channel1, 10 μm) from March 23rd to 25th in 2007. The hotspot was detected in March 23rd, the first day of the series, by MODIS fire product. Time series variation from MTSAT shows that temperatures of fire pixels transit higher than that of non-fire pixels. The biggest difference is 2K at 14:00 in local time. The difference of temperatures between fire pixels and non-fire pixels were gone during night time. From this result, even though spatial resolution of MTSAT is poorer than that of MODIS, time series variation of a thermal infrared channel of MTSAT show significant difference to detect fire pixels because time resolution is more frequently.

Figure 3-(b) shows locations of target pixels of time series variation on evergreen needle leaf forests in Siberia. Figure 4-(b) shows time series variation of the land surface temperature from MTSAT (channel1, 10 μm) from July 3rd to 5th in 2007. The time when the wildfire was detected by MODIS fire products is July 4th and July 5th. As the figure shows, both of a fire pixel and a non-fire pixel show a similar time series variation in July 3rd. However, the fire pixel displays different behavior from normal pixels in July 4th and July 5th. At the peak of the graph, the fire pixel shows about 3K higher temperatures than the non-fire pixel in July 5th. From this information, the wildfire duration time is 10 hour in July 4th and 12 hour in July 5th.

Figure 3-(c) shows locations of target pixels of time series variation on evergreen broadleaf forests in Sumatra. Figure 4-(c) shows time series variation of the land surface temperature from MTSAT (channel1, 10 μm) from Oct. 5th to 7th in 2006. The time when the wildfire was detected by MODIS fire product is Oct.5th and Oct. 6th at fire pixels A and B. As the figure shows, the peak of the time series variation at fire pixels A and B on Oct. 5th and Oct. 6th is higher than a non-fire pixel C. From this figure, duration time of wildfire is 14 hours in Oct. 5th and 9 hours in Oct. 6th. At Oct. 7th, both of the land surface temperature in pixel A, B, and C change in the almost same way, so we estimate there is no wildfire in these pixels.

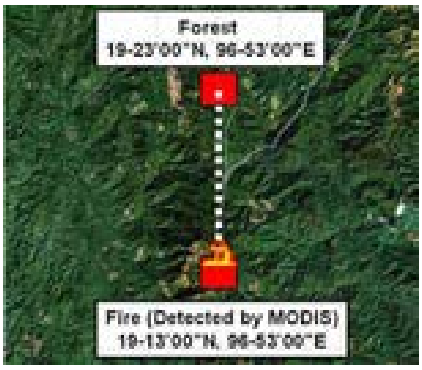

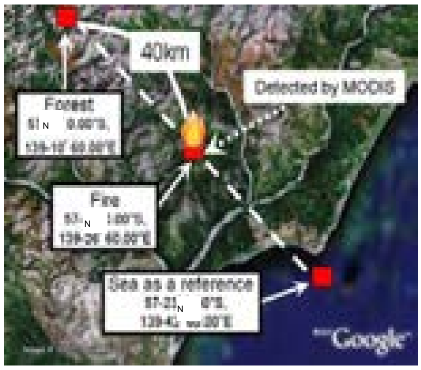

(a)Myanmar (Mar. 23-25,2007)   *(b)Far-east Siberia (Jul. 4-6,2007)*

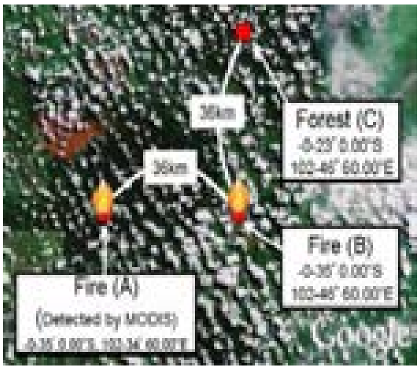

(c)Sumatra (Oct. 5-7,2007)

Figure 3: Methodology of evaluation of fire duration time using MTSAT.

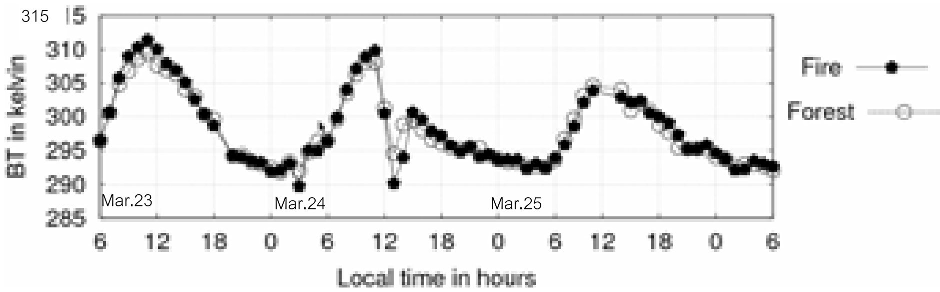

(a)Myanmar (evergreen broadleaf forest)

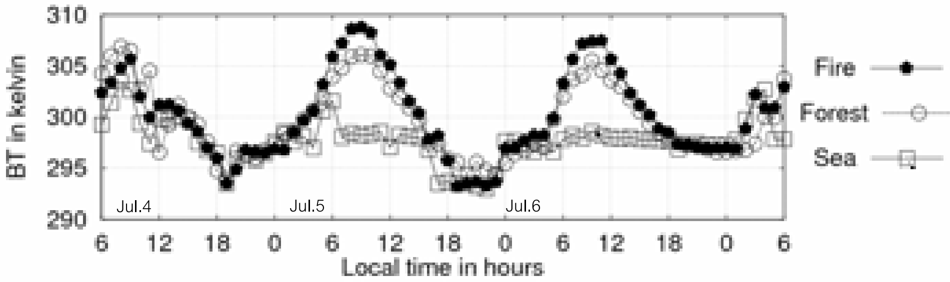

(b)Far-east Siberia (evergreen needleleaf forest)

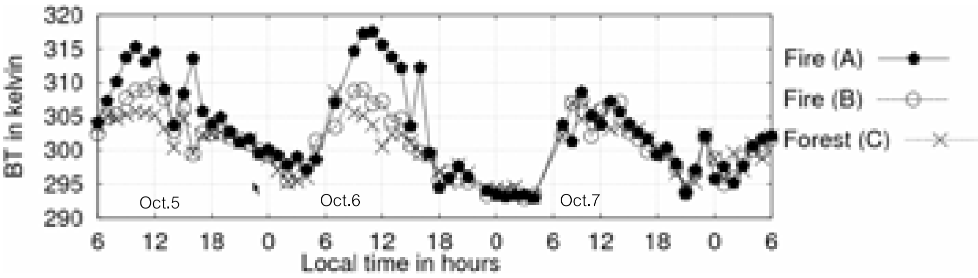

(c)Sumatra (evergreen broadleaf forest)

Figure 4: Time series variation of MTSAT thermal infrared imageries (channel 1 10.5 μ m).

4. CONCLUSION AND FUTURE WORKS

In this research, we have presented two types of research. Firstly we compare burnt area delineation with ASTER, MODIS and MTSAT that spatial resolution is different each other. Secondly, we estimate duration time of three wildfires by using time series variation of MTSAT comparing fire pixels and non-fire pixels. Our accomplishments are following three things.

- Thermal infrared imageries of ASTER, MODIS, and MTSAT shows consistent spatial distribution.
- MTSAT can be used to detect intensive wildfire that a an area is about 1.5 km^2 in this survey, even though spatial resolution of MTSAT is 4km meanwhile that of ASTER is 90m.
- Duration time of intensive wildfire can be estimated by using visual judgment from the difference of time series variation of fire pixels and non-fire pixels.

In the future research, we have to consider following two things.

- Thermal infrared imageries of MTSAT have problems about geometric correction. Therefore, when we will estimate wildfire duration time automatically, precise geometric correction should be needed
- When we compare burnt area delineation with ASTER, MODIS and MTSAT, it is very hard to find an ASTER imagery which contains burnt area because there are few ASTER imageries which contain hotspots. We should consider using another high spatial resolution data such as Landsat.

ACKNOWLEDGEMENT

This research is supported by JSPS (No. 19569002). The authors would like to thank Dr. Vivarad Phonekeo for providing MODIS data at AIT in Thailand.

REFERENCES

Glogal land cover mapping from MODIS: algorithms and early results. *Remote Sens. Environ.* ,83(1-2), 287-302.

Giglio, L., Descloitres, J., Justice, C. O., and Kaufman, Y., 2003, An enhanced contextual fire detection algorithm for MODIS. *Remote Sens. Environ.*, 87, 273-282. Japan Meteorological Agency, 2003. JMA HRIT Mission Specific Implementation, Ver. 1.2.

Kaufman, Y. J., C. O. Justice, L. P. Flynn, J. D. Kendall, E. M. Prins, L. Giglio, D. E. Ward, W. P. Menzel, and A. W. Setzer, 1998, Potential global fire monitoring from EOS-MODIS. *J. Geophys. Res.*, 103: 32215-32238.

Takeuchi, W., and Y. Yasuoka, 2005. Near-real time activefire mapping over Asia using Aqua/Terra MODIS. *Proceed. 26th Asian conf. on remote sens. (ACRS 2005)*,Hanoi, Vietnam.

Takeuchi, W., T. Nemoto, T. Kaneko and Y. Yasuoka, 2007. Development of MTSAT data processing, distribution and visualization system on WWW. *Proceed. Int. symp. remote sens. (ISRS 2007)*, Jeju, Korea.

UNDP, UNEP, World Bank and WRI, 2001, World Resources 2000-2001, *Elsevier Science*, 87-102.

SHEAR BEHAVIOR OF PARTICLES WITH RESPECT TO BONDING STATE USING PFC2D

SEON-AH JO, SEOK-KYU SONG,
SUN-AH JEONG and SEOK-WON LEE
Civil and Environmental System Engineering,
Konkuk University, Korea
asaca83@kokkuk.ac.kr
ssk81@konkuk.ac.kr
butterfly0523@hanmail.net
swlee@konkuk.ac.kr

ABSTRACT

Direct shear test was modeled using PFC2D in this study. Modeling was performed with respect to vertical stress condition, relative density, and particle shapes. Geometrical particle shape is represented by a combination of circular shape, and influence of particle shape on crushing is studied through relative comparisons between Clump (uncrushable) and Cluster (crushable) models. The results show that in Clump model, internal friction angle was largest for triangular shape and smallest for square shape. Even for cases of a same shape, internal friction angle becomes smaller when the number of balls comprising the particle shape increases, because the surface contour of the particle becomes smooth, reducing the interlocking effect. In Cluster model, when bond strength is low, most of contacts are broken during the stage of vertical stress application, and the model becomes similar to that of one ball. However, when bond strength becomes larger, the model approaches the Clump model in which particle damages occur due to vertical stress and shear application, which in turn results in reduction of peak shear stress. That is, shear resistance angle becomes reduced, and also failure envelop curve becomes nonlinear, due to the particle crushing.

1. INTRODUCTION

Granular materials are subject to static and dynamic loads during construction works as they are parts of slope, embankment, foundation, or pavement structures. They could be partially or fully crushed by the loads, and such a crushing could cause additional subsidence and reduction in water permeability by a great amount, and also alter friction angle that represents interface shear strength. Accordingly, alteration of original particles due to crushing could influence the stability of structures containing interfaces.

Factors influencing crushing of granular particles include particle size, shape, distribution, relative density, etc. In terms of granular behaviors, it is important to analyze the influences of these factors on the granular crushing, and in this study such factors are characterized by numerical analysis from a shear resistance viewpoint. For the purpose, direct shear test was modeled using PFC2D, which is a distinct element method program, and modeling was performed with respect to vertical stress condition, relative density, and particle shapes. Geometrical particle shape is represented by a combination of circular shape, and influence of particle shape on crushing is studied through relative comparisons between Clump (uncrushable) and Cluster (crushable) models. The results from the analyses are presented using stress-displacement curves, and evolution of granular crushing are presented in a time sequence.

2. PARTICLE FLOW CODE MODELING

In this study PFC2D based on distinct element method was employed in order to simulate direct shear test by numerical analysis. PFC2D was originally developed by Cundall(1995), and has been used widely in various engineering fields. Unlike finite element method or finite difference method modeling where an object is modeled by continuous nodes or mesh elements, distinct element method is based on motion and mutual interaction of spherical particles, making it more suitable for simulating sand and earth ground foundation visually.

Basically, PFC2D uses explicit method in arithmetic process, and external force, velocity, moment, and position of each granule are calculated by the equation of motion. Using the force-displacement relationship at the contact point of each particle, it is converted to interface strength, and this process is repeated every moment along the time-step.

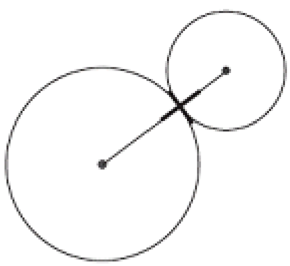

(a) Contact bond model

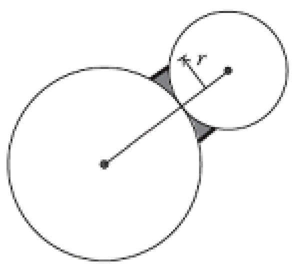

(b) Parallel bond model

Figure 1: Particle bond models

Elements' bond models in PFC2D can be determined by user's definition, and are classified into linear and nonlinear bond models based on contact stiffness, and into contact bond and parallel bond based on particle bond model. In the contact bond shown in Figure 1(a), bonding strength is represented by behaviors of one pair of spring in vertical strength and shear strength at the contact area which is represented as a minute point between the two elements. In the parallel bond shown in Figure 1(b), the contact area is represented by a cylinder or a rectangular depending on whether it is cylindrical shape or spherical shape, respectively. While only the force is transmitted at a minute contact point in the case of the contact bond, the force and the moment are transmitted together in the parallel bond, simulating strong bonding found in cement or stiff materials. If any specific bonding model is not defined, slip-separation model is applied in which frictional forces exists and slip is allowed depending on the shear component of the applied force.

3. MODEL CONSTRUCTION AND ANALYTICAL PROCESS

3.1 Direct shear model

In this study, modeling is performed by numerical analysis based on PFC2D in order to analyze shear behavior characteristics and shear mechanism with respect to particle crushing at the interface between two granular materials. Size of shear box was determined as 6cm in width and 2cm in height, based on general shear test apparatus.

Figure 2 shows a schematic of direct shear test model. In the model, upper box comprises four walls (ED, EF, FG, GH), and walls ED, FE and GH are fixed. On GF wall, vertical stress is calculated by Fish Function from contacting force between the wall and particle according to servo-controlled system, in which a certain level of stress is maintained. Shear displacements are resulted through horizontal movements of four walls (HA, AB, BC, CD) comprising the lower box, and the shear stress is calculated as contact force between the wall AB and particles interfacing this walls. Figure 2(b) shows the shear boxes and distribution of contact forces after the shearing is completed.

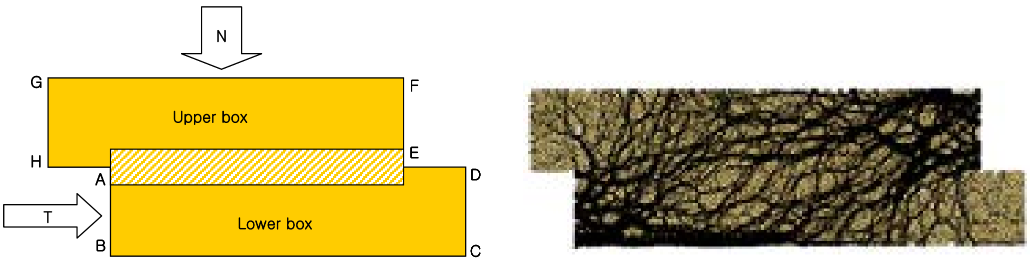

(a) Schematic of direct shear test (b) PFC2D direct shear model

Figure 2: Direct shear model

3.2 Test sample preparation

Input parameters for particles to be used in PFC2D include size, stiffness, friction coefficient, and bond strength. Particles for modeling in this study apply the blasting sands, as the physical characteristics are listed in Table 1. As for the particle size, a value corresponding to D_{50} was chosen on grain size distribution curve for blasting sand and applied to all the balls, and number of particles generated as such is 2,474. 0.75 was applied for friction coefficient, and other input parameters were chosen through numerical analysis calibration, and the resulting values are listed in Table 2.

Table 1: Basic physical characteristics of blasting sand

Blasting sand	
R_{min} (mm)	0.075
R_{max} (mm)	2
D_{50} (mm)	0.73
e_{mim}	0.7
e_{max}	0.95
Friction angle (˚)	37
Friction coefficient(μ)	0.754

Table 2: Input physical parameters in PFC2D

Micro properties		**Value**
Density (kg/m^3)		2,650
Normal stiffness (N/m)		1×10^8
Shear stiffness (N/m)		1×10^8
Friction coefficient (μ)		0.75
Gravity (m/s^2)		9.81
R_{min} (mm)		0.075
R_{max} (mm)		1
Initial porosity		0.166
Ball number		2,474
Parallel bond	Normal (Pa)	2×10^5 or 8×10^5
	Shear (Pa)	2×10^5 or 8×10^5

3.3 Conditions for analysis

Table 3 lists numerical analysis methods and conditions employed in this study. Direct shear models with respect to granular form condition are classified into one-ball, clump, and cluster. Here, one-ball model refers to single particle model of spherical shape, clump model refers to a state in which two or more spherical particles have permanent contacts without involving any crushing at the contact points, and cluster model refers to a state in which two or more spherical particles are in contact mode by a certain bonding stress and then get broken when a higher stress is applied on them.

In one-ball model, conditions were differentiated between loose state of relative density of 20% and dense state of relative state of 90%, and then vertical stress conditions of 50, 100, 200, and 300 kPa were applied in the numerical analysis. In clump and cluster models, vertical stress of 100 kPa was applied in dense state of relative density of 90%, and numerical analysis was performed for each granular formation. In clump and cluster models as shown in Figure 3, granular formations are classified into rectangular form ((a), (d)), triangular form ((b), (e)), and square form ((c), (f)), constructed by bonding of 2, 3, 4, 6, and 9 spherical granules, where each ball is assumed to be a cylinder of an unit length, and sum of the areas of balls applied is a same for all the cases. For cluster model, bond strength was set at 2×10^5 and 8×10^5 Pa in the numerical analysis.

Table 3: Methods and conditions for numerical analysis

<table>
<tr><td rowspan="6">Direct Shear Model</td><td rowspan="2">One ball</td><td colspan="2">relative density 20%</td><td>each vertical stress 50, 100, 200, 300 kPa</td></tr>
<tr><td colspan="2">relative density 90%</td><td>each vertical stress 50, 100, 200, 300 kPa</td></tr>
<tr><td>Clump</td><td colspan="2">particle formation</td><td>each 2ball, 3ball, 4ball, 6ball_R, 6ball_T, 9ball</td></tr>
<tr><td rowspan="2">Cluster</td><td>bond strength : 2×10^5 Pa</td><td rowspan="2">particle formation</td><td rowspan="2">each 2ball, 3ball, 4ball, 6ball_R, 6ball_T, 9ball</td></tr>
<tr><td>bond strength : 8×10^5 Pa</td></tr>
</table>

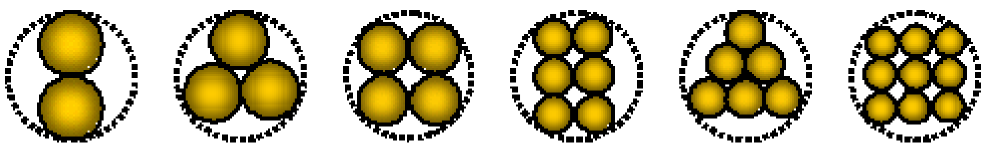

(a) 2ball (b) 3ball (c) 4ball (d) 6ball_R (e) 6ball_T (f) 9ball

Figure 3: Particle formation

4. ANALYSIS RESULTS

4.1 Characteristics of shear behavior of one ball model

A study was conducted on change of shear stress characteristics of direct shear model made of one ball while varying conditions of vertical stress and relative density. Vertical stress was set at 50, 100, 200, and 300 kPa with maximum displacement of 6mm. Figure 4 shows stress-displacement curves obtained from the analyses. Reliability of this model was established by confirming that maximum shear stress value, and horizontal displacement point where that maximum shear stress is occurring, increase when vertical stress is increased in stepwise. Also, as results on shear stress characteristics per relative density, it shows a tendency of loose condition where clear peak point does not exist when relative density is 20%, as shown in Figure 4(a), and it shows a tendency of dense condition where a peak point exists when relative density is 90% in stress-displacement curve, as shown in Figure 4(b).

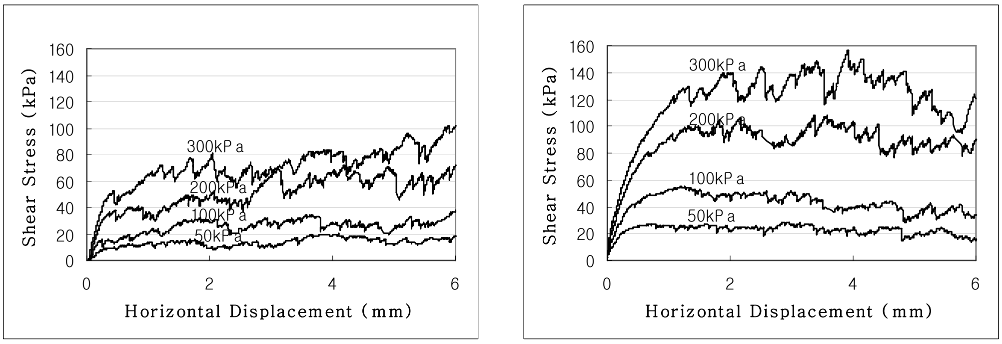

(a) Relative density 20% (b) Relative density 90%

Figure 4: Shear stress with respect to vertical stress

Mohr-Coulomb Failure envelops are shown in Figure 5 for relative density of 20% and 90%, respectively, and the curves are used to find out the change in maximum shear stress under vertical stress condition. Here, internal friction angles were 27.8°, 18.7° for the relative density of 90% and 20%, respectively. It was confirmed that the internal friction angles are somewhat lower in this study, as compared to the values 31.9° , 37.9° obtained for relative density of 25% and 75%, respectively, for the standard Joomoonjin sands(Uhm et al., 2004). This result seems to be related to a fact that the particles in this study are spherical with smooth surface, and accordingly do not reflect the shape and surface roughness of natural coarse granules in this analysis. Accordingly, it is desirable to perform the analysis while varying the shape of the particle variously in order to obtain precise analytical results, and such improved analysis is described in the following section.

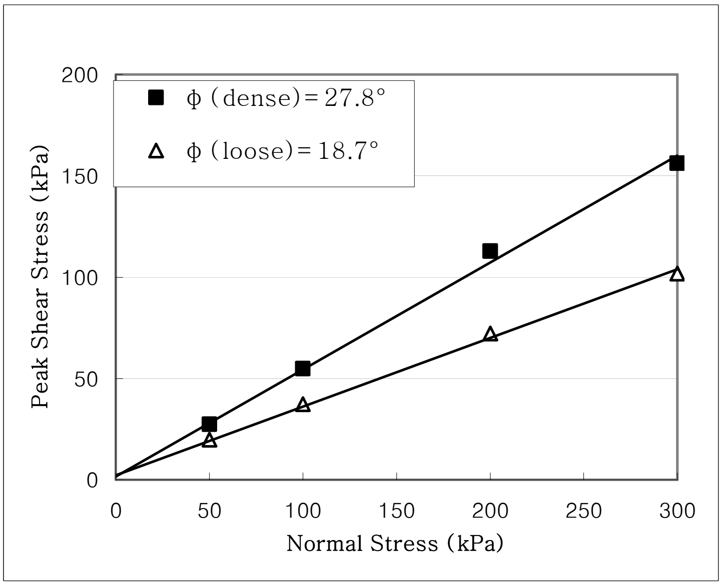

Figure 5: Failure envelope

4.2 Characteristics of shear behavior of clump model

In PFC2D, the ball is assumed to be a sphere or cylinder, thus limiting the accuracy obtainable from the analysis for actual particles that possess geometrically complicated shapes. Clump concept is one of solutions for avoiding the limitation. In clump model, a number of spherical particles are bound as a group, and geometrical shape of the particle is represented while maintaining the contacts at the contact points between the particles within the group. The group behaves as one particle element, and the contact points within the group are excluded in the calculation process, and analysis is carried out only for one the contact point between groups, thus shortening the time to conduct the analysis.

In this section, analysis was done to find out the influence of particle shapes on shear stress characteristics, while excluding particle crushing, based on clump principle, using six particle shapes as shown in Figure 3. The stress-displacement curves for clump model were obtained as shown in Figure 6. In all the shapes, peak value was reached after a certain range of displacement, after which the stress decreases before settling on a residual stress condition. Figure 7 shows Mohr-Coulomb failure envelope per particle shape, and internal friction angle for each shape is listed in Table 4. When the particle shape is triangular, the peak shear stress and internal friction angle are maximum as shown in Figure 3(b), with 155 kPa and 54.7°, respectively, while the values were minimum when the shape is square as shown in Figure 3(f), with 113 kPa and 46.5°, respectively. When comparisons are made between (a) and (d), (b) and (e), and (c) and (f), it was confirmed that the values became smaller when the number of particles is larger. The result can be understood from the view point of surface roughness of particles. That is, even for a same shape, when the number of balls is fewer, the surface contour varies more, thus becoming more rougher, while in the opposite case the contour becomes smoother. Larger variation in the contour of the particle surface increases interlocking condition, thus increasing peak shear stress and friction angle as a result.

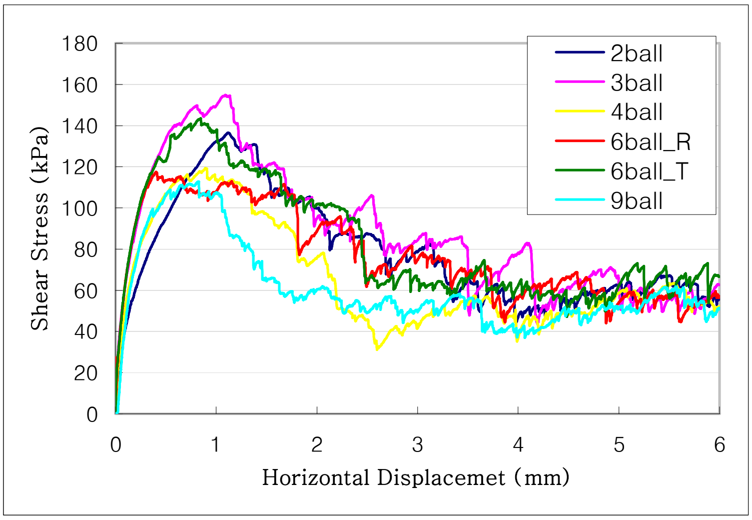

Figure 6: Stress-displacement curves regarding particle shapes

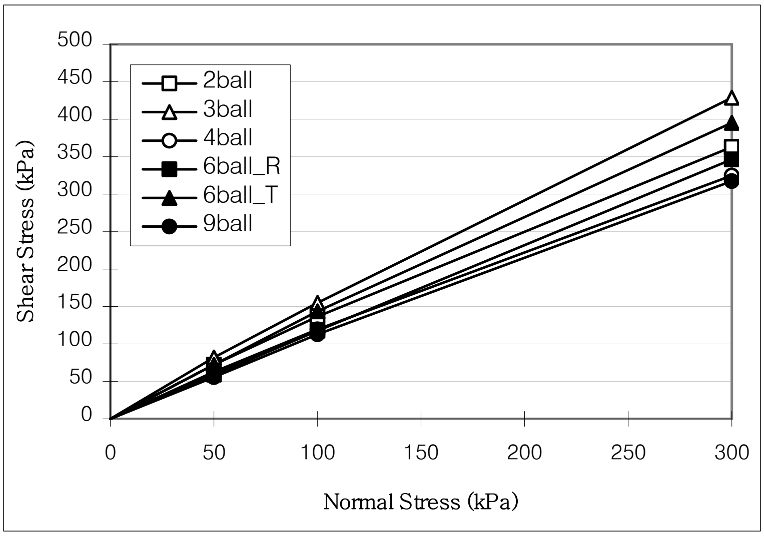

Figure 7: Failure envelope regarding particle formation

Table 4: Internal friction angle regarding particle

Particle formation	**Internal friction angle(φ)**
2ball	50
3ball	54.73
4ball	46.94
6ball_R	49.05
6ball_T	52.57
9ball	46.48

Numerical analysis based on clump principle has the advantage of shortened analysis time, but has a shortcoming of not considering the influence of particle crushing. That is, the assumption that balls in the model are bound by infinite contact strength cannot handle cases when particles are crushed. In order to resolve this limitation, cluster concept is applied in which the concept of particle crush is introduced.

4.3 Characteristics of shear behavior of cluster model

In the clump principle, there is a limitation that balls in the model are bound by infinite contact strength, thus it cannot handle cases when particles are crushed. Accordingly in this section, cluster concept is introduced in which certain level of bond strength is applied and the contact is to be destroyed when stress beyond the level is applied externally. The same six particle formations of 2ball, 3ball, 4ball, 6ball_R, 6ball_T, and 9ball conditions were employed, and parallel bond model was applied regarding the bond among the balls within one group in performing analysis. Change on shear stress with respect to bond strength was found out in order to select a proper bond strength that may represent crush strength of coarse granular soil, and the results were obtained regarding relationship between peak shear stress and bond strength as shown in Figure 8. Here, vertical stress of 100kPa and relative density of 20% were applied. As shown by the curves, when bond strength is less than 1×10^5 Pa, particle bonds are mostly crushed at a stage of vertical stress application, and shear strength becomes constant, instead of increasing. On the other hand when bond strength exceeds 1×10^6 Pa, particle bonds are not crushed even at a stage of vertical stress application, exhibiting a certain level of shear strength value. Accordingly, in this analysis, bond strength values of 2×10^5 Pa and 8×10^5 Pa were taken, corresponding to 20% and 80% values, respectively, between 1×10^5 Pa and 1×10^6 Pa, to study influences regarding particle crushing.

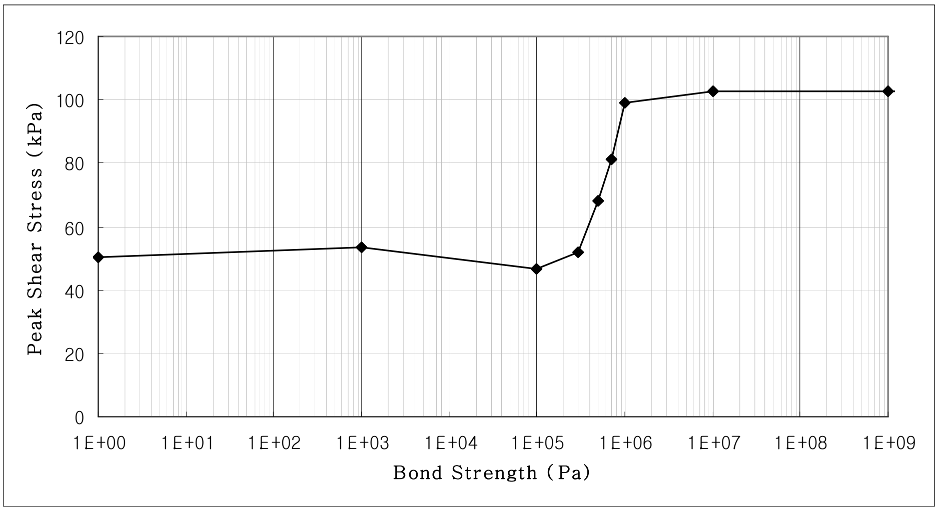

Figure 8: Peak shear stress regarding bond strength

Shear stress test results are shown in Figure 9 for two bond strength conditions of vertical stress 100kPa and relative density 20%, per particle formation. In all the models, peak shear stress value increases as bond strength increases, and breaking points appeared clearly. That is, when bond strength is small, the bond between the balls is destroyed even by a small increase in stress, reducing the influence of particle formation factor on shear stress, while when bond strength becomes larger, the influence of particle formation factor on shear stress becomes larger and breaking points appear clearly. Under a same bond condition, shear stress shows some variations with respect to particle formation, and this seems to be related to the size of balls comprising the particle.

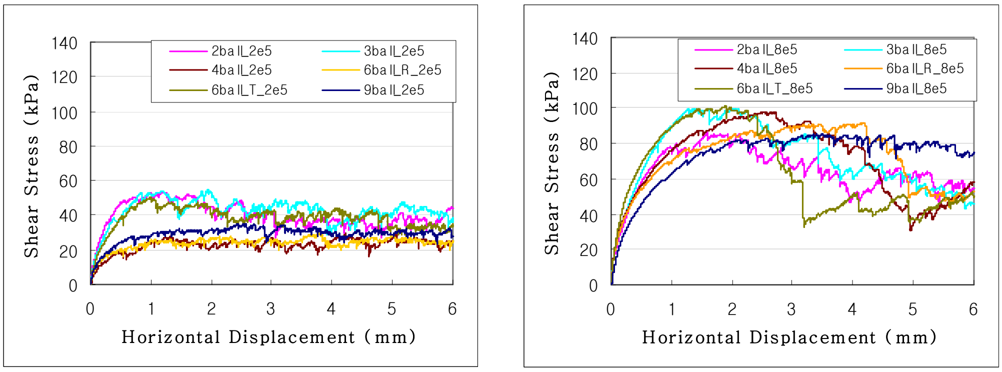

(a) Bond strength 2×10^5 Pa (b) Bond strength 8×10^5 Pa

Figure 9: Shear stress characteristics with respect to bond strength

4.4 Comparison between clump model and cluster model

In this section, results from clump and that from cluster are compared, as depicted in Figure 10. Peak shear strength from clump model is larger than that obtained from cluster model on two bond strengths. This is because, in clump model, particle crush does not occur owing to the infinite strength assumed on the contacts between balls, while, in cluster model, particle crush occurs, allowing influences from crushing. Here, Mohr-Coulomb Failure envelop is found with 2ball model in particular, as shown in Figure 11. The curve is near linear in clump model, while it is nonlinear in cluster model. This agrees with prior result (Bolton, 1986; Feda, 2002) which says that failure envelop expressing peak shear strength is nonlinear because shear resistance angle is reduced owing to particle crush. Accordingly, it is concluded from these results that it is preferred to apply cluster model in studies involving particle crushing.

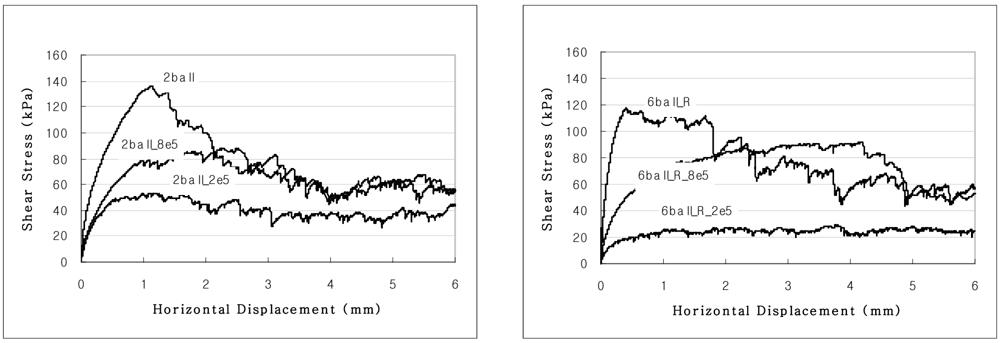

(a) 2ball (b) 6ball_R

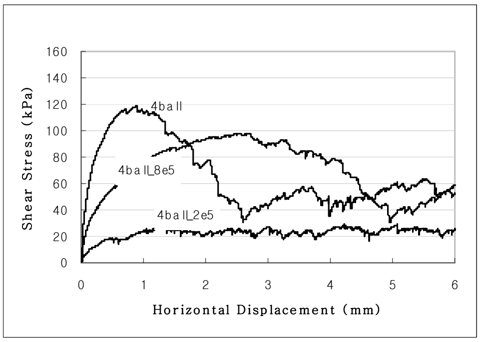

(c) 3ball

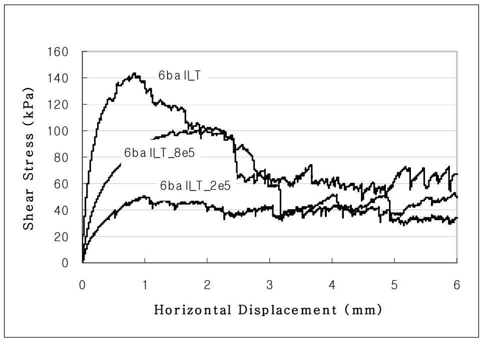

(d) 6ball_T

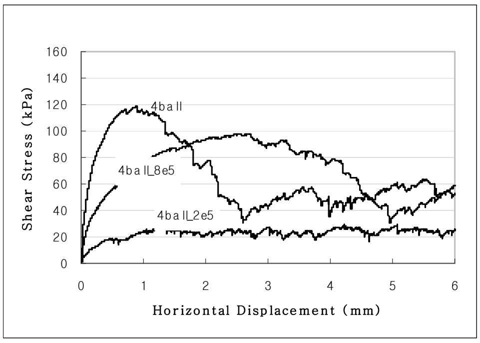

(e) 4ball

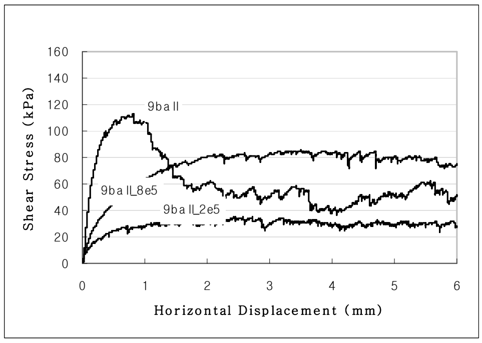

(f) 9ball

Figure 10: Comparison of Clump and Cluster shear stress values

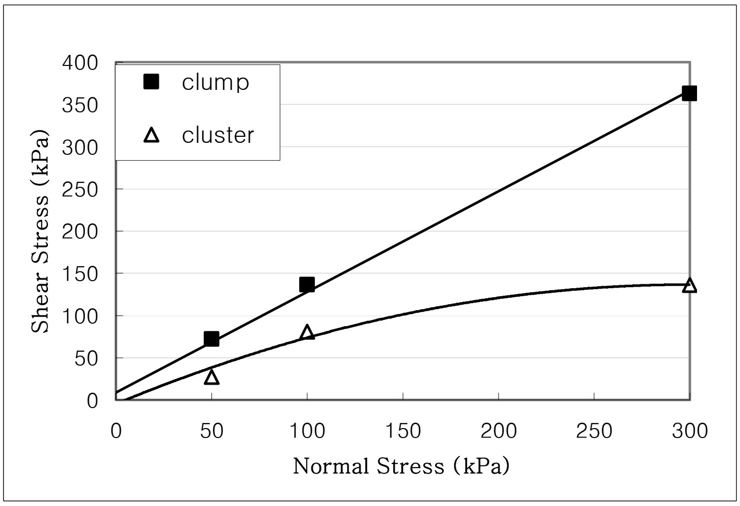

Figure 11: Failure envelope

5. CONCLUSIONS

Direct shear test was modeled using PFC2D in this study. Modeling was performed with respect to vertical stress condition, relative density, and particle shapes. Geometrical particle shape is represented by a combination of circular shape, and influence of particle shape on crushing is studied through relative comparisons between clump (uncrushable) and cluster (crushable) models. Conclusions obtained through this study are as follows:

1. In the case of One-ball model, when vertical stress increases stepwise, peak shear stress value and the horizontal displacement points where the peak shear stress occur, keep increasing in direct shear model. It shows a tendency of loose condition where clear peak point does not appear when relative density is 20%, while it shows a tendency of dense condition where a peak point appears when relative density is 90%, in which breaking points appear when a certain amount of horizontal displacement is applied. This result is similar to the typical results obtained from laboratory direct shear tests, establishing the reliability of the present numerical analysis.

2. In the case clump model, larger values were obtained for peak shear stress as compared to one-ball model, owing to an influence of particle formation, and internal friction angle was largest for triangular shape and smallest for square shape. Even for cases of a same shape, internal friction angle becomes smaller when the number of balls comprising the particle shape increases, because the surface contour of the particle becomes smooth, reducing the interlocking effect.

3. In the case of cluster, when bond strength is low, most of contacts are broken during the stage of vertical stress application, and the model becomes similar to that of one ball model. However, when bond strength becomes larger, the model approaches the clump model in which particle damages occur due to vertical stress and shear application, which in turn results in reduction of peak shear stress. That is, shear resistance angle becomes reduced, and also failure envelop curve becomes nonlinear, due to the particle crushing.

ACKNOWLEDGEMENTS

This work was supported by the Korea Research Foundation Grant funded by the Korean Government (MOEHRD) (KRF-2007-331-D00475).

REFERENCES

Barrett, P.J., 1980, The shape of rock particles, a critical review, *Sedimentology*, 27, 291-303.

Bonton, M.D., 1986, The strength and dilatancy of sands. *Geotechnique*, Vol. 36, No. 1, 65-78.

Cho, G.C., Dodds, J.S., and Santamarina, J.C., 2006. Particle shape effects on packing density, stiffness, and strength: natural and crushed sands, *Journal of Geotechnical and Geoenvironmental Engineering*, ASCE, Vol. 132, No. 5, 591-602.

Coop, M.R., Sorensen, K.K., Freitas, T.B., and Georgoutsos, G., 2004. Particle breakage during shearing of a carbonate sand. *Géotechnique*, Vol. 54, No. 3, 157-164.

Feda, J., 2002. Notes on ter effect of grain crushing on the grnular soil behavior. *Engng Geol.*, Vol. 63, No. 1, 93-98.

Itasca Consulting Group, Theory and Background.

Krumbein, W.C., 1941. Measurement and geological significance of shape and roundness of sedimentary particle. *J. Sediment. Petrol*., 11(2), 64-72.

Krumbein, W.C. and Sloss, L.L., 1963. *Stratigraphy and sedimentation*, 2nd Ed., Freeman and Company, San Francisco.

Lee, K.L. and Farhoomand, I., 1967. Compressibility and crushing of granular soil in anisotropic triaxial compression. *Can. Geotech. J.*, vol.4, 68-86.

Powers, M.C., 1953. A new roundness scale for sedimentary particles. *J. Sediment. Petrol*, 23(2), 117-119.

Wadell, H., 1932. Volume, shape, and roundness of rock particles., *J. Geol.*, 40, 443-451.

BEHAVIOR OF SOFT GROUND INSTALLED WITH EXPANDING VERTICAL DRAIN

PHUONG TUNG HOANG[1], JAI-BEOM SHIM[2],
JIHO PARK[3], SEONG-HYEON SHIM[4]
and YOUNG UK KIM[5]
[1,3,5]Department of Civil and Environmental Engineering,
Myongji University, Korea
[2,4]Samsung Corporation, Engineering and Construction, Korea
tungphhoang@gmail.com

ABSTRACT

The behaviors of soft soil were investigated by using two types of vertical drains through centrifuge modeling. The Improvement methods involve Sand Compaction Piles (SCPs) method and Expanding Vertical Drains (EVDs) method which was newly developed in the lab. The behaviors of soft soil such as displacement, pore water pressure and water content were observed and collected. The improvement processes of treated soil (with SCPs and EVDs) and non-treated soil were compared and presented in details at conclusions.

1. INTRODUCTION

Sand Compaction Piles (SCPs) method now is widely being used in marginal sites to improve stability, to control liquefaction, and to reduce settlement of various infrastructures. These piles can significantly enhance the pore water pressure-dissipation process and decrease the consolidation time when built in soft clay. In South Korea, the SCPs were first used in 1984 for the construction of the Kwang Yang Steel Mill complex and this method has advanced and found a wider application in Japan (Barksdale and Takefumi, 1991; Enoki et al., 1991).

Expanding Vertical Drains (EVDs) is, however a new method to improve soft soil which is suggested by Myongji University. The EVD's drainage principle is similar to Prefabricated Vertical Drains (PVDs). The PVDs devices are installed into the soft clay to create the artificial drainage paths. The use of PVDs along with precompression has the sole purpose of shortening the drainage path (distance to a drainage boundary) of the pore water, thereby accelerating the rate of soft clay consolidation. EVD is a high water absorbability device and made of an expanding material when subjected to water (Photo 1). Installation of EVD might create the increased water flow path due to expanding. In addition, the adjacent soil mass will be compressed by the EVDs along the horizontal direction.

This paper intended to compare the ability of soft soil treatment between EVDs and SCPs through a series geotechnical centrifuge tests. The results of experiment tests were discussed with special reference to the settlement, the pore water pressure and the moisture content of treated-soft clay (with SCP and EVDs) and non-treated soft clay.

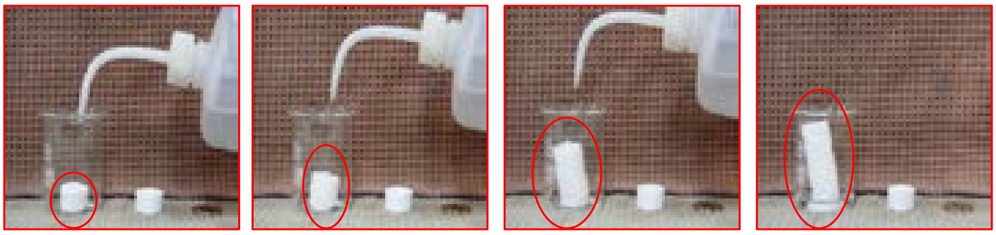

Photo 1: Expanding material applied to EVD

2. EXPERIMENTAL PROGRAM

2.1 Test cases

Three kinds of tests were carried out and are listed in Table 1. Improvement ratio is defined as the ratio between the total cross sectional area of the columns and the improved area. The improvement ratio was about 12% for all tests and the value of improvement ratio was arbitrary choosen in this research. The material of treating column was varied in every test case.

Table 1: Test case

	Case 1	Case 2	Case 3
Improvement ratio (%)	0	12	12
Improvement method	Non-treated	Sand compaction pile (fine sand)	Expanding vertical drain (paper towel)

2.2 Preparation of soft clay bed

The slurry used in the centrifuge tests was preparation by mixing the clay with de-aired water until its moisture content reaches about 115%. The slurry was also boiled in a container for about 10 hours in order to remove void air and to obtain homogeneous slurry. During boiling slurry process, clay and water were stirred regularly. After getting the slurry homogeneous slurry from the boiling process, this soft clay was self-consolidated by centrifuge rotation velocity of 173 rpm corresponding to 40 g for 8 hours. The soft ground deposit was made as following.

1. 5 cm thickness fine sand layer was compacted and embedded on the bottom of swing-up box. This sand layer will resist the lateral movement of clay layer above and another function of this deposit is an under permeable layer.

2. The homogenous slurry was poured over the sand layer. The height of this layer reached 15 cm.

3. This ground was consolidated by itself during 8 hours in centrifuge to make the normally consolidated ground whose shear strength increased linearly with the depth. The final thickness of the soft ground was around 10 cm.

2.3 Preparation of Sand Compaction Pile (SCP) model

Joomoonjin sand was used for material of SCP. A pile which has a removable core was device to install SCP into soft clay. During SCP installation process, the sand material was vibrative compacted by vibration rod. The SCP's has 20 mm diameter and 100 mm height. The vertical piles were installed in triangular pattern, with center to center spacings of 3 cm. A thin sand layer was laid on the clay surface to get a hardness surface and two linear variable displacement transducers (LVDTs) were set above to record settlement during the test. Additional two pore pressure transducers (PPTs) were installed at prescribed locations. The arrangement of SCPs in this test is shown in Figure 1a. Figure 1b shows the location of all transducers used in the test.

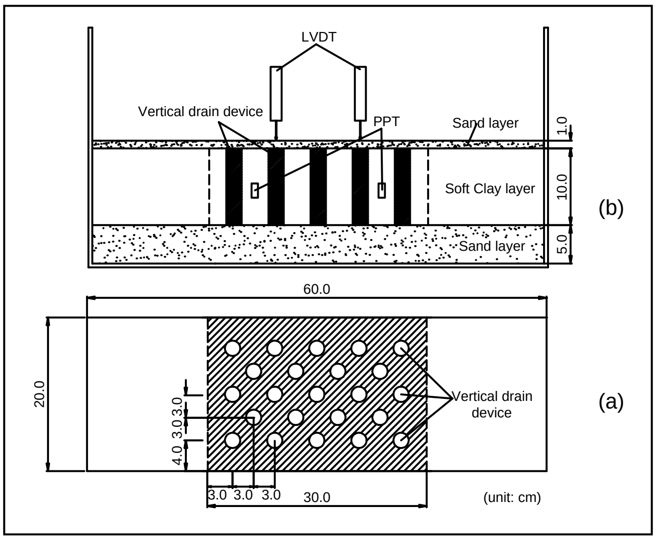

Figure 1: Schematic view of model ground

2.4 Preparation of Expanding Vertical Drain (EVD) model

EVDs which were installed directly in this test are paper expanding vertical drain. A series of paper (textile fabric material) towels having very high water absorbability was used to make an EVD. The dimension of paper towel piece is 20 mm diameter and 10 mm thickness. EVDs were made by link 5 pieces through vertical side of them to get a device which has 10 mm thickness, 20 mm width and 100 mm height which is shown in Photo 2. The paper pieces should be kept absolute dry before using in centrifuge test. The paper columns were installed along vertical direction by a long pin device. EVDs will not be folded and clay mass is least disturbed by using this pin device during installation process. The location of EVDs is triangular pattern similar to the aforementioned application SCPs. The LVDTs and PPTs were also set on the modeling among the pile group along the determined positions.

2.5 Preparation of Non-treated modeling

After pre-consolidation, the moisture content reduced from 115% to about 65% and the settlement of model was about 5 cm. The geo-centrifuge was stopped and set up LVDT devices on the clay surface, PPT equipments inside the clay deposit. A thin sand layer was also laid over the model surface.

2.6 Geo-Centrifuge running procedure

All of models were pre-consolidated under 40 g for about 8 hours. During pre-consolidation test, the ground displacement was checked. And three models gave about 5 cm settlement after pre-consolidation. After the pre-consolidation was completed, the model box was stopped, water content of clay was checked, the ground improvement methods were applied and the measurement gauges such as PPTs (Tokyo Sokki Kenkyujo KPC-500kPa) and LVDTs (CDP-25) were set at the discussed positions. Each PPT was filtered with a saturated porous stone to measure the pore water pressure and to protect the silicone diaphragm of transducer. Two linear variable differential transducers had 2.5 cm length capacity. After setting, the centrifuge ran during 15 minutes under the 10 g to check the transducers connecting and 1 hour under the 20 g to remove the influence of stress release. The improvement process was applied under 220 rpm corresponding to 65 g during 12 hours. After finished process, the data of displacement and pore water pressure of three test models were colleted by Campbell Scientific_CR1000 dataloger.

3. RESULTS AND DISCUSSION

3.1 Settlement

The relationship between the settlements at the surface of the model ground with time is shown in Figure 2. This figure shows that the amount of settlement of the improved ground installed with the EVDs is much less than that with the SCPs and the displacement value of the non-treated ground is highest.

1. At the initial settlement, the displacement values of three models went up rapidly. The amount of settlement shot up dramatically from 0 cm (at start time) to 1.47 cm (at 5000seconds elapse time) in non-treated model.

At that time, the rising of displacement value is from 0 cm to 0.83 cm and from 0 cm to 0.57 cm for SCPs and EVDs model, respectively.

2. The EVDs model reached to consolidation settlement fastest, the second is SCPs model and the third is non-treated model. The amount of displacement rise gradually and slightly to become a steady line that is fairly parallel with horizontal axis and the final settlement value of non-treated model is 1.73 cm, of SCPs model is 1.23 cm, and of EVDs is 0.81 cm.

From these results, it can be concluded that the behavior of consolidation strongly depends upon the material of ground improvement methods. Photo 2 shows the expanded drainage after the test. Changed shape of the EVD and SCP tests are seen in photo 3 and photo 4, respectively.

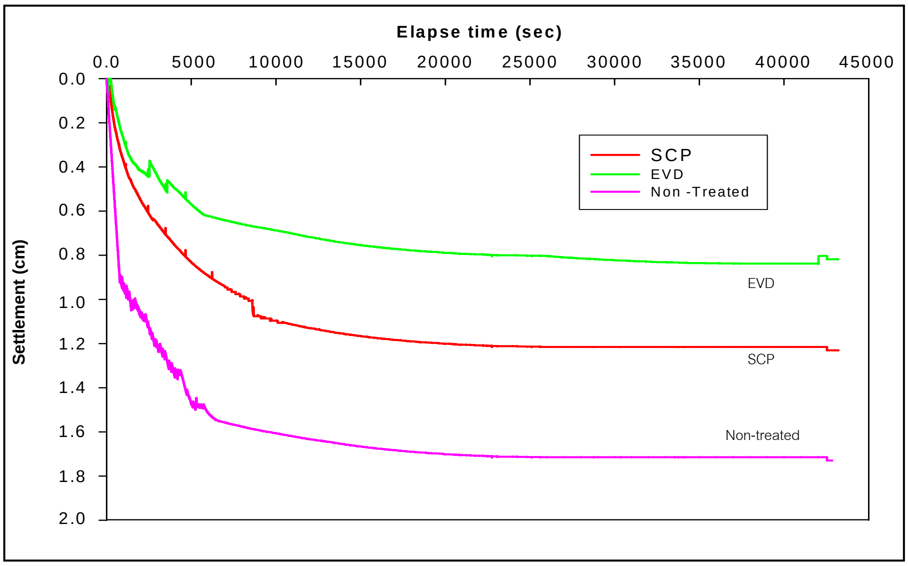

Figure 2: Settlement – time curves of model ground

Photo 2: Expanding vertical drain shape

Photo 3: EVDs model

Photo 4: SCPs model

3.2 Dissipation of pore water pressure

Figure 3 shows the relationship between the pore water pressure and the elapsed time at each centrifuge tests. The pore water pressures developed by loading of the consolidation pressure are different from each model.

1. At the start time of these tests, the pore water pressure generated by applied centrifuge stress shots up dramatically, hitting the peak at 60.71, 50.11 and 40.22 kPa for Non-treated, SCP and EVD model respectively.

2. After that, the pore water pressure gradually dissipates over along period time. The speed of dissipation of EVDs model is fastest and its final value is lowest in this test.

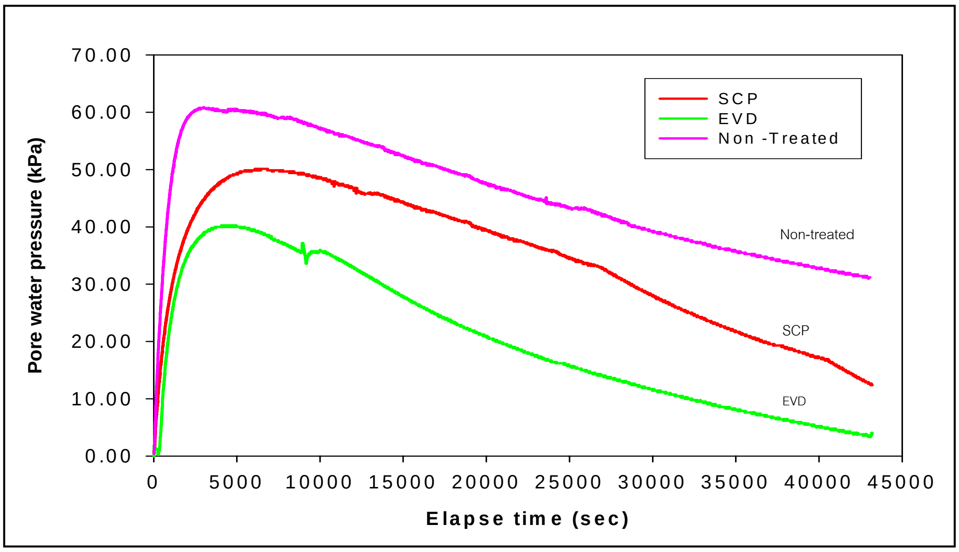

Figure 3: Pore water pressure – time curves of the ground

3.3 Moisture content

Finally, the centrifuge was stopped after 12 hours and the moisture content was checked at several locations at each test. The averaged water content values were shown in the Table 2.

Table 2: Moisture content

Moisture content (%)	**Non-treated**	**SCPs**	**EVDs**
Initial	115.5	112.3	113.4
After pre-consolidation	64.21	67.43	65.85
After ground improvement	45.12	30.14	22.75

Table 2 shows that after ground improvement method used, the water content in EVDs case is lowest and it rises up in SCPs and non-treated cases, respectively.

4. CONCLUSIONS

From the results of the geo-centrifuge model test, the consolidation behavior of the EVDs and SCPs ground improvement method and non-treated clay ground is summarized as follows.

1. The consolidation behavior of the clay ground strongly depends on the improvement material. The settlement of EVDs case is the least and it can reach the consolidation settlement earliest. Then the EVDs method can increase consolidation ratio, reduce the settlement of soft ground and the secondary consolidation time.

2. The pore water pressure dissipated rapidly in clay and the moisture content was also lowest when EVDs was installed. From high absorbability, EVDs can reduce the pore water significantly to increase the consolidation process in clay mass.

3. The horizontal expanding of EVDs is an advantageous point to ground treatment. When using EVDs, the clay ground is not only consolidated by vertical direction but also compressed with horizontal side by the expanding. By applying EVDs device, the clay deposit will be squeeze along two directions to increase the hardness and reduce the consolidation time.

4. Otherwise, the other expectations of EVDs are low cost and environmental friendliness. The material of EVDs is recycled paper or textile fabric which can be prefabricated in high quantity productions. Then the cost of EVDs is also lower than sand or the other natural materials. However, the EVDs has a drawback which is its bearing capacity will reduce because the material will be disintegrated in clay environmental for long time period.

REFERENCES

US. Department of Transportation, Federal Highway Administration (August, 1986). *Prefabricated Vertical Drains – Vol.1: Engineering Guidelines*, Report No. FHWA/RD-86/168.

J.B.Jung & T.Moriwaki, N.Sumioka, O.Kusakabe. *Consolidation behavior of composite ground improved by sand compaction piles*, Centrifuge 98, Kimura, Kusakabe & Takemura (eds) 1998 Balkema, Rotterdam, ISBN 90 5410 986 6, pp.825-830.

Y.W.Ng, F.H.Lee & K.Y. Yong. *Development of an in-flight Sand Compaction Piles (SCPs) installer,* Centrifuge 98, Kimura, Kusakabe & Takemura (eds) 1998 Balkema, Rotterdam, ISBN 90 5410 986 6, pp.837-843.

H.Hashizume, Y.Okochi & J.Dong, N.Horii, Y.Toyosawa & S.Tamate. *Study on the behavior of soft ground using Deep Mixing Method by low improvement ratio,* Centrifuge 98, Kimura, Kusakabe & Takemura (eds) 1998 Balkema, Rotterdam, ISBN 90 5410 986 6, pp.851-856.

Thomas Michael WEBER, *Development of a sand compaction pile installation tool for the geotechnical drum centrifuge,* XVI Euro Young Geotechnical Engineers Conference, 8-11 July 2004, Vienna Austria.

David Muir Wood, 2004. *Geotechnical Modeling – Centrifuge modeling,* Version 2.2, pp.269 – 307.

Braja M. Das, 1999. *Principles of Foundation Engineering,* Fourth edition, pp.796-820.

UTILIZING HETEROGENEOUS ENGINEERING IN CONCRETE MATERIAL INNOVATIONS FOR SUSTAINABLE DEVELOPMENT

MICHAEL HENRY[1] and YOSHITAKA KATO[2]
[1]Department of Civil Engineering, University of Tokyo, Japan
[2]International Center for Urban Safety Engineering,
Institute of Industrial Science, University of Tokyo, Japan
mwhenry@iis.u-tokyo.ac.jp
katoyosh@iis.u-tokyo.ac.jp

ABSTRACT

Concrete may be thought of as an artifact composed of media transformed by the transcription of design information. This design information traditionally includes only engineering experience. However, in order to improve the sustainable practices of the concrete industry, as well as maintain competitiveness, the concrete industry must consider how to include the knowledge of other fields, such as sociology, economics, politics, and so forth when developing new technologies. Heterogeneous engineering is a term used by sociologist John Law to describe an approach to technological innovation which not only considers traditional engineering philosophy, but the integration of social, political, and other systems as necessary for successful technological innovation.

Sustainability will drive changes in the way the concrete industry and concrete construction operate. Utilizing heterogeneous engineering for integrating new actors in the development of new concrete technology and innovations will be necessary for their successful implementation.

1. INTRODUCTION

Concrete is a critical component for constructing the infrastructure necessary to provide society with basic safety and living requirements. As human populations continue to grow and urbanize, so too will the demand for infrastructure increase, resulting in increased utilization of concrete to meet that demand. Therefore, the concrete industry should become a leader in promoting sustainable development as a design philosophy to enhance the longevity and quality of our construction works while minimizing their impact on society and the environment.

Unfortunately, until now concrete has been developed primarily considering an engineering perspective. In order to strengthen the competitiveness of concrete as a construction material, as well as promote sustainability, concrete engineers must look beyond their traditional fields.

In this paper, social theory of technology is proposed as a means for studying how to expand the networks which concrete engineers utilize when developing technological innovations. This theory is then applied to the design process for concrete artifacts, considering the input of actors from other fields in the design process.

2. HETEROGENEOUS ENGINEERING

Concrete is a technology, just as bicycles or guided missiles are technologies, and each of these has its own unique history of innovation and development. In order to understand the reasons for technological development, sociology should be applied. The theory of the social construction of technology (SCOT) is used by sociologists of technology to explain technological innovations. SCOT generally focuses on how new artifacts are shaped. Technological development is driven by the interactions between the social groups involved, rather than other factors such as market demand. These social groups represent different perspectives on the problems related to the innovation process, as each group has its unique interests. As a result of these diverse interests, negotiation between actors occurs in order to develop the technology. Furthermore, the technology is considered fully developed when it is accepted as such by those who developed it (Pinch and Bijker, 1987).

In order to achieve successful innovation, John Law proposed that innovators must be more than just engineers or scientists; that they needed to become “heterogeneous engineers” (Law, 1987). Heterogeneous engineers gather not only technological knowledge, but attempt to create networks which contain the people, skills, and artifacts necessary to achieve successful technological development. This network-building derives from Bruno Latour and Michael Callon’s “actor-network theory,” which studies the formation of networks consisting of both human and non-human actors during times of change (Latour, 2005). Successful engineering, as explained by Donald MacKenzie (borrowing from Law), involves building networks which bind together the human and organizational with the technological (MacKenzie, 1987).

3. CONCRETE & SUSTAINABILITY

3.1 Development of concrete technology

Concrete material and infrastructure may be thought of as artifacts. These artifacts are created from raw materials, or media, by the transcription of design information, as shown in Figure 1. In the case of concrete material, these media include Portland cement, water, aggregates, and admixtures. Concrete infrastructure is more complicated, therefore a greater amount of media is necessary for its creation; however, some examples include concrete material, steel reinforcement, and formwork.

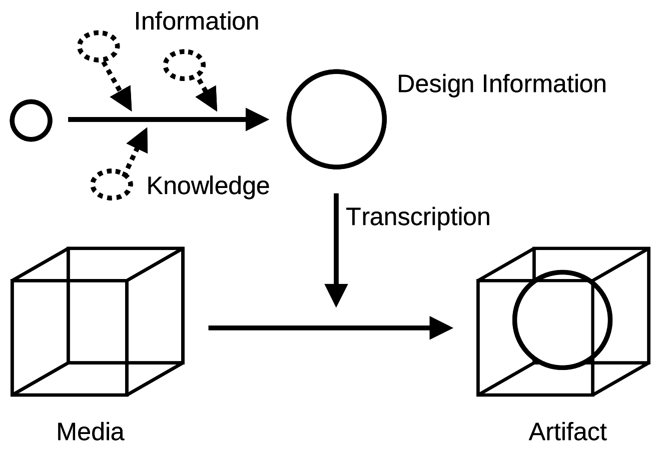

Figure 1: Artifact design process (Yoshida and Yashiro, 2007)

Design codes and specifications, such as mixture proportions and mixing procedures, make up the design information necessary to form concrete material artifacts. These design information are the accumulation of years of experimental work as well as field experience, and are the product of negotiation between actors in the concrete field as to the appropriate form of the concrete artifact being developed. When the final design information is agreed upon by the participating actors, then it becomes the governing design code to be utilized by concrete engineers in the field.

3.2 Sustainability

Sustainability was originally defined by the Brundtland Commission in a report for the United Nations on sustainable development and its political implications. In this report, sustainable development was described as practices which meet the needs of the present without compromising the needs of future generations to meet their needs (United Nations, 1987). This report established the precedent for sustainable development.

The American Society of Civil Engineers (ASCE) adopted an engineering-focused definition of sustainability in 1996, which stated that sustainable development should meet human needs while considering the environment and natural resources necessary for the future. Furthermore, the ASCE Code of Ethics was revised to contain language requiring engineers to follow sustainable practices (ASCE, 2006).

As mentioned earlier, population growth and urbanization are driving an increase in the need for concrete to construct the infrastructure necessary to meet society’s needs. Therefore the concrete industry is facing two opposing problems; it must meet increasing demand while reducing the industry’s environmental impact and resource consumption. The American

Concrete Institute (ACI) and the Portland Cement Association (PCA) organized the Concrete Summit on Sustainable Development in March 2007 in order to discuss these problems as well as develop a plan of action for the concrete industry. At this summit, opportunities for sustainable development were identified as energy consumption, generation of greenhouse gases, land use, resource consumption, dust and diesel emissions, and reduce/reuse/recycle applications. The committee understood that, while there are many areas in which concrete is not meeting sustainable practices, there are aspects of concrete construction which should be enhanced to increase the competitiveness of concrete as a construction material: fire and force protection, thermal mass, and durability (Bédard and Sordyl, 2007). A sustainable development framework was constructed to encompass and illustrate these discussions (Figure 2).

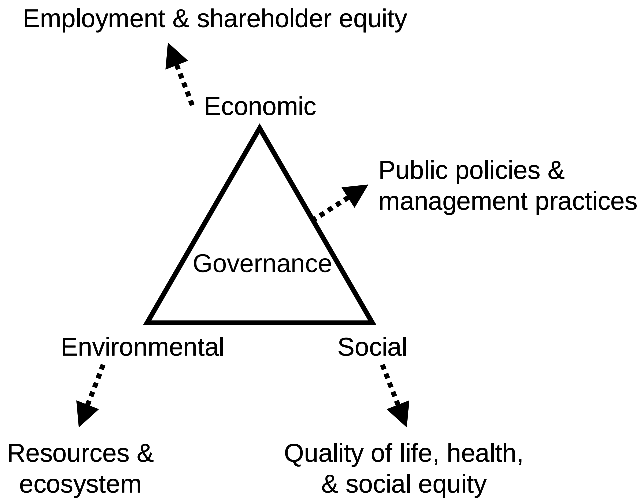

Figure 2: Sustainable development framework (Bédard and Sordyl, 2007)

As shown in Figure 2, the framework for building sustainable development in the concrete industry necessarily includes non-traditional engineering fields. In order to successfully implement this philosophy, concrete engineers must become heterogeneous engineers, reaching outside their traditional engineering field to mobilize the resources of other fields, to create networks which include not only engineers but citizens and government officials, sociologists and economists, researchers and industry professionals alike.

3.3 Integrating sustainability concepts

When building design information for the transformation of media into an artifact, engineers have traditionally included only engineering knowledge and information. However, as discussed in the previous section, concrete engineers should consider the integration of other fields' knowledge in order to enhance the development of innovations to meet the needs of sustainability, as illustrated in Figure 3.

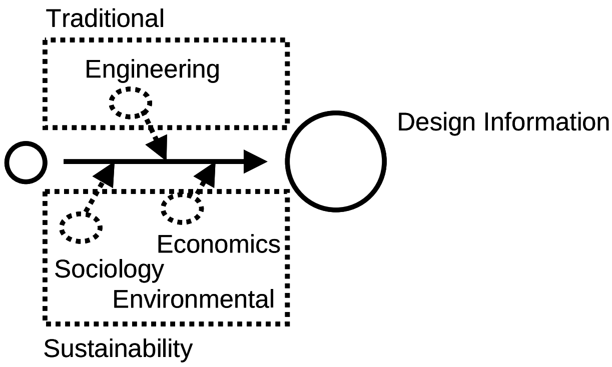

Figure 3: Integrating sustainable concepts into design information

Integrating the knowledge from other fields will necessarily require their input in the formation of design information. Concrete engineers will need to include these non-engineer participants as actors in concrete construction. By including the needs of these new participants, aspects of the artifact will change as the design information changes to reflect new knowledge and information. In some cases, the artifact itself may change; in some cases, the process for transforming media may change; finally, it's also possible that the form and process remain the same but the cost decreases. A combination of these is also possible.

4. CONCLUSIONS

The concrete industry faces change as sustainable development is adopted into the very ethics which civil engineers must practice by. This will necessarily result in the development of new innovations to meet these challenges while maintaining concrete as a competitive construction material. In order to promote sustainable practices, ACI proposed a framework whereby the considerations of other fields should be integrated into the concrete industry. This integration will require adding new actors to the networks which produce concrete technology.

The sociology of technology has proposed that heterogeneous engineering is necessary for successful technological innovation. By negotiating the development of technology amongst actors representing different technological perspectives, new artifacts may be formed based upon the needs of those participants. Sustainable concrete practices must, therefore, consider heterogeneous engineering as a means for integrating those actors from other fields.

REFERENCES

American Society of Civil Engineers, 2006. Code of Ethics. Retrieved 2008 June 5. http://www.asce.org/inside/codeofethics.cfm

Bédard, C., and Sordyl, D., 2007. Concrete summit on sustainable development. *ACI International July*, 54-58.

Latour, B., 2005. *Reassembling the Social*, Oxford Press.
Law, J., 1987. *Technology and heterogeneous engineering*. The Social Construction of Technological Systems, MIT Press.
MacKenzie, D., 1987. *Missile accuracy: a case study in the social pressures of technological change*. The Social Construction of Technological Systems, MIT Press.
Pinch, T., and Bijker, W., 1987. *The social construction of facts and artifacts*. The Social Construction of Technological Systems, MIT Press.
United Nations, 1987. *Report of the world commission on environment and development*. General Assembly Resolution 42/187, December.
Yoshida, S., and Yashiro, T., 2007. Study of the basic logic of diffusion using specific models. *PICMET'07 conference proceedings*, Portland, Oregon, USA.

A SIMPLIFIED 3D NUMERICAL SIMULATION FOR BANGKOK MRT SUBWAY TUNNEL

TRAN VIET DUNG and KYUNHG-HO PARK
School of Engineering and Technology
Asian Institute of Technology, Thailand
vietdungtran82@gmail.com

ABSTRACT

This study deals with the evaluation of measured longitudinal surface settlements obtained from the Blue Line subway project and the corresponding 3D numerical simulation for a single tunnel. The simplified numerical procedure, proposed by Mroueh and Shahrour (2008), is adapted with two main parameters: the partial stress release factor α_{dec} and the length of unlined zone L_{dec}. The effect of these parameters on the longitudinal surface settlements is investigated.

1. INTRODUCTION

Bangkok crams more than 10 million people into a rapidly growing area. Anyone, travelling through the city, braces for an ordeal of wasting hours in impenetrable traffic. Concern about Bangkok's increasing heavy traffic led to the implementation of the first phase of the Bangkok Blue Line Subway project which was completed and opened in 2004 (Figure 1). In this project, the tunneling construction was done mostly in soft ground, using EPB (Earth pressure balance) shield.

Numerical simulation of the tunneling requires complex aspects, such as the soil excavation, the overcut or annular space between the jacking pipe and the excavation, the application of the pressure, the install of definitive support constituted of lining rings and the grouting of annular space, non-linear behaviour of the soil and the lining, and the soil-structure interaction. In particular, in order to take into account of the boundary condition during the construction process (for example, overcut, injection of the annular void, installation of the definite tunnel support), two approaches have been used (Cheng et al., 2008): the forced controlled approach and the displacement controlled approach.

The displacement controlled approach simulates tunnelling by applying displacements to nodes around the tunnel (Sagaseta, 1987; Loganathan and Poulos, 1998; Park, 2004, 2005; Cheng et al., 2008), while the force controlled approach simulates tunnelling by removing nodal forces corresponding to the initial soil stress state. The forced controlled method predicts wider surface settlement trough accompanied with higher far field settlement than field or centrifuge test data (Simpson et al., 1979; Dasari, 1996: Leca, 1996: Stallebrass et al., 1996). Recently Mroueh and Shahrour (2008) proposed a simplified modelling technique by applying the convergence-confinement concept to 3D numerical simulation.

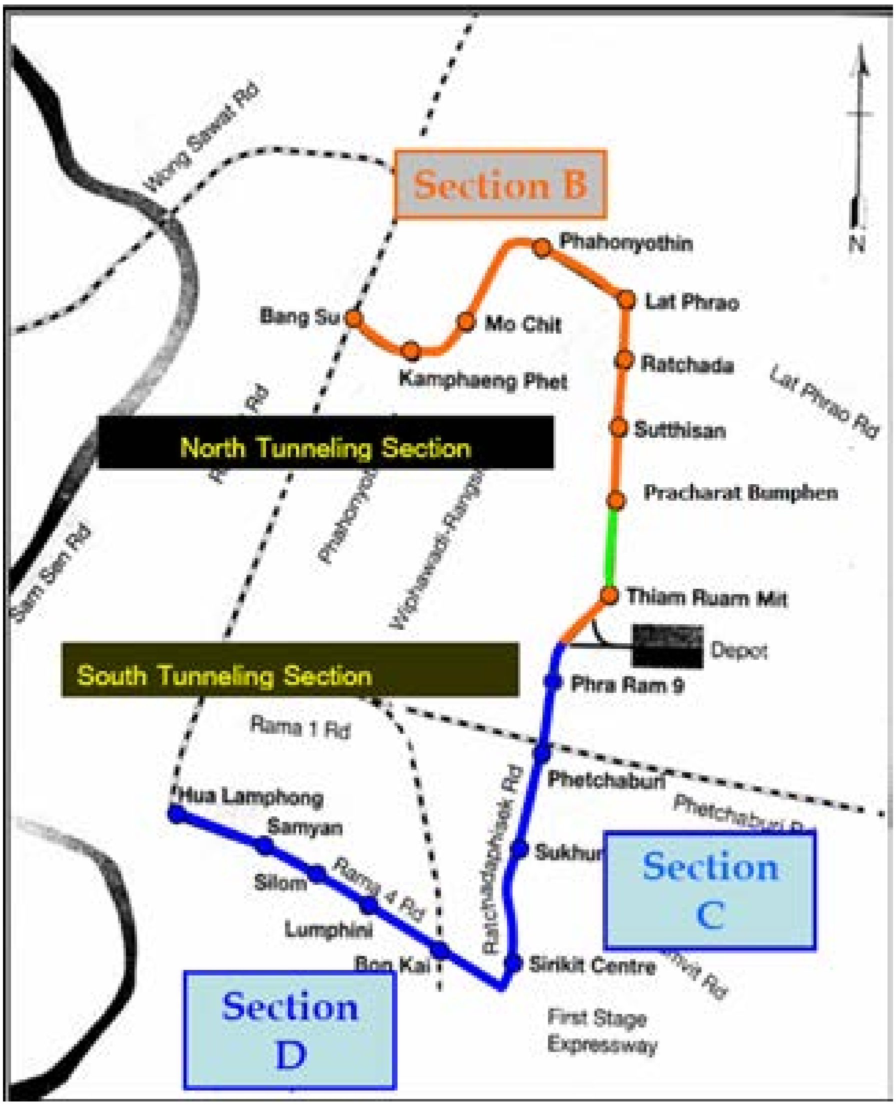

Figure 1: Route of the Bangkok MRT Blue Line Project

This study deals with the evaluation of measured longitudinal surface settlements obtained from the Blue Line subway project and the corresponding 3D numerical simulation for a single tunnel. The simplified 3D numerical procedure, proposed by Mroueh and Sharouh (2008), is adapted. In this model, there are two main parameters: the partial stress release α_{dec} and the length of unlined zone L_{dec}. The effect of those parameters on the surface settlements is investigated.

2. EVALUATION OF THE MEASURED SURFACE SETTLEMENT DATA

All of the measured surface settlement data are collected for the Zone 23, from Thiam Ruam Mit to Pracharar Bumphen. The location and ground conditions are shown in Figures 2 and 3, respectively. Three different types of surface settlement makers were installed approximately at 50 m interval along the tunnel alignment. The primary object of the measurements with settlement makers is to measure the maximum surface settlements above the centreline. In addition, the reading was taken over time covering a period before shield approaching and after shield passing. The surface settlement data of total 25 points are collected. Among those, the data of only 11 points are selected for the further study to avoid the possible measurement error from other points.

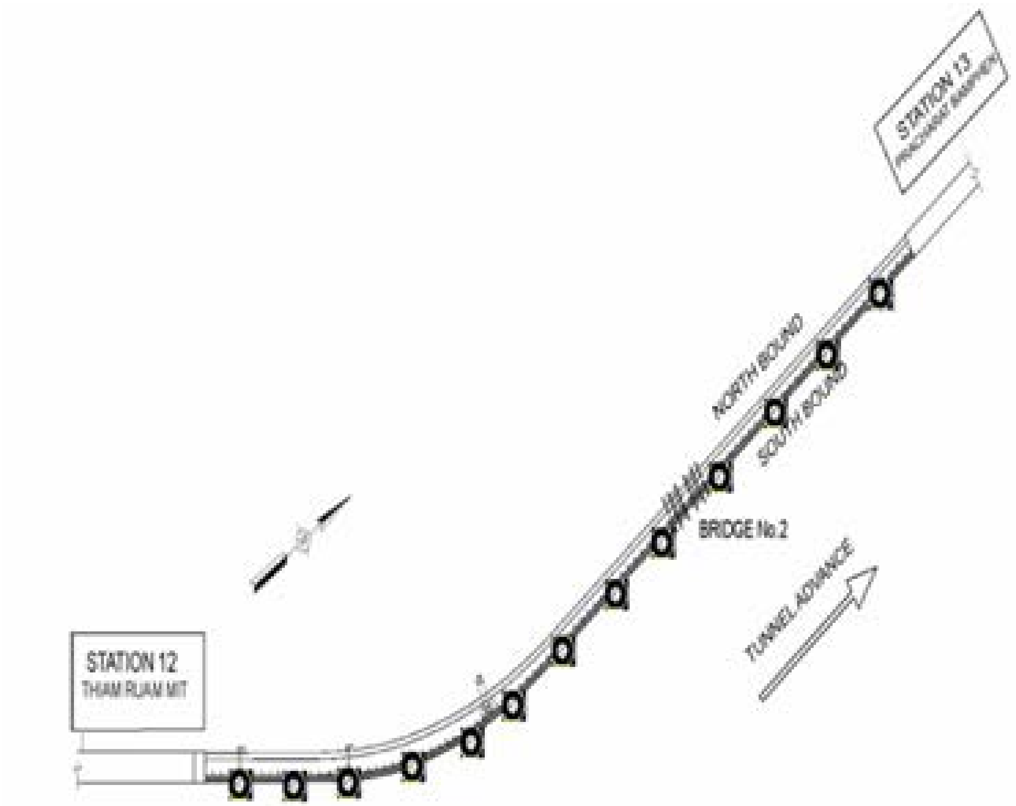

Figure 2: Location of ground settlement makers

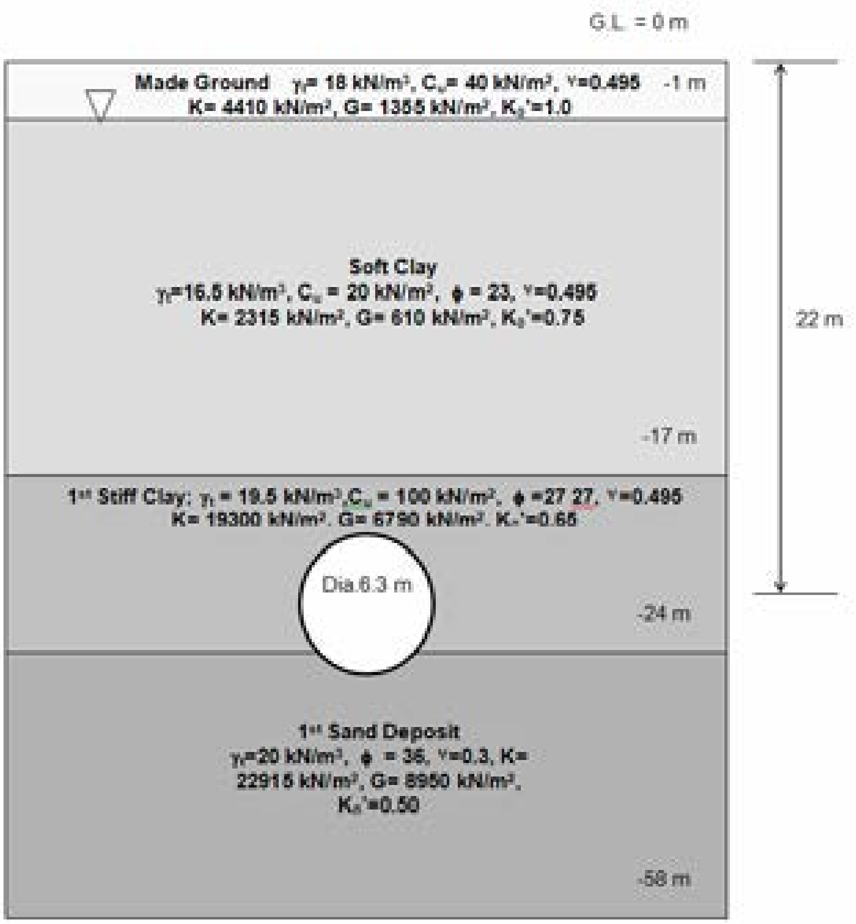

Figure 3: Typical soil profile for Zone 23

Figure 4 and Figure 5 show the summary of the surface settlement measurements by Type 2 and Type 3, respectively. From Figures 4 and 5, it can be seen that the maximum surface settlement varied from 14 mm to 33 mm. The longitudinal surface settlement mostly occurred between 40 m (≈ 7D) to – 40 m (≈ 7D) and can be divided into three zones: Zone 1, about 30 m distance, the ground begins to deform but the shield not reached; Zone 2, about 15 m distance, starts from the distance in front of the shied face and develops significantly during the shield passing; Zone 3 begins after the performance of the tail void grouting. The surface settlement at the tunnel face (w_a), w_a = 4 ~ 16 mm, the surface settlement induced in the unlined zone (w_b), w_b= 2 ~ 6 mm and the surface settlement due to complete released stress of the confinement (w_c), w_c = 8 ~ 22 mm.

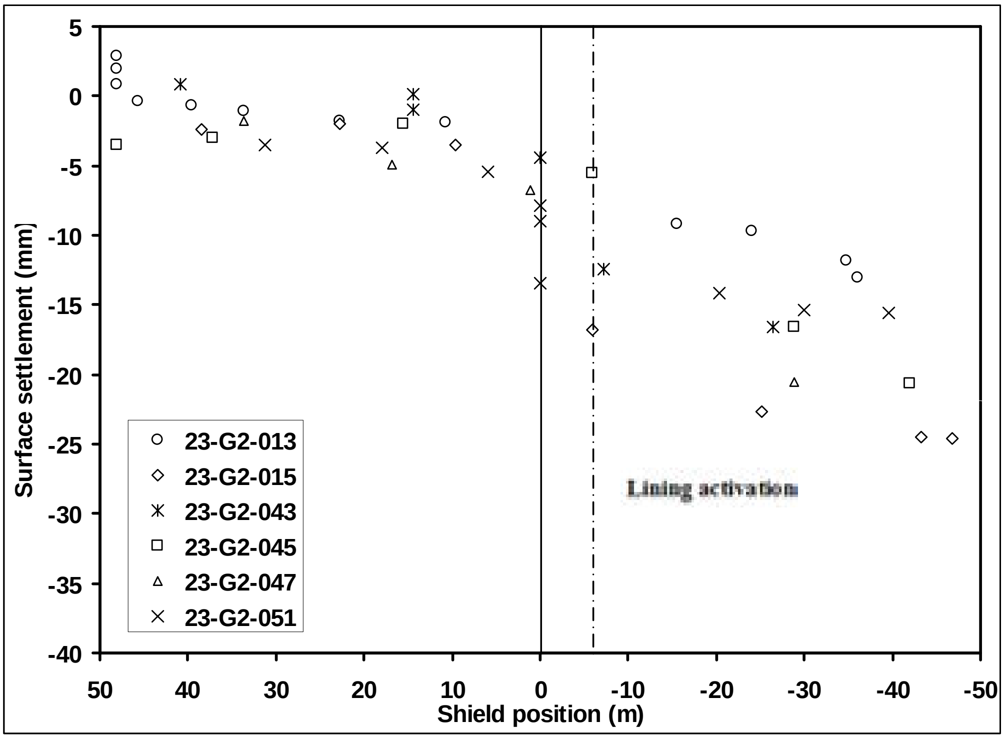

Figure 4: Measured surface settlement (Type 2)

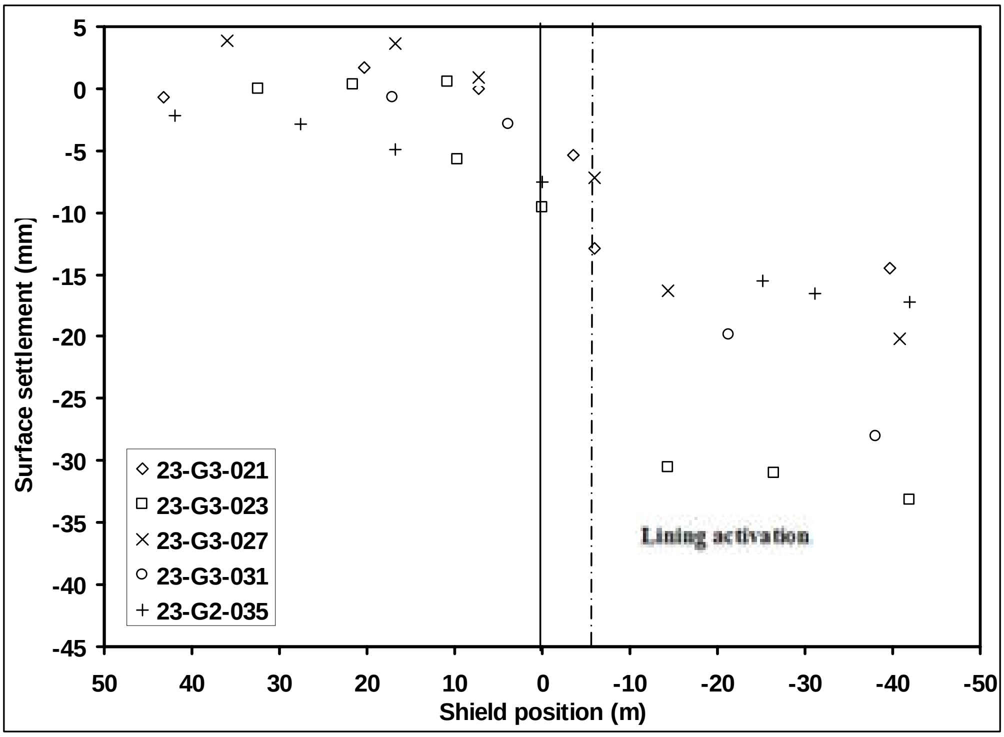

Figure 5: Measured surface settlement (Type 3)

3. 3D NUMERICAL SIMULATION

Numerical simulation has been conducted using the commercial finite different code FLAC^{3D}. Figure 6 shows the modelling mesh with 44800 zones and 49245 grid-points, assuming symmetric loading conditions. The left right boundaries are hinged to prevent the movement in horizontal direction but are free to allow vertical direction. The width of the left through the right boundaries is set to prevent boundaries effect on the perimeter of the tunnel. At the bottom, the boundary is fixed against vertical movement. Although, using EPB shield, the face pressure is varied and dependent on the ground condition, the average value of 150 kN/m^2 is used in this study.

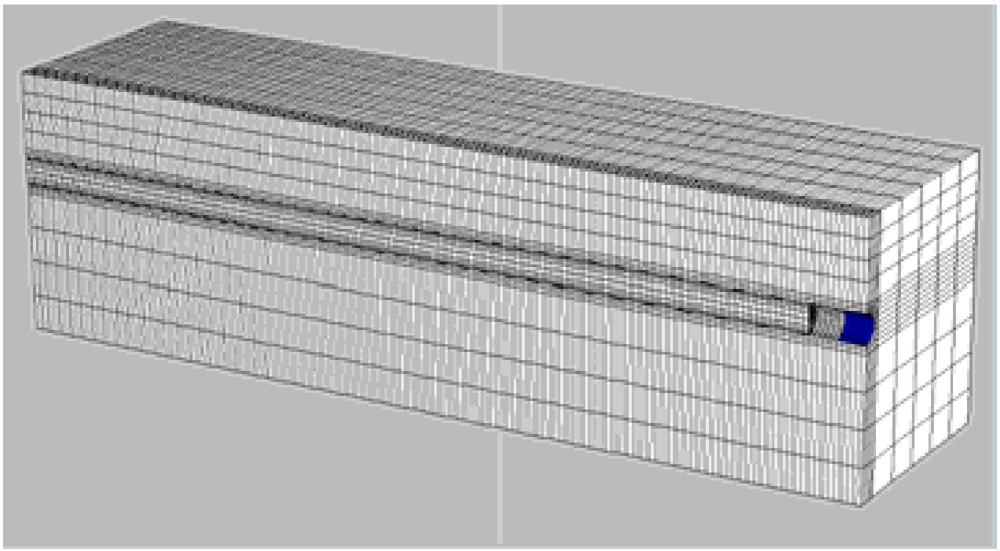

Figure 6: Modelling mesh

The constitute law used for the soil element is the elasto-plastic associated Mohr-Coulomb model. The material parameters of soil and lining are given in Figure 3.

Excavation and the shield advance are simulated through the step by step procedure as follows:

In the first step of excavation, (a) remove the ring of soil element equal to 7 m ahead of the shield (6m for length of the shield and the length of the unlined zone and 1 m for the supported zone where the lining will be installed), (b) release stress around the tunnel, (c) grout the removed area, (d) install lining 1 m at the end of the excavated and measure the displacement at the tunnel boundary and at the surface, (e) back fill material and apply face pressure to prepare for the next excavation.

In the step of tunnel face advance, (a) remove the ring of soil element ahead of the tunnel face, (b) release the stress using α_{dec} and L_{dec}, (c) grout the removed area, (d) activate the lining element in removed are with the length of L_{lin} and take the measurement for the element displacement, (e) apply the pressure at the tunnel face. Then repeat from (a) to (e).

4. RESULTS

4.1 Influence of α_{dec}

The parameter α_{dec} stands for the stress release before the lining installation. Figure 7 shows the numerical results of the longitudinal surface settlement using α_{dec} = 0.2, 0.5 and 0.7, together with the measured one. L_{dec} = 6 m is used. It shows that the parameter α_{dec} highly affects the maximum surface settlement. As α_{dec} increases, the maximum surface settlement increases. The measured surface settlements can be ranged within α_{dec} = 0.2 ~ 0.7.

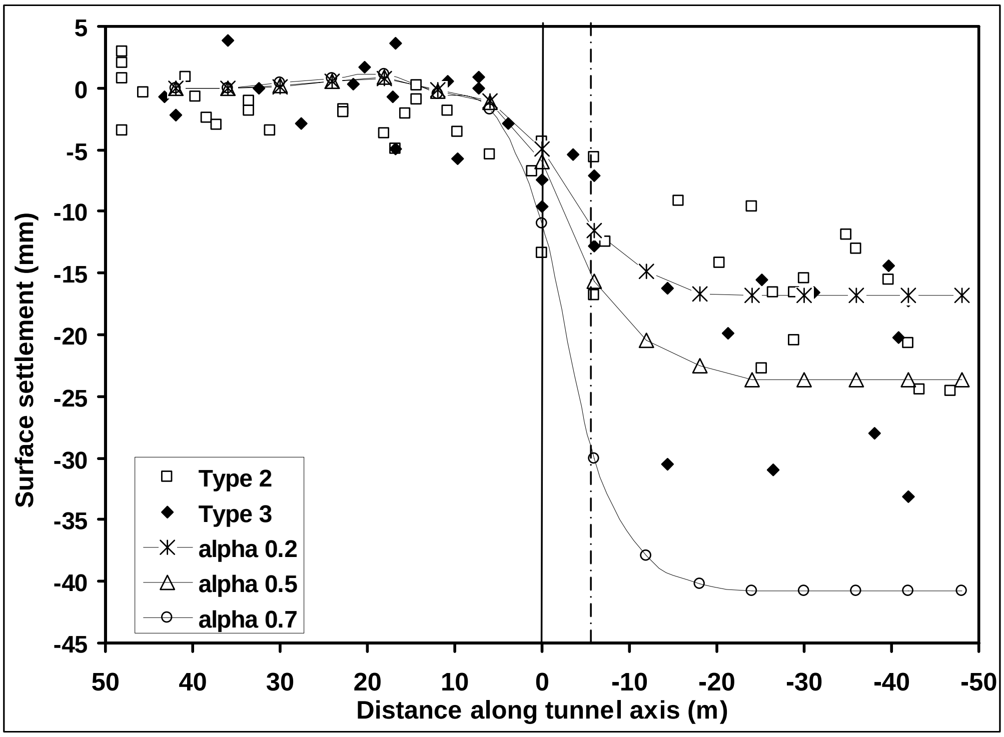

Figure 7: Effect of α_{dec} (longitudinal direction)

4.2 Influence of L_{dec}

The parameter L_{dec} stands for the length of the unlined area of the tunnel. Figure 8 shows the numerical results of longitudinal surface settlements using L_{dec} = 6 m and 10 m, together with the measured one. α_{dec} = 0.2 is used. It shows that the parameter L_{dec} affects slightly. As L_{dec} increases, the maximum surface settlement slightly increases. As suggested by Mroueh and Sharour (2008), the parameter can be fixed to L_{dec} = 1D.

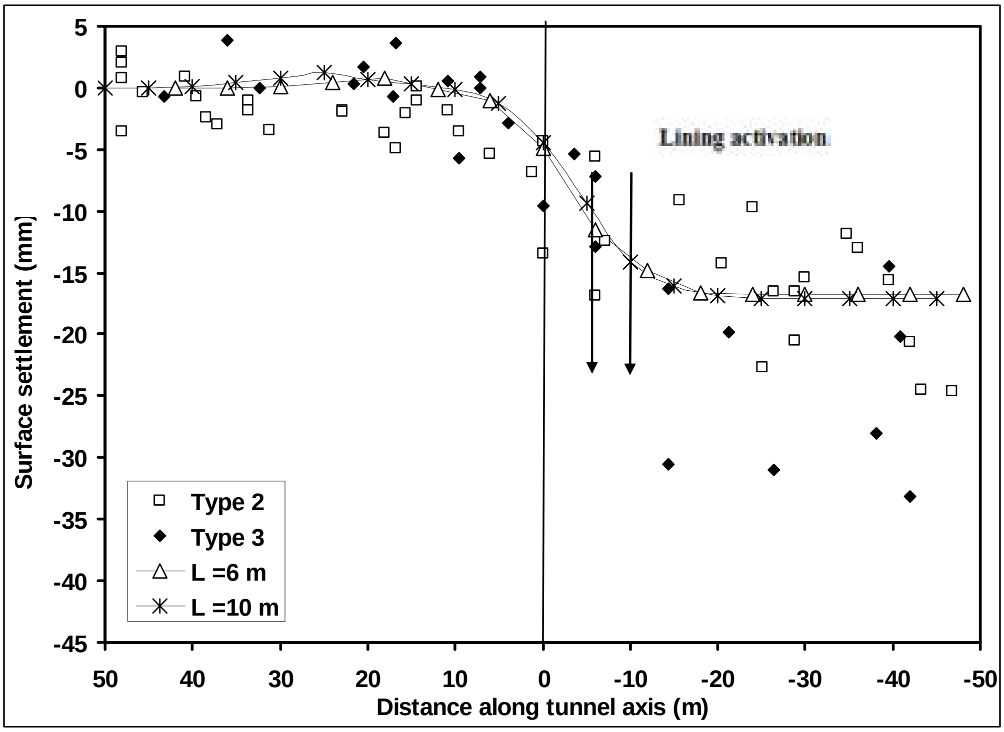

Figure 8: Effect of L_{de}

5. CONCLUSION

Measured longitudinal surface settlements, obtained from the Blue Line subway project, have been evaluated and the corresponding 3D numerical simulation for a single tunnel has been performed. The effect of the model parameters was investigated. The following conclusions can be drawn:

1. The maximum surface settlements varied from 14 mm to 33 mm: $w_a = 4 \sim 16$ mm, $w_b = 2 \sim 6$ mm and $w_c = 8 \sim 22$ mm.
2. The longitudinal surface settlement mostly occurred between 40 m (≈ 7D) to – 40 m (≈ 7D) and can be divided into three zones
3. The parameter α_{dec} highly affects the maximum surface settlement. As α_{dec} increases, the maximum surface settlement increases. The measured surface settlements can be ranged within $\alpha_{dec} = 0.2 \sim 0.7$.
4. The parameter L_{dec} affects slightly, the parameter can be fixed to L_{dec} = 1D.

REFERENCES

Cheng, C.Y., Dasari, G.R., Chow, Y.K., Lueng, C.F., 2008. Finite element analysis of tunnel-soil-pile interaction using displacement controlled model. *Tunnelling and Underground Space Technology*, 22, 450-466.

Dasari, G.R., Rawlings, C.G., Bolton, M.D., 1996. Numerical modeling of a NATM tunnel construction in London Clay. *Proceedings of*

International Symposium on Geotechnical Aspects of Underground Construction in Soft Ground, Balkema, London, 491–496.

Flac^{3D} Fast Lagrangian analysis of continua in 3 Dimension version 2.0, 1997.

Leca, E., 1996. Modelling and prediction for bored tunnels. *Proceedings of International Symposium on Geotechnical Aspects of Underground Construction in Soft Ground*, Balkema, London, 27–42.

Longanathan, N., Poulos, H.G., 1998. Analitical prediction for tunneling induced ground movement in clay. *Journal of Geotechnical and Geoenviromental Engineering*, 124(9), 846-856.

Mroueh, H., Shahrour, I., 2008. A simplified 3D model for tunnel construction using tunnel boring machine. *Tunnelling and Underground Space Technology*, 23, 38-45.

Park, K.H., 2005. Analytical solution for tunnelling-induced ground movement in clays. *Tunnelling and Underground Space Technology*, 20(3), 249-261.

Park, K.H., 2004. Elastic solution for tunnelling-induced ground movement in clays. *International Journal of Geomechanics ASCE*, 4(4), 310-318.

Sagaseta, C., 1987. Analytical of undrained soil deformations due to ground loss. *Geotechnique*, 37(3), 301-320.

Simpson, N.J., O'Riordon, Croft, D.D., 1979. A computer model for the analysis of ground movements in London clay. *Geotechnique*, 29(2), 149–175.

Stallebrass, S.E., Grant, R.J., Taylor, R.N., 1996. A finite element study of ground movements measured in centrifuge model tests of tunnels. *Proceedings of International Symposium on Geotechnical Aspects of Underground Construction in Soft Ground*, Balkema, London, 595–600.

SEISMIC BEHAVIOR OF PRECAST HYBRID MOMENT RESISTING FRAMES

EKKACHAI YOOPRASERTCHAI,
PENNUNG WARNITCHAI and MATRIN SUTHASIT
School of Engineering and Technology
Asian Institute of Technology, Thailand
st106327@ait.ac.th
pennung@ait.ac.th
st106326@ait.ac.th

ABSTRACT

It is the first challenge to introduce the construction of an innovative structural system, Precast Hybrid Moment Resisting Frames (PHMRF), in Thailand. Under a project initiated by National Housing Authority of Thailand (NHA), a relatively large amount of typical 5-story residential buildings will be constructed in the moderate seismic risk zone. Because of the requirements for rapid construction of low-cost, seismic resistant, mid-rise residential buildings, PHMRF was chosen as the structural system. This structural system is consisted of precast concrete beam and precast concrete column assembled together using a combination of post-tensioning tendons and mild steels.

To comprehensive understand the behavior of hybrid systems, two 2/3-scale model interior and exterior beam-column joints representing the 5-story residential buildings were tested under quasi-static reversed cyclic loads. The capacity design concept was used to design the hybrid connections as well as the precast members to limit the inelastic behavior in the beam to column interfaces. Test results demonstrate that the hybrid connections can dissipate a lot of energy with low or zero strength degradation up to story drift of 6.00%. In addition, the specimens demonstrated the self-centering behavior. The damage was limited to the grout interface. Only minor cracks could be observed in the beams and columns.

1. INTRODUCTION

The boom of the use of precast concrete structures in many countries requires innovative deliberation since many regions are located in the seismic hazard areas. There are many evidences demonstrated that the precast concrete buildings are vulnerable to the effects of earthquake loading, especially in the connections. Consequently, the challenge is to discover economical and practical ways to assemble the precast elements together to have sufficient strength and ductility. Normally, precast concrete seismic structures can be divided into two systems. The first system is emulation of monolithic reinforced concrete construction. Another system is jointed precast. In the first approach, typically referred to as "emulation" of cast in place concrete, precast elements are jointed by using wet connection. Many solutions have been studied and developed for beam-column connections. The connection can either be located within the beam-column joint or in the middle of a structural member. In this approach, the joint must have adequate strength and stiffness as the cast in place concrete. To achieve this target, the joint planes and the protruding bars must be detailed in proper ways. The reinforcing bars between the precast concrete elements may be connected together by using the mechanical couplers or grout ducts and filled later by cast in place concrete or pressure grout.

This paper studies the seismic performance of jointed precast concrete moment resisting frames by experimental program. The beams illustrated here rock about their columns and self-center upon unloading which developed by Priestley and Tao (1993) and Stone et al. (1995) as a part of the *PREcast Seismic Structural Systems (PRESSS) Research Program*. These beams and columns are assembled to form moment resisting frames by using the combination of unbonded post-tensioning tendons to provide flexural strength and self-centering with mild steel for inelastic energy dissipation. The plane of significantly reduced stiffness and strength would be limited at the interface between adjacent precast concrete elements.

2. DESCRIPTION OF PRECAST HYBRID BEAM-COLUMN CONNECTIONS

The unbonded post-tensioning tendons are placed at the center of the beams where the elastic strain in the tendons minimize, thus, the self-centering can be achieved. In order to get the maximum energy dissipation, mild steels are placed near the top and bottom of the beams. However, the maximum nonlinear strains in the bars would be concentrated on the interface between precast concrete beams and columns when the gaps are opened. This effect make the bars fracture in the seismic event. To delay bar fracturing during the deformations of the bars in tension, bond between the mild steels and the grout cement should be prevent over a predetermined length at the ends of the beams by wrapping the bars with flexible ducts. In addition, high compressive stress occurs in the opposite side. Presence of steel angle at the beam corners could confine and prevent the spalling of the concrete in this zone (Figure 1).

3. DESCRIPTION OF PROTOTYPE BUILDINGS

The 5-story residential building was designed to resist possible earthquake loads in Thailand. The typical span and story height are 3000 mm and 2800 mm respectively. Seismic zone 2A according to UBC1997 comparable to required seismic zone in North of Thailand was selected as seismic loading in elastic 2-D model. The computer model was constructed and analyzed by using SAP2000 program. The capacity design concept was used to design beam and column sections. The inelastic zone would be expected to limit at the interface between beam and column. The design procedure is out of scope of this paper. The design detailing of the buildings is described elsewhere in Warnitchai et al. (2008). Since the floor span in longitudinal direction of the building has uniform length, the interior and exterior beam-column joints at the second floor were selected to construct the physical model and test in laboratory.

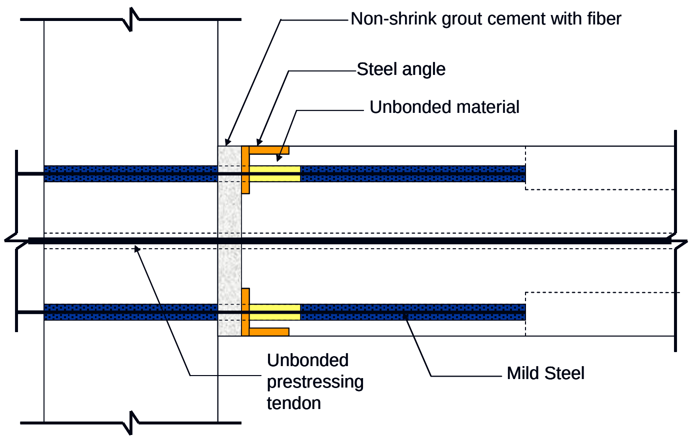

Figure 1: Configuration of precast hybrid beam-column connection

4. EXPERIMENTAL PROGRAM

The seismic performance of precast hybrid beam-column connection was carried out through the experiment. The two-third scaled sub-assemblage elements were constructed and tested in the laboratory under quasi-static cyclic loading test. Both interior and exterior hybrid joints were investigated.

4.1 Test specimens

4.1.1 Interior beam-column connection specimen

The typical dimension and reinforcing bar details of precast beam and precast column are shown in Figure 2. Beam section is 170×270 mm and column section is 320×320 mm. Circular corrugated ducts of 25 mm diameter were preformed on the required positions at beam and column. Two deform bars of 10 mm diameter were used to pass through between beam and column. The unbonded length of 60 mm was applied on the inserted bars at the beam surface. Two post-tensioning strands with 12.7 mm diameter were inserted passing two PVC ducts placed at the center of beams. PVC ducts were not grout in order to simulate the unbonded situation. The stressing force after losses was approximately 0.45f_{pu} where f_{pu} is ultimate stress of the tendon. Axial force in column, approximately $0.10f_c^{'}A_g$ where $f_c^{'}$ is ultimate compressive strength in the column and A_g is the total cross section area, was simulated by using two 15.4 mm post-tensioning tendons. Steel angles, 75 mm width, 75 mm depth, 6 mm thickness, were provided at beam faces to confine the concrete at the beam ends. It could prevent the crushing and spalling of concrete at precast beams, since high compressive stress occurs in this area. The fiber grout cement was poured in the beam-column interfaces to make the integrity of the structures. The fibers are benefit to reduce the spalling of the grout pad.

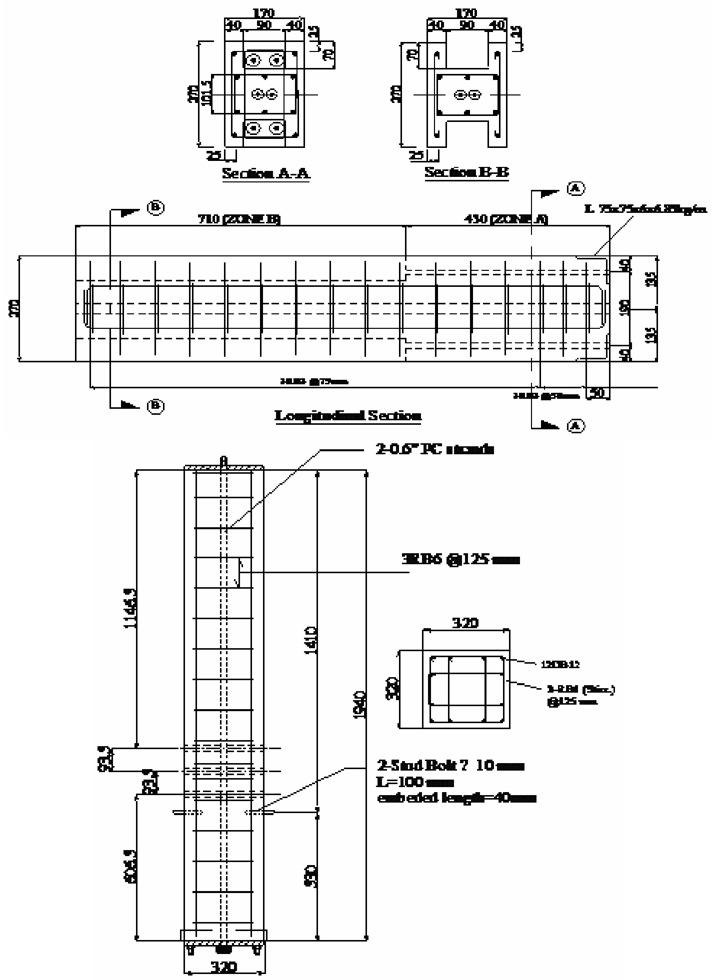

Figure 2: Detailing of the test specimens.

4.1.2 Exterior beam-column joint specimen

Exterior beam-column subassemblage was tested in order to deeply understand seismic behavior and performance of the hybrid connection. In addition, it was to ensure that the hybrid connection can maintain seismic performance and behavior even in exterior joint. This specimen has the details and dimensions of precast beams and column as same as interior beam-column joint specimen, except for only one precast beam installed. Besides, the anchorages were embedded in the beam-column joint to simulate the actual construction. In general, the anchorage must be provided at the exterior joint to grip the post-tensioning steels. Moreover, to prevent the bursting cracking in the column during stressing the post-tensioning tendons, the spiral transverse reinforcement bars were applied in the column to confine the concrete in that region.

4.2 Experimental setup

All specimens were tested under quasi-static loading. Lateral load was applied at the top of the precast concrete column by a MTS servo-hydraulic actuator with capacity of ±500 kN. Figure 3 and Figure 4 show the schematic of the experimental setup for interior and exterior beam-column connection respectively. The bottom support of the precast concrete column is hinge connection, and the top of precast concrete columns is designed to move freely. The beam supports is designed to be the roller connection to force the precast concrete beam moving in horizontal direction only. Hence, the inflection point of the beam-column subassemblies could be achieved in this test setup.

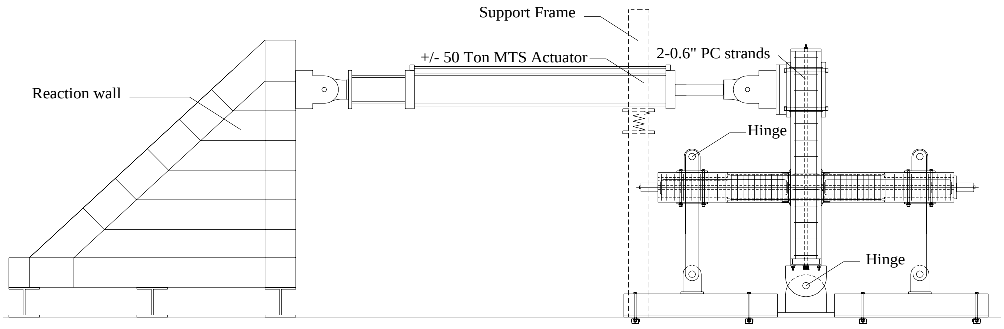

Figure 3: Experimental setup for interior joint.

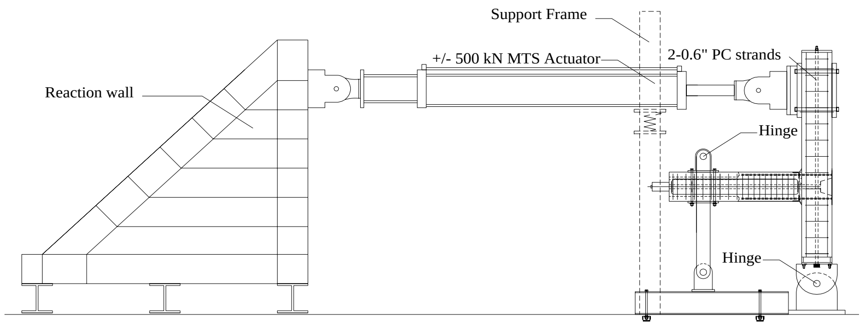

Figure 4: Experimental setup for exterior joint.

4.3 Instrumentation

The instrumentation consisted of 1) horizontal force measurement and horizontal displacement, 2) flexural rotation in beam and column, 3) shear deformation in beam, column and joint, 4) gap at the interface between joint face and beam and 5) strains of inserted mild steel.

4.4 Loading history

The load applied slowly to the specimen was lateral cyclic displacement-controlled. The column was pushed and pulled with gradually increasing story drifts of ±0.25%, ±0.50%, …, and ±6.00% as shown in

Figure 5. At each drift level, the displacement was repeated three times to check the degradation of strength and stiffness as well as to examine the energy dissipation.

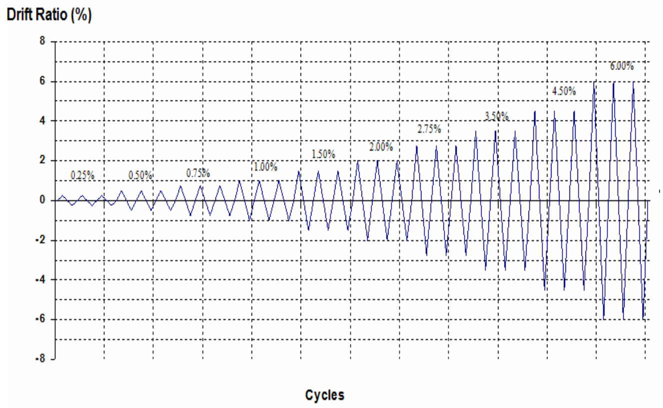

Figure 5: Cyclic loading history.

5. EXPERIMENTAL RESULTS

The hysteretic loops of both specimens were plotted in range of story drift from 0.25% to 6.00% as shown in Figure 6 and Figure 7, respectively. Based on experimental results, they showed good stiffness in elastic range, and low stiffness degradation in high story drift levels. The hysteretic loops also showed the stable behavior of measured peak lateral forces. The measured peak lateral forces considerably increased in range of story drift 0.25% to 1.50%. After that, the peak lateral force slightly increased from the 1.50% story drift level to the 6.00% story drift. Low-level degradation of the peak lateral forces was observed. At the end of the test, as expected, the test specimen demonstrated that primary deformation and severe damage took place at the grout pad between beam-column interfaces. There were only small cracks observed. These cracks were invisible upon unloading due to axial forces contributed by unbonded post-tensioning tendons. The beam-column interfaces also experienced large opening at the high story drift levels. However, when the frame returned to the initial position or zero story drift level, the gaps were returned to the original condition. The various key parameters are concluded in Table 1.

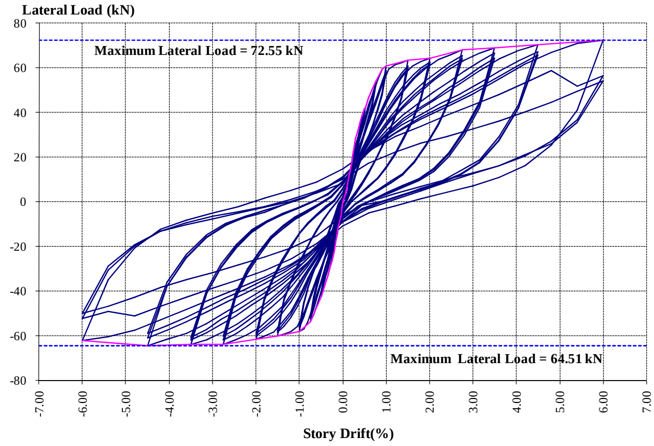

Figure 6: Hysteretic responses of interior joint.

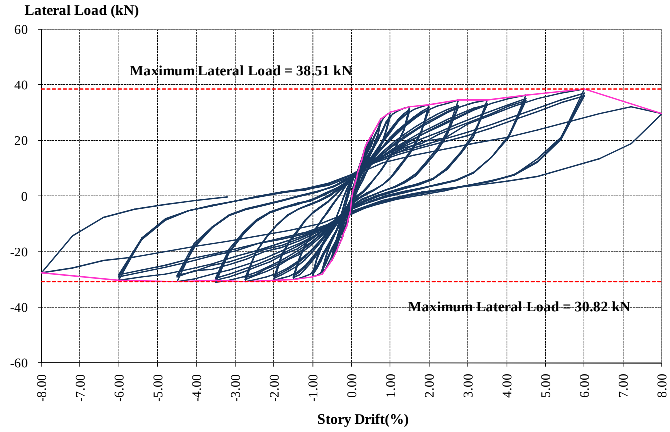

Figure 7: Hysteretic responses of exterior joint.

Table 1: Test results of key parameter at various story drifts.

Description	**Interior beam-column joint**	**Exterior beam-column joint**
Elastic	±0.75%	±0.75%
Yielding of special reinforcement	±1.50%	±1.00%
Elastic Stiffness	4,975 kN/m	2,335 kN/m
Maximum strength (push direction)	72.55 kN (+4.50%)	38.51 kN (+6.00%)
Maximum strength (pull direction)	64.51 kN (-4.50%)	30.82 kN (-6.00%)
Strength ratio between 3rd cycle and 1st cycle at drift of 3.50%	0.93	0.96
Energy dissipation ratio at drift of 3.50%	0.236	0.254

6. CONCLUSION

In this study, the precast concrete ductile joints are reviewed. The experiment was conducted to get comprehensive understanding of the precast hybrid frames. The two 2/3-scale model precast hybrid beam-column connections were tested under the quasi-static cyclic loading test. Based on the test results, the following conclusion and observation can be made.

1. The post-tensioning tendons were used to connect the precast members and mild steel used as energy dissipators. The tendons provide not only the cramping forces to resist the vertical load at beam-column interfaces, also the self-centering force to bring the structure back to the original position.

2. As expected, the short unbonded length between mild steel and concrete can prevent fracturing and reduce cracking of the concrete.

3. The hybrid system can be designed to have the same flexural strength as a cast in place concrete system with members of the same size.

4. The specimens have shown a very large drift capacity. Both can be tested up to the story drift of ±6.00% with slightly damage observed. The strength degradation of the specimens is also very low.

5. Most of the damage was limited to the beam-column interfaces. In this area, the inelastic characteristics were provided by the opening of the gaps and yielding of the mild steel.

6. The hybrid connection has been shown to be a superior candidate for precast concrete frames constructed in seismic hazard zones.

ACKNOWLEDGEMENTS

This research work was funded by the National Housing Authority of Thailand. We wish to express our sincere appreciation to the organization for providing the opportunity to undertake this research work.

REFERENCES

Priestley, M. J. N., and Tao, J. R., 1993. Seismic Response of Precast Prestressed Concrete Frames with Partially Debonded Tendons. *PCI Journal*, V.38 No.1, January-February, pp. 58-69.

Stone, W., Cheok, G., and Stanton, J., 1995. Performance of Hybrid Moment-Resisting Precast Beam-Column Concrete Connections Subjected to Cyclic Loading. *ACI Structural Journal*, V.91, No. 2, March-April, pp. 229-249.

Warnitchai, P., Matupayont, S., Pimanmas, A., Yooprasertchai, E. and Suthasit M., 2008. Development of Precast Concrete Frame Buildings for Seismic Regions. *Research Report submitted to NHA of Thailand (in Thai)*.

LABORATORY STIFFNESS MEASUREMENTS ON TOYOURA SAND

HIROAKI EBIZUKA[1], RUTA IRENG WICAKSONO[2]
and REIKO KUWANO[3]
[1-2]Department of Civil Engineering, The University of Tokyo, Japan
[3]International Centre for Urban Safety Engineering,
Institute of Industrial Science, The University of Tokyo, Japan
ebizuka@iis.u-tokyo.ac.jp
ruta@iis.u-tokyo.ac.jp
kuwano@iis.u-tokyo.ac.jp

ABSTRACT

A triaxial test apparatus combined with two independent wave measurement methods, i.e. Trigger Accelerometer and Bender Element, was employed. A series of tests was conducted to the specimens of Toyoura sand. Analyses were performed on the test results to obtain statically and dynamically measured moduli. The values of shear modulus resulted from static measurement, Trigger Accelerometer, and Bender Element methods were compared at different isotropic stress levels. The effects of specimen size on static and dynamic measurements were studied.

1. INTRODUCTION

In the past, dynamic measurements regarding wave velocity analysis, based on the cross-hole and down-hole methods, have been used for a long time in real construction sites (Stokoe & Hoar, 1978). Recently measurement of wave velocities in the laboratory has also become popular, and researchers have recognized that “dynamic” and “static” properties are no more different from each other except for the strain levels (Woods, 1991). Precise static small strain measurements in the laboratory tests have bridged the gap of strain levels between “dynamic” and “static” behavior (Tatsuoka and Shibuya, 1992). However, following the pioneer work by Tanaka et al. (2000), AnhDan and Koseki (2002) found that the difference on dynamic and static properties is not only caused by strain level but also by some other factors like grain size and wave length.

Among many laboratory tests with dynamic measurements based on elastic wave propagation, this study focused on two independent wave measurement methods in a series of triaxial tests, i.e. Trigger-Accelerometer (TA) method and Bender Element (BE).

2. MATERIAL, APPARATUS, AND TEST PROCEDURES

Air-dried Toyoura sand (Gs=2.635, e_{max}=0.966, e_{min}=0.600, D_{50}=0.20 mm) was used as the test material. The material particles were pluviated through air to prepare cylindrical specimens. As the initial condition, the specimens were consolidated with a confining stress (σ_c') of 25 kPa in the air-pressured cell. Seven tests of specimens having different dry densities (ρ) were performed as presented in Table 1.

Table 1: List of the tested specimens

Test No.	Material	Dry density, ρ_d (gram/cm^3)	Specimen Size [dia. (cm); height (cm)]
T1	Toyoura sand	1.458	5 ; 10
T2	Toyoura sand	1.590	5 ; 10
T3	Toyoura sand	1.533	5 ; 10
T4	Toyoura sand	1.595	5 ; 10
T5	Toyoura sand	1.597	5 ; 10
T6	Toyoura sand	1.602	5 ; 10
T7	Toyoura sand	1.604	5 ; 10

The triaxial test apparatus was used for this study. To evaluate dynamic measurement based on elastic wave propagation, two independent wave measurement methods were employed, i.e. Trigger Accelerometer (TA) and Bender Element (BE). Triggers and accelerometers were combined to observe the wave propagation through the specimens using P and S waves (AnhDan et al. 2002). On the other hand, only S wave was employed during dynamic measurement with BE. Photo and schematic figure of Trigger Accelerometer (TA) and Bender Element (BE) methods are presented in Figure 1.

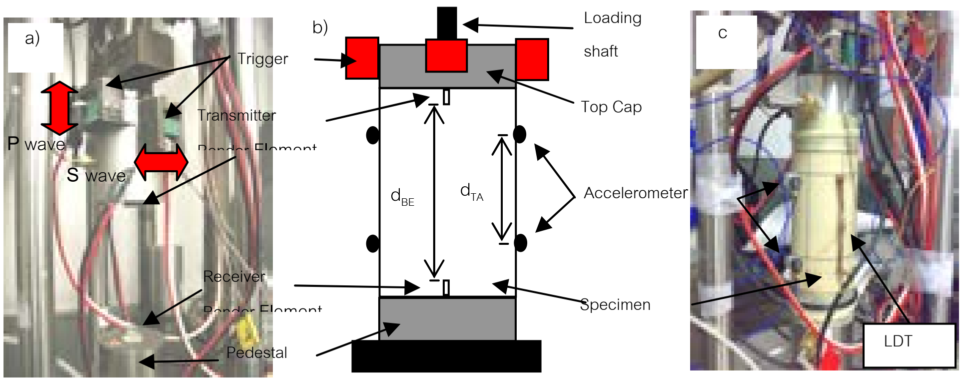

Figure 1: Specimen, Trigger Accelerometer, and Bender Element

Starting from a confining stress (σ_c') of 25 kPa, the isotropic stress levels were increased to 50 kPa, 100 kPa, 200 kPa, and 400 kPa. At each stress level, after a 10 minute stage with constant stress state, 11 cycles of vertical loading with a single axial strain amplitude of about 0.002% measured by Local Deformation Transducer, LDT (Figure.1c), were carried out as a static measurement of soil stiffness. During the cyclic loading stage, the vertical stress was unloaded first then reloaded to the original stress level under drained condition. After completing the cyclic loading, another stage with constant stress state was maintained while conducting the dynamic measurement using TA and BE methods.

3. PROCEDURES FOR ANALYZING TEST RESULT

In order to evaluate quasi-elastic stiffness modulus based on static measurement, data of the fifth and the tenth cycles among 11 cyclic loading were analyzed. A typical result is shown in Figure 2, where increments of the vertical strain and stress were detected with LDTs and the load cell, respectively. The stress-strain relationship was fitted by a straight line and the quasi elastic vertical Young's modulus (E_s) was evaluated from the slope of the line.

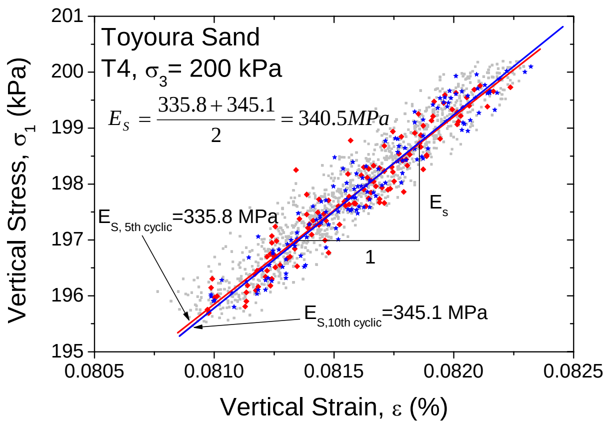

Figure 2: Analyzing Young's Modulus resulted from cyclic loading

In the dynamic measurement analysis, a wave velocity (V) was evaluated using equation (1), as follows:

$$V = \frac{d}{t} \tag{1}$$

where d is the effective distance between two sensors/transducers as shown in Figure 1b, where d_{TA} and d_{BE} are the effective distance between 2 accelerometers and 2 bender elements, respectively. Meanwhile, t is the travel time (i.e. the time difference between input and output waves). In this study, input wave is the wave which is captured by upper accelerometer (Figure 1b) or is recorded by transmitter BE. Output wave is the wave which is captured by lower accelerometer (Figure 1b) or receiver BE.

In wave velocity evaluation, the determination of travel-time plays an important role, considering the fact that it often depends on subjective interpretation of each researcher. In this study, to avoid the uncertainties and the unreliable wave forms while computing wave velocity, the travel-time values were evaluated with sinusoidal excitation and rising-to-rising technique in both the TA and the BE methods. As shown in Figure 3 as a typical definition used in TA and BE methods, the rising-to-rising travel time is defined as a distance at time-history-axis from a point obtained after applying a zero-crossing line at the first input-signal to a point obtained after applying zero-crossing line at the first output-signal. The zero-crossing line is applied to correct for the near field effect.

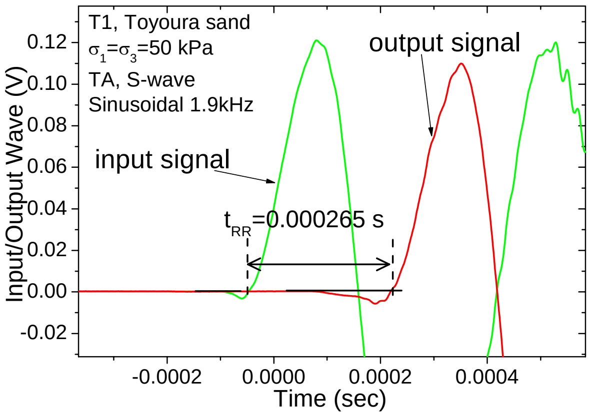

Figure 3: Definition and Evaluation of travel time

By knowing density of the specimen (ρ), the soil stiffness can be obtained. Since Primary (P) and Secondary (S) waves are employed, both dynamic Young's modulus (E_D) under unconstrained condition and dynamic shear modulus (G_D) can be evaluated using equation (2) and equation (3) respectively, as follows:

$$E_D = \rho \cdot V_P^2 \tag{2}$$

$$G_D = \rho \cdot V_S^2 \tag{3}$$

where V_P and V_S are wave velocities corresponding to P and S waves, respectively.

In addition, to compare the values of moduli resulted from static and dynamic measurements in this study, the dynamic Young's modulus (E_D) and the static Young's modulus (E_s) were converted to the dynamic shear modulus (G_D) and the statically measured shear moduli (G_{sta}) using equation (4) and equation (5), respectively, under isotropic assumption as follows:

$$G_D = \frac{E_D}{2(1+\nu)} \tag{4}$$

$$G_{sta} = \frac{E_s}{2(1+\nu)} \tag{5}$$

where ν is Poisson's ratio. The value of Poisson's ratio was set as 0.17 (Hoque, 1996) for Toyoura sand.

4. TESTS RESULTS AND DISCUSSIONS

Figure 4 shows typical graphs of comparison between static and dynamic moduli of Toyoura sand at different isotropic stress states under dry and saturated conditions, respectively. Hereafter, the values of shear modulus under dry and saturated conditions are plotted on the graph with solid and hollow symbols, respectively.

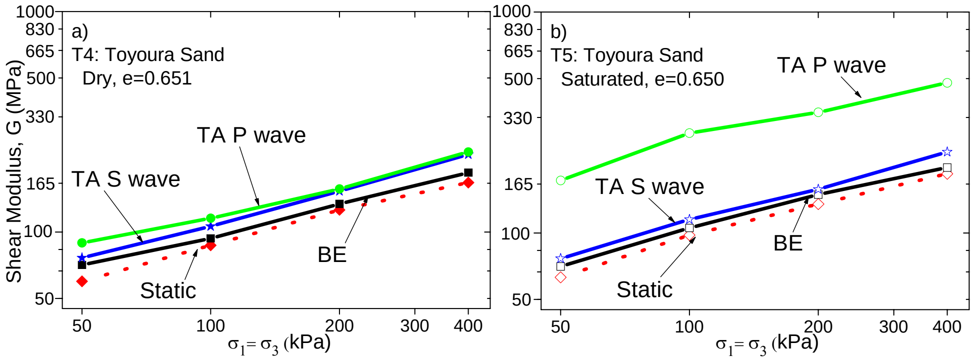

Figure 4: The values of shear moduli on Toyoura sand

As shown in Figure 4a and 4b for under dry and saturated conditions respectively, the values of dynamic shear modulus with the BE ($G_{D,BE}$) and the value of the statically measured shear modulus (G_{sta}) on Toyoura sand are compared. The values of $G_{D,BE}$ were at largest 20% larger than those of G_{sta}. Similar tendency was observed between the specimens under dry and saturated conditions. Under dry condition, the values of the dynamic shear modulus with TA method using S wave ($G_{D,TA-S}$) were 15% - 50% larger than those of G_{sta}, while the values of dynamic shear modulus with TA method using P wave ($G_{D,TA-P}$) were 20% - 70% larger than those of G_{sta}. Under saturated condition, the values of $G_{D,TA-S}$ showed the tendency that was similar to those observed under dry condition. On the other hand, the values of $G_{D,TA-P}$ were significantly larger than those of G_{sta} under saturated condition. The values of $G_{D,BE}$ were larger than those of G_{sta}, but were smaller than those of $G_{D,TA-S}$.

The small strain shear stiffness of Toyoura sand was strongly stress level dependent. For the specimen with initial void ratio of 0.65, small strain shear modulus G is proportional to $(p')^{0.48}$ in all the measurements. This tendency also appeared in a saturated specimen. However, the magnitude of stiffness obtained from different methods including static and dynamic measurements were not always the same. Usually, the order of the magnitude was $G_{D,TA-S}$ and $G_{D,TA-P} > G_{BE} > G_{STA}$. Noticeably large value of $G_{D,TA-P}$ seen in Figure 4b is due to the fact that the observed wave was likely to transmitting through the water rather than soil skeleton in the saturated specimen.

Possible explanations for the discrepancy of stiffness values obtained from different methods are;

1. In the static measurement, the stiffness modulus reflects the overall cross-sectional property of the specimen. On the other hand, in the dynamic measurement the wave travels through the shortest path made by interlocking of bigger particles that resulting into larger stiffness modulus as compared to those by the static measurement (Maqbool, 2005).

2. The difference between two kinds of dynamic shear moduli measured with the TA and the BE methods is due possibly to the effects of bedding error at the interface between the bender element and the specimen at both the top-end and the bottom-end. Gravelly soil yielded in larger size of the locally loose zone at the interface as compared to that with sandy soil seems to result in longer travel time (i.e. smaller dynamic shear modulus) (Wicaksono, 2007).

The above explanations are more relevant to coarser material. Wicaksono (2007) conducted similar study on Hime gravel having the mean diameter of 2mm, and found that the difference of G obtained from static, BE and TA method were more significant.

5. CONCLUSIONS

1. The small strain shear stiffness of Toyoura sand was strongly stress level dependent. Small strain shear modulus G is proportional to $(p')^{0.48}$ in all the measurements for both dry and saturated specimen.

2. The values of shear moduli resulted from dynamic measurements were always larger than those resulted from static measurement, and the values of shear moduli obtained from Bender Element method were always smaller than those from Trigger Accelerometer method.

REFERENCES

AnhDan, L.Q., Koseki, J. and Sato, T., 2002. Comparison of Young's Moduli of Dense Sand and Gravel Measured by Dynamic and Static Methods. *Geotechnical Testing Journal*, ASTM, Vol. 25 (4), pp. 349-368.

Hoque. E., 1996. Elastic Deformation of Sands in Triaxial Tests. *PhD. Thesis*, University of Tokyo, Japan.

Maqbool, S., 2005. Effects of Compaction on Strength and Deformation Properties of Gravel in Triaxial and Plane Strain Compression Tests. *PhD Thesis*, Dept. of Civil Engineering, The University of Tokyo, Japan.

Stokoe, K.H., II and Hoar, R.J., 1978. Field Measurement of Shear Wave Velocity by Crosshole and Downhole Seismic Methods. *Proc. of Conf. on Dynamic Methods in Soil and Rock Mechanics*, Karlsruhe, Germany, Vol. 3, pp. 115-137.

Tanaka, Y., Kudo, K., Nishi, K., Okamoto, T., Kataoka, T. and Ueshima, T., 2000. Small Strain Characteristics of Soils in Hualien, Taiwan. *Soils and Foundations*, Vol. 40 (3), pp. 111-125.

Tatsuoka, F. and Shibuya, S., 1992. Deformation Character-istics of Soils and Rocks from Field and Laboratory Tests. *Proc. of 9th Asian Regional Conf. of SMFE*, Bangkok, Vol. 2, pp. 101-170.

Wicaksono, R.I., Tsutsumi, Y., Sato, T., Koseki, J. Kuwano, R., 2007. Small Strain Stiffness of Clean Sand and Gravel Based on Dynamic and Static Measurements. *Proc. of 9th IS Symposium*, JSCE, pp. 171-174.

Woods, R.D., 1991. Field and Laboratory Determination of Soil Properties at Low and High Strains. *Proc. of 2nd Intl. Conf. on Recent Advances in Geotechnical Earthquake Eng. and Soil Dynamics*, pp. 1727-1741.

WEAKLY-SINGULAR INTEGRAL EQUATIONS FOR CRACKS IN 3D LINEAR PIEZOELECTRIC FINITE MEDIA

WEERAPORN PHONGTINNABOOT
JAROON RUNGAMORNRAT and CHATPAN CHINTANAPAKDEE
Department of Civil Engineering, Faculty of Engineer
Chulalongkorn University
wera371@yahoo.com
Jaroon.R@chula.ac.th
fceccn@eng.chula.ac.th

ABSTRACT

This paper presents the development of a pair of weakly-singular, weak-form integral equations for cracks in a three-dimensional, linear piezoelectric finite medium. A systematic regularization technique is established based upon the integration by parts via Stokes' theorem and special decompositions of certain singular kernels. The resulting integral equations contain only weakly singular kernels of order **O***(1/r) and, as a result, they allow continuous interpolations to be employed everywhere in the numerical approximation. This pair of weak-form integral equations forms a basis for the development of a well-known numerical technique, a symmetric Galerkin boundary element method (SGBEM), well-suited for analysis of cracks in a piezoelectric finite body.*

1. INTRODUCTION

Boundary integral equation methods (BIEMs) are ones of well-known numerical techniques that have proven efficient for modeling linear boundary value problems involving a homogeneous domain. An attractive feature associated with the reduction of one spatial dimension of the key governing equation and its subsequent discretization renders the methods superior than the standard finite element method when the volume-surface ratio of the domain becomes large. Among various types of BIEMs, a weakly-singular, symmetric Galerkin boundary element method has successfully been used to accurately and efficiently model problems involving embedded-singularity such as cracks and dislocations in elastic media (e.g. Xu and Ortiz, 1993; Li *et al*., 1998; Xu, 2000; Frangi *et al*., 2002; Rungamornrat and Mear, 2008b). The key feature of the technique besides the symmetric form of the governing weak-form equation (SGBEM) is that all integrals contain only weakly-singular kernels of order **O**(1/r). This crucial feature significantly eases both the interpretation and the numerical treatment of all involved integrals in comparison with those containing strongly and/or hypersingular kernels (e.g. Gray et al., 1990; Martha et al., 1992; Martin and Rizzo, 1996; Pan and Yuan, 2000) and, in addition, allows continuous interpolations be used in the numerical approximation. To suit such the numerical technique (i.e. SGBEM), it necessitates a nontrivial regularization technique to derive a complete set of weakly singular integral equations and this effort has extensively been investigated within the context of Laplace's equation, linear elasticity, and elastic fracture analysis (e.g. Rungamornrat and Wheeler, 2006; Bonnet, 1995; Li and Mear, 1998; Rungamornrat and Mear, 2008a). It is noted, however, that work on the development of the weakly-singular SGBEM to treat cracks in piezoelectric solids is still relatively few.

Most recently, Rungamornrat and Mear (2008c) derived a weakly-singular, weak-form integral equation for the generalized surface traction for three-dimensional, piezoelectric infinite media and then used this equation to implement the weakly singular SGBEM to solve various boundary value problems involving isolated cracks. Nevertheless, their development is still restricted to the case of cracks in an infinite medium. In this investigation, we generalize the work of Rungamornrat and Mear (2008c) to establish a pair of weakly-singular, weak-form integral equations sufficient for modeling cracks in a piezoelectric finite domain. Such a pair of integral equations can further be employed in the development of the SGBEM for analysis of cracks in piezoelectric components.

2. BASIC EQUATIONS

Let Ω denote a linear, homogeneous, anisotropic, piezoelectric finite medium and let the elastic displacement and the electric potential at any point $\boldsymbol{x} \in \Omega$ be denoted by u_i with i $\in$ {1, 2, 3} and u_4, respectively. Note that a four-component vector u_I with I $\in$ {1, 2, 3, 4} is introduced only as a matter of convenience and it is termed as the "generalized displacement". From here and what follows, the lower case indices range from 1 to 3; the upper case indices range from 1 to 4; and repeated indices imply the summation over their range. In a similar fashion, the "generalized stress", denoted by σ_{iJ}, is defined such that σ_{ij} is the elastic stress tensor and σ_{i4} is the electric induction vector, and the "generalized surface traction", denoted by t_I, is defined such that $t_I = \sigma_{iJ} n_i$. The latter definition implies that $t_i = \sigma_{ij} n_i$ is the surface traction and $t_4 = \sigma_{i4} n_i$ is the surface electric charge.

For a medium that is free of the body force and body charge, a law of conservation dictates that

$$\frac{\partial \sigma_{iJ}}{\partial x_i} = 0 \tag{1}$$

For linear piezoelectricity, the generalized stress is related to the gradient of the generalized displacement by

$$\sigma_{iJ} = E_{iJKm} \frac{\partial u_K}{\partial x_m} \tag{2}$$

where E_{iJKm} is termed as the generalized moduli of the medium. Consistent with the definition of both σ_{iJ} and u_I, E_{ijkm} represent the elastic moduli, $E_{i4km} = E_{mk4i}$ represent the piezoelectric constants, and $E_{i44m} = E_{m44i}$ denote the dielectric permittivities (see also the work of Deeg, 1980).

3. STANDARD INTEGRAL RELATIONS

Consider a linear, homogeneous, anisotropic, piezoelectric finite body containing a crack as depicted in Figure 1. While the crack surface consists of two geometrically coincident surfaces, denoted by S_c^+ and S_c^-, it is sufficient and standard to characterize the crack geometry only by a single surface S_c^+. The ordinary boundary of the body, denoted by S_o, can be decomposed into two surfaces: a surface S_u on which the generalized displacement is prescribed and a (compliment) surface S_t on which the generalized surface traction is prescribed. For convenience, let $S = S_o \cup S_c^+$ denote the total boundary of the domain and let $S_T = S_t \cup S_c^+$.

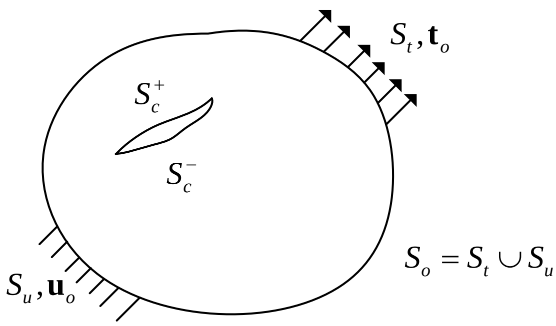

Figure 1: Schematic of a linear piezoelectric body containing a crack.

By generalizing Somigliana's identity to the case of piezoelectricity and then employing the constitutive equation (2), one can obtain the integral relations for the generalized displacement and for the generalized stress at any interior point ***x*** as (see also Denda and Lua, 1999; Liu and Fan, 2001; Qin and Noda, 2004)

$$u_P(\mathbf{x}) = \int_S U_J^P(\boldsymbol{\xi} - \mathbf{x})\pi_J(\boldsymbol{\xi})dS(\boldsymbol{\xi}) - \int_S S_{iJ}^P(\boldsymbol{\xi} - \mathbf{x})n_i(\boldsymbol{\xi})\upsilon_J(\boldsymbol{\xi})dS(\boldsymbol{\xi}) \tag{3}$$

$$\sigma_{lK}(\mathbf{x}) = -\int_S S_{lJ}^{K}(\boldsymbol{\xi}-\mathbf{x})\pi_J(\boldsymbol{\xi})dS(\boldsymbol{\xi}) + \int_S \Sigma_{iJ}^{lK}(\boldsymbol{\xi}-\mathbf{x})n_i(\boldsymbol{\xi})\upsilon_J(\boldsymbol{\xi})dS(\boldsymbol{\xi}) \tag{4}$$

where

$$\pi_J(\boldsymbol{\xi}) = \begin{cases} t_J(\boldsymbol{\xi}); & \boldsymbol{\xi} \in S_o \\ t_J^+(\boldsymbol{\xi}) + t_J^-(\boldsymbol{\xi}); & \boldsymbol{\xi} \in S_c^+ \end{cases} \tag{5}$$

$$\upsilon_J(\boldsymbol{\xi}) = \begin{cases} u_J(\boldsymbol{\xi}); & \boldsymbol{\xi} \in S_o \\ u_J^+(\boldsymbol{\xi}) - u_J^-(\boldsymbol{\xi}); & \boldsymbol{\xi} \in S_c^+ \end{cases} \tag{6}$$

$U_J^P(\boldsymbol{\xi}-\mathbf{x})$ and $S_{iJ}^P(\boldsymbol{\xi}-\mathbf{x})$ are the generalized displacement and generalized stress fundamental solutions, and $\Sigma_{iJ}^{lK}(\boldsymbol{\xi}-\mathbf{x})$ is a singular kernel defined by $\Sigma_{iJ}^{lK}(\boldsymbol{\xi}-\mathbf{x}) = E_{lKPq}\partial S_{iJ}^P / \partial \xi_q$.

Since the kernel $S_{iJ}^P(\boldsymbol{\xi}-\mathbf{x})$ is singular of $\mathbf{O}(1/r^2)$ at $\boldsymbol{\xi} = \mathbf{x}$ and the kernel $\Sigma_{iJ}^{lK}(\boldsymbol{\xi}-\mathbf{x})$ is singular of $\mathbf{O}(1/r^3)$ at $\boldsymbol{\xi} = \mathbf{x}$, the integral equations for the generalized displacement and for the generalized surface traction established directly from (3) and (4) are, therefore, strongly singular and hypersingular, respectively. Evaluation of such integrals is computationally challenging and, in particular, requires special integral quadratures (e.g. Gray et al., 1990; Martha et al., 1992; Martin and Rizzo, 1996; Pan and Yuan, 2000).

4. COMPLETELY REGULARIZED INTEGRAL EQUATIONS

To reduce the strength of singularity of kernels appearing in above two integral relations (3) and (4), the integration by parts is employed to transfer the derivative from the kernels to the boundary data. To ease such an integration by parts process, we introduce the following two special decompositions, one for the kernel $S_{iJ}^P(\boldsymbol{\xi}-\mathbf{x})$ and the other for $\Sigma_{iJ}^{lK}(\boldsymbol{\xi}-\mathbf{x})$:

$$S_{iJ}^P(\boldsymbol{\xi}-\mathbf{x}) = H_{iJ}^P(\boldsymbol{\xi}-\mathbf{x}) + \varepsilon_{ism}\frac{\partial G_{mJ}^P(\boldsymbol{\xi}-\mathbf{x})}{\partial \xi_s} \tag{7}$$

$$\Sigma_{iJ}^{lK}(\boldsymbol{\xi}-\mathbf{x}) = -E_{iJKl}\delta(\boldsymbol{\xi}-\mathbf{x}) + \varepsilon_{ism}\frac{\partial}{\partial \xi_s}\varepsilon_{lrt}\frac{\partial}{\partial \xi_r}C_{mJ}^{tK}(\boldsymbol{\xi}-\mathbf{x}) \tag{8}$$

where $H_{iJ}^P(\boldsymbol{\xi}-\mathbf{x}) = -\delta_{JP}(\xi_i - x_i)/4\pi r^3$ and G_{mJ}^P and C_{mJ}^{tK} are functions that are singular of $\mathbf{O}(1/r)$ at $\boldsymbol{\xi} = \mathbf{x}$. A particular solution of G_{mJ}^P and C_{mJ}^{tK} can explicitly be obtained by solving the systems of partial differential equations (7) and (8) by a method of integral transform (also see the work of Rungamornrat and Mear, 2008a).

4.1 Weakly singular integral equation for generalized displacement

A singularity-reduced integral relation for the generalized displacement can be obtained by substituting the decomposition (7) into the integral relation (3) and then performing integration by parts via Stokes' theorem. The resulting integral relation is subsequently employed to form the displacement integral equation through an appropriate limiting process and, finally, the weakly singular, weak-form integral equation for the generalized displacement is established via the introduction of the test function $\tilde{t}_P$ to obtain

$$\begin{aligned}\frac{1}{2}\int_S \tilde{t}_P(\mathbf{y})u_P^*(\mathbf{y})dS(\mathbf{y}) &= \int_S \tilde{t}_P(\mathbf{y})\int_S U_J^P(\boldsymbol{\xi}-\mathbf{y})\pi_J(\boldsymbol{\xi})dS(\boldsymbol{\xi})dS(\mathbf{y}) \\ &+ \int_S \tilde{t}_P(\mathbf{y})\int_S G_{mJ}^P(\boldsymbol{\xi}-\mathbf{y})D_m\upsilon_J(\boldsymbol{\xi})dS(\boldsymbol{\xi})dS(\mathbf{y}) \\ &- \int_S \tilde{t}_P(\mathbf{y})\int_S H_{iJ}^P(\boldsymbol{\xi}-\mathbf{y})n_i(\boldsymbol{\xi})\upsilon_J(\boldsymbol{\xi})dS(\boldsymbol{\xi})dS(\mathbf{y})\end{aligned} \tag{9}$$

where

$$u_P^*(\mathbf{y}) = \begin{cases} u_P(\mathbf{y}); & \mathbf{y}\in S_o \\ u_P^+(\mathbf{y}) + u_P^-(\mathbf{y}); & \mathbf{y}\in S_c^+ \end{cases} \tag{10}$$

The resulting weak-form integral equation (9) contains only weakly singular kernels of order **O**(1/*r*), i.e. U_J^P, G_{mJ}^P and $H_{iJ}^P n_i$.

4.2 Weakly singular integral equation for generalized surface traction

To obtain singularity-reduced integral relation for the generalized stress, we apply the decompositions (7) and (8) to the integral relation (4) and then perform the integration by parts of the result via Stokes' theorem. Such integral relation is then used to form an integral equation for the generalized surface traction. Finally, the weakly singular, weak-form integral equation is established by multiplying the integral equation for the surface traction by a test function $\tilde{\upsilon}_K$ and then performing an additional integration by parts via Stokes' theorem. The resulting weak-form integral equation is given by

$$\begin{aligned}-\frac{1}{2}\int_S \tilde{\upsilon}_K(\mathbf{y})t_K^*(\mathbf{y})dS(\mathbf{y}) &= \int_S D_t\tilde{\upsilon}_K(\mathbf{y})\int_S C_{mJ}^{tK}(\boldsymbol{\xi}-\mathbf{y})D_m\upsilon_J(\boldsymbol{\xi})dS(\boldsymbol{\xi})dS(\mathbf{y}) \\ &+ \int_S D_t\tilde{\upsilon}_K(\mathbf{y})\int_S G_{tK}^J(\boldsymbol{\xi}-\mathbf{y})\pi_J(\boldsymbol{\xi})dS(\boldsymbol{\xi})dS(\mathbf{y}) \\ &+ \int_S \tilde{\upsilon}_K(\mathbf{y})\int_S H_{iK}^J(\boldsymbol{\xi}-\mathbf{y})n_i(\mathbf{y})\pi_J(\boldsymbol{\xi})dS(\boldsymbol{\xi})dS(\mathbf{y})\end{aligned} \tag{11}$$

where

$$t_K^*(\mathbf{y}) = \begin{cases} t_K(\mathbf{y}); & \mathbf{y} \in S_o \\ t_K^+(\mathbf{y}) - t_K^-(\mathbf{y}); & \mathbf{y} \in S_c^+ \end{cases} \tag{12}$$

Note that the integral equation (11) contains only weakly singular kernels of order $\mathbf{O}(1/r)$, i.e. C_{mJ}^{tK} , G_{tK}^{J} and $H_{iK}^{J} n_i$.

5. SYMMETRIC FORMUALATION

Now, let focus attention to the case that the generalized surface traction is fully prescribed on the entire crack surface. A system of the governing integral equations for this particular boundary value problem is obtained as follow: the weak-form integral equation for the generalized displacement (9) is applied to the surface S_u (with $\tilde{t}_P = 0$ on S_T) and the weak-form integral equation for the generalized surface traction (11) is applied to the surface S_T (with $\tilde{\upsilon}_P = 0$ on S_u). The resulting governing equations are given by

$$\begin{aligned} \mathbf{A}_{uu}(\tilde{\mathbf{t}},\mathbf{t}) + \mathbf{B}_{uT}(\tilde{\mathbf{t}},\boldsymbol{\upsilon}) &= \mathbf{R}_1(\tilde{\mathbf{t}}) \\ \mathbf{B}_{uT}(\mathbf{t},\tilde{\boldsymbol{\upsilon}}) + \mathbf{C}_{TT}(\tilde{\boldsymbol{\upsilon}},\boldsymbol{\upsilon}) &= \mathbf{R}_2(\tilde{\boldsymbol{\upsilon}}) \end{aligned} \tag{13}$$

where the bi-linear integral operators $\mathbf{A}_{PQ}$, $\mathbf{B}_{PQ}$ and $\mathbf{C}_{PQ}$ (with P, Q $\in \{u, T\}$) are given by

$$\mathbf{A}_{PQ}(\mathbf{X},\mathbf{Y}) = \int_{S_P} \tilde{X}_K(\mathbf{y}) \int_{S_Q} U_J^K(\boldsymbol{\xi}-\mathbf{y}) Y_J(\boldsymbol{\xi}) dS(\boldsymbol{\xi}) dS(\mathbf{y}) \tag{14}$$

$$\begin{aligned} \mathbf{B}_{PQ}(\mathbf{X},\mathbf{Y}) = &\int_{S_P} \tilde{X}_K(\mathbf{y}) \int_{S_Q} G_{mJ}^K(\boldsymbol{\xi}-\mathbf{y}) D_m Y_J(\boldsymbol{\xi}) dS(\boldsymbol{\xi}) dS(\mathbf{y}) \\ &- \int_{S_P} \tilde{X}_P(\mathbf{y}) \int_{S_Q} H_{iJ}^P(\boldsymbol{\xi}-\mathbf{y}) n_i(\boldsymbol{\xi}) Y_J(\boldsymbol{\xi}) dS(\boldsymbol{\xi}) dS(\mathbf{y}) \end{aligned} \tag{15}$$

$$\mathbf{C}_{PQ}(\mathbf{X},\mathbf{Y}) = \int_{S_P} D_t \tilde{X}_K(\mathbf{y}) \int_{S_Q} C_{mJ}^{tK}(\boldsymbol{\xi}-\mathbf{y}) D_m Y_J(\boldsymbol{\xi}) dS(\boldsymbol{\xi}) dS(\mathbf{y}) \tag{16}$$

and the linear integral operators $\mathbf{R}_1$ and $\mathbf{R}_2$ are given by

$$\mathbf{R}_1(\tilde{\mathbf{t}}) = \frac{1}{2} \int_{S_u} \tilde{t}_P(\mathbf{y}) u_P(\mathbf{y}) dS(\mathbf{y}) - \mathbf{A}_{uT}(\tilde{\mathbf{t}},\boldsymbol{\pi}) - \mathbf{B}_{uu}(\tilde{\mathbf{t}},\mathbf{u}) \tag{17}$$

$$\mathbf{R}_2(\tilde{\boldsymbol{\upsilon}}) = -\frac{1}{2} \int_{S_T} \tilde{\upsilon}_K(\mathbf{y}) t_K^*(\mathbf{y}) dS(\mathbf{y}) - \mathbf{B}_{TT}(\boldsymbol{\pi},\tilde{\boldsymbol{\upsilon}}) - \mathbf{C}_{Tu}(\tilde{\boldsymbol{\upsilon}},\mathbf{u}) \tag{18}$$

It is evident that the governing integral equations (13) are in a symmetric form.

6. CONCLUSION

A pair of completely regularized, weak-form integral equations for the generalized displacement and the generalized surface traction has been established to treat cracks in a three-dimensional, piezoelectric finite medium. The key feature of the developed integral equations is that they contain only weakly singular kernel of order $O(1/r)$ and this offers both theoretical and computational advantages. In particular, all integrals exist in an ordinary sense and continuous interpolations can be employed everywhere in the numerical approximation.

Such a pair of weak-form integral equations has properly been employed to form a set of governing integral equations for boundary value problems involving cracks in piezoelectric finite bodies. The resulting governing equations are in a symmetric form and essentially weakly-singular, and they constitute a basis for the development of a well-known numerical technique called a symmetric Galerkin boundary element method (SGBEM).

REFERENCES

Bonnet, M., 1995. Regularized direct and indirect symmetric variational BIE formulations for three-dimensional elasticity. *Engrg. Anal. Bound. Elem.* 15, 93-102.

Deeg, WFJ., 1980. The analysis of dislocation, crack, and inclusion problems in piezoelectric solids. *Ph.D. Dissertation*, Standford University, California.

Denda, M. and Lua, J., 1999. Development of the boundary element method for 2D piezoelectricity. *Composites: Part B* 30, 699-707.

Frangi, A., Novati, G. and Springhetti, R., 2002. 3D fracture analysis by the symmetric Galerkin BEM. *Comput. Mech.* 28, 220-232.

Gray, L.J., Martha, L.F. and Ingraffea, A.R., 1990. Hypersingular integrals in boundary element fracture analysis. *Int. J. Numer. Meth. Engrg.* 29, 1135-1158.

Li, S. and Mear, M.E., 1998. Singularity-reduced integral equations for displacement discontinuities in three-dimensional linear elastic media. *Int. J. Fracture.* 93, 87-114.

Li, S., Mear, M.E. and Xiao, L., 1998. Symmetric weak-form integral equation method for three-dimensional fracture analysis. *Comput. Methods Appl. Mech. Engrg.* 151, 435-459.

Liu, Y. and Fan, H., 2001. On the conventional boundary integral formulation for piezoelectric solids with defects or of thin shapes. *Engrg. Anal. Bound. Elem.* 25, 77-91.

Martha, L.F., Gray, L.J. and Ingraffea, A.R., 1992. Three-dimensional fracture simulation with a single-domain, direct boundary element formulation. *Int. J. Numer. Meth. Engrg.* 35, 1907-1921.

Martin, P.A. and Rizzo, F.J., 1996. Hypersingular integrals: how smooth must the density be?. *Int. J. Numer. Meth. Engrg.* 39, 687-704.

Pan, E. and Yuan, F.G., 2000. Boundary element analysis of three-dimensional cracks in anisotropic solids. *Int. J. Numer. Meth. Engrg.* 48, 211-237.

Qin, T. and Noda, N.A., 2004. Application of hypersingular integral equation method to a three-dimensional crack in piezoelectric materials. *JSME Int. J.* 47, 173-180.

Rungamornrat, J. and Wheeler, M.F., 2006. Weakly-singular integral equations for Darcy's flow in anisotropic porous media. *Engrg. Anal. Bound. Elem.* 30, 237-246.

Rungamornrat, J. and Mear, M.E., 2008a. Weakly-singular, weak-form integral equations for cracks in three-dimensional anisotropic media. *Int. J. Solids Struct.* 45, 1283-1301.

Rungamornrat, J. and Mear, M.E., 2008b. A weakly-singular SGBEM for analysis of cracks in 3D anisotropic media. *Comput. Methods Appl. Mech. Engrg.*, Article in press.

Rungamornrat, J. and Mear, M.E., 2008c. Analysis of fractures in 3D piezoelectric media by a weakly singular integral equation method. *Int. J. Fracture*, Article in press.

Xu, G. and Ortiz, M., 1993. A variational boundary integral method for the analysis of 3-D cracks of arbitrary geometry modelled as continuous distributions of dislocation loops. *Int. J. Numer. Meth. Engrg.* 36, 3675-3701.

Xu, G., 2000. A variational boundary integral method for the analysis of three-dimensional cracks of arbitrary geometry in anisotropic elastic solids. *J. Appl. Mech.* 67, 403-408.

UNDRAINED SHEAR STRENGTH ESTIMATION OF MARINE CLAY USING SHEAR WAVE VELOCITY

TAE-MIN OH, ILHAN CHANG and GYE-CHUN CHO
Department of Civil and Environmental Engineering,
Korea Advanced Institute of Science and Technology
ohtaemin@kaist.ac.kr
ilhanchang@kaist.ac.kr
gyechun@kaist.ac.kr

ABSTRACT

Undrained shear strength is a critical property in the evaluation of ground resistance. Generally, undrained shear strength is estimated by a vane shear test in the field and an undrained triaxial test in a laboratory. However, accurate evaluation of the undrained shear strength is difficult because of the total depth in the field and because of the difficulty of providing reliable continuous monitoring of the whole construction process. Moreover, after the construction of structures, it is impossible to perform in situ measurements such as a vane shear test on the site. To overcome existing disadvantages, this study attempts to estimate the in situ undrained shear strength by using the relations between the verified shear wave velocity, the void ratio, and the undrained shear strength. The Shear wave velocities of marine clay are measured with different void ratios by means of consolidation cells with piezoelectric bender element sensors; furthermore, the results show the correlation between the shear wave velocity and the void ratio. In addition, laboratory vane tests are performed with different void ratios to verify the relation between the undrained shear strength and the void ratio.

A profile of the undrained shear strength can be predicted by means of correlated equations with the in situ profile of shear wave velocity. A comparison of the real undrained shear strength measured in situ and the estimated undrained shear strength in a laboratory confirms that the results of the estimated undrained shear strength have reasonable values and tendencies with depth.

1. INTRODUCTION

Undrained shear strength is an important property in determining ground stabilization, and the monitoring of undrained shear strength requires a nondestructive method. A shear wave is very simple to measure and analyze. Furthermore, shear wave velocity can indicate characteristics of soil, such as density. Because the shear wave velocity increases as the void ratio decreases, there is a corresponding increase in material density

(Santamarina et al. 2001). It is also well known that, in clay, the undrained shear strength decreases as the void ratio increases (Bartetzko & Kopf 2006; Sharmasms & Bora 2002; Lambe et al. 1969). This behavior confirms that the void ratio is a critical factor in determining the undrained shear strength in clay. Previous studies have shown the relation between the shear wave velocity and the void ratio, and between the void ratio and the undrained shear strength. Hence, the undrained shear strength appears to be directly correlated to the shear wave velocity. The shear wave velocity, the void ratio, and the undrained shear strength are correlated and verified with a consolidation test and a bender element in a laboratory test.

2. THEORETICAL BACKGROUND

2.1 Relation between the shear wave velocity and the void ratio

A shear wave has good applicability in soil because it propagates only through the soil skeleton, and its velocity depends on the effective stress of the soil. The shear wave velocity of particulate materials under a zero lateral strain loading (with a one-dimensional consolidation) can be expressed in terms of the vertical effective stress as follows (Hardin & Richart 1963; Santamarina, et al. 2001):

$$V_s = \alpha\left(\frac{\sigma'}{1\text{kPa}}\right)^{\beta} \quad (1)$$

where V_s is the shear wave velocity, σ' is the effective stress, and the parameters α (the shear wave velocity at 1 kPa) and β are experimentally determined. Clays with a higher plasticity index generally have a higher β exponent and a lower α factor.

The relation between the effective stress and the void ratio can be expressed as two linear lines based on pre-consolidation stress in the semi-log scale. The constant A can be the compression index (C_c) or the swelling index (C_s) depending on the consolidation state. The effective relation between stress and the void ratio is expressed as follows:

$$e = A\cdot\ln(\sigma') + B \quad (2)$$

where e is the void ratio and A and B are constants. If equation 1 and 2 are combined, the effective stress can be removed and the relation between the void ratio and the shear wave velocity can be expressed as follows:

$$e = A\cdot\ln\left(\frac{V_s}{\alpha}\right)^{\frac{1}{\beta}} + B = k_1\cdot\ln(V_s) + k_2 \quad (3)$$

where k_1 and k_2 are constants. Equation 3 should be applied differently with a normal consolidation (NC) state and an over-consolidation (OC) state.

2.2 Relationship between void ratio and undrained shear strength

In clay, the relation between the void ratio and the undrained shear strength is generally linear or linear in a log-log scale (Bartetzko et al. 2007; Huang et al. 1990; Athy 1930). Using the probability and statistics method, Bartetzko (2007) confirmed that, in clay, the linear relation between the void ratio and the undrained shear strength is almost the same as the linear relation in the log-log scale. In this study, the void ratio is assumed to be correlated with the undrained shear strength in a linear tendency as shown in the following equation:

$$S_u = -c_1 \cdot e + c_2 \tag{4}$$

where S_u is the undrained shear strength and c_1 and c_2 are empirical constants.

3. EMPERIMENTAL STUDY

3.1 Specimen preparation

The specimens were prepared by boring from a depth of 0 m to 18 m in reclaimed ground in the Busan - Jinhae Hawjon region. The tested ground consists of four layers. A thin-walled sampler (D=74mm) was used to obtain undisturbed specimens. As shown in Table 1, the representative specimens were selected at depths of 3 m (clayey silt), 6 m (silty sand), 9 m (clay 1), 13 m (clay 2), and 15 m (clay 3). In the laboratory, the specimens were cut into 40 mm samples for use in consolidation tests.

Table 1: Specimen properties

Depth [m]	**0.0~5.4**	**5.4~8.1**	**8.1~11.0**	**11.0~14.0**	**14.0~17.8**
Soil type	**Clayey silt**	**Silty sand**	**Clay**		
			Clay 1	**Clay 2**	**Clay 3**
Water content	0.390	0.313	0.540	0.521	0.534
Initial void ratio	1.034	0.829	1.431	1.381	1.415
Unit weight [t/m^3]	1.845	1.931	1.744	1.706	1.623
Liquidity limit [%]	-	-	63.2	73.5	78.6
Plasticity limit [%]	-	-	26.7	29.5	35.5
plasticity index [%]	-	-	36.5	44.0	43.1

3.2 Experimental setup

The experiment was performed by measuring the shear wave velocities during the consolidation tests, which were divided into five effective steps for each specimen. The test consisted of a consolidation cell with two bender elements for the shear wave. The equipment used in the experiment was a function/arbitrary wave form generator, an oscilloscope, and a Multimeter. After the consolidation tests, the undrained shear strengths were obtained by means of vane tests.

Bender elements (L=12 mm, W=4 mm, and T=0.6 mm) were used to obtain the shear wave velocities in the laboratory. The bender elements, which were installed at the center of the top and bottom plate, were coated with polyurethane to prevent direct contact with water; water can affect other aspects of the bender element operation through leakage of electric current from the opposite bender element. In addition, silver paint was used as a shield on the bender elements to prevent the effect of electromagnetic cross-talk. During the loading, a wave was generated as a pulse signal (10 kHz, AC 10 V) and sent to the source bender element. The response of the receiver bender element was recorded. The vertical shear-wave travel time was measured between the top and bottom bender elements. The vertical deformation of the specimen was measured with a dial gage. The vertical shear wave velocity (in meters per second) was calculated by dividing the specimen height (in meters) by the vertical shear wave travel time(in seconds). Thus, the shear velocity inside the specimen was measured continuously during the consolidation.

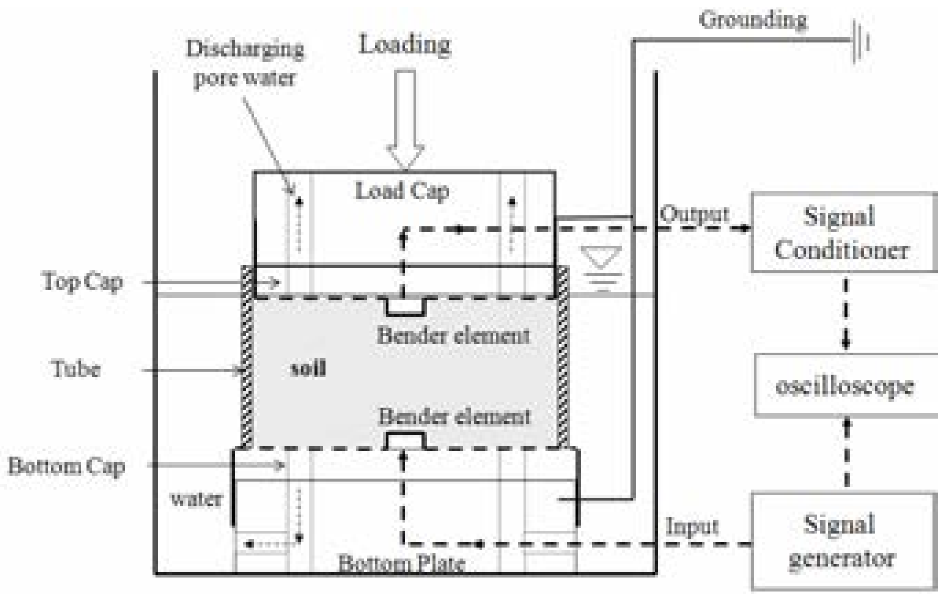

Figure 1: Laboratory test setup

4. RESULTS

4.1 Results of the correlation for the shear wave velocity and the void ratio

The results of the shear wave velocity and the void ratio show that each specimen has two linear lines in a semi-log scale at the pre-consolidation state shown in equation 3. The results of each specimen are shown in Figures 2, 3, 4, 5, and 6.

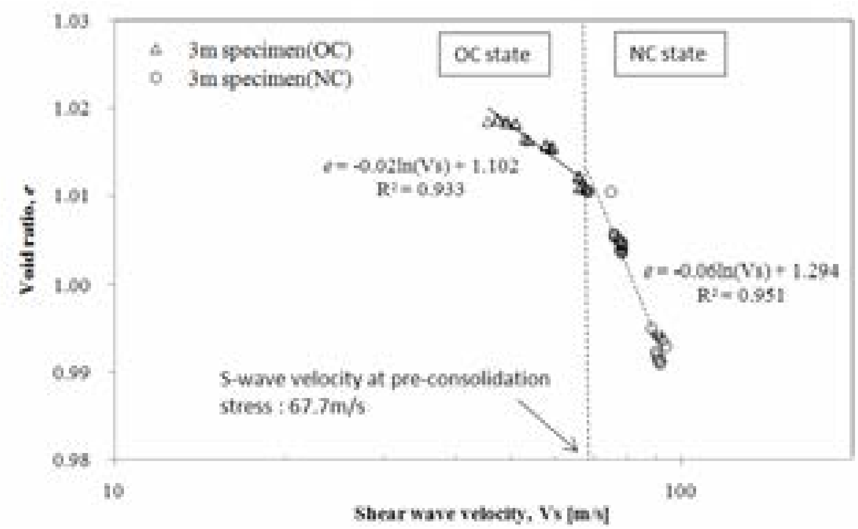

Figure 2: Shear wave velocity-void ratio test result in 3m specimen

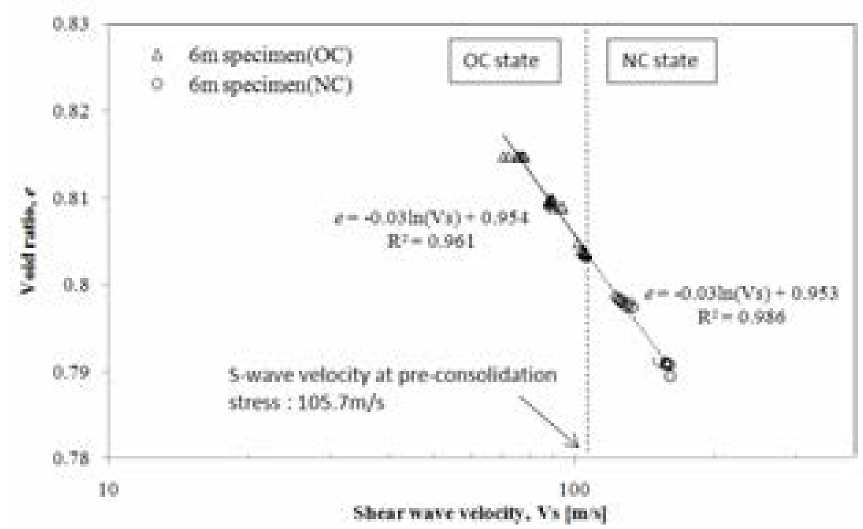

Figure 3: Shear wave velocity-void ratio test result in 6m specimen

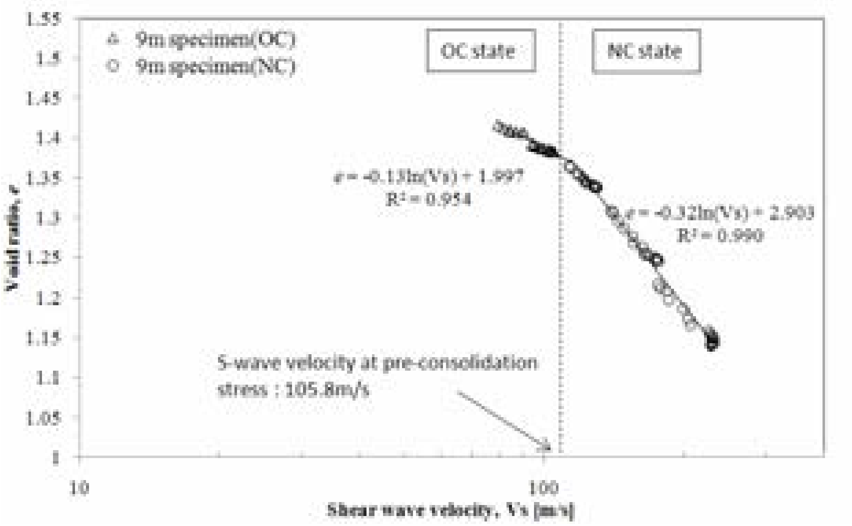

Figure 4: Shear wave velocity-void ratio test result in 9m specimen

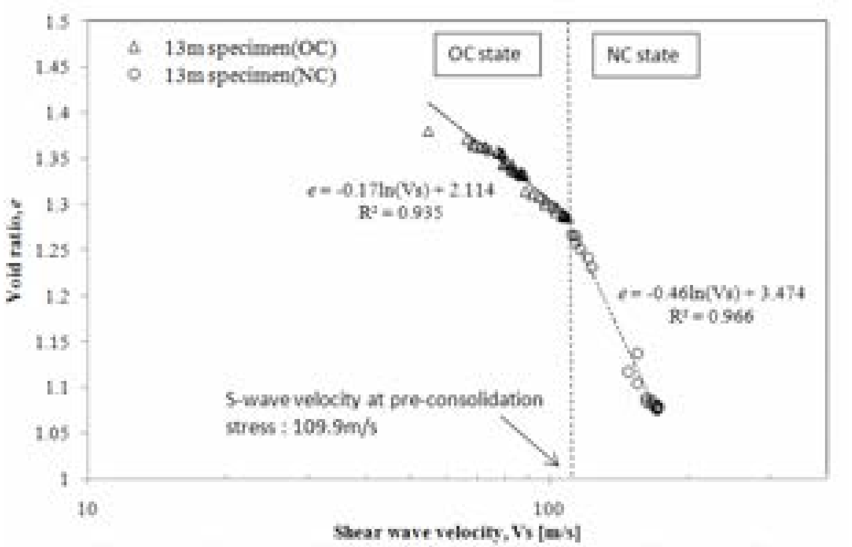

Figure 5: Shear wave velocity-void ratio test result in 13m specimen

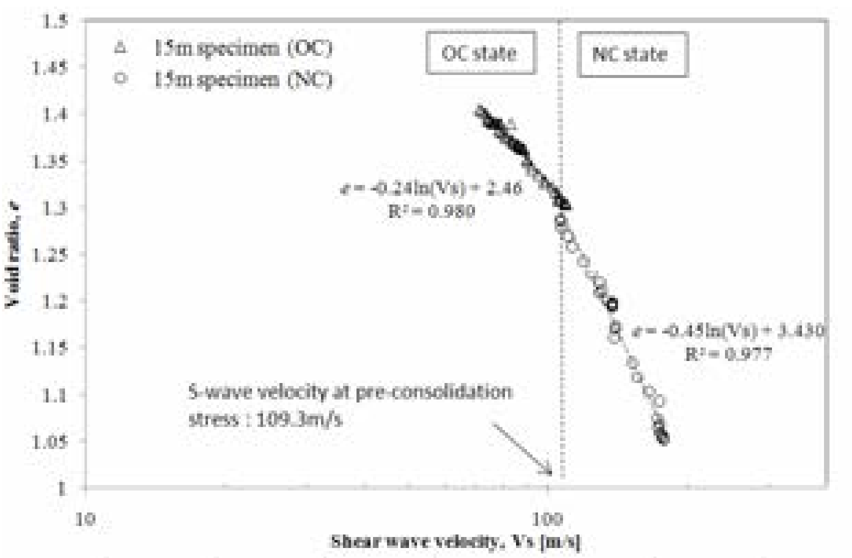

Figure 6: Shear wave velocity-void ratio test result in 15m specimen

The results of the 6 m specimen show a single linear line, regardless of the consolidation state, because at a depth of 5.4 m to 8.1 m the specimen consists of silty sand. On the other hand, the clay specimens show two clear linear lines, indicating that the consolidation state affects the clayey soil more than the sandy soil.

4.2 Void ratio-undrained shear strength correlation results

Vane tests are performed four times with void ratios to obtain a reliable correlation of the void ratio and the undrained shear strength. The test results are shown in Figure 7. No data was obtained for the 6 m specimen because of its silty sand nature.

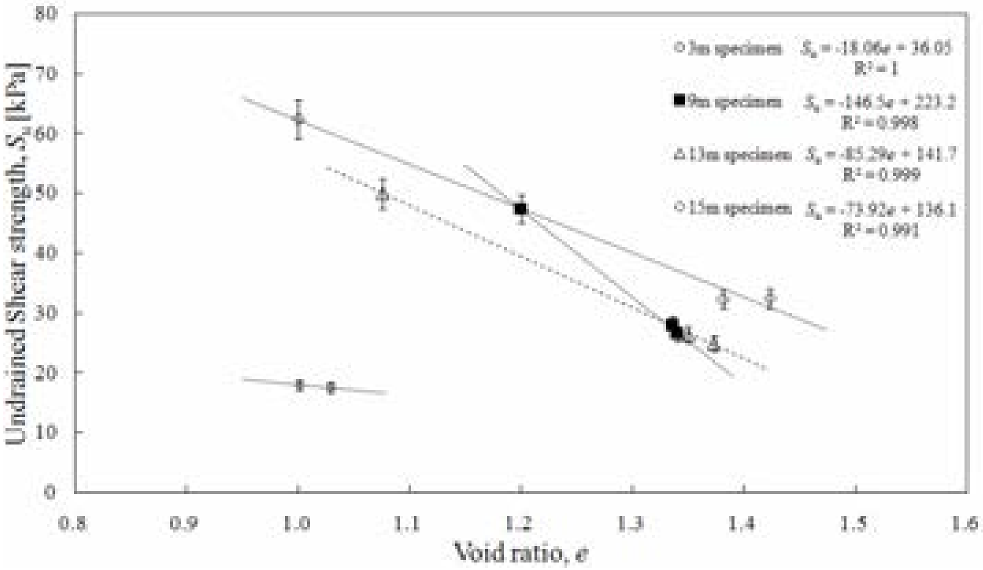

Figure 7: Undrained shear strength measured by laboratory vane tests

Table 2: Constants in undrained shear strength-void ratio relationship

Depth[m]	3	6	9	13	15
c_1	18.06	-	146.5	88.78	73.92
c_2	36.05	-	223.2	146.5	136.1

5. ANALYSIS AND DISCUSSION

As a way of verifying the proposed method's capability of estimating undrained shear strength with shear wave velocity, the in situ undrained shear strength was compared with the estimated in situ undrained shear strength. Real data of in situ undrained shear strength were obtained from the Korea Institute of Geoscience and Mineral Resources (KIGAM); for the collection of that data, the institute used a resistivity seismic flat dilatometer (RSDMT). The in situ undrained shear strength values were calculated from typical equations suggested by Marchetti (1980) and Kamei and Iwasaki (1995).

On the basis of laboratory tests for each specimen's relation and constant (k_1 and k_2) between the shear wave velocity and the void ratio, the in situ void ratio profile can be estimated with the aid of the in situ shear wave velocity profile. The tested clay is normally in a consolidation state. Hence, the linear line at the NC state should be used to infer the in situ void ratio. As shown in Figure 8, the results of the in situ void ratio profile are inferred.

The undrained shear strength can be estimated from the combination of the inferred in situ void ratio profile and equation 4 with the constants (c_1 and c_2) in Table 2. As a result, the estimated in situ undrained shear strength has a similar tendency and values as the measured in situ undrained shear strength data in field (Figure 9).

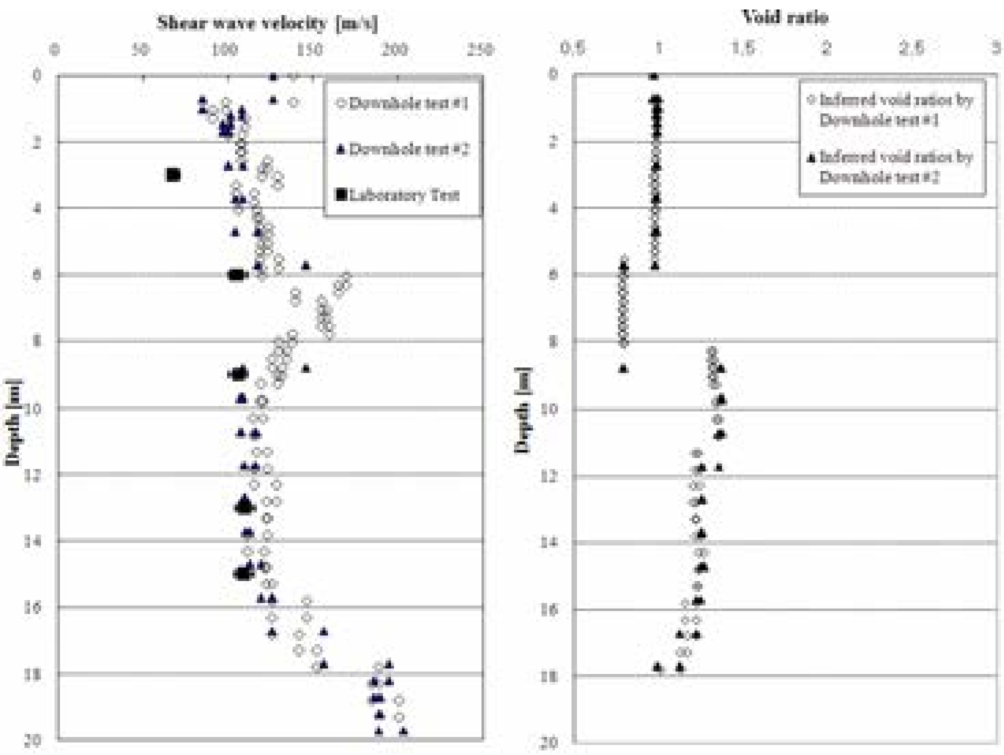

(a) Shear wave velocity comparison (b) Estimated in-situ void ratio

Figure 8: Estimated in-situ void ratio with in-situ shear wave velocity

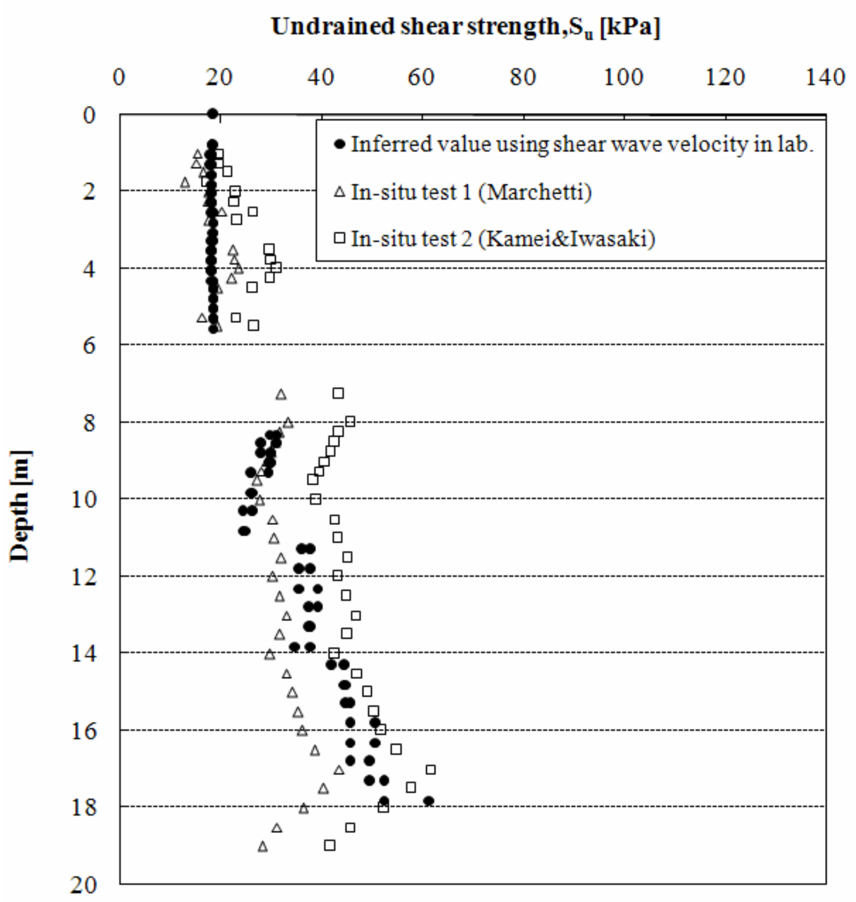

Figure 9: Comparison between in-situ undrained shear strength

6. CONCLUSION

The relation of the shear wave velocity and the void ratio was obtained by measuring the shear wave velocities with the void ratio. The measurements were taken with the aid of consolidation cells with bender elements. Vane tests were used to obtain the relation of the void ratio and the undrained shear strength. The results show that when the void ratio is used as an intermediary, the undrained shear strength can be directly correlated with shear wave velocity.

As a result of measuring the shear wave velocity under the same effective stress conditions, the marine clay is determined to be in an NC state. The whole procedure of estimating the undrained shear strength is therefore performed in the NC state. However, if the real field conditions are changed from an NC state to an OC state due to the removal of the surcharge, the estimation of the undrained shear strength should be performed in the OC state. The estimated undrained shear strength can be changed to a consolidation state because the consolidation state is very critical in determining the clay characteristics. The method suggested in this study can reflect either an NC state or an OC state.

On the basis of clay samples, the estimated undrained shear strength with shear wave velocity is compared with the undrained shear strength as measured with the resistivity seismic flat dilatometer. The results show that the method of estimating the undrained shear strength with shear wave velocity is very reliable and reasonable. Through this estimation method, the undrained shear strength can be monitored with the shear wave velocity under different conditions, such as the void ratio or the consolidation state.

REFERENCES

Bartetzko, A. and Kopf, A. J., 2007. The Relationship of Undrained Shear Strength and Porosity with Depth in Shallow Marine Sediments. *Sedimentary Geology*, Vol.196, p.235-249.

Bang, E. S., Sung, N. H., Park, S. G., Kim, J. H., Kim, Y. S., Seo, D. N., Kim, D. S., and Lee, S. H., 2008. Development and verification of a resistivity seismic flat dilatometer testing system for efficient soft soil site charaterization. *Geotechnical and Geophysical Site Characterization*, p.1247-1253.

Blake, W. D. and Gilbert, R. B., 1997. Investigation of Possible Relationship between Undrained Shear Strength and Shear Wave Velocity for Normally Consolidation Clays. *Offshore Technology Conference*, p.411-419.

Chang, I. H. and Cho, G. C., 2007. A Labolartory Procedure to Characterize Reclained Clay Using Shear Wave. *Geotechnical Special Publication 164-Innovative Applications of Geophysics in Civil Engineering, ASCE*.

Hardin, B. O. and Richart, F. E., 1963. Elastic Wave Velocities in Granular Soils. *Journal of Soil Mechanics and Foundations*, ASCE, Vol.89, SM1, p.33-65.

Kamei T. and Iwasaki K., 1995. Evaluation of undrained shear strength of cohesive soils using a Flat Dilatometer. *Soils and Foundations*, Vol.35, No.2, p.111-116.

Lambe, T. W. and Whitman, R. V., 1969. *Soil Mechanics*, John Wiley & Sons, LTD.

Marchetti, S., 1980. In situ tests by flat dilatometer. *ASCE Journal of Geotechnical Engineering Division*, Vol.196, GT3, p.299-167.

Santamarina, J. C., Klein, K. A., and Fam, M. A., 2001. *Soils and Waves*, John Wiley & Sons, LTD.

SEISMIC RETROFITTING PROMOTION MODEL FOR MASONRY HOUSES USING PP-BAND METHOD AND MICRO-EARTHQUAKE INSURANCE

NAOKI SORIMACHI[1] and KIMIRO MEGURO[2]
[1]Department of Civil Engineering, The University of Tokyo, Japan
[2]International Center for Urban Safety Engineering,
Institute of Industrial Science, The University of Tokyo, Japan
sorry@risk-mg.iis.u-tokyo.ac.jp

ABSTRACT

This study aims to contribute to reducing earthquake damage in developing countries that are mainly caused by the collapse of masonry houses. A new model was proposed and analyzed to promote seismic retrofitting by eliminating the retrofitting cost from the government and the residents. Instead, insurance companies were incorporated to bear the retrofitting cost. By setting a condition that this model is valid if retrofitting promotion cost is smaller than the reduced amount of government's reconstruction expenses due to retrofitting, the possible compensation for the residents and the wage for local engineers were estimated to see the effect of this model quantitatively. The results showed that this model enables to pay enough compensation for reconstruction to the residents, and to raise the wage of local engineers by retrofitting business. Therefore, the proposed model will give incentive of retrofitting to the government and the residents.

1. INTRODUCTION

Looking at damage by earthquake disasters in developing countries, collapse of masonry houses is one of the major causes of casualties. Therefore, seismic retrofitting of weaker masonry houses is the key to reduce earthquake damage. In order to solve this problem, the author's research group has developed PP-band method. PP-band method is a simple, cheap, easy and local acceptable retrofitting method. However, the retrofitting cost of PP-band method (about $30/house for materials) proved to be still unaffordable for the very low income people. Our research group has then proposed a "two-step incentive system" to solve this problem. In this system, the government will provide retrofitting materials for free and ask the residents to retrofit their houses. After checking that the houses were retrofitted properly, the government will give subsidy to the residents (1st incentive). In addition, the residents who have performed retrofitting will be assured to receive more compensation (for example, twice) by the government than those who have not in case their houses were damaged by the earthquake in the future (2nd incentive). This system proved to reduce the total damage by the earthquake drastically in case of Iran Bam (2003), Pakistan Kashmir (2005) and Indonesia Java (2006) earthquakes (Iritani, Meguro, 2007). At least 85% of the death toll could be saved, and, the total expenditure by the government could be reduced by 96% in Iran, 81% in Pakistan and 76% in Indonesia. However, in this system, the initial retrofitting cost prepared by the government was the key issue, which this study will focus on.

This study aims to propose and analyze a new model to promote retrofitting in developing countries by using PP-band method. In this model, insurance companies will bear retrofitting cost instead of the government or the residents. A condition that indicates the validity of this model was set, and, under this condition, possible compensation for the residents and possible wage for local engineers was estimated to see the effect of the model quantitatively. Case studies were done in Iran Bam area, Pakistan Kashmir area and Indonesia Java area. The results showed that this model enables to pay enough compensation for the residents in case of earthquake disasters, and, enables to raise the wage of the local engineers by PP-band retrofitting business. Therefore, this model gives incentive of retrofitting in developing countries.

2. MECHANISM OF MODEL

The proposed model gives incentive of promoting seismic retrofitting to both the government and the residents by eliminating their retrofitting cost. In this model, the insurance companies will bear the retrofitting cost, and, at the same time, the retrofitted houses will be insured for free. In addition, when the houses were damaged by the earthquake in the future, insurance companies will promise to pay higher compensation to those who have performed retrofitting than those who have not. On the other hand, the insurance companies will receive reinsurance money from the government when the retrofitted houses were damaged by the earthquake. The government will pay the reinsurance money in range of the reduced amount of expenditure due to retrofitting in advance. The reinsurance money will cover the retrofitting cost and the interest because the reconstruction expenses will be reduced greatly due to retrofitting. Figure 1 shows the expense share in the proposed model. The advantages of this model are that 1) the damage by the future earthquake can be reduced drastically, 2) the residents can perform retrofitting and be insured for free, 3) the government will not have to prepare a huge budget for retrofitting in advance, and 4) the government will not have to decide the priority of the selection of the retrofitting area because the insurance companies will do that based on their business viewpoints.

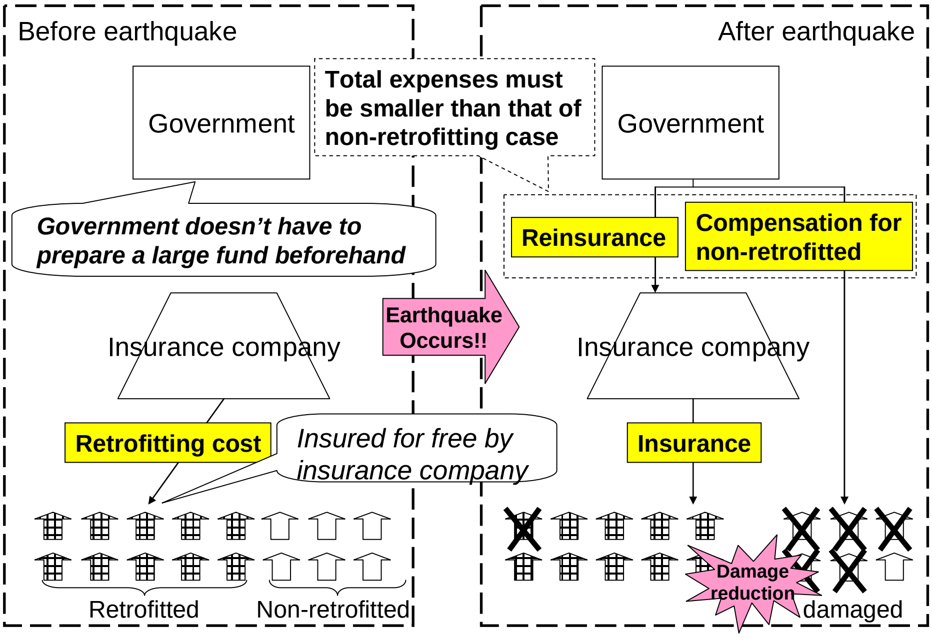

Figure 1: Expense share in proposed model

3. MODEL EFFECT ANALYSIS METHOD

3.1 Outline of model effect analysis method

In order to analyze the effect of the model, the possible compensation for the residents and the possible wage for the local engineers, under the condition that the model is valid, were estimated. In this study, case study was done in Iran Bam area, Pakistan Kashmir area and Indonesia Java area. A hypothesis was made that the model is valid under the condition as follows:

$$(I) < (D) \qquad (1)$$

where (I) is retrofitting promotion cost, and (D) the reduced amount of housing reconstruction expense.

Figure 2 shows the estimation flow of (I) and (D). (I) and (D) were estimated from the scenario earthquake damage (building damage and human loss), the government's compensation (for housing reconstruction and casualties) data of the past earthquake disasters (Iran Bam 2003, Pakistan Kashmir 2005 and Indonesia Java 2006) and the retrofitting cost of PP-band method.

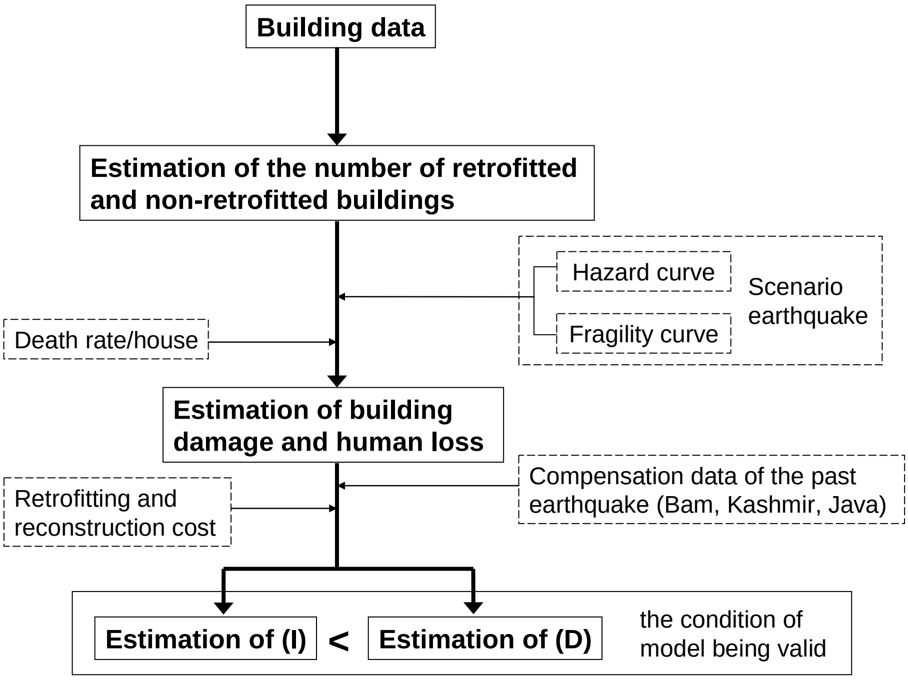

Figure 2: Estimation flow of (I) and (D)

3.2 Earthquake damage estimation

Earthquake damage was estimated by calculating the probability of buildings being damaged by the earthquake in the future (P), as follows:

$$P = \int_{-\infty}^{+\infty} HF ds \cong \sum_{s} H_s F_s \tag{2}$$

where S is seismic intensity, H_s the probability of earthquake (intensity S) occurring at least once in 50 years, and F_s the fragility of building against earthquake (intensity S).

Occurrence probability (H_s), as shown in Figure 3, was calculated by multiplying earthquake occurrence probability of intensity S in 50 years by the number of times the earthquake occurred. Because of lack of data of the target areas, hazard curve of Japan (Japan Seismic Hazard Information Station, 2008) and earthquake frequency in Japan were substituted for these two. (H_s) was calculated for exceed probability 10 % in 50 years of MMI (Modified Mercalli Intensity) 6.5, 6.7, 6.8, 7.2, 7.5, 7.6, 7.8, 7.9, 8.1, 8.2, 8.4, 8.6, 8.7, 9.0 and 9.7, so as to apply to various areas with different earthquake potentials. For example, the earthquake potential of Iran Bam area is MMI 7.33-8.66 of exceed probability 10% in 50 years.

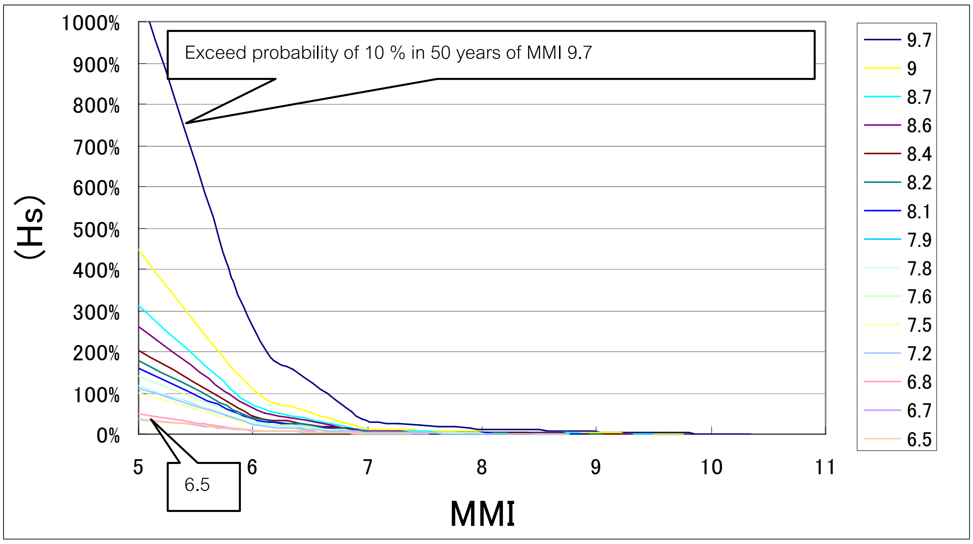

Figure 3: Probability of earthquake occurring at least once in 50 years

Fragility of building (F_s), as shown in Figure 4, was estimated by standard normal distribution formula as follows:

$$F_s = \int_{-\infty}^{s} e^{\{-\frac{(s'-\mu)^2}{2\sigma^2}\}} ds' \qquad (3)$$

where S is seismic intensity.

(Fs) represents the damage rate of the buildings as a group in certain area, respect to MMI. Fragility curves as shown in Figure 4 for Iran Bam (collapse), Pakistan Kashmir (collapse and partially damaged), Indonesia Java (collapse) and PP-band retrofitted (collapse and partially damaged) were used (JICA, 2000; Iritani et al., 2007).

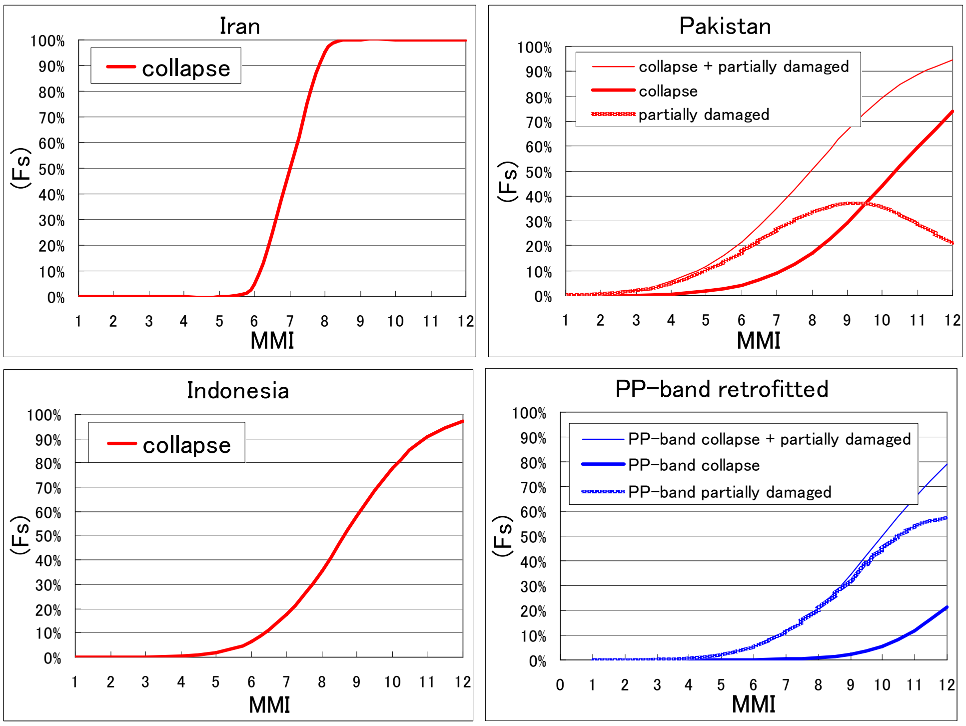

Figure 4: Fragility of building

From the above (H_s) and (F_s), probability of buildings being damaged by the earthquake in the future (P) was calculated as shown in Figure 5.

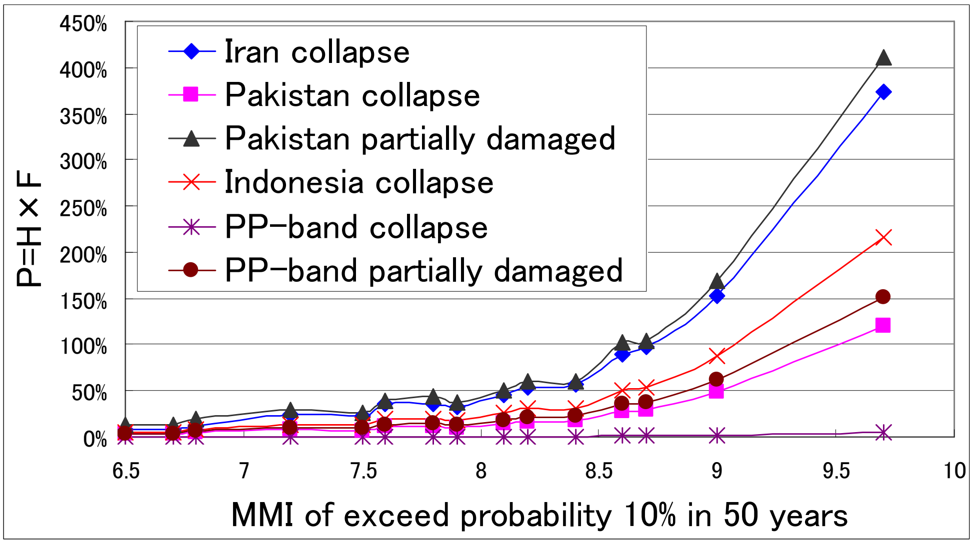

Figure 5: Probability of buildings being damaged by the earthquake

3.3 Compensation and retrofitting cost

Compensation for earthquake damage involves reconstruction cost and compensation for casualties. Table 1 shows the compensation data used in this study, obtained from the data of recent earthquake disasters (Iran Bam 2003, Pakistan Kashmir 2005, Indonesia Java 2006).

Table 1: Compensation for reconstruction and casualties

Compensation	Reconstruction [yen]	Casualties [yen]
Iran	218,000	104,000
Pakistan	379,000	180,000
Indonesia	383,000	172,000

Since PP-band method construction can be carried out by the residents, “resident construction” cost and “engineer construction” cost were assumed for retrofitting cost of PP-band method, as shown in Table 2. Resident construction cost means material cost, and engineer construction cost means material + construction cost of PP-band method. Construction cost corresponds to the local engineers’ wage (EERI, World Housing Encyclopedia, 2007).

Table 2: Retrofitting cost of PP-band method

Retrofitting cost	Iran[yen]	Pakistan[yen]	Indonesia[yen]
Resident construction	7,120	3,370	7,120
Engineer construction	67,180	26,770	27,440

4. RESULTS AND DISCUSSION

Under the condition that the model is valid, the possible compensation for the residents (resident construction type) and the possible wages for the local engineers (engineer construction type) were estimated. Wages for the local engineers were estimated under the condition that residents will receive the same amount of money for compensation as reconstruction cost. Figure 6 shows the results of the case in Iran.

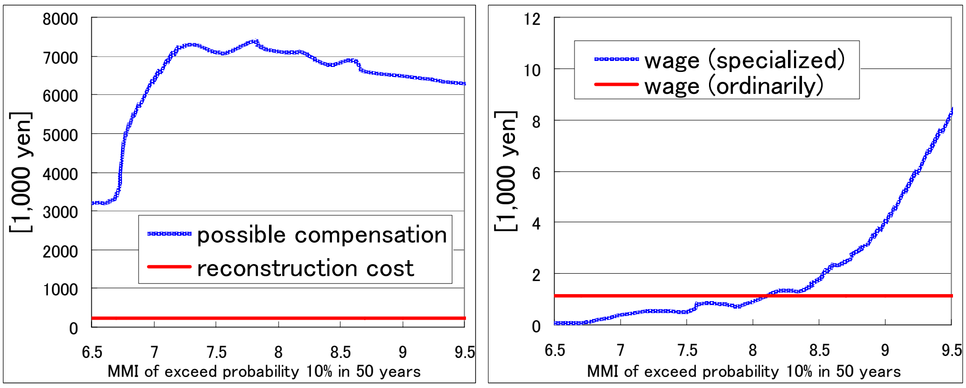

Figure 6: Possible compensation (left) and wage (right), Iran

In case of Iran, in resident construction type, up to about 7,000,000 yen of compensation was possible for residents, which is enough for reconstruction cost of 218,000 yen (Figure 6, left). In engineer construction type, with the condition that the earthquake potential is over MMI 8.2 of exceed probability 10 % in 50 years, even if the residents will receive enough compensation for reconstruction (= 218,000 yen), the construction cost of PP-band method (= wages for PP-band engineers) can be raised than the ordinarily wages of local engineers (Figure 6, right).

5. CONCLUSION

The results show that this model gives incentive to both the residents and the local engineers. In this model, the residents can perform retrofitting and can be insured for free. In addition, the residents can accept enough compensation for reconstruction in case if their houses were damaged by the earthquake. For local engineers, raising wages for PP-band method construction is possible. For the government, they will not have to prepare retrofitting cost in advance. At the same time, this model will not cause insurance companies any losses. These are all incentives for promoting seismic retrofitting in developing countries. Our future aim is to estimate the expenses in detail by considering indirect damages.

REFERENCES

Earthquake Engineering Research Institute, 2007. *World Housing Encyclopedia*.

JICA, 2000. *The Study on Seismic Microzoning of the Greater Teheran Area in the Islamic Republic of Iran*.

National Research Institute for Earth Science and Disaster Prevention, 2008. *Japan Seismic Hazard Information Station*.

Sathiparan Navaratnarajah, Paola Mayorca, Nesheli Kourosh Nasrollahzadeh and Kimiro Meguro, 2005. *Evaluation of retrofitting masonry structures with polypropylene band meshes by means of diagonal compression tests*, the Proceedings of the JSCE Annual Meeting.

Satoshi Iritani, Paola Mayorca and Kimiro Meguro, 2008. *Proposal of a system to promote retrofitting of vulnerable masonry houses in developing countries*, Bulletin of Earthquake Resistant Structure Research Center No.41, 55-60.

STIFFNESS CHARACTERISTICS OF VANISHING MIXTURES

Q. HUNG TRUONG, YONG-HUN EOM and JONG-SUB LEE
Civil, Environmental and Architectural Engineering,
Korea University, Seoul, 136-701, Korea
jongsub@ korea.ac.kr

ABSTRACT

Particle dissolution is a natural phenomenon that may happen and cause changes in microstructure of particulate media, such as the increase of local strain and permeability. The study focuses on stiffness characteristics of vanishing materials modeled by particulate mixtures of sand and salt at different fractions. Experiments are carried out in a conventional oedometer cell integrated with bender elements. Saturation process used to dissolve the salt particles in the mixtures are implemented at different confining stresses. Axial deformations and shear wave signals are recorded after each loading stage and during saturation process. Experimental results showed that microstructural changes due to transformation of form of particles were greatly effect to the stiffness of mixtures. Specimens prepared by sand and salt are proved to be able to provide a valuable insight in macrostrucral behaviors of the mixtures.

1. INTRODUCTION

Geology, climate and environment have a great influence on formations of soil. There may be ingredients of soluble minerals in engineered soils that may be under the foundation or inside an earth structure, etc. A vanishing mixture usually consists of soil particles and vanishing materials, such as salt, gypsum, anhydrite, dolomite, and halite, etc. Effects of the dissolution materials in engineering mixtures have been studied by many researchers in various aspects:

- Craft et al. (2005) developed a guide to planning seepage chemistry investigations for dam effected by dissolution of soluble materials.
- Fam et al. (2002) addressed mechanical properties changes of sands subjected to local strain increase created by washing salt in sand-salt mixtures.
- Azam (2000) focused on compressibility and collapse of calcareous clay represented by mixtures of clay and highly soluble calcium sulphate.

Changing phase of particle may play an important role in mechanical behaviors of soil. Dissolution of particle, which may cause changes in microstructure of particulate media, produces the local void increase. Mechanical properties of material in macroscale may be subjected to a large effect as loosen. Besides, void ratio increase will increase the permeability of soil which may raise problem for an earth structure with the present of vanishing mixtures inside.

This study addressed the small and large strain engineering properties of the soluble mixtures in K_o-loading conditions by using a conventional cell equipped by bender elements. Experiments using oedometer cell with bender element have been widely used and graduatedly become one of standard tests for soil properties. Many researchers contributed to the developments of this test:

- Fam and Santamarina (1995) studied the small strain stiffness of sand in K_o loading condition.
- Yun and Santamarina (2005) captured the changes in small strain stiffness of loose soil during decementation and softening process and collapse.
- Lee et al. (2007a) focused on effect of mica to mechanical behaviors of sand soils.
- Lee et al. (2007b) studied behaviors of rigid-soft mixtures (fine sand-rubber particle) during cementation and uncementation, decementation.

This paper starts with the experimental program that was performed on sand-salt mixtures to demonstrate the effect of dissolved material in mixtures. Following is experimental results and discussions. Finally, some conclusions are cited out.

2. EXPERIMENTAL PROGRAM

2.1 Sample preparation

Uniform, fine, quite round sand (Jumunjin 40/50 sand) with D50= 0.36mm, Gs= 2.62 was used to evaluate the effect of vanishing material to mechanical behavior of soils. Uniform, fine, hexagonal grain salt (50/70) with D50= 0.25mm, Gs= 2.16 was mixed with sand at 0, 2, 5, 7, 10% mixing ratios in volume. Microscopic particle images of the sand and salt particle are shown in Figure 1. Salt particles were selected finer than sand particles to minimize the corresponding change in total volume during the salt dissolution stage. Specimens are prepared at same initial void ratio for saturation to create local void due to salt dissolution at different confining stress during K_o loading.

The sand is oven dried overnight before testing. Sand and salt were placed in two papers, and then they were poured at the same time to a container to create homogeneous specimens. Then, the mixture is mixed in 5 minutes and funneled carefully into the oedometer cell in 5 layers. The same weight of mixtures is added to form each layer when tamping is used to attain initial designed dense condition (e_0= 0.76).

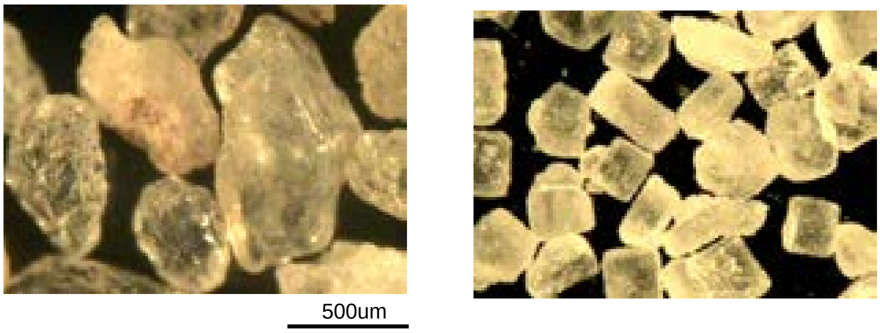

Figure 1: Sand and salt particle images: (a) sand; (b) salt

2.2 Device

The effects of local void on the small and large strain mechanical properties of the materials were explored by implementing shear wave measurement in a conventional oedometer cell equipped with bender element. The oedometer cell is 74mm in diameter and 63mm in height. The bender elements integrated on the top cap and the bottom plate of the oedometer cell were used to excite and capture shear waves. The dimension of bender elements is about 5 mm in cantilever length and 5 mm in width. Figure (2) shows the detailed sketch of the experimental system. Discussion on bender element configuration and performance can be referenced in Lee and Santamarina (2005)

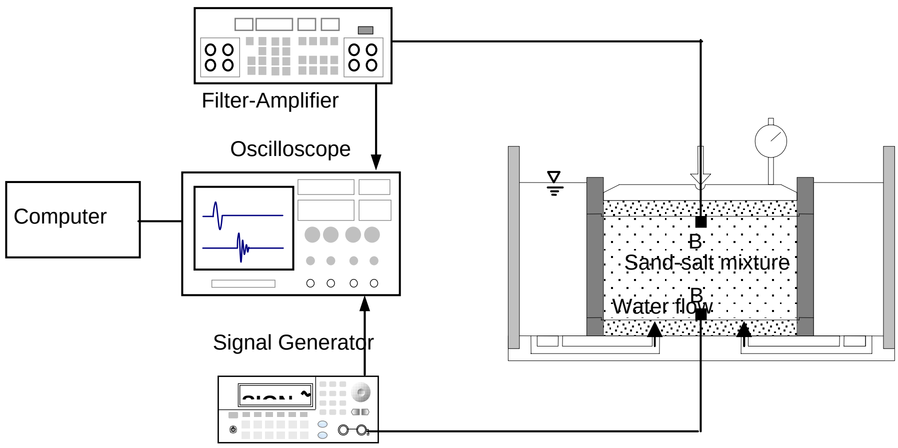

Figure 2: Experiment setup

The 20 Hz square signals were delivered from the signal generator (Agilent 33220A) to the sourced bender element. Shear waves emitted from the source and traveled through the specimen were captured and transformed into the electrical signal in the receiver bender element. The electrical signal was fed through a filter-amplifier (Krohn-Hite 3944). The cutoff frequency for the low-pass filter is 100 kHz, ten times grater than the highest resonance frequency to ensure the Nyquist condition. The filtered and amplified signal was digitized through an oscilloscope. Note the 1024 signals were usually averaged to remove the high frequency uncorrelated noise. Since this technique takes time, at least 10 second, for each stable and accuracy measurement, the signals during saturation stage to dissolve soluble materials ware captured without averaging in the first 30 minutes. Well designed of shielding to prevent the emissions of electromagnetic waves can help to obtain clear signals.

2.3 Test procedure

K_o loading with three stages, loading, unloading and reloading, were carried out. The normal stress was doubled at each loading stage during loading test. Four specimens were saturation to dissolve salt at different effective confinement stress level and one without salt dissolution (i.e. testing is conducted in dry condition). The other five specimens, with the salt fraction changed from 0, 2, 5, 7, 10% are carried out at the same confining stress for dissolving. The electrolyte NaCl 0.01M is slowly and carefully poured into consolidation cell to minimize the total change of specimen due to saturation process. Salt grains were dissolved at the confine stresses of 41, 80, 158 and 315kPa. Each loading stage lasted for 30 minutes except the loading stage with saturation lasted for 1000 minutes.

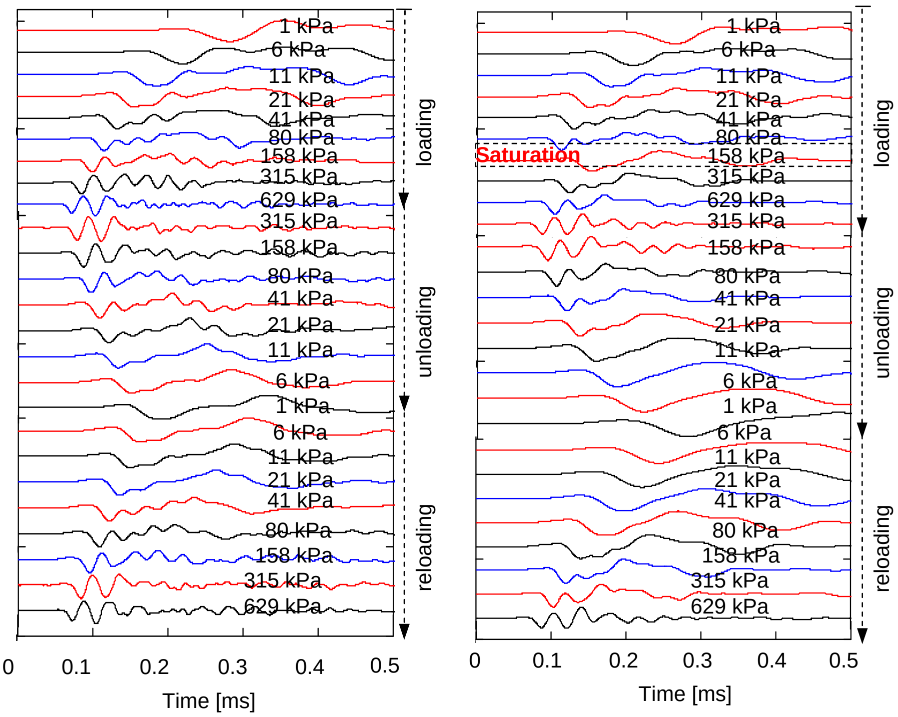

Figure 3: Shear wave signals gathered during loading, unloading, and reloading stages: (a) sand-salt specimen without salt dissolution; (b) sand-salt specimen with salt dissolved at 79.90kPa. The numbers in figure denote the applied vertical effective stress [kPa].

2.4 Shear wave velocity

Shear wave is recorded at the end of each loading or unloading stage. Shear wave velocity is calculated based on the travel distance and travel time. The travel times, from tip to tip of source and receiver, are picked from recorded traces in consideration of near field effects (Lee and Santamarina 2005). The travel distance L is equally to the tip-to-tip distance between these bender elements. Finally, the shear wave velocity is computed as Vs = L/ttip-to-tip.

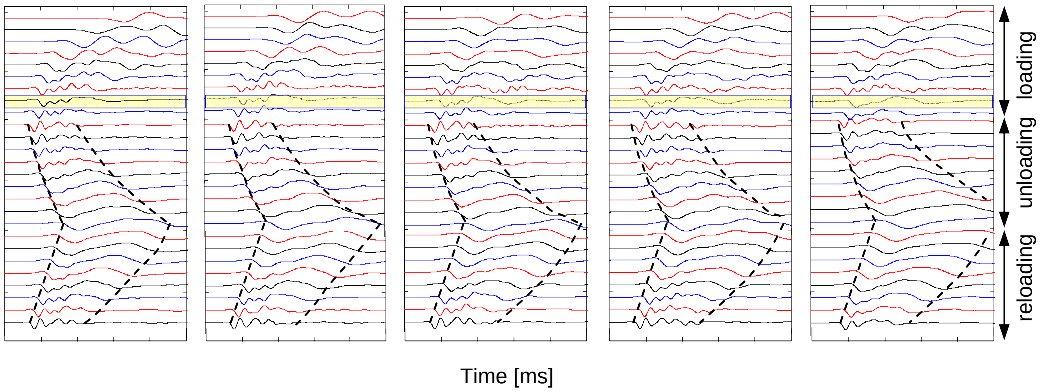

(a) sf=0% *(b) sf=2%* *(c) sf=5%* *(d) sf= 7%* *(e) sf = 10%*

Figure 4: Shear wave signatures of specimens with different salt fractions saturated at same confining stresses.

3. RESULTS AND DISCUSSIONS

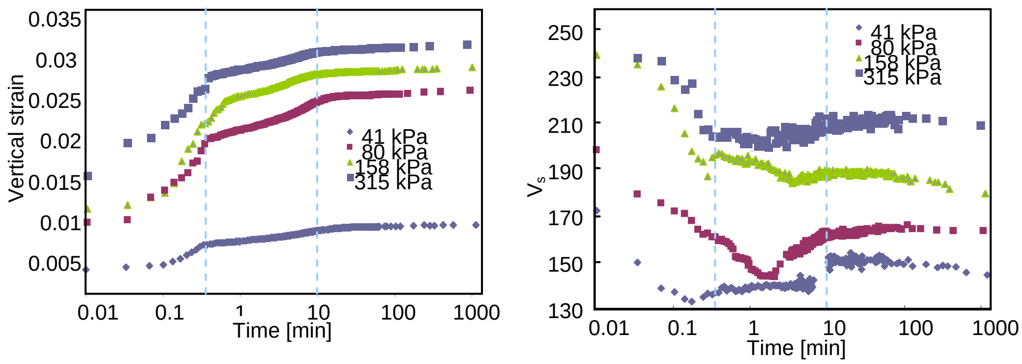

Figure 5: Saturation stage: (a) Axial strain versus time; (b) Shear wave velocity versus time for salt particle dissolved at different loading stages. The sketched solid line shows the general trend of shear wave velocity during saturation stage.

The measured shear wave signals were plotted versus time during loading, unloading and reloading in specimens with and without salt dissolution in Figure 3. The following observations can be made:

- The increase in travel time after vanishing process denotes the decrease in small strain shear stiffness of sand specimen.

- The shear wave signals after the salt dissolved is smoother than the signals obtained before dissolution happen and in the specimen without dissolution. It is because that the salt particles (finer than sand) were dissolved, the specimen was more homogenous after saturation. The vanishing of salt, finer particle, worked as a high pass filter here.

The signatures of shear waves of vanishing mixtures with different salt fractions at the same confining stress for saturation process are shown in Figure 4. Since the salt fraction increase, the band of response signals are increase. It is right because the specimen become softer as the salt fraction increases.

After the saturation, all salt particles dissolved. Although the tip-to-tip distances between top and bottom bender elements reduce due to the settlement caused by the salt vanishing, the travel times of shear wave still increase. It means that there is a reduction on effective stress acting normally on bender elements and/or an increase in real travel length of shear wave. The travel length of shear wave may increase due to the increase of local voids. Here, the specimen is sand, the effective stress keep constant before and after the salt dissolution due to its high permeability properties. Therefore, the real travel length of wave in particle level increases due to the particle contact area reduces. The effect of density is not a key factor here because when the salt particles dissolved, the sand particles moved to the new void area. Even though, the void occupied by sand is not so much because the sand is bigger than salt. So that, the density may be reduce a little.

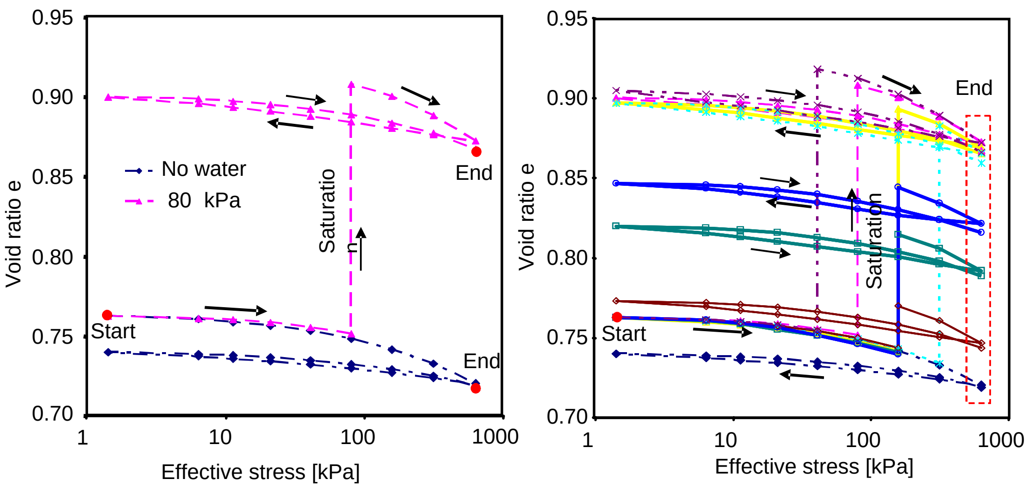

Figure 6: Consolidation test for sand-salt mixtures :0, 2, 5, 7, 10% during loading stage with and without salt dissolved at effective stress of 41, 80, 158, 315kPa.: (a) typical e v.s. effective stress; (b) e v.s. effective stress.

Figure 5 shows the change of axial strain and shear wave velocity during the saturation stage. The history of shear wave velocity during saturation stage can be divided into three periods. In the first period, from

0~0.2 minutes after saturation started, the axial strain and the velocity of shear wave tremendously reduced. It means that there is a large effect of the water flow and the vanishing of salt particle on the specimen during this period. In the second period, from 0.2~10 minutes, since there is only effect of salt dissolution, the shear wave velocity slowly reduced and increased. Firstly, the shear wave velocity reduced because the effect of salt vanishing overwhelmed the effect of loading, the void ratio increase. Then the local void ratio reduced because the loading was prevailing. As a result, the shear wave velocity was increase. After 10 minutes, shear wave velocity almost gets to a stable value because the salt dissolution process almost finished. There is no or very small effect of salt dissolution. The effect of salt vanishing largely happened in the first ten minutes. In this measurement, not only the effect of local void ratio changed due to salt dissolution but also the water diffusion had been investigated.

The evolutions of void ratio and shear wave velocity are plotted versus effective stresses for the specimens with and without salt dissolution in Figure 6 and 7. It can be seen that:

- Void ratio always increases and shear wave velocity always decreases after saturation stage at any load steps of this sand-salt mixture.
- Compression and recompression coefficients, cs and cc, of specimens with and without salt dissolved are nearly same.
- While the shear wave velocity versus effective stress shown the unstable value among specimens, the void ratio versus effective stress graphs show a consistent value. It means that the shear wave velocity can detect the non-homogeneous level of specimen locally while the The void ratio versus effective stress graph could not show the non-homogenous of specimen

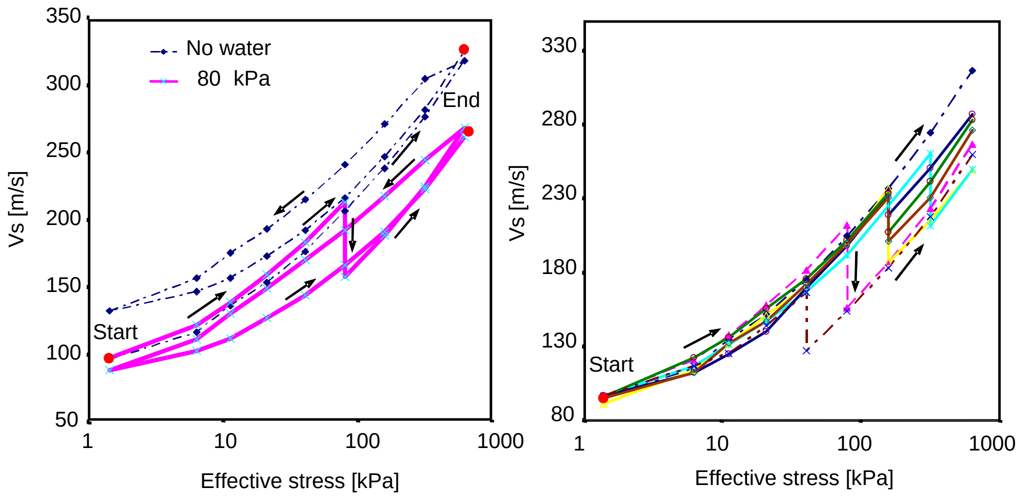

Figure 7: Consolidation test for sand-salt mixtures: 0, 2, 5, 7, 10% during loading, unloading and reloading stage for specimens with and without salt dissolved at 41, 80, 158, 315kPa: (a) typical Vs vs. effective stress for 2 specimens: no saturation and saturated at 80 kPa; (b) Vs vs. effective stress in loading stage for all specimens.

4. CONCLUSIONS

Changes in small-strain shear stiffness in k0 loading of sand subjected to local void ratio increase were investigated by conducting shear wave measurements in conventional oedoemeter cell with bender elements. The main observations from this study follow:

- During saturation stage in which the salt particle dissolved, shear wave velocity reduces dramatically at the first 0.2 minutes, and then reduces and increase slowly at the next 10 minutes, and finally gets to stable. The effect of salt dissolution to specimen almost happens at the first ten minutes.
- Smaller particle vanishing works as a high pass filter.
- Shear wave measurement clearly captures the microstructural changes due to particle dissolution.
- Sand-salt mixture is useful for laboratory test on controlled artificial specimen.

ACKNOWLEDGMENTS

This work was supported by BK-21 Global Leaders in Construction Engineering, Korea University, Korea.

REFERENCES

Azam, S., 2000. *Collapse and compressibility behaviour of arid calcareous soil formations*. Bulletin of Engineering Geology and the Environment, Springer Berlin, 59(3).

Craft, D., Cain, C. and Sullivan, C., 2006. *Seepage Geochemistry and Mineral Dissolution at Clark Canyon Dam, Pick-Sloan Missouri Basin Project, East Bench Unit, Montana*. Technical Memorandum 86-6829010, U.S. Department of the Interior - Bureau of Reclamation, Denver, Colorado, p 48.

Craft, D., 2005. *Seepage Chemistry Manual*. Report DSO-05-03, US Department of the Interior, Bureau of Reclamation, Dam Safety Technology Development Program, Denver, Colorado, p 76 pp.

Fam, M. A., Cascante, G., and Dusseault M. B., 2002. Large and Small Strain Properties of Sands Subjected to Local Void Increase. *J. Geotech. Geoenviron. Eng.*, ASCE, 128(12), 1018-1025.

Lee, J. S. and Santamarina, J. C., 2005. Bender elements: performance and signal interpretation. *J. Geotech. Geoenviron. Eng.*, ASCE, 131(9), 1063-1070.

Lee, J.S., Guimaraes, M., and Santamarina, J. C., 2007. Micaceous sand: Fabric, stiffness, and strength. *Journal of Geotechnical and Geoenvironmental Engineering*, ASCE, 133(9), 1136-1143.

Lee, J.S., Dodds, J., and Santamarina, J.C., 2007. Behavior of rigid-soft particle mixtures. *Journal of Materials in Civil Engineering*, ASCE, 19(2), 179-184.

Santamarina, J. C., Klein, K. A., and Fam, M. A., 2001. *Soils and Waves –*

Particulate Materials Behavior, Characterization and Process Monitoring. JohnWiley and Sons. New York.

Yun, T.S. and Santamarina, J.C., 2005. Decementation, softening and collapse: Changes in small-strain shear stiffness in Ko-loading. *Journal of Geotechnical and Geoenvironmental Engineering*, ASCE, 131(3), 350-358.

OD VARIATION ANALYSIS ON THE TOKYO METROPOLITAN EXPRESSWAY USING ETC-OD DATA

HIROAKI NISHIUCHI
Doctoral Course of Department of Civil Engineering,
University of Tokyo, JAPAN
nishiuch@iis.u-tokyo.ac.jp

ABSTRACT

This research analyzes origin-destination traffic volumes (OD) on the Tokyo Metropolitan Expressway (MEX). The aim of this study is to understand the characteristics of daily OD variation since such kind of knowledge is crucial for short-term OD prediction. The OD data in this study is obtained by electronic toll collection (ETC).

Aggregated 12 hours (7am to 7pm) and hourly OD were analyzed by analysis of variance (ANOVA) and multiple comparisons. Results show, the main factor of 12 hours' OD variation is the day of the week, and hourly OD varies by the day of week. Therefore, day of week and time of day are used as explanatory variable for estimating OD volumes using a Bayesian Network. The estimation results show that the model is able to estimate average OD volumes.

1. INTRODUCTION

Recently, usage of dynamic traffic information is recommended to mitigate the traffic congestion by Dynamic Traffic Management. At the Tokyo Metropolitan Expressway (MEX), they are developing real time traffic simulation system, using dynamic origin-destination (OD) volumes. Current OD traffic volumes are based on census survey result, carried out at one day in several years. Therefore, it is difficult to reflect the real time traffic condition in the simulation system.

In Japan, electronic toll collection (ETC) is applied on expressways. Drivers with an ETC on-board unit in their car, do not have to stop at toll gates and the payment is done electronically when the vehicle passes the sensors. The ratio of ETC users smoothly increased, being now 80% of drivers on MEX (2008). The system records the usage of on-ramps and off-ramps. With that, we can acquire the origin and destination of drivers. Aggregating this information, we obtain time-dependent OD volumes which have been a difficult task until now.

Since OD Data from ETC records are time-dependent and huge in amount, we can identify the characteristics of OD volume variation and the significant factor for that variation. Researchers e.g. IIDA (1981), RAKHA (1995) have tried to identify these through link flow variation. However, without measured OD data there was no final proof. Therefore, this research aims to be a foundation for future OD volume estimation from historical OD pattern.

In this paper, characteristics of OD variation are discussed with daily OD variation using 12 hours aggregated and hourly OD volume. Then this knowledge will be used for short-term OD prediction which is still in a preliminary stage.

2. ETC-OD DATA

ETC-OD Data used here is collected from June 2006 to December 2006 (157days in this period). Time-period of data collection is 12 hours (from 7am to 7am). In this research, we used aggregated ETC-OD Data as 30 minutes, 1hour and 12hours aggregation.

Toll system of MEX is used fixed price system. Therefore, price of toll is decided depending on toll area e.g. Tokyo toll area, Kanagawa toll area and Saitama toll area. That means when driver travel from Tokyo to Kanagawa, they need to pay again at mainline toll gate which is located on border of each toll area. However, we focused on trips in same price area in this study e.g. travel in Tokyo toll area. Using above definition of data, number of target OD pair become 6729.

3. DAILY OD VARIATION

3.1 Characteristics of daily OD variation

To know how 12hours OD traffic volume normally varying, coefficient of variance is evaluated. Coefficient of variance is calculated by (1).

$$CV_i = \frac{\sqrt{Var_i}}{E_i} \tag{1}$$

$$Var_i = \frac{\sum_{n=1}^{N}(E_i - x_i^n)^2}{N} \tag{2}$$

where,

CV_i : Coefficient of Variance of OD pair i

Var_i : Variance of OD pair i

E_i : Averaged 12 hours OD traffic volume of OD pair i

x_i^n : 12 hours OD traffic volume of OD pair i of day n

N : Number of available days = 157days in this paper

Figure 1 shows the relationship between averaged weekday's 12hours OD traffic volume and its coefficient of variance, and cumulative number of OD pair. Blue dot represents one OD pair, and pink line is cumulative number of OD. From the figure, if averaged 12hour OD traffic volume is low level, its coefficient of variance is high, but if OD traffic volume level is increase, its coefficient of variance is low level. And according to shape of cumulative number of OD, about 90% of OD pair are less than 120[veh/12hours]. That means OD traffic volume is normally varying e.g. when OD traffic volume is greater than 500[veh/12hours], coefficient of variance is around 10%.

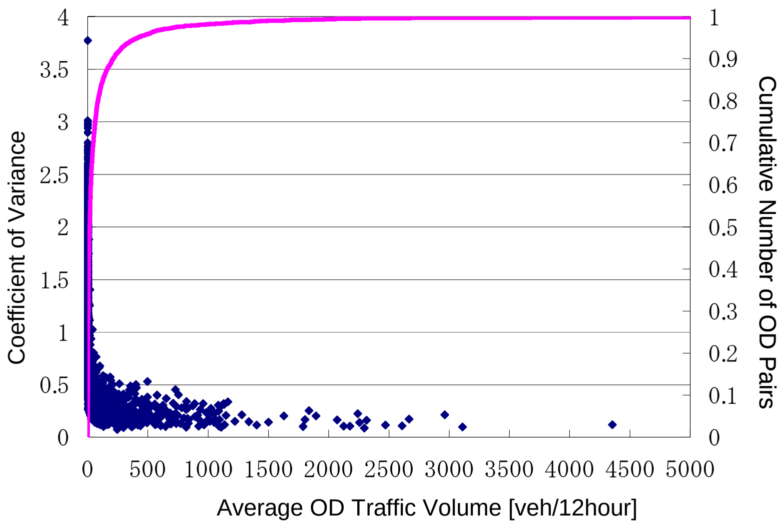

Figure 1: Relationship between averaged weekday's OD traffic volume and its coefficient of variance, and cumulative number of OD pair

3.2 Factors of daily OD variation

The factor of 12 hours OD variation is specified in this section. Following indexes are chosen as the factor of daily OD variation. To confirm they can be the factors, one-way Analysis of Variance (ANOVA) is implemented. The output of ANOVA tells us whether there is significant difference between categories of each factor. Therefore, if ANOVA shows significant difference to each category of the factors, the factors affect to variation of 12 hours OD traffic volume.

Factor 1: Weekday and Holiday
Factor 2: Weekdays (Monday, Tuesday, Wednesday, Thursday, Friday)
Factor 3: Holidays (Saturday, Sunday, Holidays including middle of August*)
Factor 4: Daily inflow of MEX
Factor 5: Daily amount of jam of MEX
Factor 6: Season
Factor 7: Daily amount of rain at Tokyo
Factor 8: Daily number of accident at MEX

* Many Japanese take holiday during middle of August.

Since Number of target OD pair here is 6729, results should be different tendency depending on level of average 12hours OD traffic volume. Therefore grouping by average 12 hours OD traffic volume are implemented. The definition of grouping and number of OD at each groups are shown in Table 1.

Table 1: Number of OD at each group

Group (Definition of group)	Number of OD pair
High ($E_i \geqq 500$ [veh/12hour])	120
Middle ($500 > E_i \geqq 50$ [veh/12hour])	1077
Low ($500 > E_i \geqq 50$ [veh/12hour])	5532

Figure 2 shows the ratio of number of significant OD at each factor. From the results, “Weekday vs. Holiday”, “Weekday”, “Holiday”, “Daily Inflow” and “Daily Amount of Jam” are significantly different distribution of OD traffic volume by each category, especially High and Middle of OD traffic volume groups.

On the other hand, “Season”, “Rain” and “Accident” are not significant at all of group. “Season” was difficult to show the significance since number of days for analysis is 157 days. Therefore, analyzing “season” by adding data of another month is strongly recommended. In case of “rain” and “accident”, they are also possible to have impacts to traffic in more short time-period. However 12 hours data are evaluated here, therefore when dynamic OD traffic volume is evaluated, these factors’ impact should be considered.

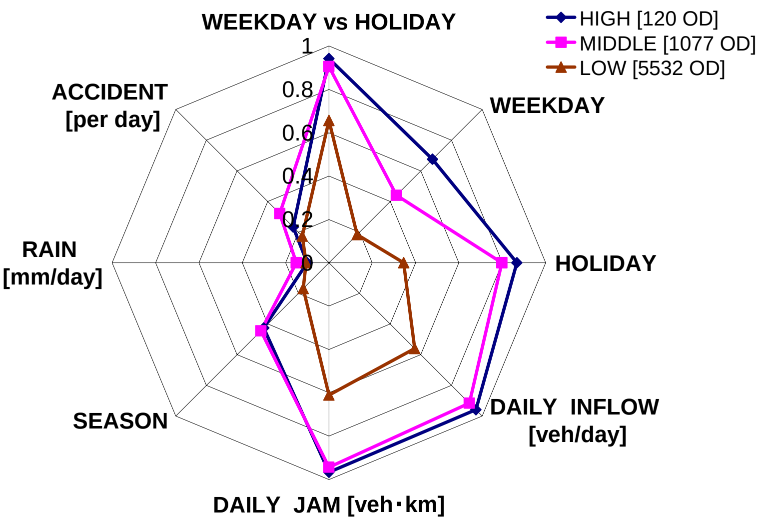

Figure 2: Ratio of number of significant OD at each factor

3.3 The difference between each day of weeks

In previous section, the analysis showed that weekdays are important factor of daily OD variation. However, ANOVA didn't mention which combinations of day of week are significantly different. Therefore, multiple comparisons are implemented to see the difference between all of combinations of day of week.

Table 2 shows the number of OD pair which is significant different combination of day of week. From the table, if Friday is compared with another day of week, then more than 20% of OD pairs have statistically differences in case high and middle level group. However Thursday and Friday are not significantly difference, and there is no significantly difference in low level of OD traffic volume group. It can be considered that most of low traffic volume' OD are varying as just random, therefore it is difficult to define normal distribution and to find significance.

Table 2: The ratio of number of significant OD by multiple comparisons

	MON vs TUE	**MON vs WED**	**MON vs THR**	**MON vs FRI**	**TUE vs WED**	**TUE vs THR**	**TUE vs FRI**	**WED vs THR**	**WED vs FRI**	**THR vs FRI**
HIGH	0.10	0.14	0.23	0.59	0.04	0.06	0.43	0.03	0.35	0.13
MIDDLE	0.03	0.07	0.10	0.31	0.03	0.03	0.21	0.03	0.24	0.08
LOW	0.03	0.00	0.03	0.08	0.02	0.01	0.04	0.02	0.05	0.03

On the other hand, RAKHA (1995) mentioned that Monday also should have significant difference with from Tuesday to Thursday. However, the result here Monday is not really different with other days. The one of reason can be problem of aggregation by 12hours, and then it is possible that the significance can appear using OD data aggregated by time of the day. Therefore same analysis using hourly OD traffic volume is implemented. Figure 3 to 5 shows the results of multiple comparisons by time of the day, and graphs shows the results in case "Monday vs. Tuesday", "Monday vs. Wednesday" and "Monday vs. Thursday".

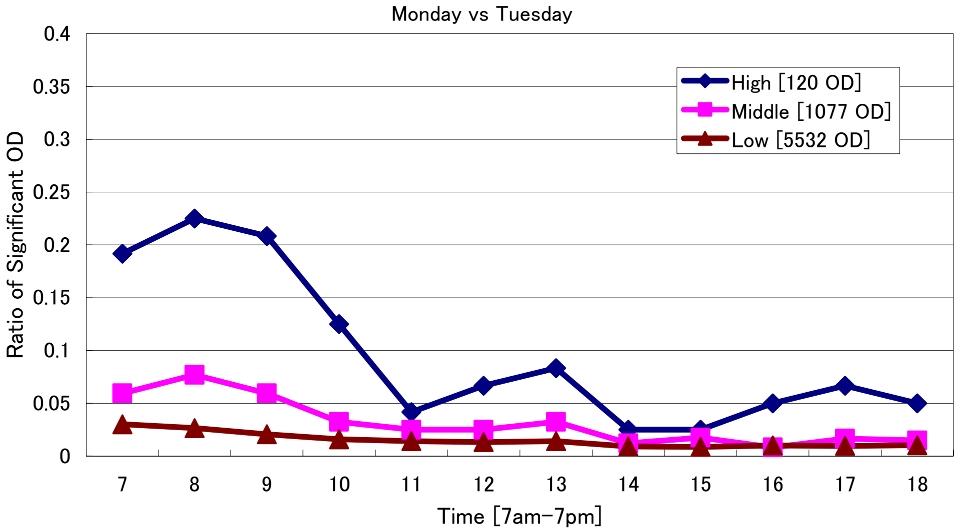

Figure 3: Ratio of number of significant OD by time of the day [Monday vs. Tuesday]

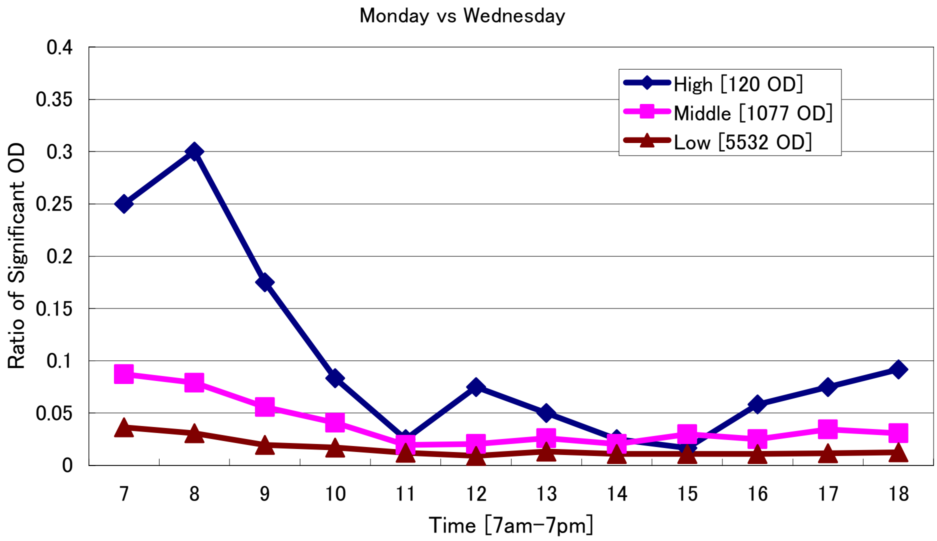

Figure 4: Ratio of number of significant OD by time of the day [Monday vs. Wednesday]

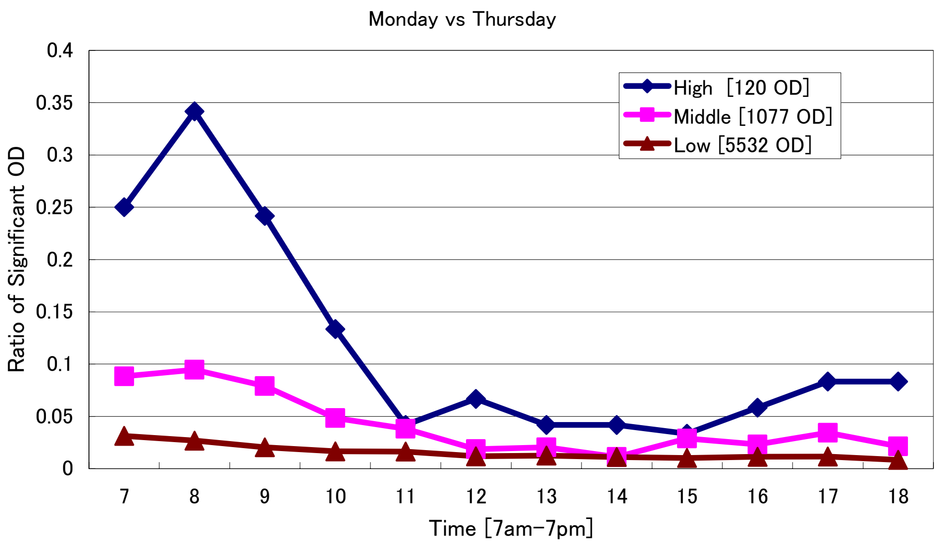

Figure 5: Ratio of number of significant OD by time of the day [Monday vs. Thursday]

The results at 7am to 9am in all figures of high level of OD traffic volume group has significant different, but not in another OD group. Therefore, the time of the day is also important factor for explaining OD variation.

4. OD ESTIMATION USING FACTOR OF DAILY OD VARIATION

OD variation is mainly affected by day of the week and time of the day. Therefore, in this chapter, the example of usage of this knowledge is shown by estimating dynamic OD traffic volume using Bayesian Network model.

4.1 Bayesian Network Model

Bayesian Network Model (BN) is the stochastic model by using acyclic network structure as shown at Figure 6. Figure 6 is described a example of BN structure and conditional probability table (CPT) which is output from BN. BN consist by son node and parent node, and parent node's conditional probability is calculated depending on condition of their son node. For example, if we want to estimate x1, it depends on condition of x2, x3 and x4 as CPT in Figure 6.

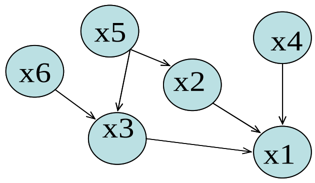

CPT of $P(x1 \mid x2, x3, x4)$

x2		0				1			
x3		0		1		0		1	
x4		0	1	0	1	0	1	1	1
x1	0	0.2	0.3	0.1	0.15	0.6	0.65	0.7	0.8
	1	0.8	0.7	0.9	0.85	0.4	0.35	0.3	0.2

CPT: Conditional Probability Table

Figure 6: Example of Bayesian Network Model and CPT

4.2 OD Estimation using ETC-OD Data

To estimate dynamic OD traffic volume using BN, day of the week and time of the day is chosen as son node of 30 minutes OD traffic volume. The 133days ETC-OD data set are used for calculating CPT. Figure 7 is the BN structure, and the conditional probability of 30 minutes OD traffic volume occur is calculated. And then the expected value of 30min OD traffic volume is calculated using the CPT.

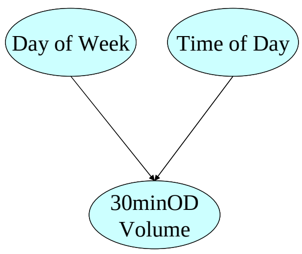

Figure 7: Bayesian Network Model for estimating 30minutes OD

Monday’s 30 minutes OD traffic volume from 7am to 7pm is estimated as shown at Figure 8. The blue line represents an estimation result, and another 3 lines are each Monday’s on December 2006 OD traffic volume profile. The estimation result can follow only the tendency of each Monday’s profile since there is no dynamic information in the model for representing each of the day and the time. And then estimation result couldn’t describe details of OD traffic volume profiles. Therefore, OD estimation using BN including the dynamic information is recommended to improve their accuracy e.g. Travel Time between OD at the time, accident information at the time and so on.

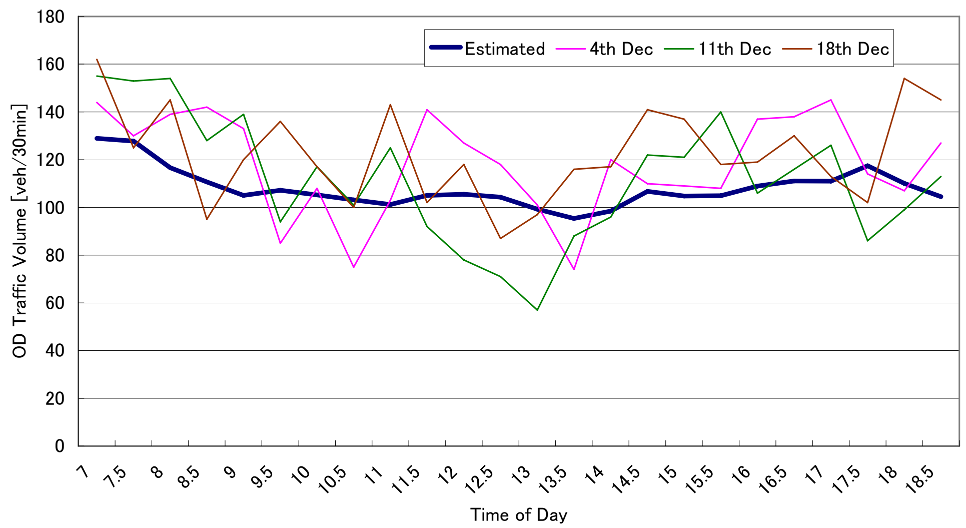

Figure 8: Profile of Estimated OD traffic volume and Monday's OD traffic volume on December 2006

5. CONCLUSION

In this paper, 12 hours OD traffic volume is analyzed to understand the factor of its variation by implementing ANOVA and Multiple Comparisons. ANOVA showed some differences that Weekdays and Holidays are different variation, and weekdays also have different tendency in each day of week. Especially Friday‘s OD traffic volume has different distribution with the other weekdays. And Multiple Comparison using hourly OD traffic volume showed Monday's OD traffic volume is also different tendency with Tuesday, Wednesday and Thursday. Therefore, day of week and time of day were important factor of OD variation.

And OD traffic volume is estimated using Bayesian Network Model. The result could not represent one day's OD traffic volume since dynamic information was not included to the model. Therefore improving the model is strongly recommended through empirical analysis of dynamic OD traffic volume e.g. Temporal-Spatial OD correlation, Impact of traffic condition to OD traffic volume and so on.

REFERENCES

H. RAKHA., M. VAN AERDE, 1995. Statistical Analysis of Day-to-Day Variation in Real-Time Traffic Flow Data. *Transportation Research Record* 1510, 26-34.

Website of Ministry of Land, Infrastructure, Transport, 2008. http://www.mlit.go.jp/road/yuryo/riyou.pdf

Y. IIDA., J. TAKAYAMA., 1981. A Statistical Analysis of Characteristics of Traffic Flow on Expressway. *Expressway and Automobile*, Vol.24, 22-32.

STUDY OF PROPERTIES OF PARA-RUBBER PLATES FOR USING AS THE CAPPING ON CONCRETE SPECIMENS FOR COMPRESSION TEST INSTEAD OF MOLTEN SULPHER

KITTIPONG SUWEERO and PRACHOOM KHAMPUT
Department of Civil Engineering, Faculty of Engineering,
Rajamangala University of Technology Thanyaburi,
Pathumthani, Thailand
siam_macho@hotmail.com

ABSTRACT

This paper aims to study the using para-rubber plate for transferring the force on concrete specimens instead of capping with sulphur. Four formulas for mix design of para-rubber plate are setup. Each formula is mixed in two rolls mill machine and formed the para-rubber plate by Compression Molding. After obtaining the para-rubber plate specimens, the measuring of compression set, tensile strength, % strain, tear strength, hardness of para-rubber plate are performed. Consequently, the para-rubber plates are taken into capping the concrete and tested the compressive strength. These results are compared to that with sulphur capping. From the results, it is found that adding carbon black over 60 phr affects to develop the hardness but the other properties are declined. In testing the compressive strength of concrete with para-rubber plate, it is found that the formula that gives the results close to that using of sulphur is the formula that uses latex at 100 phr, carbon black (grade N330) at 100 phr and calcium carbonate at 50 phr. In this formula, the compressive strength is larger than using sulphur at 7%. This indicates that there is possibility in developing the formula of para-rubber plate for capping material in the future.

1. INTRODUCTION

Normally, there are 2 types of compressive tests of the concrete. One is test on the cubic of size 15x15x15 cm. (BS 1881 part 108) (British Standard Institute, 1983) This method uses widely in Europe. Another method which extremely uses in America, France, Canada, Australia and New Zealand performs on cylinder at diameter 15 cm. and height 30 cm. according to ASTM C192 ((American Society for Testing and Materials, 2001). The tested concrete must be capped with cement paste or plaster cement or sulphur ((American Society for Testing and Materials, 2001). Among three types of capping materials, the sulphur is mostly exploited. However the sulphur is the toxic substance which can harm the respiratory system of the users, then many organizations replace the using of sulphur in capping concrete with the other materials such as synthetic-rubber plate with steel case (see Figure 1a). We can find the synthetic-rubber plate from both aboard (see Figure 1b) and in the country. However the price of synthetic-rubber from aboard is relatively high, then there is an attempt on research the new materials for capping the concrete instead of sulphur (P.M. and R.L., 1988, Grygiell and Amsler, 1977, Khamput and Boksuwan, 2006, Anusiri, 2006) The results from those studies are still unsatisfied. Thus in this research, we look for the formulae of para-rubber (from latex in Thailand) plate. The compressive strengths of purposed rubber plate will be compared to those with sulphur for finding the suitable formula which gives the results close to those using the sulphur.

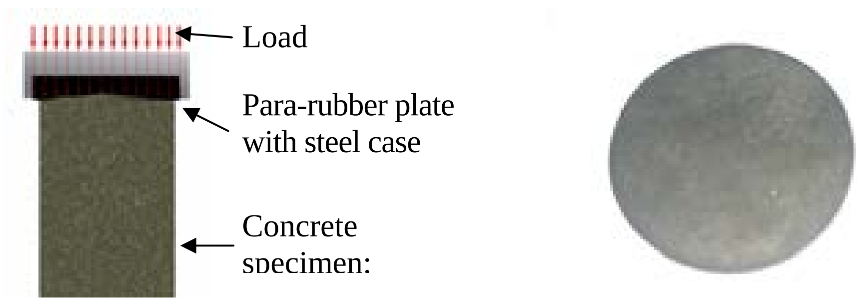

(a) (b)

Figure 1: a) Loading of para-rubber plate with steel case.
b) Fiber reinforced synthetic rubber-plate from aboard.

2. METHODOLOGY

2.1 Materials and equipments

1) Para-rubber no. STR20: the characteristics of this type of para-rubber are

i) There is the double bond.

ii) There is the alpha-methylene which makes the vulcanizing reaction with sulphur. The properties of this para-rubber are shown in Table 1.

2) Sulphur that serves as vulcanizing agent (or curing agent). The benefit of adding sulphur is to make the link between molecules of rubber.

3) Carbon black of four grades according to ASTM D1765 (N220, N330, N550 and N660). The properties of carbon black in each grade are summarized in Table 2.

4) Calcium carbonate ($CaCO_3$).

5) Two-roll mill.

6) Compression Molding.

7) Tension machine.

8) Shore durometer.

9) Universal testing machine.

10) Steel case.

Table 1: Specification of STR 20 Rubber (Sae-Oui, 2004)

Specification	Standard Value
The contaminations that are larger than 44 micron (max%wt)	0.16
Ash (max % wt)	0.80
Nitrogen (max % wt)	0.60
Vaporous matter (max % wt)	0.80
Initial plasticity (PO) (min)	30
Plasticity Retention Index (PRI) (min)	40
Mark color	Red on with surface
Color of film (LDPE)	Transparency
Color of polyethylene	White

Table 2: Properties of Carbon Black.

Fundamental properties	Carbon Black			
	N220	**N330**	**N550**	**N660**
Iodine absorption (g/kg) ASTM D1510	121	82	43	36
Nitrogen absorption (m/g) ASTM D3037	119	83	42	35
DBPA (cm/100g) ASTM D2414	114	102	121	90
DBPA of compressed sample (cm/100g), ASTM D3493	100	88	88	75
CTAB (m/g), ASTM D3765	111	83	42	35

2.2 Research methodology

The methodology is divided into three sections: i) By using only carbon black as a major component in producing the para-rubber plate, the most suitable grade of carbon black will be selected according to fundamental properties of carbon black (Table 2) and mechanical properties from testing under ASTM standard (American Society for Testing and Materials, 1996). ii) By using calcium carbonate ($CaCO_3$) and carbon black, the $CaCO_3$ is added for reducing the cost of carbon black. The 3 ratios of carbon black to $CaCO_3$ are given and tested similar to the first case. iii) The para-rubber plates from sections 1 and 2 are taken into capping the concrete specimens with steel cases and examined the compressive strength under ASTM C39 (American Society for Testing and Materials, 2001). The results from two types of para-rubber plates are compared for selecting the appropriate formula. Before explaining the step of forming para-rubber plate, it is important to note that the unit of defining the quantity of substances in this paper is phr or pphr (part per hundred of rubber). For example, carbon black 50 phr means there are 50 parts of carbon black per 100 parts of rubber. The steps of forming the para-rubber plate are shown below.

1. Mastication in open system and at temperature 30-70 degree Celsius, the chemical substances such as carbon black, $CaCO_3$ and sulphur

were added respectively. After complete mixing, we obtained the rubber compound.

2. The rubber compound was formed by hot rolling at temperature 160 degree Celsius.

3. The para-rubber plate was cooled down and then we had the para-rubber plate that has 15 cm. in diameter and 1 cm. in thickness.

4. The following mechanical properties were evaluated using the ASTM standard (American Society for Testing and Materials, 1996).

- Compression set (ASTM D395)
- Tensile strength (ASTM D412)
- Strain (ASTM D412)
- Hardness (ASTM D1415)
- Tear strength (ASTM D624)

5. The concrete specimens were capped with para-rubber plates and tested the compressive strength of the concrete. The results were compared to those with sulphur capping. Each formula had 30 specimens for finding the average value of compressive strength. The strength of concrete in mix design is 280 ksc.

The symbols for testing are listed in Table 3. The readers should keep in mind that all of quantities in Table 3 are compared with 100 parts of para-rubber.

Table 3: The Symbols in this research.

Symbol	**Definition**
S	Sulphur
60N:0C	Carbon black 60 parts per $CaCO_3$ 0 part
60N:50C	Carbon black 60 parts per $CaCO_3$ 50 parts
80N:50C	Carbon black 80 parts per $CaCO_3$ 50 parts
100N:50C	Carbon black 100 parts per $CaCO_3$ 50 parts

3. RESULTS

The mechanical properties of para-rubber mixed with carbon black are shown in Table 4 and Figure 3.

Table 4: Mechanical properties of para-rubber plate with carbon black.

Grades	**Mechanical Properties**				
	Compression set (%)	**Tensile strength (MPa)**	**Strain (%)**	**Hardness (Shore D)**	**Tear strength (N/mm)**
N220	76	14	478	64	64
N330	74	13	451	65	53
N550	62	13	474	64	43
N660	66	12	428	60	36
N220	76	14	478	64	64

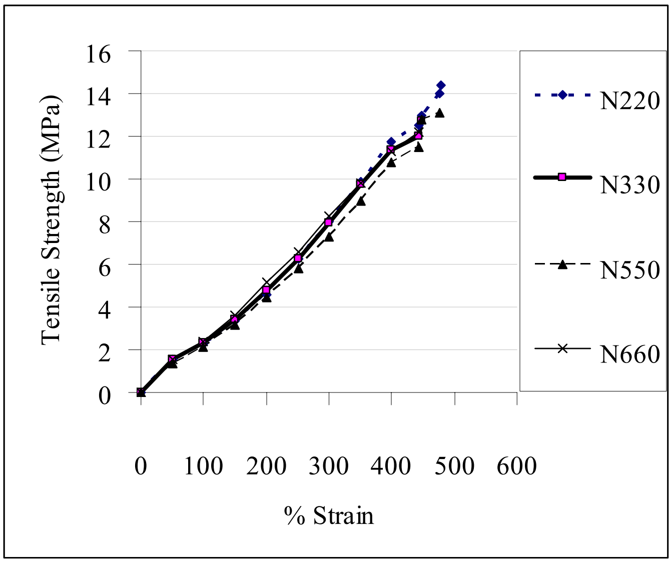

Figure 3: Stress strain relationship of para-rubber plate.

The important property of para-rubber plate is the hardness so it is considered as a major property in selecting the para-rubber plate. From Table 2, para-rubber plate with carbon black N330 gives the maximum hardness (measures from Shore D (Na-Ranong, 2001.) and the other properties are in acceptable range (see Figure 3), then we select the carbon black grade N330 as a filter in this research.

The mechanical properties of para-rubber plate with carbon black and $CaCO_3$ are shown in Table 5. The $CaCO_3$ is added for reducing the cost of para-rubber plate.

Table 5: Mechanical properties of para-rubber plate with Carbon Black and $CaCO_3$.

Carbon black: $CaCO_3$	**Mechanical Properties**				
	Compression set (%)	**Tensile strength (MPa)**	**Strain (%)**	**Hardness (Shore D)**	**Tear strength (N/mm)**
60N:0C	63	14	404	60	60
60N:50C	74	13	451	66	53
80N:50C	46	12	327	72	33
100N:50C	54	10	219	77	25

From Table 5 and focusing on formulae 60N:0C and 60N:50C, it is found that CaCO3 makes higher in compression set, strain and hardness. However the tear and tensile strengths are a little bit decreased. By considering formulae 60N:50C, 80N:50C and 100N:50C, the compression set, tensile strength, strain and tear strength are inversely proportional to amount of carbon black. In contrast with the hardness, it is proportional to amount of carbon black.

Normally, the content of carbon black should not excess 60 phr (Chuayjuljit ,Bangkok, 2005) but our main objective is to find the formula that gives the maximum hardness. Then in this study, we extend the range of carbon black to 100 phr. The results of formula 100N:50C indicate that the hardness reaches the highest value but the other properties are lowest. These results from lose of dispersion and distribution of carbon black's particles, and then rubber cannot bind the filters effectively (Chuayjuljit, 2005) and leads to low values in many properties. While many properties have low values when using carbon black 100 phr but the hardness gives the highest value since higher density of the para-rubber plate.

The results of compressive strength of concrete capping with para-rubber plate and steel case are compared to that with sulphur and shown in Figure 4.

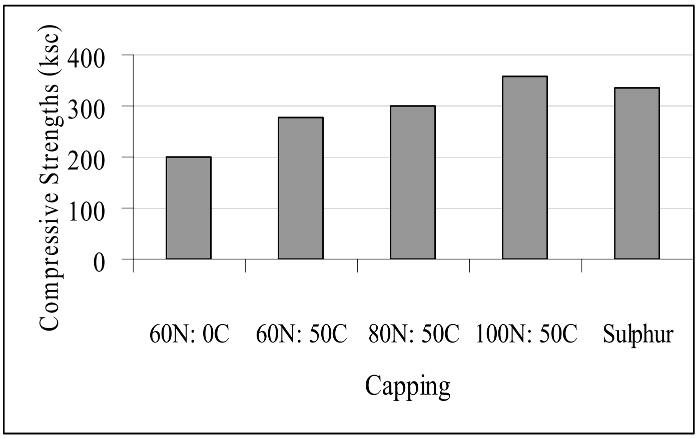

Figure 4: Compressive strengths of concrete capping with various formulae of para-rubber plate and sulphur.

From Figure 4, it reveals that the using of $CaCO_3$ can reduce not only the cost of para-rubber plate but also give the higher value of compressive strength (for case 100N:50C). Thus the suitable formula from this research is 100N:50C. With this formula, we obtain the compressive strength higher than capping with sulphur around 7%. The lower compressive strengths, in descending order, are 80N:50C, 60N:50C and 60N:0C.

4. CONCLUSION

From the testing, we found that the most suitable formula of para-rubber plate is 100N:50C. At this formula, the compressive strength is in good agreement with those from sulphur capping (larger than sulphur capping around 7%). In view of cost, the cost of para-rubber plate from this research is not over than 50 baths/sheet. In comparison with para-rubber plates that produce at aboard and in the country, the costs of these para-rubber plates are 500-800 baths/sheet and 180 baths/sheet respectively. Thus the proposed formula of para-rubber plate has the potential in developing into large scale of economic.

5. SUGGESTIONS

The results from this formula should be compared with the para-rubber plate from aboard and in the country.

In order to reduce the cost, the formula should be modified for capping without steel case.

ACKNOWLEDGMENT

The authors extremely gratitude Thailand Research Fund (TRF) through the small rubber project (SPR) grant No.RDG4950125.

REFERENCES

American Society for Testing and Materials, 1996. *Annual Book of ASTM Standards*.

ASTM C192/C192 M-00, 2001: *Standard Practice for Making and Curing Concrete Test Specimens in the Laboratory*, Annual Book of ASTM Standards, Volume 04.02.

ASTM C39/C39M-01, 2001: *Standard Test Method for Compressive Strength of Cylindrical Concrete Specimens,* Annual Book of ASTM Standards, Volume 04.02.

ASTM C617-98, 2001: *Standard Practice for Capping for cylindrical Concrete Specimens,* Annual Book of ASTM Standards, Volume 04.02.

J.S. Grygiell, and D.E. Amsler, 1977. Capping concrete cylinders with neoprene pads. *Research Report, New York State Department of Transportation,* Albany. No.46.

M. Anusiri, 2006. The applications of bagasse paper for replacing sulphur in capping cylindrical concrete head, *NCCE 11*, Phuket.

Method of Making Test Cube from Fresh Concrete, 1983. *British Standard Institute*, BS 1881: Part 108.

N. Na-Ranong, 2001. Testing for mechanical properties of rubber, Rubber Technology Division, *Rubber Research Institute*, Department of Agriculture, Bangkok, 2001.

P.M. Carrasquillo, and R.L. Carrasquillo, 1988. Effect of using unbounded capping systems on the compressive strength of concrete cylinders. *ACI Materials Journal*, vol. 85, no. 3, pp. 141-147.

P. Khamput and A. Boksuwan, 2006. A study of compressive strength of concrete capping with Neoprene. *Technology and Innovation for sustainable development Conference*, Khon Kaen.

P. Sae-Oui, 2004. *Rubber: types, properties and usage,* MTEC, Prathumthani.

S. Chuayjuljit, 2005. *Rubber Technology,* Department of Science, Chulalongkorn University, Bangkok.

PARTICLE ASSOCIATED DISCHARGE OF PATHOGEN INDICATOR ORGANISMS FROM DIFFUSE SOURCES IN AGRICULTURAL-FORESTRY WATERSHEDS

KYUNGMIN HAN and GEONHA KIM
Department of Civil and Environmental Engineering,
Hannam University Ojungdong 133, Daedukku,
Daejeon, Republic of Korea, 306-791
kimgh@hnu.kr

ABSTRACT

Many concerns have recently been raised about the pathogens in surface water originating from diffuse pollution. It is well known that die off rate of the pathogens could be very slow when pathogens are associated with suspended solids. This study aims to understand the pathogen levels and their affecting factors to alleviate loadings to a receiving water body. Forty rainfall events were monitored for their runoff quality at four watersheds mainly composed of agricultural and forestry land. Ascetically taken water samples were analyzed in the laboratory for their pathogen indicator organism levels and chemical characteristics. From the correlation analysis between suspended solid and pathogen indicator organisms, it could be understood that pathogen indicator organism levels has highly related with suspended solid and flow rate. It could be suggested that large amount of pathogens can be removed from rainfall runoff by removing of suspended solid from the raw water.

1. INTRODUCTION

Many concerns are raised about the fecal contamination originated from rainfall runoffs recently (Conboy and Goss, 2000), since pathogens originated from fecal directly impact on the human health (US. EPA, 1993). The pathogen levels of water can be assessed by measuring the indicator organism population in the water. The indicator organism should: i) be easily detected using simple laboratory tests; ii) generally not be present in unpolluted water; iii) be present in concentrations that can be correlated with the extent of contamination; iv) have a die-off rate that is not faster than the die-off rate for the pathogens under consideration (U.S. EPA, 2001; Thomann and Mueller, 1987).

Total coliform, fecal coliform, fecal *streptococci*, and *Escherchia coli* are common indicator organisms to be monitored. Diffuse sources of fecal contaminations are numerous. Illicit sewage connections, wildlife, septic systems, livestock, landfills, and pastures would be the potential sources. Storm water runoff can transport significant loads of pathogens from livestock pastures, livestock and poultry feeding facilities, and feedlots. Indicator organisms are often used as a tool to identify the contaminant sources as well. Maul and Cooper (2000) used enterococci and fecal coliform bacteria concentration to assess the variability of water quality of the agricultural field during wet weather. Whitlock *et al*. (2002) used fecal coliform to identify the sources in an urban watershed.

UNEP and WHO established water quality criteria of coliform concentration for primary contact recreation purpose. Fecal coliform concentration from a geometric mean of at least 5 samples should be less than 100/100ml for 50% and less than 1000/100ml for 90%. US EPA restricts *E. coli* density less than 126/100ml for fresh water for logarithmic average for a period of 30 days of at least five samples (WHO, 1999). The Korean Government regulates coliform concentration of surface water by the fundamental environmental law. Table 1 shows the environmental criteria for river water quality in Korea.

Table 1: Environmental criteria of Korea for the surface water quality

Class	**Water Use**	**pH**	**BOD (mg/l)**	**SS (mg/l)**	**DO (mg/l)**	**Coliform (MPN/100ml)**
I	Source water class 1 Nature Env. Conserv.	6.5-8.5	≤ 1	≤ 25	≥ 7.5	≤ 50
II	Source water class 2 Swimming	6.5-8.5	≤ 3	≤ 25	≥ 5	≤ 1,000
III	Source water class 3 Indust. use cls. 1	6.5-8.5	≤ 6	≤ 25	≥ 5	≤ 5,000
IV	Indust. use class 2 Agricultural use	6.0-8.5	≤ 8	≤ 100	≥ 2	--
VI	Indust. use class 3 Life Env. Conserv.	6.0-8.5	≤ 10	--	≥ 2	--

pH, Biological Oxygen Demand (BOD), Suspended Solid (SS), Dissolved Oxygen (DO) and coliform concentration are regulated by the law. Class 2 in the table is for the second class of the source water use, and swimming use of the water. To meet the second class of water quality, pH should be in the range of 6.5 and 8.5, BOD should be less than 3 mg/L, SS should be less than 25 mg/L, DO should be larger than 5mg/L, and coliform concentration should be less than 1,000 MPN/100 ml. Among 5 constituents, however, only a criteria for BOD concentration is considered for the water resource planning purposes in the practice. This is possibly due to insensitiveness of the parameter range between classes such as pH, SS, and DO, lack of existing data for coliform concentration. In addition, BOD is well-known parameter to the public including Non-Government

Organizations. Even though BOD is now emphasized for regulation purpose, understanding fecal contamination is of importance for protecting public health. Usually high uncertainty is associated with fecal contamination in water quality analysis and data interpretation. If we suppose the main objectives of water resource planning is “to provide healthy water to the public”, the importance of coliform concentration in the surface water is clear.

The research objectives of this study were: i) to present pathogen indicator organism level of rainfall runoff; ii) to study the relationship between indicator organism concentration and suspended solid; and iii) to study the possibility of pathogen removal from rainfall runoff by removing suspended solid from water.

2. MATERIALS AND METHODS

Four watersheds of areas between 2.85 km^2 and 27.37 km^2 were selected for monitoring rainfall runoff. Accessibility, safety issues of field workers, representative land use, and ease of sampling were major factors considered in selecting the study watersheds. Study watersheds are located in the Geum River basin, one of the four major river basins in the Republic of Korea. The length of the river is 401.4 km, and the river basin covers 988.5 km^2.

Table 2 is the summary of topography variables and land use description of the four study watersheds. Ten rainfall events were monitored at each study watershed, mostly during March to September, 2002. Rainfall events to monitor were selected among several rainfall events considering field worker’s safety and data quality. Runoff volumes were measured using a velocity meter probe, Global Water® FP-101 of Plano Molding Company, USA. Water samples were taken manually and some by automatic samplers to minimize sampling errors. About 150 samples of the concentration data were obtained for each study watershed, and approximately, fifteen samples were taken for each rainfall event. Quantity and quality of the low flow were monitored two times a week at each site as well.

At the six monitoring stations in the Geum River, water samples were taken on a weekly basis during drought season from October, 2002 to April, 2003. The monitoring stations located 10 km apart, respectively, along the river. Flow rate of the monitoring points were estimated using the rating curves provided by the Korea Water Resources Corporation. Average annual rainfall depth at the Geum River Basin is 1,279 mm.

All samples were analyzed within 8 hours after collection. Suspended solid concentrations were measured by using the Standard Methods 20th ed. For the microbial analysis, aseptic water samples were taken in a sterilized, separate container. Water samples were brought to the laboratory refrigerated and analyzed using aseptic techniques. Total coliform (TC) and

E. coli (EC) concentrations were analyzed using Petrifilm™, from 3M Corporation. Petrifilm™ is a variation of the heterotrophic plate count method and thus enumeration is expressed as Colony Forming Units (CFU/100 ml). The technique is effective for low-to-medium concentration samples and is also inexpensive (Lisle, 1993).

SPSS ver. 10.0 was used to compute the descriptive statistics and the Pearson correlation matrices. Skewed data were log transformed for further analysis.

Table 2: Topography and land use description of the study watersheds

Watershed	**Area (Km^2)**	**Length[a] (Km)**	**Mean slope (%)**	**$RAIN_{ave}$[b] (mm)**	**Land use (%)**
1	3.38	2.875	62.61	1356.7	forest 99.5, road 0.1, others 0.4
2	2.85	1.575	22.64	1252.1	rice paddy 1.8, cropland 0.7, forest 94.2, road 0.7, others 2.6
3	4.97	1.649	41.17	1252.1	rice paddy 8.4, cropland 6.4, forest 82.3, road 1.4
4	27.37	6.173	5.97	1356.7	rice paddy 35.9, forest 44.8, residential 13.3, others 6.0

[a] channel length
[b] average annual precipitation depth

3. RESULTS AND DISCUSSION

Figure 1 shows the hydrograph and time series variation of SS and TC concentrations for runoff of fourth rainfall event at watershed 4. It can be seen from the figure that SS concentration follows the shape of hydrograph.

Table 3 is the descriptive statistics of runoff concentration of constituents by study watersheds. The maximum average SS value 116.4 mg/L was given by watershed 3, followed by watershed 4, watershed 2, and watershed 1. The magnitude of standard deviation and standard error were in the same order. In Table 1, watershed 4 showed the highest ratio of agricultural land use to total area and the lowest mean slope among the 4 watersheds. Maul and Cooper (2001) reported that runoff quality varied greatly within agricultural sites, indicating that the responses of some agricultural fields are different from those of others in terms of SS, and maybe related to watershed characteristics other than land uses. As SS can be removed from water by settling, flow velocity may affect SS concentration. Average concentration of pathogen indicator showing increasing tendency as the proportion of agricultural increased such as TC and EC.

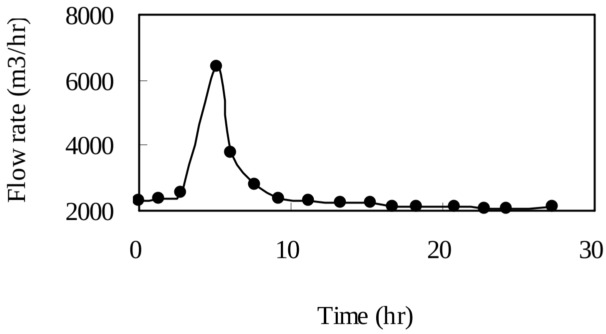

(a) Hydrograph

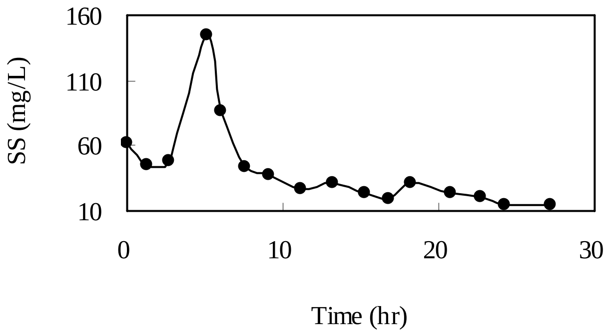

(b) Suspend solid concentration variation as a function of time

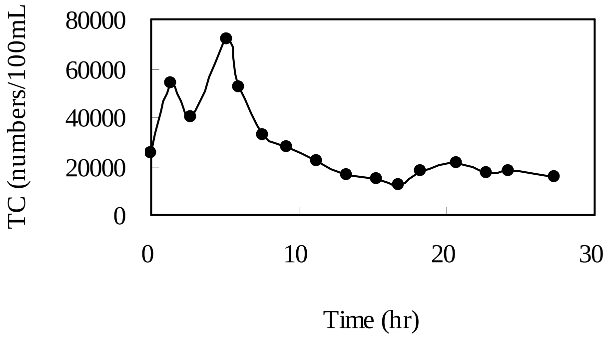

(c) Total coliform concentration variation as a function of time

Figure 1: Hydrograph and time series variations of contaminant concentrations of rainfall runoff for fourth rainfall event at watershed 4

Table 3: Descriptive statistics of runoff concentration for study watersheds

	Watershed	n[a]	Average[b]	SD[d]	SE[e]	Minimum	Maximum
SS	1	147	2.1	10.0	0.8	0	112.3
	2	150	60.8	180.4	14.7	0.3	1425.0
	3	149	116.4	398.1	32.6	0.3	3510.0
	4	143	86.2	294.0	24.6	2.5	2612.0
Average[c]			66.4				
TC	1	147	4225	6211	512	0	32000
	2	150	1759	15883	1297	0	58000
	3	149	15750	13479	1104	200	50000
	4	143	30250	25187	2106	400	146000
Average			16863				
EC	1	147	156	389	32	0	3200
	2	150	3875	7480	611	0	40000
	3	149	3392	5655	463	0	42000
	4	143	11278	12952	1083	0	70500
Average			4622				

[a] number of samples taken at the designated watershed.
[b] average for the designated watershed.
[c] average for all four study watershed.
[d] standard deviation.
[e] standard error.

Table 4 is the Pearson coefficients from the correlation analysis of between EMCs of SS, TC, and EC. Pearson correlation coefficient ranges between –1~ +1. Complete correlation shows +1, and complete inverse correlation shows –1.

Table 4: Correlation analysis result between suspended solid and coliforms

	SS	TC	EC
SS	1.00	0.408**	0.380**
TC	0.408**	1.00	0.523**
EC	0.380**	0.523**	1.00

Figure 2 is the time series variation of rainfall depth, flow rate, concentration of suspended solids, biological oxygen demand, total coliform and fecal coliform at monitoring station R5 from January, 2001 to February, 2003. Data were obtained from concentration database of the automatic monitoring network of the Korean Ministry of Environment. The monitoring station is located at the vicinity of Gongju city. This point was selected because large discrepancies occur between measured water quality data and predictions made by the water quality model, QUAL2E, carried out by the authors. These errors were caused mainly due to the inaccurate non-point source pollution loading data input. As the concentration of fecal coliform was measured by the multiple fermentation technique in the unit of MPN/100 ml, the concentration shows 6 to 20 times higher compared to the concentration measured by the heterogeneous plate count method as done in the research.

From Figure 2, it can be seen that the shape of pollutographs follows the shape of the hydrograph except BOD. As suspended solid and coliform concentration dynamics are highly related with the flow rate, correlation analysis between flow rates and concentration were carried out. Table 5. is the Pearson correlation coefficients between water level and water quality concentrations (number of data = 144). The Pearson coefficient between flow rate and BOD is -0.36, indicates weak inverse correlation. Suspended solid concentration showed weak correlation with flow rate (0.375), same as fecal coliform (0.018). The Pearson coefficient for flow rate against total coliform was 0.71 and significant at 0.01 level. High correlations between flow rate and coliforms were occurred because the majority of microorganisms attached on sediment (Borst and Selvakumar, 2003) can be transported to downstream when high mobility occurs during wet weather. Even though most of coliform bacteria decayed as soon as they left their host, organisms attached on sediment remain active up to months, depending on the nature of the soil, temperature, pH, moisture, and microflora (Howell *et al.*, 1996). These organisms may be re-suspended when high flow condition arises. It is noticeable that coliform concentrations are more related with flow rate that BOD concentration.

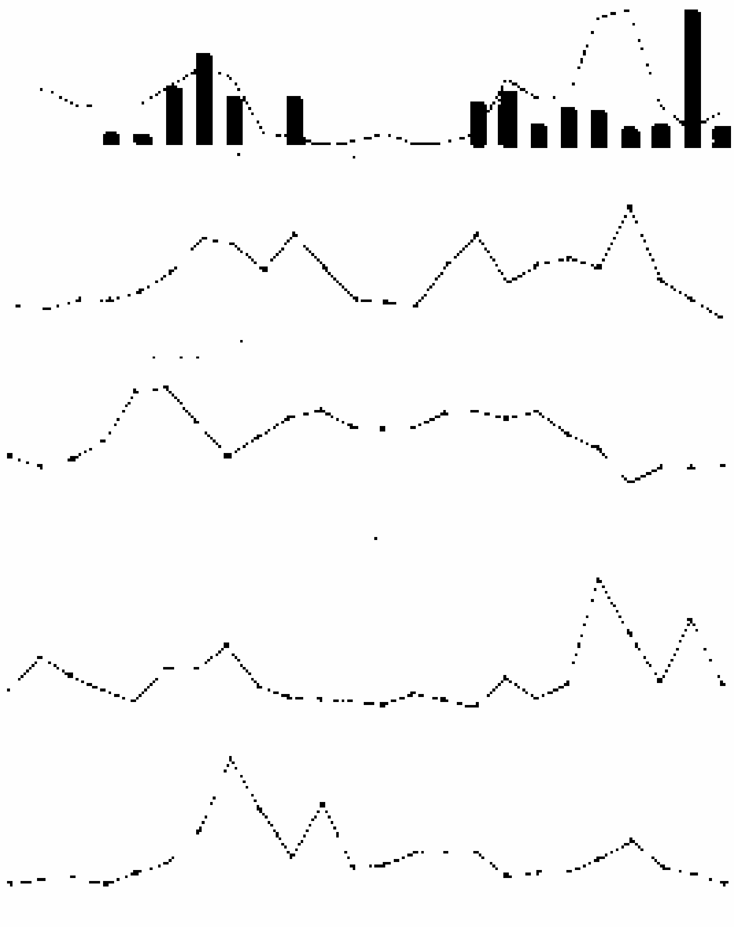

Figure 2: Precipitation depth, suspended solid, BOD, total coliform, and fecal coliform variations of the Geum River.

Table 5: Pearson correlation coefficients between water level and water quality concentrations

	Level	**BOD**	**COD**	**SS**	**TC**	**FC**
Level		-.363	-.252	.375	.712**	.018
BOD	-.363		.621**	.130	-.515**	.023
COD	-.252	.621**		.288	-.385	-.116
SS	.375	.130	.288		.192	.534**
TC	.712**	-.515**	-.385	.192		.134
FC	.018	.023	-.116	.534**	.134	

** Correlation is significant at the 0.01 level (2-tailed).

4. SUMMARY AND CONCLUSIONS

The main objectives of this study were to understand impacts of topography and land use on rainfall runoff water quality in watersheds mainly consisting of forestry and agricultural land use. Forty rainfall events were monitored for organics and nutrients at four study watersheds. The ratio of agricultural land use to the total area of study watersheds were in the range of 0.01 to 0.36.

This study aimed to characterize the coliform concentrations of the Geum River, Korea and to understand the relationship between flow rate and coliform concentrations. Rainfall runoff is one of the main diffuse pollution sources to degrade the surface water in microbial aspect. From the water quality monitoring of the river, it can be seen that rainfall runoff from a watershed with more agricultural activities showed higher coliform concentrations. The correlation analysis between the indicator organisms, suspended solid, and flow rate of the river revealed that the total coliform concentration was highly correlated with the flow rate while BOD concentration has a weak inverse correlation with the flow rate. High correlations between flow rate and coliforms were occurred because the majority of microorganisms attached on sediment, and can be transported to downstream when high mobility occurs during wet weather.

ACKNOWLEDGEMENT

This research was supported by a grant (code # 1-5-1) from the Sustainable Water Resources Research Center of the 21st Century Frontier Research Program, Korean Ministry of Science and Technology Please place tables in their intended location in the text (Table 1).

REFERENCES

Conboy M.J. and Goss M.J., 2000. Natural protection of groundwater against bacteria of fecal origin. *J. of Contaminant Hydrology*, 43(2000), 1-24.

Lisle J., 1993. *An operator's guide to bacteriological testing*, American Water Works Association, Denver, CO, USA.

Maul, J.D., Cooper, C.M., 2000. Water quality of seasonally flooded agricultural fields in Mississipi. USA. Agriculture Ecosystems & Environment. 81(2000), 171-178.

Thomann R.V. and Mueller J.A., 1987. *Principle of Surface Water Quality Modeling and Control*, Harper & Row, New York, NY.

U.S. Environmental Protection Agency, 1993. *Preventing waterborne disease*. EPA/640/K-93/001, United States Environmental Agency, Washington DC, USA.

U.S.Environmental Protection Agency, 2001. *Protocol for developing1 pathogen TMDLs*. EPA 841-R-00-002. Office of Water (4503F). Washington, DC., United States Environmental Protection Agency.

Whitlock J.E., Jones D.T. and Harwood V.J., 2002. Identification of sources of fecal coliforms in an urban watershed using antibiotic resistance analysis. *Water Research*, 36(2002), 4273-4282.

World Health Organization., 1999. Health-based monitoring of recreational waters: the feasibility of new approach (The 'Annapolis protocol'), WHO/SDE/WSH/99.1, World Health Organization, Geneva.

PHYSICAL PROPERTIES OF GROUT FOR CLOSE-LOOP VERTICAL GROUND HEAT EXCHANGER

CHULHO LEE, HUJEONG GIL and HANGSEOK CHOI
Department of Civil, Environmental and Architectural Engineering,
Korea University, 5-ga, Anam-dong Seongbuk-gu, Seoul 136-701, Korea
cryfreer@korea.ac.kr

ABSTRACT

Thermo-mechanical properties of grout materials have been investigated, which are used for backfilling a ground heat exchanger in the geothermal heat pump (GHP) system. The thermal conductivity and viscosity of nine different bentonite grouts and a cementitious grout with various mix proportions have been considered in this study. The bentonite grouts indicate that the thermal conductivity and viscosity increase with the content of bentonite or filler (silica sand). In addition, material segregation can be observed when the viscosity of grout is relatively low. The saturated cement grouts appear to possess much higher thermal conductivity than the saturated bentonite grouts, and the reduction of thermal conductivity by drying the cementitious grout is less than the case of the bentonite grouts. Maintaining the moisture content of grouts is a crucial factor in enhancing the efficiency of ground heat exchangers.

1. INTRODUCTION

The efficiency of heat exchange in a close-loop vertical ground heat exchanger is one of the most crucial factors to enhance the geothermal heat pump (GHP) system. Influence factors on heat exchange can be the thermal conductivity of backfilling grout and HDPE pipes, heat interference between the pipes, the thermal conductivity of adjacent geologic formations. In this paper, thermo-mechanical properties of grout materials, i.e., thermal conductivity and viscosity, have been investigated, which are used for backfilling the ground heat exchanger. The backfilling grout should be used not only to seal the annulus between the borehole and heat exchanger loop but also to exchange properly heat between the ground formation and the loop.

Increase in the thermal conductivity of backfilling grouts leads to considerable reduction in installation cost for ground heat exchanger by shortening the required bore length. In addition, acceptable groutability of grouts should be guaranteed during the installation of the heat exchanger in order to fill completely the annulus without any gaps that may cause thermal discontinuity.

The thermal conductivity and viscosity of nine different bentonite grouts from different producers have been experimentally evaluated in case of both neat bentonite grouts and thermally enhanced bentonite grouts with addition of silica sand as a filler. In addition, a phenomenon of material segregation was observed when the viscosity of the thermally enhanced bentonite grout was low.

Cementitious grouts as an alternative grout material (Allan, 2000; Allan and Philippacopoulos, 2000) with various mix proportions have been considered in this study. Allan and Philippacopoulos (1999, 2000) reported a series of experimental results on the thermal conductivity of cementitious grouts and proposed an optimized cementitious grout formulation, namely Mix 111, which enhances thermal conductivity. The cementitious grouts are relatively inexpensive, safe and easy to work. The thermal conductivity and viscosity of cementitious grout have been investigated and compared to the thermo-mechanical properties of bentonite grouts.

2. MATERIALS

Nine bentonite grouts provided by three different producers in Korea have been chosen for this study. The fundamental properties of each grout are summarized in Table 1. Bentonite 1 is a low grade bentonite used for a casting process, and Bentonite 2 is improved by adding montmorillonite to increase swelling potential. Bentonite 3, 4, and 5 are produced for the purpose of civil engineering construction such as a mixture for a landfill liner or bentonite slurry. Especially, Bentonite 5 possesses very high viscosity and swelling potential but is more expensive than the other grouts. Bentonite 6 is used in constructing a landfill liner. Bentonite 7 is a granular product and used in waterproofing. On the contrary, Bentonite 8 is powdered and produced for geothermal application. In particular, Bentonite 9 includes silica sand to an extent during manufacturing process to enhance the thermal conductivity. Silica sand was used as a filler of which gradation curve is shown in Figure 1.

Considering the cementitious grout, potland cement was selected as a main grouting material with mixture of the silica sand used in the bentonite grout as a filler, and a small amount of bentonite was added for preventing the bleeding or segregation of the cementitious grout.

Table 1: Fundamental physical properties of bentonites

Bentonite	Producer	Water Content (%)	Swelling Index (ml/2g)	pH
1	D	10.0	12-15	9-11
2	D	10.0	24-30	9-11
3	S	8.9	15.0	10.0
4	S	9.5	23.0	10.1
5	S	9.5	24.5	10.0
6	C	12.0	18.0	6-12
7	C	12.0	29.0	6-12
8	C	12.0	10.0	6-12
9	C	12.0	11.0	6-12

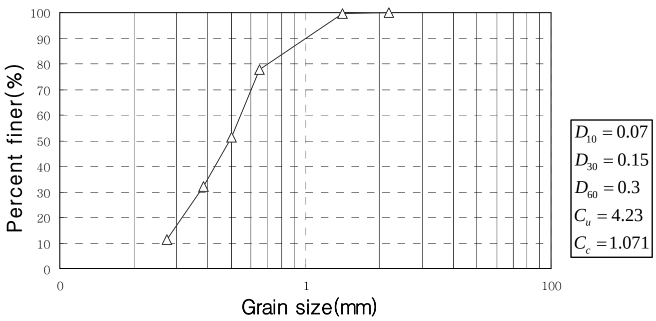

Figure 1: Gradation curve of silica sand.

3. EXPERIMENTAL

3.1 Thermal conductivity

The thermal conductivity of grouts was measured using QTM-500K thermal conductivity meter (Kyoto Electronics) which is equipped with PD-13 probe of which dimension is 95 mm × 40 mm. The equipment adopts the transient hot wire method to measure the thermal conductivity of grout material.

Because the bentonite grout paste is amorphous, an acrylic container box was devised to fill the paste in it and to permit the measurement of thermal conductivity. The container box consists of a water jacket, a perimeter passage, which is connected to a water tank to flow water of controlled temperature through it, and thus a room temperature of 20°C is presumably maintained in bentonite grout specimens during measuring thermal conductivity.

After curing the cementitious grouts in a rectangular mold for 14 days, the thermal conductivity of both the wet and air-dried specimens were measured using the QTM-500K thermal conductivity meter.

3.2 Viscosity

The viscosity of bentonite grouts was measured by a vibration-type viscometer of which measuring plate vibrates with a frequency of 30 Hz. The viscosity range measurable in the viscometer is from 0.003 to 120 P. In order to investigate the isothermal change in viscosity with time after mixing bentonite grouts, a similar acrylic container box to that used for measuring thermal conductivity was devised, which is also equipped with a water jacket to flow water at a room temperature of 20°C.

Viscosity of cementitious grout paste was indirectly estimated by flowability. It is measured by both the V-Funnel test and the slump flow test.

4. RESULTS

4.1 Bentonite grout

When bentonite is used for backfilling the ground heat exchanger, 15% to 25% bentonite by weight is usually mixed with water. Therefore, two mix proportions of 20% and 30% bentonite by weight were chosen to investigate the thermal conductivity of the nine neat bentonite grouts with no addition of fillers. Figure 2 compares the measured thermal conductivity of each neat bentonite grout in the fully saturated condition. In case of 20% bentonite by weight, the thermal conductivity lies in a narrow range of 0.74-0.81 W/m°C. For 30% bentonite case, the range of thermal conductivity is 0.76-0.95 W/m°C.

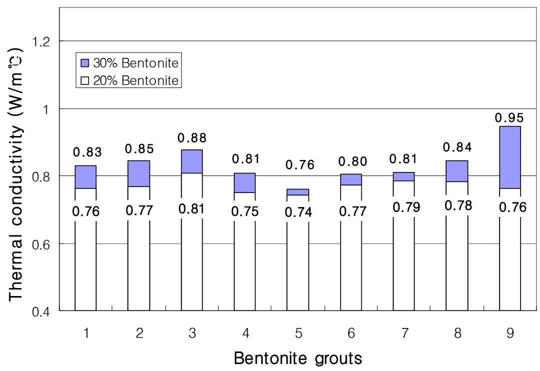

Figure 2: Thermal conductivity of neat bentonite grouts

After air-drying the specimens for 10 days, the thermal conductivity of the dried bentonite grout was measured to show how much thermal conductivity decreases by drying process, which may represent a situation of groundwater table drawdown. In the case of 30% bentonite, the thermal conductivities of Bentonite 1 and 2 were substantially reduced from 0.83 to 0.27 W/m°C and from 0.85 to 0.31 W/m°C, respectively. Note that maintaining bentonite grout saturated should be required to avoid unpredictable reduction of heat conduction performance of underground heat exchangers.

The thermal conductivity of bentonite grouts can be enhanced by the addition of a small amount of fillers such as silica sand (Han et al., 2005). For the two cases of bentonite content (20% and 30%), the improvement of thermal conductivity by the addition of silica sand was investigated. The amount of added silica sand was 15, 30, 45, and 60% of bentonite by weight. Figure 3 shows the variation of thermal conductivity for the case of 20% bentonite. At each 15% increase of silica sand content, the thermal conductivity increased by 0.08-0.12 W/m°C on the average. A similar tendency can be observed for the case of bentonite content 30% as shown in Figure 4. The result indicates that the increase in the thermal conductivity due to the addition of silica sand is not significant, and even the case of 60% of silica sand results in the thermal conductivity less than 1.4 W/m°C.

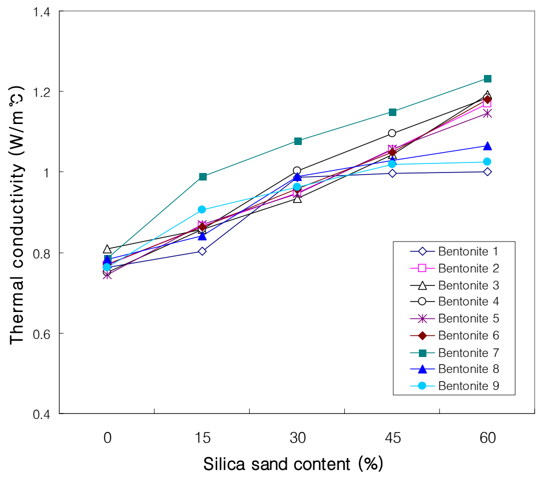

Figure 3: Thermal conductivity of 20% bentonite grout with various contents of silica sand

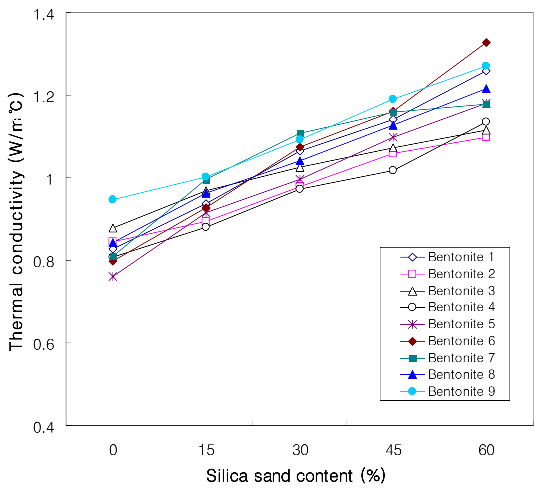

Figure 4: Thermal conductivity of 30% bentonite grout with various contents of silica sand

In case of the 20% bentonite in Figure 3, the thermal conductivity of Bentonite 1 increases to a maximum value at the silica sand content of 30% and then is kept to the value. The reason for this can be explained by a phenomenon of material segregation. Bentonite 1 possessed the lowest viscosity at the same bentonite content compared to the other bentonite grouts, and thus the silica sand mixed in the Bentonite 1 grout paste settled down and separated from the bentonite paste. Settled silica sands were observed at the bottom of the container as shown in Figure 5.

Figure 5: Settled silica sand at the bottom of container

The viscosity of bentonite grouts after being mixed with water should increase with time due to the rheological characteristic (Choi et al., 2008). A considerable increase in viscosity can make pumping grout difficult during installing ground heat exchangers. In this paper, a change in viscosity with time has been quantitatively investigated for two bentonite grouts, Bentonite 1 and 3, with the bentonite content of 20%. In this comparison, the effect of magnitude of mixed silica sand was also examined. Figure 6 shows the significant increase in viscosity with time for 6 hours. In addition, the rate of viscosity increase becomes greater when the amount of silica sand mixed in the grout increases. Especially, the viscosity of Bentonite 3 mixed with 60% of silica sand reaches the measurement limitation of the viscometer (i.e., 120 P). Therefore, care must be taken not to delay significantly grout pumping operation after preparing the grout paste in the field.

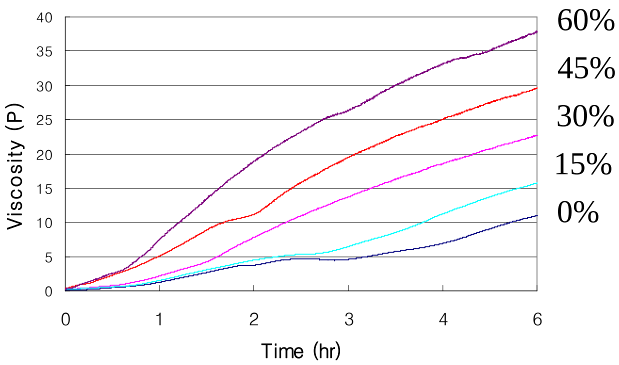

(a) Bentonite 1 (20%)

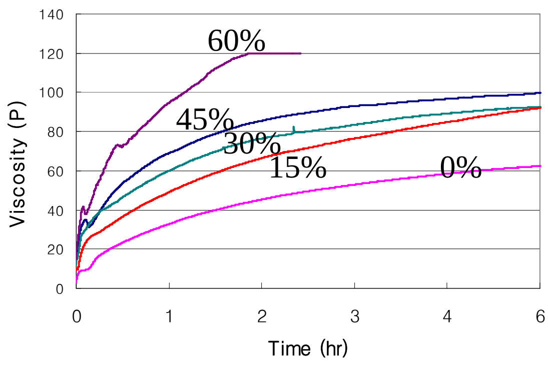

(b) Bentonite 3 (20%)
Figure 6: Comparison of increase in viscosity with time

4.2 Cementitious grout

Allan and Philippacopoulos (1999, 2000) reported from a series of laboratory tests that the thermal conductivity of neat cement grout ranged from 0.80 to 0.87 W/m°C. In addition, an optimized grout formulation, namely Mix 111, yielded the thermal conductivity of up to 2.42 W/m°C. The grout consists of cement, water, a particular grade of silica sand, superplasticizer, and a small amount of bentonite.

In this paper, the role of influence factors such as water/cement ratio, silica sand/cement ratio, and bentonite dosage on the thermal conductivity and viscosity of cementitious grouts has been investigated. The experimental results are as follows:

4.2.1 Water/cement ratio

Five different mix proportions for neat cement were prepared by only varying the water/cement ratio as 0.4, 0.5, 0.6, 0.7, and 0.8, as shown in Table 2 and thermal conductivity and viscosity with time were measured on the specimens. The measured thermal conductivity and slump flow for the five mix proportions are described in Figure 7. Increasing the water/cement ratio leads to a decrease in thermal conductivity and an increase in slump flow which means the enhancement of flowability. The thermal conductivity decreases by 0.01 - 0.07 W/m°C with the increment of water/cement ratio of 0.1. When the specimens were air-dried, the thermal conductivity was reduced only by around 0.25 W/m°C. This reduction is far smaller than the case of bentonite grouts, and thus the cementitious grout may be less vulnerable to a drying condition due to water table drawdown.

Allan and Philippacopoulos (1999) reported that it is important to maintain a minimized water/cement ratio for increasing thermal conductivity and decreasing hydraulic conductivity. However, when it comes to groutability or pumpability, very small values of water/cement ratio with high viscosity can result in difficulty of pumping cementitious grout into the borehole. Accordingly, it is necessary to consider not only thermal conductivity but also viscosity in order to determine an optimized mix proportion for cementitious grouts.

Table 2: Effect of water/cement ratio and viscosity

Cement	Geo-1	Geo-2	Geo-3	Geo-4	Geo-5
w/c ratio	0.40	0.50	0.60	0.70	0.80
Slump Flow(mm)	164-168	220-231	284-288	350-355	355-385
V-Funnel(sec)	5.6	2.1	< 1	< 1	< 1

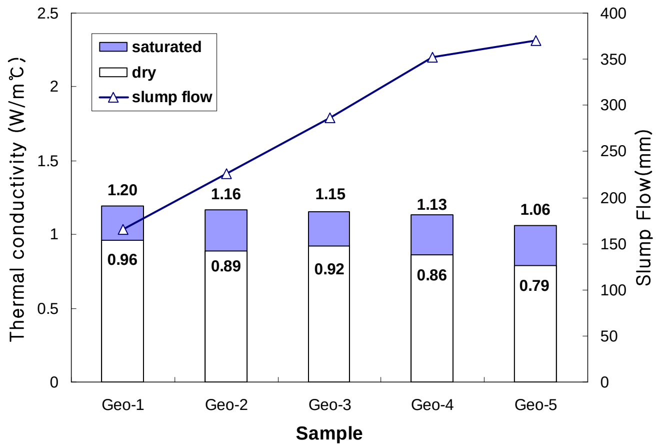

Figure 7: Thermal conductivity and slump flow with varying water/cement ratio

4.2.2 Silica sand/cement ratio

Five different mix proportions with the water/cement ratio of 0.6 were considered with varying the silica sand/cement ratio as 2.0, 2.2, 2.4, 2.6, and 2.8, as shown in Table 3. In this case, a small dosage of superplasticizer is added to the mixture by 0.1% of cement weight to maintain proper groutability. The measured thermal conductivity and slump flow for the five mix proportions are described in Figure 8. Increasing the silica sand/cement ratio leads to an increase in thermal conductivity and a reduction in slump flow which decreases groutability. The thermal conductivity increases by 0.01 - 0.09 W/m°C with the increment of silica sand/cement ratio of 0.2. When the specimens were air-dried, the thermal conductivity was reduced by around 0.20 – 0.42 W/m°C that is far smaller than the case of bentonite grouts, and thus the cementitious grout mixed with silica sand may be less vulnerable than bentonite grout to a drying condition.

Allan and Philippacopoulos (1999) added a superplasticizer of about 8.8 litres per a unit volume (1 m3) of cementitious grout to assure suitable groutability. However, properties of superplasticizer should be different for each product, and it is difficult to characterize quantitatively the role of superplasticizer in cementitious grout mixed with silica sand.

Table 3: Effect of silica sand/cement ratio and viscosity

Cement	Geo-6	Geo-7	Geo-8	Geo-9	Geo-10
w/c ratio	0.60	0.60	0.60	0.60	0.60
Sand/cement ratio	2.00	2.20	2.40	2.60	2.80
Slump Flow(mm)	195-210	180-187	107-110	100	100
V-Funnel(sec)	2.5	2.6	4.5	300	300

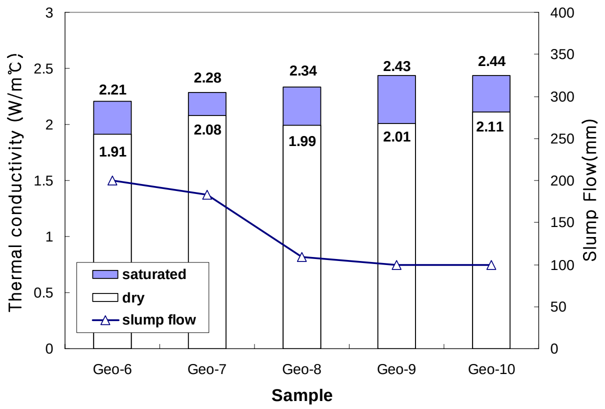

Figure 8: Thermal conductivity and slump flow with varying silica sand/cement ratio

4.2.3 Bentonite content

Five different bentonite dosages with the water/cement ratio of 0.6 and the silica sand/cement of 2.4 were considered with varying the bentonite content of 1, 2, 3, 4, and 6% of cement weight as shown in Table 4. Allan and Philippacopoulos (1999) noted that the purpose of a small dosage of bentonite added into cementitious grouts was prevention from bleeding and the segregation of silica sand.

As can be seen in Figure 9, the bentonite content of 1 – 6% of cement weight does not affect significantly the thermal conductivity of cementitious grouts. On the contrary, the addition of a small amount of bentonite leads to a considerable reduction in the flowability of the grouts, that is, only 2% of bentonite made the value of slump flow become the minimum value of 100 mm. When the specimens were air-dried, the thermal conductivity was reduced by around 0.34 – 0.44 W/m°C that is slightly larger than the case of no bentonite addition.

Table 4: Effect of bentonite addition and viscosity

Cement	Geo-11	Geo-12	Geo-13	Geo-14	Geo-15
w/c ratio	0.60	0.60	0.60	0.60	0.60
Sand/cement ratio	2.40	2.40	2.40	2.40	2.40
Bentonite/cement ratio	1 %	2 %	3 %	4 %	6 %
Slump Flow(mm)	105-107	100	100	100	100
V-Funnel(sec)	4.5	300	300	300	300

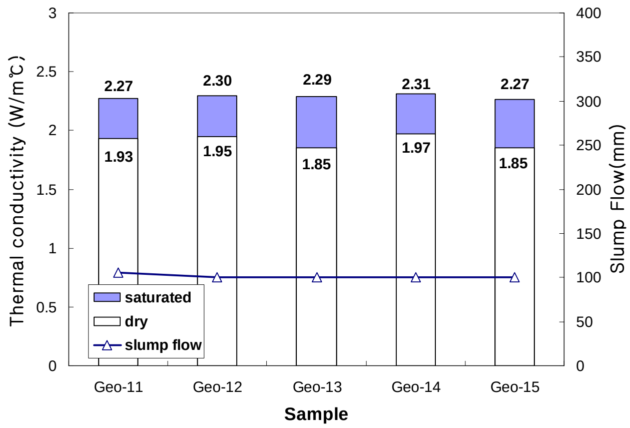

Figure 9: Thermal conductivity and slump flow with different bentonite content

5. CONCLUSION

The following conclusions are based on the findings for the thermal conductivity and viscosity of bentonite grouts and cementitious grouts.

1. In case of the nine neat bentonite grouts with no addition of fillers, two mix proportions of 20% and 30% of bentonite by weight show a range of thermal conductivity in the fully saturated condition of 0.74-0.81 W/m°C and 0.76-0.95 W/m°C, respectively, which are far smaller than the cementitious grouts. When the specimens are air-dried, the thermal conductivity significantly decreases. Increase in thermal conductivity due to the addition of silica sand is not significant, and even the case of 60% of silica sand results in the thermal conductivity less than 1.4 W/m°C.

2. The viscosity of bentonite grouts significantly increases with time. The rate of viscosity increase becomes greater when the amount of silica sand mixed in the grout increases. It is highly recommended to be careful to prepare grout paste with no delay in the field when pumping it into the borehole.

3. For neat cementitious grouts, increasing the water/cement ratio leads to a decrease in thermal conductivity and an increase in slump flow which means the enhancement of flowability. A reduction of thermal

conductivity due to air-drying is about 0.25 W/m°C which is far smaller than the case of bentonite grouts, and thus the thermal conductivity of cementitious grout may be less vulnerable to a drying condition than the bentonite grouts.

4. Addition of silica sand to cementitious grouts leads to an increase in thermal conductivity and a reduction in slump flow which decreases groutability. However, addition of a small dosage of bentonite does not affect significantly the thermal conductivity of cementitious grouts.

ACKNOWLEGEMENT

The writers appreciate the financial support by grant No. 06 construction-core D04 from KICTEP, The ministry of land, transport and maritime affairs. The views expressed in this paper are the writers and do not reflect the views of KICTEP.

REFERENCES

Allan, M. L., 2000. Material characterization of superplasticized cement-sand grout. *Cement and Concrete Research* 30. pp. 937-942.

Allan, M. L., Philippacopoulos, A., 1999. *Properties and performance of cement -based grouts for geothermal heat pump application*. FY 1999 Progress Report, BNL 67006, 53pp.

Allan, M. L., Philippacopoulos, A., 2000. *Performance characteristics and modelling of cementitious grouts for geothermal heat pumps*. Proceeding of World Geothermal Congress 2000. 10th June, Beppu and Morioka, Japan, pp. 3355-3360.

Choi, H., Lee, C., Choi. H-P, and Woo, S-B., 2008. A study on the physical characteristics of grout material fro backfilling ground heat exchanger. *Journal of the Korean Geotechnical Society*. 24(1). pp. 37-49.

Han, J., Han, G., Han, H., and Han, C., 2005. *Geothermal Heat Pump (GHP) System*. in Korean. Han Lim Won.

ESTIMATION OF ULTRASONIC CAVITATION ENERGY IN A LARGE-SCALE SONOREACTOR

YOUNGGYU SON, MYUNGHEE LIM and JEEHYEONG KHIM
Department of Civil, Environmental and Architectural Engineering,
Korea University, 5-ga, Anam-dong Seongbuk-gu, Seoul 136-701, Korea
hyeong@korea.ac.kr

ABSTRACT

In this study, ultrasonic cavitation-energy distributions were analyzed in a large-scale sonoreactor, using three-dimensional mapping methods. The highest and most stable cavitation energy state, through the whole length, was obtained with an ultrasound application of 72 kHz. However, very poor energy distributions were obtained at ultrasound applications of 110 and 170 kHz. In the presence of a reflector, cavitation energy distribution in the sonoreactor was much dependent on the location of opposite reflective wall, which determined by wavelength of applied ultrasound. . Interestingly, in 35 kHz average energies were slightly higher in the case of 20 cm than in the case of 50 cm although the volume of sonoreactor in the case of 20 cm was 2.5 times larger than in the case of 50cm.

1. INTRODUCTION

Chemical and mechanical effects caused by ultrasonic cavitation in homogeneous and heterogeneous systems have been widely studied.[1,2] The important factors that affect cavitation include: ultrasonic frequency; acoustic power; dissolved gasses; ambient temperature; and ambient pressure, etc.[2,3] Most of the previous research concerning the study of ultrasonic reactions was conducted in small-scale sonoreactors and it was assumed in these studies that the effects of these factors were approximately the same for every position in the reactors. However, this assumption is not valid when ultrasonic reactions are conducted in large-scale sonoreactors. In particular, the distribution of ultrasonic energy attributed to input acoustic power can change significantly according to the size and shape of the sonoreactors as well as to the location of the transducers. Therefore, the degree of chemical and mechanical effects in each position becomes uneven.

Several methods have been reported that analyze ultrasonic energy distribution. These include a hydrophone for the local pressure amplitudes,[4] optical fiber tips for the local pressure amplitudes and aluminium foil analysis for the mechanical effects,[5] and a cavitation activity indicator for the instantaneous cavitational intensity.[6] However, there has not been an investigation that has focused on measuring ultrasonic energy distribution for large-scale sonoreactors.

This present study was designed to evaluate the performance of a pilot-scale sonoreactor under various ultrasonic frequencies. The specific objectives of this investigation were to analyze the ultrasonic cavitation energy in the sonoreactors through three-dimensional cavitation energy measurements and to understand the effect of a reflector in a large-scale sonoreactor.

2. EXPERIMENTAL PROCEDURE

2.1 Reactor configuration

The pilot-scale sonoreactor used in this study consisted of an acrylic bath (L 1.20 m × W 0.60 m × H 0.40 m) and an ultrasonic transducer module (Mirae Ultrasonic Tech.) placed at the center of the side of the bath as shown in Figure 1. The transducer module (L 0.20 m × W 0.20 m × H 0.07 m) contained nine PZT transducers and could produce ultrasound of 35, 72, 110, and 170 kHz frequency. The maximum power of the transducer module was 400W. Acoustic absorbents made of polyurethane were equipped on all the sidewalls and the bottom, with the exception of the sidewall where the module was placed in order to prevent the reflection of ultrasound. The reactor was filled with 250 L of tap water.

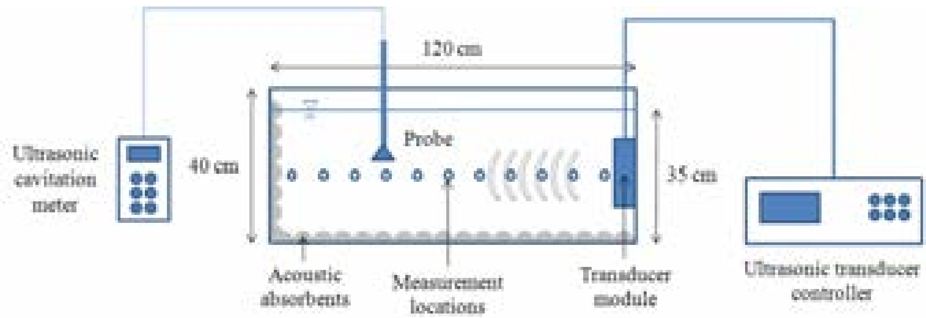

Figure 1: Schematic of the pilot-scale sonoreactor and the location of measurement of cavitation energy (side view)

2.2 Measurement of ultrasonic cavitation energy

A three-dimensional cavitation energy analysis was carried out for the four frequencies of 35, 72, 110, and 170 kHz, with 160 W input power. From the transducer module to the end of the reactor, 11 sections were divided along the length. The dimensions of each section were, L 10 cm × W 20 cm × H 20 cm, and 99 points were selected for the measurements of the cavitation energy in the whole reactor.

The ultrasonic/megasonic cavitation meter (ppb, pb-502) was used for the analysis of cavitation energy in the sonoreactor. This instrument could detect cavitation, or the collapse of the cavitation bubbles as they imploded on the surface of a probe. It could also display the energy density of cavitation as a unit of W/cm2. The diameter of the probe was 5 cm.

2.3 Reflector

A reflector was placed at 20 and 50 cm and was moved by λ (wave length)/4 in order to compare the average cavitation energy in 35 kHz and 240 W. The reflector had two 10 mm thick glass plates with a 10 mm air layer between the two plates.

3. RESULTS AND DISCUSSION

3.1 The effect of frequency

Figure 2 shows the change of cavitation energy at each section throughout the whole length. In 110 and 170 kHz, very poor energy values were obtained in comparison to the cases of 35 and 72 kHz. The average cavitation energies in the whole reactor were 53.50, 83.87, 6.41, and 0.10 W for 35, 72, 110, and 170 kHz, respectively. Therefore, it was identified that 110 and 170 kHz of ultrasound would not be applied to the sonoreactor whose irradiation distance is over several tens centimeters. Meanwhile, 35 and 72 kHz ultrasound were estimated as high applicable wave energies.

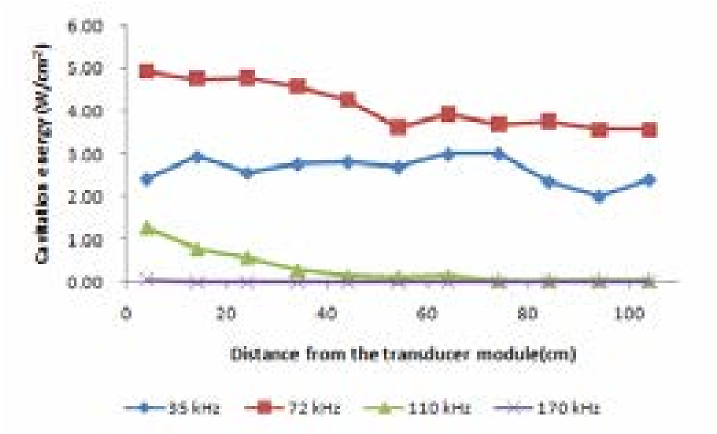

Figure 2: Change of cavitation energy at each section throughout the whole length.

3.2 The effect of reflector

Figure 3 shows the effect of a reflector in the sonoreactor. Average cavitation energies were significantly dependent on the reflector location, which was determined by the wavelength of ultrasound. Interestingly, in 35 kHz average energies were slightly higher in the case of 20 cm than in the case of 50 cm although the volume of sonoreactor in the case of 20 cm was 2.5 times larger than in the case of 50cm.

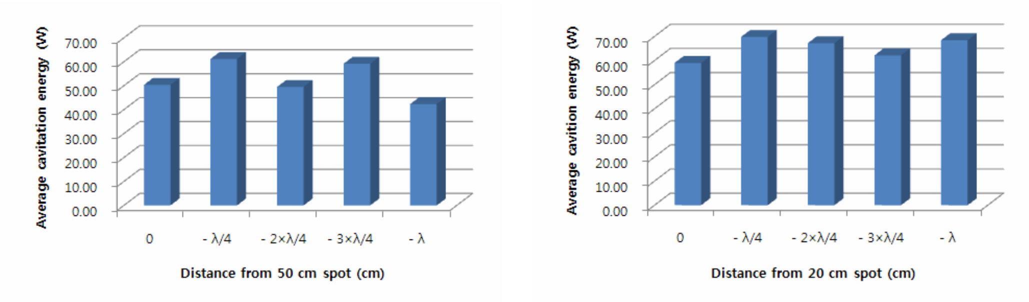

(a) 35 kHz, 240W, λ = 4.3 cm

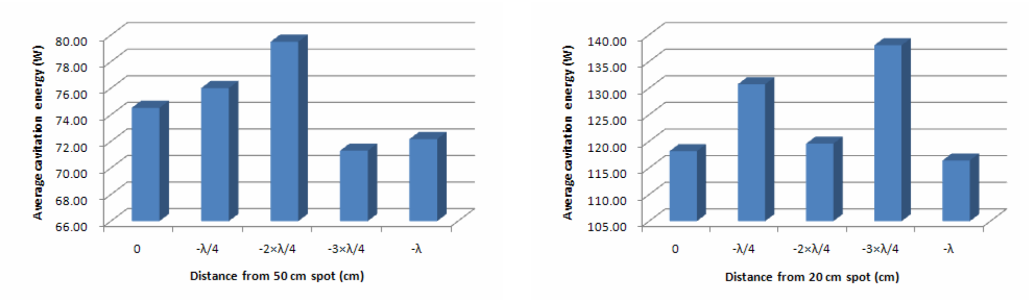

(a) 72 kHz, 240W, λ = 2.0 cm

Figure 3: Change of average cavitation energy in the presence of a reflector

4. CONCLUSIONS

Three-dimensional cavitation energy analyses were conducted in a large-scale sonoreactor. The following results were found:

1. Various distributions of cavitation energy under different frequency conditions were measured, even though the experiments were conducted in the same power intensity.

2. Application of 72 kHz ultrasound showed the most stable and highest energy distribution in three-dimensional energy analysis.

3. Cavitation energy distribution in the sonoreactor was much dependent on the location of opposite reflective wall.

ACKNOWLEDGMENTS

This research was supported by a grant (R01-2007-000-20886-0) from the Korea Science and Engineering Foundation (KOSEF).

REFERENCES

Adewuyi, Y. G., 2001. Sonochemistry: Environmental Science and Engineering Applications. *Industrial and Engineering Chemistry Research* 40, 4681-4715.

Thompson, L. H. and Doraiswamy, L. K., 1999. Sonochemistry: Science and Engineering *Industrial and Engineering Chemistry Research* 38**,** 1215-1249

Gogate, P. R., 2007. Application of cavitational reactors for water disinfection: Current status and path forward. *Journal of Environmental Management* 85, 801-815.

USE OF SUPERFINE CRUMB RUBBER TO IMPROVE THERMAL & SOUND PROPERTIES OF CONCRETE

PITI SUKONTASUKKUL and SOMYOT WIWATPATTANAPONG
Department of Civil Engineering, Faculty of Engineering
King Mongkut University's of Technology-North Bangkok
piti@kmutnb.ac.th

ABSTRACT

Abandoned tires are a well recognized environmental problem worldwide. One way to dispose them is to grind them into crumb rubbers. Crumb rubber can be used in wide range of applications such as pavement, blocks, sealant, supplement fuel etc. In Thailand, crumb rubbers are produced by grinding and can be found in several sizes depending on the applications (several millimeters to microns). The smallest size that can be achieved is about 500 to 600 micron (0.0197 to 0.0234 in). These superfine crumb rubbers are used mainly in crack sealant and joint filler applications. In this study, the superfine crumb rubbers are mixed with concrete by replacing fine aggregate at the rate of 10%, 20% and 30% by weight. The role of small particles of crumb rubbers is to act as a filler to fill small voids in concrete to reduce water absorption and porosity. Also, by replacing high density aggregate with low density crumb rubber, the average density of concrete is found to decrease. The decrease in density also results in better thermal and sound properties.

1. INTRODUCTION

1.1 Manufacturing crumb rubber

Around the world, millions ton of tires are being discarded every year. In Thailand, total consumption of rubber products was about 242 metric tons (533,368 US tons), this number included about 90 metric tons (198,360 US tons) of vehicle tires (2000)[0]. In general, the wasted tires are disposed by dumping them on empty lands. But the dumping yards could become fire hazard and insect or animal habitation (Figure 1). Another way to dispose is by burning, but it causes enormous air pollution and considers irresponsible. Recently, grinding the discarded tires into small particles (called crumb rubber) presents another solution. Crumb rubber can be used in several applications such as asphalt, sealants, rubber sheets or mix with cementitious materials like concrete.

Figure 1: Piling yard of abandoned tires in Thailand

In Thailand, the crumb rubbers obtained from reclaiming plants are produced by grinding which consists of three steps. The first step is to cut and sort out the grindable parts (parts without radial steels). In the next process, rubber pieces are fed into the cutting wheel several times until the desired size is achieved. Finally, crumb rubbers are sorted out according to the particle size. The grinding technique allows the crumb rubbers to be produced in various sizes. Size of crumb rubber depend mainly the number of feeding. At present, about 7 to 8 different sizes of the crumb rubber can be produced. The biggest one has a diameter of about 5 mm (0.197 in) while the smallest one has a diameter of about 600 micron (0.0234 in).

1.2 Concrete microstructure

Concrete consists mainly of three components: cement, aggregates and water. During the mixing, when water comes in contact with cement, series of chemical reactions called “hydration reactions” begin. The hydration reactions are exothermic and involve series of temperature changes from beginning to end (until concrete get harden).

In harden concrete, the micro structure can be divided into two parts: 1) solid and 2) void (or Porosity) part. The solid part consists of hydrated cement (Calcium Silicate Hydrate (CSH), Calcium Hydroxide (CH), etc.), aggregates, unhydrated cement and interface zones between cement and aggregates. As for the porosity, there can be divided into 3 different kinds: 1) capillary pores, 2) gel pores, and 3) interface pores. The pores in concrete come in various sizes. Capillary pores caused primarily by entrapped water and are considered the largest of all. Gel pores are consider smallest and causes by the formation and compaction of CSH(0,0).

Usually, the pore structure plays a significant role on the durability of concrete. This is because the existing of these pores allows external substances (moisture and gas) to migrate in and out of concrete structures.

Some substances can be harmful and caused deterioration in concrete. Therefore to increase concrete durability, engineers have to deal directly with the pore structures. Theoretically, the migrations of water and gas occur mostly through the capillary pores which are large pores and some of them might still interconnected[(0)]. To stop the migrations, the volume of large sized pores must be reduced. This can be achieved by using small w/c ratio or using fillers (such as silica fume, fly ash etc.).

1.3 Need for better insulation

Nowadays, the design and construction purposes of a modern house are not focused on the residential purpose only, but also on energy conservation and on becoming an integral part of the environment. As we know, the earth’s average temperature is rising slowly every year due to the effect of global warming. Cares for the environment are urgently needed by reducing the use of fuel energy, encouraging the use of recycled materials, reducing the emission of carbon dioxide gas, etc0[)]. The construction industry can help by employing site management to minimize wasted materials, using recycled aggregates, selecting environmental friendly materials, etc.

In the case of an individual household, architectural design based on environmental aspect should be considered in order to achieve such goal. From a concrete engineer’s point of view, material selection also plays an important role. The use of better insulating materials can directly reduce long-term energy consumption.

2. RESEARCH SIGNIFICANCE

In the last 20 years, material properties of crumb rubber concrete have been investigated quite exclusively0[-0]. Information on the mechanical properties of crumb rubber concrete with particle size varied from 1 mm (0.039 in) and larger in terms of compressive, tensile, flexural strengths, thermal and sound, is quite well-known. However, information on the effect of crumb rubber with particle size smaller than 1 mm on properties of concrete is still limited. With much smaller particle size, some mechanisms may be different from those with larger size. For example, the overall absorption of concrete may be declined due to the decreasing of volume of capillary pores. In addition, the slump or workability of concrete may be decreased due to the increase in overall specific surface area.

Therefore, the objective of this study includes;

- Encourage the use of crumb rubber to reduce waste from abandoned tires.
- Find concrete with better insulation (thermal and sound) properties that can be manufactured easily, cost effective, and environmental friendly.

- Investigation on the effect of superfine crumb rubber on properties of concrete such as compressive strength, slump, absorption, porosity, thermal and sound properties (such as thermal conductivity factor, thermal resistivity, heat transfer, sound absorption at different frequencies and noise reduction).

3. EXPERIMENTAL PROCEDURE

3.1 Materials

Materials used in this study consisted of Portland cement type I, 3/8" (10 mm) coarse aggregate, river sand, crumb rubber (Figure 2), water and superplasticizer Type F (13 cc /1 kg (0.36 in^3/lb) of cement weight. Crumb rubber with particle size pass through sieve No. 25; the properties and gradation of crumb rubbers are given in Table 1 and Figure 3. The mix proportion for the control specimen (no crumb rubber) was set at 1.00:0.45:1.64:1.95 (Cement : Water : Fine Aggregate : Coarse Aggregate).

In the case of the superfine crumb rubber concrete (SCRC), fine aggregate were replaced with crumb rubber at 20% and 30% by weight. Gradation of sand and sand+crumb rubber is given in Figure 4. Details on the casting and assigned designations are given in Table 2.

Table 1: Properties of crumb rubber

Categories	No.26
Average Bulk Specific Gravity (oven dry)	0.61
Average Bulk Specific Gravity (SSD)	0.62
Average Apparent Specific Gravity	0.62
Average Absorption (%)	1.05
Finess Modulus	2.83

Figure 2: Crumb rubber

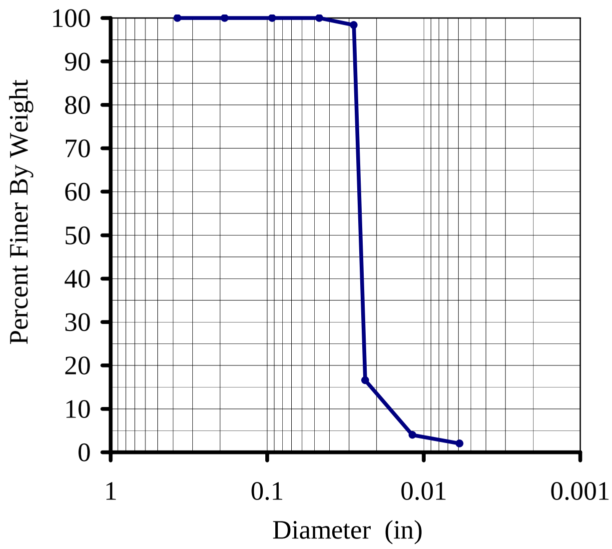

Figure 3: Gradation of crumb rubber

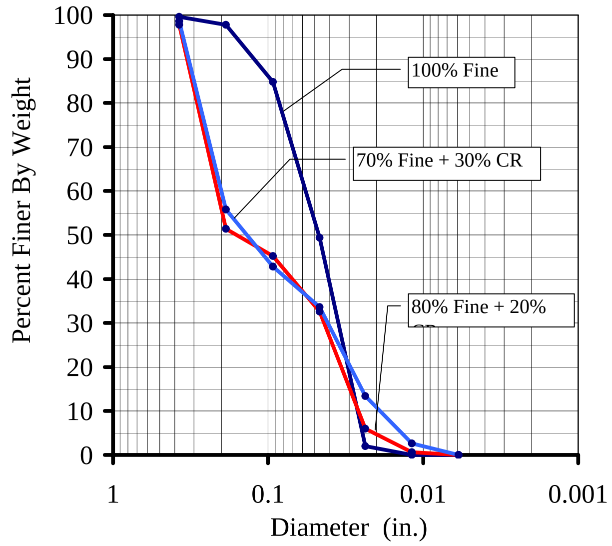

Figure 4: Gradation of fine aggregate + crumb rubber

Table 2: Details and assigned designations

Designation	w/c ratio	Weight per m^3 (ft^3)				
		Crumb Rub kg (lb)	Cement kg (lb)	Coarse Agg kg (lb)	Fine Agg kg (lb)	Water kg (lb)
PC	0.47	0	478.7 (29.8)	933.5 (58.1)	783.8 (48.8)	215 (13.4)
10SCRC	0.47	78.4 (4.9)	478.7 (29.8)	933.5 (58.1)	705.5 (43.9)	215 (13.4)
20SCRC	0.47	156.8 (9.8)	478.7 (29.8)	933.5 (58.1)	627.1 (39.0)	215 (13.4)
30SCRC	0.47	235.2 (14.6)	478.7 (29.8)	933.5 (58.1)	548.7 (34.2)	215 (13.4)

3.2 Casting and testing the specimen

Concrete was dry-mixed using pan mixer for about 5 minutes, then added water and continued mixing for another 5 minutes, after that it was poured into molds. Three tests were carried out: 1) Density, Voids and Absorption (ASTM C642-97)[00], 2) Steady-State Heat Flux Measurement and Thermal Transmission Properties (ASTM C177)[0] (Figure 5), and 3) Acoustics Determination of Sound Absorption Coefficient and Impedance in Impedance Tube (ISO 10534-1:1996)[0](Figure 6). Number of samples for each test is summarized in Table 3.

Table 3: Casting schedule

Type of concrete	**Number of specimen**		
	Thermal Conductivity	**Sound Absorption**	**Density Void & Absp**
PC	3	8	3
10SCRC	3	8	3
20SCRC	3	8	3
30SCRC	3	8	3
Total	12	32	12

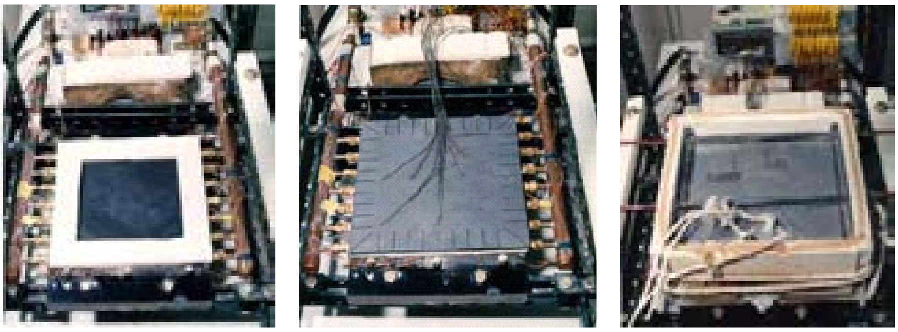

Figure 5: Steady-state heat flux measurement (ASTM C177)

Figure 6: Acoustics determination of sound absorption coefficient and impedance in impedance tube (ISO 10534-1:1996)

4. EXPERIMENTAL RESULTS

4.1 Density, absorption and voids

As shown in Table 4 and Figure 7 the bulk density of concrete mixed with crumb rubber was found to decrease gradually with the rubber content comparing normal concrete. While the bulk density of normal concrete was about 2330 kg/m^3 (145 lb/ft^3), the average bulk density of 10%, 20% and 30% crumb rubber concrete were 2090, 1970 and 1820 kg/m^3 (130, 122 and 113 lb/ft^3) , respectively.

The decrease in bulk density of concrete was partly due to the replacement of a material with heavier specific gravity (fine aggregate) by a lighter one (crumb rubber). The fine aggregate (River sand) used in this study has an average specific gravity (oven dry) of 2.42, while the crumb rubber has an average of about 0.61. By calculation, at 10%, 20% and 30% replacement ratio, the overall density of concrete was expected to decrease (due to the effect of crumb rubber alone) by 7.5%, 14% and 19.5%, respectively. The actual results are slightly higher than the calculation and this, perhaps, due to the effect of moisture in fine aggregate that did not taken into account in the calculation.

In the case of the absorption and permeable void (Table 4, Figure 8, unlike other lightweight aggregated concrete, the effect of crumb rubber adding into concrete appeared to lower both absorption and permeable void content. For conventional lightweight concrete, these two values would be quite high because of the high porosity in aggregates or large amount of air bubble in cement paste. But when using super fine crumb rubber, even though the overall density of concrete decreased gradually with the rubber content, the permeable void was found to decrease instead of increase.

Table 4: Bulk density, void and absorption

Type	Bulk Density		Void	Absorption
	kg/m3	(lb/ft3)	(%)	(%)
PC	2330.0	(145.1)	9.35	4.26
10%CR	2090.0	(130.1)	6.79	3.51
20%CR	1970.0	(122.7)	5.90	3.39
30%CR	1820.0	(113.3)	5.81	2.98

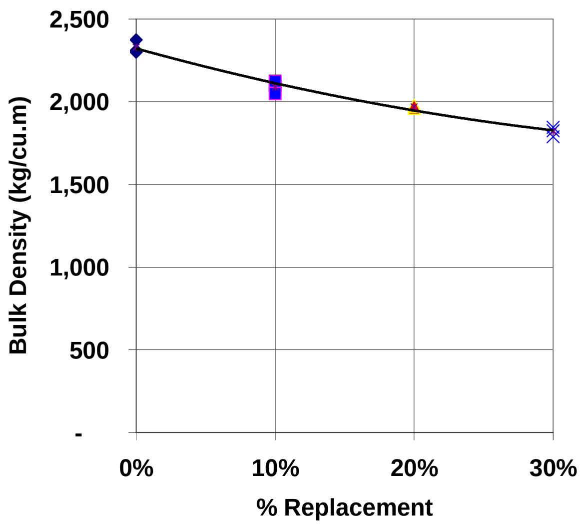

Figure 7: Bulk density of PC vs. crumb rubber concrete

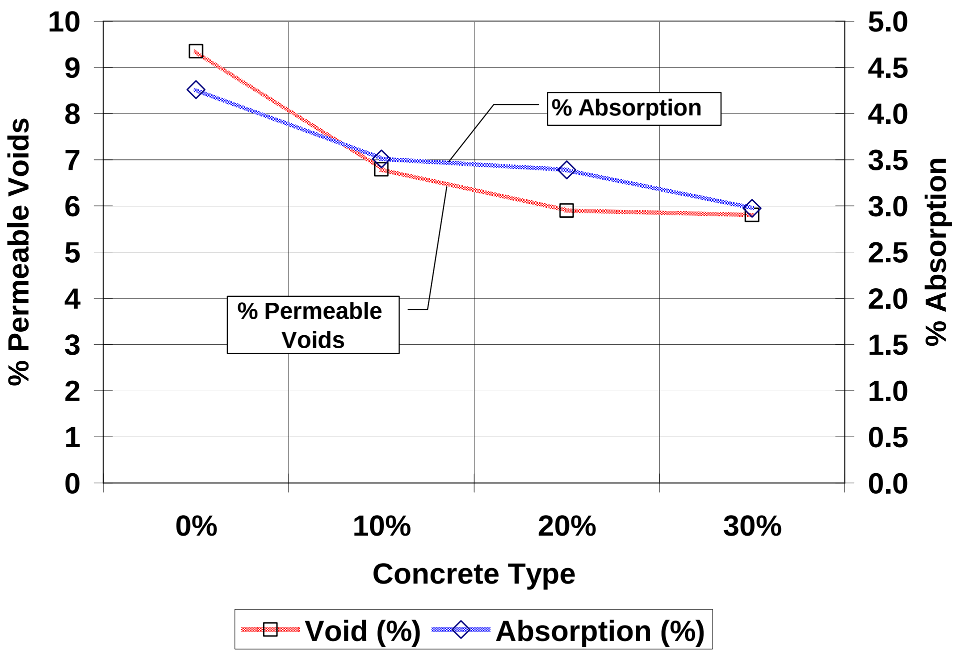

Figure 8: Permeable voids and absorption

The decrease in permeable void and absorption was due to 1) the porosity of crumb rubber particle and 2) the filling effect. In the case of porosity, refer to Table 1, it could be seen that the specific gravity of superfine crumb rubber under both SSD and oven dry conditions were quite similar (0.61 and 0.62, respectively). These unchanged values indicated that crumb rubber was not a porous material. Therefore, by adding them into concrete, no additional pore was added into the concrete pore system.

As for the filling effect, the small particle of superfine crumb rubber (SCRC) played a significant role in this part. With small particle size as 500-600 micron (0.0197 to 0.0234 in), the crumb rubbers were able to fill up some of the capillary pores which led to the decrease in absorption from 4.26% to 2.98% as show in Figure 8.

4.2 Thermal conductivity

By definition, the quantity of heat transmitted through a unit thickness in a direction normal to a surface of unit area, due to a unit temperature gradient under steady state conditions is defined as the thermal conductivity value (k). There are several parameters affecting the value of k in materials, such as density, moisture content, temperature etc. In this case, let consider only the density. Theoretically, the value of thermal conductivity is directly proportional to the density; this means materials with low density will usually exhibit low value of k.

Based on the test results as shown in Figure 9 the k value of plain concrete was found at 0.531 W/m.K (0.016 W/ft.K), while those of SCRC were at 0.290, 0.275, and 0.267 W/m.K (0.0088, 0.0084, and 0.0081 W/ft.K) for 10SCRC, 20SCRC and 30SCRC, respectively. Comparing in percentage, they are lower by about 44% to 49%. The lower values of k indicated that SCRC is essentially a better insulator than plain concrete and is partly due to the lower density of SCRC than that of plain concrete.

According to Thailand Industrial Standard (TIS), the allowable values of k are specified within the range of 0.303 to 0.476 W/m.K (0.0092 to 0.0145 W/ft.K) for conventional lightweight concrete. The k-values of SCRC obtained from this study were found to be less than or within the allowable range of those specified by TIS.

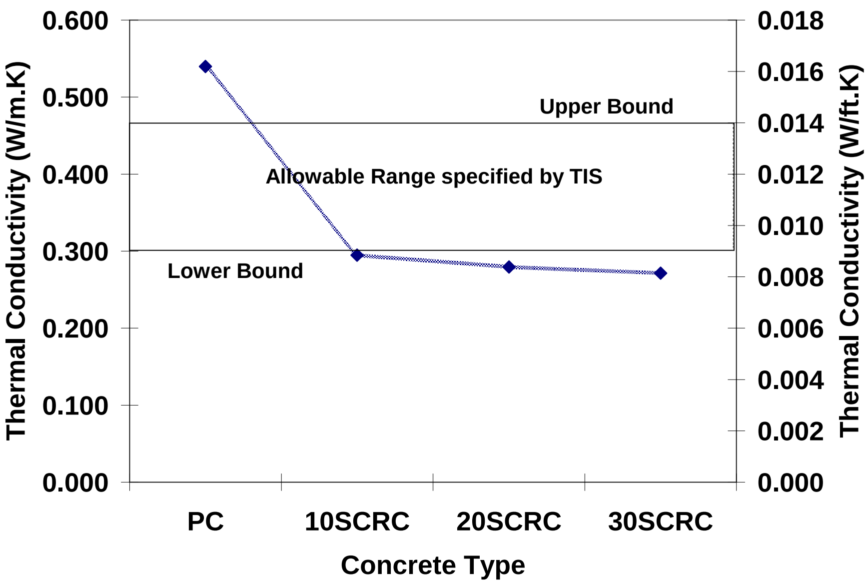

Figure 9: Thermal conductivity (k)

4.3 Heat transfer rate and heat resistivity

The rate of heat transfer per unit time (hour) and heat resistivity can be calculated using the following equations:

$$q = \frac{kAdT}{t} \tag{1}$$

$$r = \frac{t}{k} \tag{2}$$

where q = heat transferred per unit time (W/ hour), r = heat resistivity (m^2/kW, ft^2/kW), A = heat transfer area (m^2, ft^2), k = thermal conductivity (W/m.K or W/m.^{o}C, Btu/(hr ^{o}F ft^2/ft)), dT = Temperature difference across the material (K or ^{o}C, ^{o}F), t = material thickness (m, ft)

Using the value of k from the test and assuming that the temperature difference between night and day is 12^o C (= 285.15^o K), the area is 1 x 1 m^2 (0.093 ft^2) and the thickness is 0.10 m (0.031 ft), the heat transfer and resistivity of both plain and CR concrete can be calculated as shown in Table 5.

Table 5: Rate of heat transfer and heat resistivity

Type	Heat Transfer W/h	Heat Resistivity m^2/kW	(ft^2/kW)
PC	1,514	0.19	(0.018)
10SCRC	827	0.34	(0.032)
20SCRC	784	0.36	(0.033)
30SCRC	761	0.37	(0.034)

According to Table 5, all SCRC exhibited lower heat transfer rate and better heat resistivity than plain concrete. Both values were related to the rubber content. The rate of heat transfer was found to decrease with the increasing rubber content, while the heat resistivity went the opposite direction.

4.4 Sound absorption

The ability of material to absorb sound at any particular frequency is defined in form of the sound absorption coefficient (α). In general, for a healthy young person, the hearing range is 15 to 18,000 hertz[0)]. According to the standard test, six different ranges of sound frequencies were used to measure the sound absorption of both plain and SCRC: 125, 250, 500, 1000, 2000 and 4000 Hz.

The variation of α for each material over the wide range of frequencies can be high or low depending on material type. On the low side, for example, a marble tile exhibits quite consistency values of 0.01, 0.01, 0.01, 0.01, 0.02, and 0.02 over the six frequency ranges. On the high side such as a plaster board (for ceiling), it has rise and fall values from 0.15, 0.11, 0.04, 0.04, 0.07, and 0.08[(0)].

Results of both plain and SCR concrete are shown in Figure 10. It could be seen that at the low frequency ranges of 125 and 250 Hz, both plain and SCR concrete exhibited similar values of α. However, at frequencies higher than 500 Hz, those of SCRC started to separate and became higher than that of plain concrete (Figure 10). High α indicated that SCRC can absorb sound better at high frequency ranges than plain concrete.

In addition, the sound absorption of material can be illustrated using another value so called the noise reduction coefficient (NRC). The NCR is an average value of α at four frequencies in the middle range, can be calculated using the following equation.

$$NCR = \left(\alpha_{250} + \alpha_{500} + \alpha_{1000} + \alpha_{2000}\right)/4 \tag{3}$$

Results of NCR against the density are given in Figure 11. Clearly, the noise reduction depended mainly on the density of material. As the density decreased, the noise reduction increased. For SCRC which density less than plain concrete by about 20%, the noise reduction increased by about 46%.

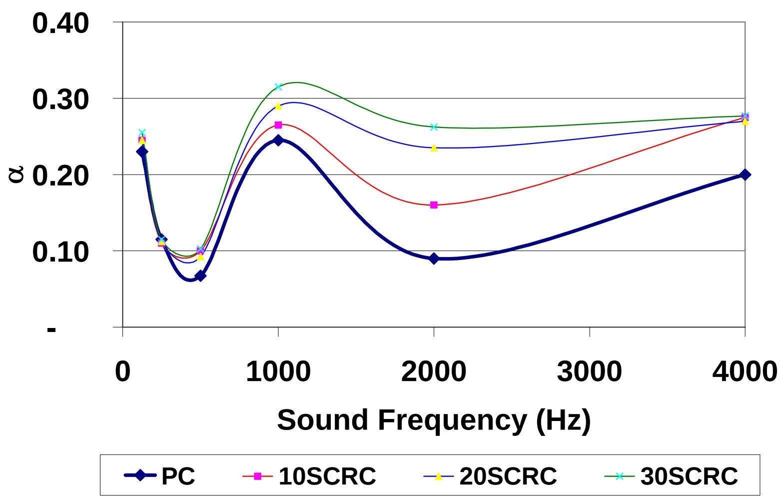

Figure 10: Sound absorption coefficient

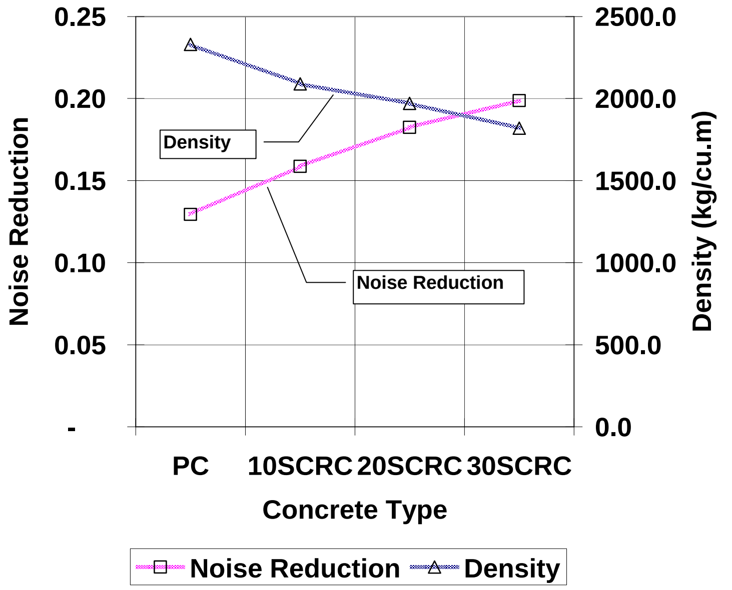

Figure 11: Noise reduction coefficient

5. CONCLUSIONS

1. Superfine particle crumb rubber has proved to improve the porosity and absorption of concrete by reducing both values up to about 38% and 30%, respectively (at 30% replacement rate). With small particle size, the crumb rubber is able to fill up some capillary pores and voids in concrete.

2. With smaller specific gravity than conventional fine aggregate, the crumb rubber can reduce the density of concrete up to about 20% at the 30% replacement rate.

3. SCRC also provides better insulating properties in both thermal and sound as seen by the decreasing thermal conductivity value and increasing sound absorption coefficient as compare to those of plain concrete.

ACKNOWLEDGEMENT

The authors would like to thank the Thailand Research Fund-Master Research Grants (TRF-MAG) for financially support this study and also Union Pattanakit Co., Ltd., for providing crumb rubber.

REFERENCES

Rubber Research Institute, *Statistic on the Use of Vehicle Tires in Thailand*, Ministry of Agriculture, Thailand (in Thai).

Mindess, S., Young, JF., and Darwin, D., 2003. *Concrete 2nd Edition*, Prentice Hall.

Neville, A.M., 1996. *Properties of Concrete 4th Edition*, Longman.

Young, JF., Mindess, S., Gray, RJ., Bentur, A., *1998*. *The Science and Technology of Civil Engineering Materials*. Prentice Hall.

Montreal Protocol, 1997. United Nations Environment Program, United Nation.

Blackwell, M. C., and Pierce, C. E., 2002. Potential of Scrap Tire Rubber as Lightweight Aggregate in Flowable Fill. *Journal of Waste Management*, October, 23(9), 197-208.

Chesner, W. H., Collins, R.J., and MacKay, M.H., 1998. *Users Guidelines for Waste and By-Product Materials in Pavement Construction.* Report No. FHWA-RD-97-148, Commack: Chesner Engineering, P.C., April.

Eldin, N., and Senouci, A., 1994. Measurement and Prediction of the Strength of Rubberized Concrete. *Cement and Concrete Composite*, No. 19, 287-298.

Eldin, N., and Senouci, A., 1993. Rubber-Tire Particles as Concrete Aggregate. *ASCE: Journal of Materials in Civil Engineering*, Vol.5, No.4, 478-496.

Fattuhi, N., and Clark, L., 1996. Cement Based Materials Containing Shredded Scrap Truck Tyre Rubber. *Construction and Building Materials*, Vol. 10, No. 4, 229-236.

Goulias, D.G., and Ali, A.H., 1998. Evaluation of Rubber-Filled Concrete and Correlation between Destructive and Nondestructive Testing Results. *Journal of Cement*, *Concrete and Aggregates*, 20(1), 140-444.

Huynh, H., Raghavan, D., and Ferraris, C., 1996. *Rubber Particles from Recycled Tires in Cementitious Composite Materials*. NISTIR 5850 R; May.

Khatib, Z.K., and Bayomy, F.M., 1999. Rubber Portland Cement Concrete. *Journal of Materials in Civil Engineering*, 11(3), 206-213.

Maupin G.W., and Payne, C.W., 1997. *Final Report Evaluation of Asphalt-Rubber Stress Absorbing Membranes*, VTRC98-R11, Virginia Transportation Research Council, September.

Morris, G. R., and McDonald, C.H., 1976. Asphalt -Rubber Stress Absorbing Membranesfield Performance. *Transportation Research Record*, 595, 99-108.

Rostami, H., Lepore, J., Silverstraim, T., and Zandi, I., 2000. *Use of Recycled Rubber Tires in Concrete*, Proc. Int. Conf. Concrete , University of Dundee, UK, 391-399.

Scofield, L. A., 1989. *The History, Development, and Performance of Asphalt Rubber at ADOT*, Report Number AZ-SP-8902, ADOT, December.

Topcu, I., 1995. The Properties of Rubberized Concrete. *Cement and Concrete Research*, No. 25, 304-310.

Zube, E., 1951. *Experimental Field Use of Powdered Rubber in Bituminous Plant Mix Surfacing*. ID. 51-08, Division of Highway, State of California.

ASTM DESIGNATION: C 136-96a, *Test Method for Sieve Analysis of Fine and Coarse Aggregates*.

ASTM DESIGNATION: C 642-97, *Test Method for Density, Absorption, and Voids in Hardened Concrete.*

ASTM DESIGNATION: C 177-97, *Test Method for Steady-State Heat Flux Measurements and Thermal Transmission Properties by Means of the Guarded-Hot-Plate Apparatus.*

ISO DESIGNATION: 10534-1, *Test Method for Acoustics-Determination of Sound Absorption Coefficient and Impedance in Impedance Tubes*. Part 1: Method Using Standing Wave Ratio.

Lerder, Francis C., 2004. *The Human Ear*, Encarta Encyclopedia Deluxe. CD-ROM.

http://www.saecollege.de/reference_material/pages/Coefficient%20Chart.htm

Student Report

REPORT FROM STUDENT PARTICIPANTS ON THE JOINT STUDENT SEMINAR ON CIVIL INFRASTRUCTURES

Venue: Asian Institute of Technology, Bangkok, Thailand
Date: July 3 – 4, 2008

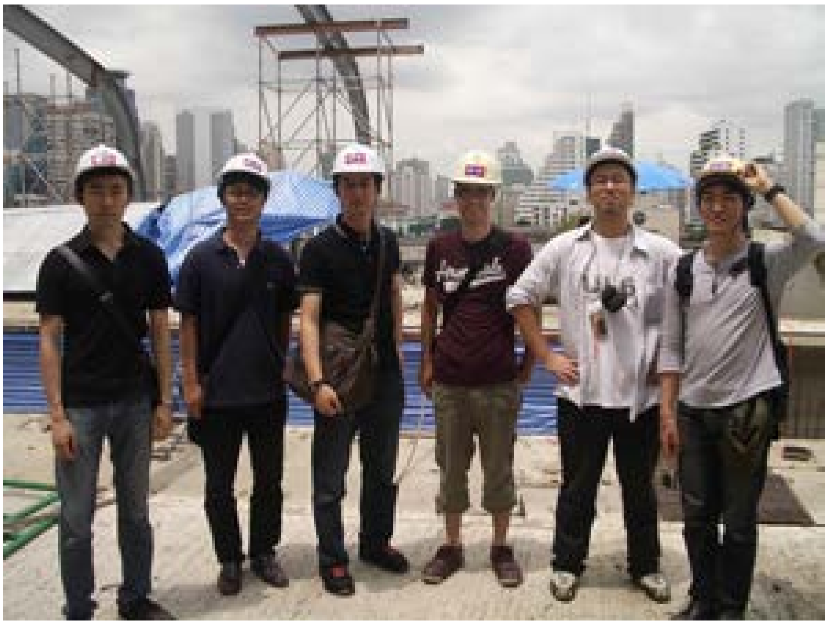

Student Participants (from left to right)
Naoki Sorimachi
Tomoya Kawasaki
Hiroaki Ebizuka
Michael Henry
Hiroaki Nishiuchi
Yusuke Matsumura

Presentation Session


Seminar Venue

On July 3rd, the presentation session was held at the AIT Conference Center. First, five professors from the participating countries (Japan, Korea, and Thailand) gave lectures on their research topics.

After the professors' lectures, 17 civil engineering students delivered their presentations. The contents of the student presentations included a variety of topics such as soil engineering, traffic management, disaster mitigation, concrete engineering, and so on. Since there was such a wide range of topics, I could learn about some fields which I normally don't experience. The six Japanese participants also delivered their presentations. The presentation titles were:

- **Tomoya Kawasaki:** *Intermodal mode choice between Japan and Russia*
- **Yusuke Matsumura:** *Evaluation of wildfire duration time over Asia using MTSAT and MODIS*
- **Michael Henry:** *Utilizing heterogeneous engineering in concrete material innovations for sustainable development*
- **Hiroaki Ebizuka:** *Laboratory stiffness measurements on Toyoura sand*
- **Naoki Sorimachi:** *Seismic retrofitting promotion model for masonry houses using PP-band method and micro-earthquake insurance*
- **Hiroaki Nishiuchi:** *OD variation analysis on the Tokyo Metropolitan Expressway using ETC-OD data*


Lively Discussion

All the presenters gave their best effort during their presentation. I thought the Japanese members are conducting meaningful and interesting research works, and the foreign students seemed to be quite interested. The question and answer sessions were also very productive and we had useful discussion on the research results. Through this session, we could get a lot of information about the hot topics in civil engineering in Asian countries. Furthermore, it was a good opportunity to practice presentation and English skills.
(by Yusuke Matsumura)

Technical Visit: "Airport Rail Link Construction Site"

On July 4th, we visited the Suvarnabhumi airport rail link and city air terminal project. This project aims to connect the airport to the central part of Bangkok by constructing 28 kilometers of elevated light rail and the accompanying train stations. Currently, the only public transportation from the airport to Bangkok is by bus, so the airport users often suffer from the traffic jams which occur in the city. This project aims to increase accessibility to the airport as well as ease travelers' troubles.

This project utilizes pre-cast segmental box-girder short-line casting method to construct the elevated bridge. This method connects the pre-cast segments at the construction site and integrates them by pre-stressing. Applying this method reduces the period of work at the site and improves quality.


Airport Transit Extension

The construction of the city air terminal required a special method to erect the roof trusses. The trusses were assembled next to the city air terminal and then lifted onto the building and slide into place.


City Air Terminal Project Site

The construction site itself was huge, with equipment and construction materials piled everywhere. There were even some dogs wandering around inside the construction site, and the ground was covered with puddles from a recent squall. The picture on the right shows the station under construction, including the impressive roof shape. The station roof was composed of several sliding units, each containing one steeple roof, and these units were slide into place before being connected to the adjacent unit, as discussed above.


Inside the Main Building

The inside the station was also huge. The picture on the right shows the inside of the station. The scope of the project could be felt in the main terminal area, where construction workers were assembling panels for the ceiling about 30 meters above the floor. We could walk around the construction area quite freely and approach near the workers. This sort of accessibility is impossible in Japan due to security and safety issues.

(by Hiroaki Ebizuka & Naoki Sorimachi)

Impressions from the Student Participants

I attended the Joint Student Seminar on Civil Infrastructures held at the Asian Institute of Technology (AIT) in Thailand on the 3rd and 4th of July, 2008. AIT, my alma mater, is located in the Thailand Science Park (TSP), 50 kilometers north of Bangkok. This location is similar to Tsukuba city in Japan. The topic of my presentation was international intermodal logistics. After my presentation, a Vietnamese student from a Korean university asked about my presentation. This time was very fruitful to deepen my awareness towards study and stimulate my thinking. In addition, I was fortunate to have the opportunity to discuss with a Korean professor the current logistics condition and issues in Korea. Thanks to several discussions at this seminar, I again realize the importance of communication with researchers. Lastly, I would like to express my profound gratitude and appreciation to the professors and students from the University of Tokyo (UOT) and AIT. I got a lot of stimulation from this seminar and would like to use this experience towards my future activities.
(by Tomoya Kawasaki)

The Joint Student Seminar on Civil Infrastructures provided me with a good opportunity to visit Thailand (for the first time), as well as share my research works and practice making presentations. The other students' presentations were from a wide variety of fields, which gave me the chance to learn about different areas in civil engineering. The site visit was extremely interesting; Thai construction companies run their construction sites in such a different manner from Japan or the USA that I was quite surprised. We were able to wander around the inside of the main train terminal, even as construction works were going on around us. Also, the construction site itself was very cluttered, with garbage and materials. However, on the whole, it was definitely a valuable chance to not only learn about other countries' research works, but also to see how construction is managed in a different country. **(by Michael Henry)**

The AIT seminar was the first international conference in my life that I participated in as a presenter. I learned that the most important thing when presenting is to make listeners understand what you want to say. Use easy words and phrases, and be simple. I think this is true in international communication, too. I strongly felt this when I was chatting with a guy from Korea during lunch. I'm looking forward to joining AIT seminar again.
(by Naoki Sorimachi)

This is my first international seminar and first visit to Thailand, and even my first presentation to people who belong to other universities. I experienced many things that I had not done before through this seminar. They made me able to see things in perspective. Contact with Thai and Korean students studying in the same field as me helped increase my motivation to study. I want to make good use of these experiences and keep studying. I wish to express my gratitude to those people related to this seminar. **(by Hiroaki Ebizuka)**

The Joint Student Seminar on Civil Infrastructures gave me a good opportunity to discuss with other fields' researchers and students. There were not a lot works related to my research area (Traffic Engineering), but I received some comments which reminded me to think about basic background, concept, methodology and so on. We also had a technical visit to see the "Airport rail link" construction site. This is the new railway between Bangkok International Airport and Bangkok. First we listened to an introduction about the construction method and then moved to the actual construction site. I was impressed by the construction method of the station roof, especially since it was designed with such a modern style! I really look forward to riding the new train system next time I visit. I also had a good time with a researcher from Thailand who stayed in our laboratory. These days were an amazing time in Thailand!

(by Hiroaki Nishiuchi)

It was a great pleasure for me to join the Joint Student Seminar for Civil Infrastructures. This was my first time to give a presentation in front of foreign students and researchers. I learned a lot through the experience, not only by giving my presentation at AIT but also the preparation for it in Japan. It really cheered me up to develop English skills. Moreover, events other than presentation session during the seminar like the engineering tour were also very meaningful and enjoyable. I hope to join this kind of seminar again in the future if I have the chance. For the student seminar next year, I think it is better to better encourage inter-cultural communication among the participants. I appreciate the effort and work of everyone who organized and supported this great event.

(by Yusuke Matsumura)

I had a great time when I attended the Joint Student Seminar on Civil Infrastructures held at the Asian Institute of Technology (AIT) in Thailand. I had my presentation in English in front of many foreigners for the first time and also I was able to listen to various presentations of other foreign students. Actually, I am studying about the structure analysis in master's course, so I don't know well other parts of civil engineering. Nevertheless it was very interesting and really good experience to me because I seldom had a chance to listen to other fields of civil engineering. Lastly, I want to thank all of people attended this seminar for giving me a chance to have wonderful memories in Thailand. I hope this Joint Student Seminar will be activated and held continuously.

(by Choi, Sung Woo)

The first joint student seminar was so impressive. I would like to express my sincere thanks to all participants, particularly to the organizing team who brought this seminar to one of my memorable events at AIT. The thing I loved most is that every student can have their own stage to present and contribute their scholastic idea along with listening to others. I really wish not only the continuance of this precious activity, but also the long-lasting relationship among the participants.

(by Adisorn Owatsiriwong)

This is the first time for me to join the international conference as a presenter. It can be said that a lot of presentation experience has been gained through the conference. Moreover, this is a good chance for me to know more about education in other country and can improve my English skill. I hope that I could join the next year conference.

(by Tran Viet Dung)

It is my great opportunity to present my research work at the Joint Student Seminar on Civil Infrastructures held at Asian Institute of Technology, Thailand. I get appreciably not only the experience in the presentation in the English communication, also the technical information from various fields in Civil Engineering which I never focus on. This seminar, in addition, pushes me to develop an idea and expand scope of the study in my doctoral dissertation. I finally would like to use this chance to thank all attendees who give me the valuable knowledge.
(by Ekkachai Yooprasertchai)

The Joint Student Seminar on Civil Infrastructures held at the Asian Institute of Technology (AIT) in Thailand on the 3rd and 4th of July, 2008. This was my first time to give a presentation in front of foreign students and researchers. I learned that the most important thing when presenting is to make listeners understand. It really cheered me up to develop English skills. The other students' presentations were from a wide variety of fields, which gave me the chance to learn about different areas in civil engineering. They made me able to see things in perspective. I'm looking forward to joining AIT seminar again and appreciate the effort and work of everyone who organized and supported this great event. Finally, thank you everyone to make this conference.
(by Kittipong Suweero)